CARDIFF UNIVERSITY
PRIFYSGOL CAERDYDD

SCHOOL OF CHEMISTRY

A DFT study of graphite supported catalysts

Thesis submitted for the degree of Doctor of Philosophy

by Carlo Buono

September 2016

Acknowledgments

I would like to thank all the people who contributed in some way to the research project which is described in this thesis. Firstly, this work would not been possible without the constant support, the continuous encouragement and the excellent guidance of my two supervisors: Dr. Dave J. Willock and Prof. Philip R. Davies.

I would like to express my special appreciation and thanks to my mentor Prof. Peter Knowles and my tutor Prof. Kenneth Harris for the many useful advices and precious suggestions they gave me during the progression meetings.

Thank you to all the members of the theoretical group at Cardiff University: Prof. Peter Knowles, Dr. James Platts and Dr. Stefano Leoni and to their research students for the many hours we spent together discussing and collaborating on various research projects.

Thank you to all the members of the Dr Willock's research group. Although during these three years so many students have stepped in the room 5.19 that I cannot recall their names, I will always cherish the happy memories of the serene and funny experiences (Fridays' breakfasts and conference travels are included) I spent with my closest collaborators: Costantinos Zeinalipour-Yazdi, Adam Thetford, Filippo Marozzelli, Soon Wen Hoh, Christopher Lee, Liam Thomas, Christian Reece and Shaoliang Guan.

I would like to thank the many students which are part of the Prof. Davies and Prof. Mike Bowker groups for the interesting and stimulating scientific discussions we had every Wednesday morning about XPS and AFM experiments.

Above all, my deepest expression of gratitude goes to my parents and my sister. Their love, support and motivational talks have largely contributed to make my dreams come true.

This research was supported by EPSRC Grant EP/I038748/1 and the Cardiff University. Computing resources were obtained locally from the Cardiff ARCCA division, HPC-Wales and via our membership of the UK's HPC Materials Chemistry Consortium (EPSRC EP/L000202), this work made use of the facilities of HECToR and ARCHER, the UK's national high-performance computing service, which is funded by the Office of Science and Technology through EPSRC's High End Computing Programme.

Published Papers

- **The functionalisation of graphite surface with nitric acid: Identification of functional groups and their effect on gold deposition**
  Rebecca Burgess, Carlo Buono, Philip R. Davies, Robert J. Davies, Thomas Legge, Amy Lay, Rayan Lewis, Neil Robinson, David J. Willock
  Journal of Catalysis 323 (2015) 10-18.

- **Spectroscopic and atomic force studies of the functionalisation of carbon surfaces: new insights into the role of the surface topography and specific chemical states.**
  Carlo Buono, Philip R. Davies, Robert J. Davies, Thomas Jones, Jiří Kulhavýc, Ryan Lewis, David J. Morgan, Neil Robinson and David J. Willock, Faraday Discussions 173 (2014) 257-272.

Table of Contents

Abstract

Gold catalysed hydrochlorination of acetylene is a convenient alternative to the use of toxic mercury derivatives in large scale production of vinyl chloride. The catalytic performance of supported gold nanoparticles is highly dependent on a series of factors. Amongst them the catalyst support plays a fundamental role. Acid wash of carbonaceous supports has proven to influence the catalytic performances of gold nanoparticles. Atomic force microscopy revealed that after acid treatments the morphology of the graphite support presents spherical features. X-ray photoemission spectra detected the presence of hydroxyl and carbonyl groups which were formed at the surface sites after acid treatments. DFT calculations have been used to give an insight on the mechanisms of formation these features, functional groups and, to support the experimental data. In good agreement with the experiment, it has been found that when water molecules are intercalated within the interlayer space, the graphitic surface presents a curvature and the interlayer distance is largely increased. While pristine graphite is hydrophobic and inert to water, defective surfaces presenting under coordinated carbons show increased reactivity and are able to dissociate water also at room temperature. Pristine graphite surface has a poor particle adhesion but unsaturated carbons of defects or edges can chemisorb atoms and molecules to form strong bonds. Finally, in good agreement with the experiment, DFT results show that the interactions between gold nanoparticles and the hydroxyl groups are stronger than those between gold and carboxyl groups suggesting that the hydroxyls are better anchoring sites for gold nanoparticles than carbonyls.

To Cardiff City, where I met friendly people.

Chapter 1

In the past, gold was considered an inert metal, less reactive than its neighbours in the periodic table but the recent years have seen a revolution in the gold chemistry. The discovering of the exceptional catalytic activity of gold nanoparticles finely dispersed on inorganic oxide paved the way to a new research field in heterogeneous catalysis. Since the seminal discovery of Haruta and co-workers [1] that Au nanoparticles are catalytically active toward CO oxidation at sub-zero temperatures, research efforts have increased exponentially to explore the potential of gold as catalyst.

1. Introduction

The seminal discovery of Haruta and co-workers that gold nanoparticles are catalytically active toward CO oxidation at sub-zero temperatures [1] led to an exponential increasing of the research efforts in exploring the potential of gold in catalysis [2-5]. Gold has been found as an effective catalyst for a wide range of reactions, such as the oxidation of alcohols [6] and aldehydes [7], the hydrogenation of the nitro group in the synthesis of anilines [8] and the addition of hydrochloric acid to acetylene and higher alkynes to form the vinyl chloride for the industrial production of polyvinyl chloride via a mercury free route [9]. These applications have also shown how the performance of gold catalysts depends on several variables, but the factor which plays a key role is related to the dimensions of the nanoparticles which need to be maintained into a given nanometre range [10]. In the pioneering research works, gold nanoparticles were detected to have strong interactions with reactive oxide surfaces [11] and it was soon clear, from these early observations, that gold cations (Au^{+}/Au^{3+}) were the catalytically active species. The

size, electric properties and geometry of gold nanoparticles are intimately related to their interactions with materials. For instance, exceptionally high activities for oxidation of CO have been reported for highly dispersed Au on reducible oxides, such as TiO_2, Fe_2O_3, and NiO that has revealed the role of the support in supplying oxygen to form active oxidic gold sites [12]. Haruta et al., in particular, proposed that sites at gold-support interface are responsible for the activity of CO oxidation [1]. The high activities for gold catalysed oxidation of CO have been also attributed to the charge transfer between the support which presents negatively charged defects and the Au particles [1]. The range of gold catalysed reactions, as well as the suitability of different supports and the influence of the preparation conditions have been widely explored and optimized in applied research. The aim of the following sections is that of describing some of the aspects which are relevant in catalysis by gold. Firstly, some of the most important chemical processes catalysed by gold are briefly discussed. Since the chosen preparation method of the catalyst has a great influence in enhancing the catalytic activity, the conventional methods used to load gold on the supports are presented.

2. A brief overview on gold catalysed reactions.

The range of reactions catalysed by gold is wide. It spans from selective hydrogenation reactions to selective oxidation reactions including many other reactions which are extensively used in industrial applications.

In this section, a brief overview of the most popular reactions, proceeding well by gold catalysts, is given with emphasis on the advantages of using gold as catalysts instead of other transition metals.

Selective hydrogenation of alkenes and dienes is one of the most important industrial process. In the past metals such as Ni, Ru, and Pt catalysts were preferentially used. Since gold shows a strong resistance toward oxidation reactions, it was considered a poor catalyst. Only at the end of the 1980s, when it was proven that depositing with the opportune methodology gold nanoparticles on different supports gave active catalysts, gold was tested again in hydrogenation reactions and resulted in a very promising catalyst especially in selective hydrogenation reactions.

Amongst the hydrogenation reactions the selective hydrogenation of 1,3-butadiene to butene has been investigated since the 1970s. The hydrogenation reaction of the 1,3-butadiene may produce three isomers of butene, namely, 1-butene (Fig. 1, structure 1), *trans*-2-butene (Fig.1, structure 2) and *cis-2*-butene (Fig. 1, structure 3) [12]:

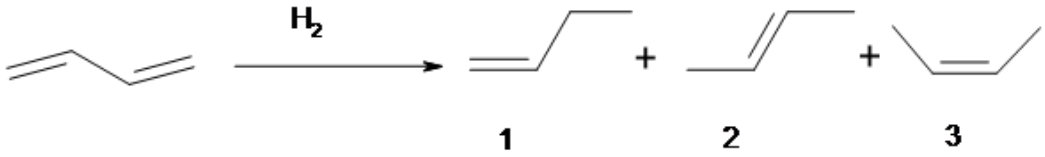

Fig. 1 – Possible isomers which are produced in the 1,3-butadiene hydrogenation reaction: 1) 1-butene, 2) *trans*-2-butene and 3) *cis*-2-butene. The reaction process has been adapted from reference [12].

When the reaction was catalysed by gold/Al_2O_3, the conversion from 1,3-butadiene was complete and the formation of 1-butene exceeded the 60%. Thus, it was shown for the first time that supported nano-gold catalyst prepared by deposition-precipitation method exhibited better catalytic performance. The effect of the support was studied considering other oxides such as TiO_2, CeO_2, Al_2O_3 and ZrO_2 which did not show any significant difference on the catalytic activity [13]. Finally, Xu et al. [14] reported a simple method for preparing zirconia-supported nano-gold catalyst with low gold loading. The catalysts showed high activity for selective hydrogenation of 1,3-butadiene without the formation of butane as byproduct. In addition, by characterisation of the catalyst with TPR and XPS, it was possible to demonstrate that the most active sites for the selective hydrogenation were the isolated Au^{3+} ions at the zirconia surface. Successively, it was suggested that gold oxidation state and hydroxyl groups on the support oxide surface play a crucial role. In fact, if hydroxyl were removed from the surface by high temperature, the catalyst became inactive. The catalyst activity could be re-established if the support was treated with water.

The hydrogenation of α,β-unsaturated aldehydes to unsaturated alcohols is another example of a successful application of the gold catalysis. The selective hydrogenation of an α,β-unsaturated aldehyde to α,β-unsaturated alcohol leads to saturate aldehydes or saturated alcohols when the conventional hydrogenation is used (Fig 2). In fact, the addition of H_2 to a C=C double bond is thermodynamically favoured than the hydrogenation of the carbonyl group, C=O. In addition, due to kinetic reasons the C=C double bond is also more reactive. Hutching et al. investigated on the hydrogenation of crotonaldehyde by catalysed by gold nanoparticles deposited on ZnO, ZrO_2 and SiO_2 [15]. They observed an improved selectivity to crotyl alchol when catalytic amount of thiophene was added into the reaction flow. Thiophene and its byproducts modify the

surface of Au as evidenced by the FT-IR study. In addition, the influence of the support was detected. In fact, hydrogenation of crotonaldheyde via Au/ZnO catalyst gave more than 80% of crotyl alcohol with 7.7 % crotonaldehyde conversion.

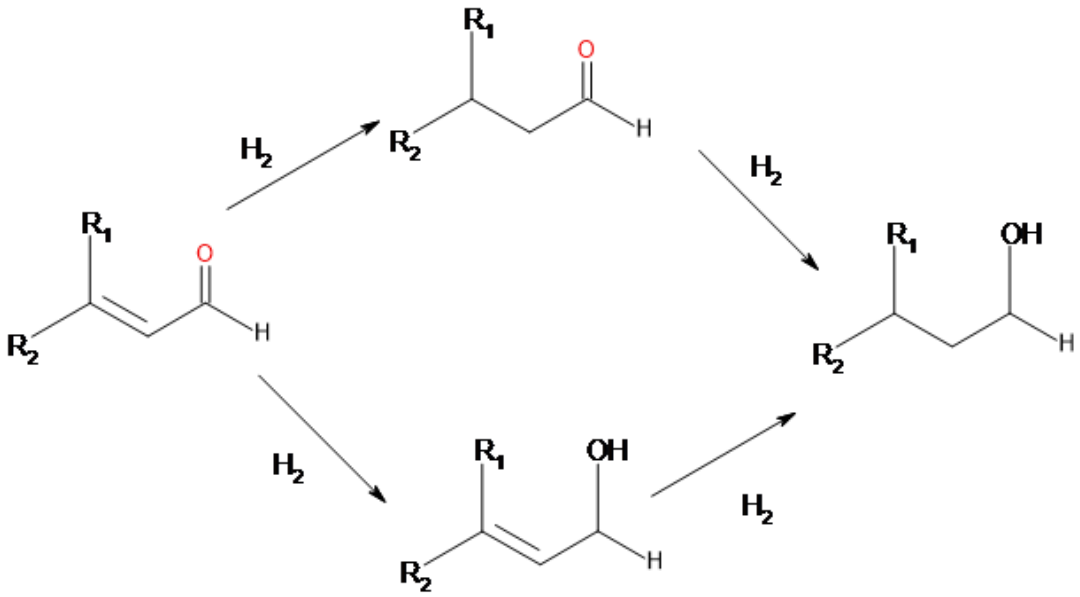

Fig 2. Conventional hydrogenation of α,β-unsaturated aldehydes to saturate alcohols. Figure adapted from reference [16]

Industrial methods for the conversion of a nitroarene to aniline require catalytic hydrogenation reactions. The catalytic reduction of chloronitrobenzene leading to aromatic amines which are used in pharmaceuticals, dyes and ligands for transition metal-catalysts has been extensively investigated. It has been reported that nano-gold catalysis overcomes the problem of the limited selectivity of hydrogenation as it was observed in the gold-catalysed selective reduction of chlorobenzene. The gold catalyst was supported by SiO_2 and under optimised conditions, i.e., 140 C, 4.0 MPa H_2, and 2-5 h, the conversion of the *o*-, *m*- and *p*-chloronitrobenzene was of 100%. Such a catalyst is also active for the hydrogenation of other nitrobenzene with different functional groups [17]. Gold on ZnO_2 is an efficient catalyst for selective hydrogenation of chlorobenzenes with the benefit that dechlorination is not required.

The hydrogenation of anhydrides is also another important industrial process. An example of this class of reactions is given by reduction of succinic anhydride to γ-butyrolactone and pyrrolidone. These are important solvents or fine chemical

intermediates in industry. The hydrogenation of succinic anhydride is catalysed by Au/TiO_2. In the case of γ-butyrrolactone the obtained selectivity was of 99% at 80% conversion. The catalytic efficiency can be improved without decreasing in sectivity by addition of a small amount of Pt. Au/TiO_2 catalyses the synthesis of pyrrolidone and pyrrolidone derivatives from succinic anhydrides and ammines with more than 80% of conversion. Fig. 3 shows the scheme of hydrogenation and successive dehydrogenation of succinic anhydride to produce γ-butyrolactone and pyrrolidone [18].

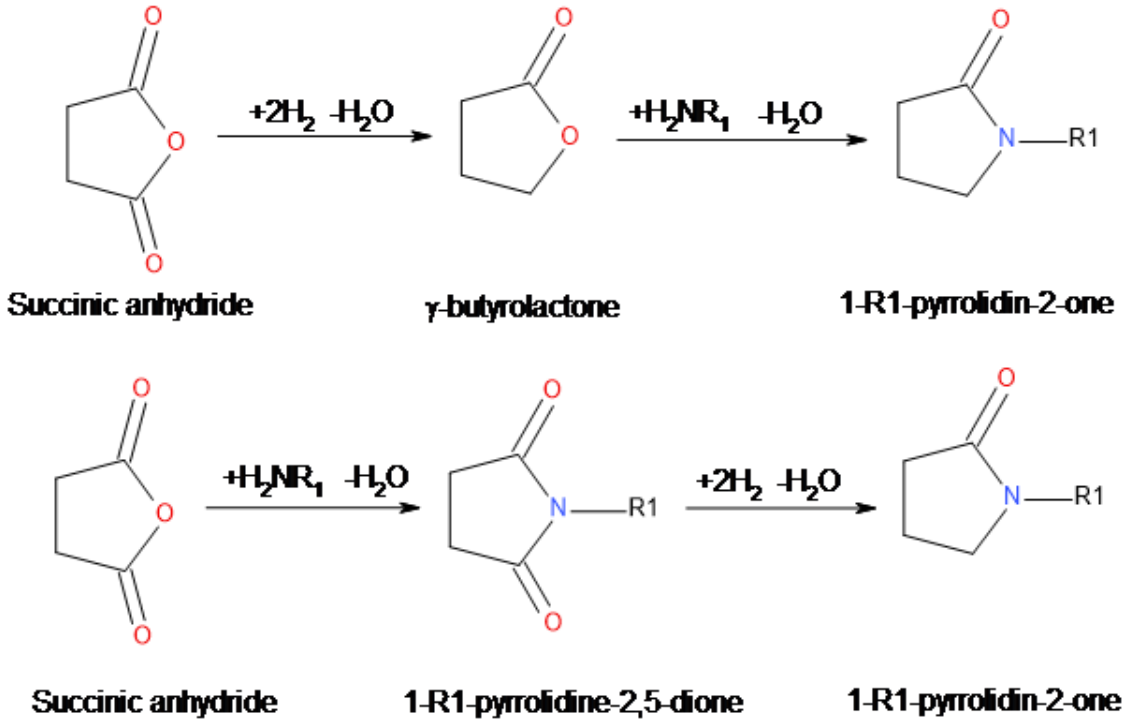

Fig. 3 Hydrogenation and dehydrogenation of succinic anhydride to form γ-butyrolactone and 1-pyrrolidone derivatives. The figure has been adapted from reference [18]

Another important class of reactions with large applications in industry is represented by the selective oxidation reactions. These reactions permit to convert bulk chemical to useful products of higher oxidation states and the development of green oxidation system is one of the most important challenges in catalysis.

The most representative gold catalysed oxidation is surely the selective oxidation of alkanes. Hutchings [19] and collaborators were the first to studying the benzylic and allylic C-H bonds by Au/C and Bi-Au/C. The first investigation was made on selective oxidation of cyclohexene. This study revealed the role that the solvent plays in this class

of reactions. In a polar solvent such as water, methanol or tetrahydrofuran no reaction was observed. A mixture of products was obtained when the 5% of *ter*-butyl hydroperoxide was added to the solution. In 1,3,5-trimethylbenzene, the main product was cyclohex-2-enone with a selectivity of 78.1% and 8% conversion. When 1,4-dimethyl benzene was used as solvent, the main product was cyclohexane-1,2-dione with 45% selectivity and 53.5% conversion.

One of the starting point in pharmaceutical preparations and fine chemicals is the selective epoxidation of olefins with air, O_2 and H_2/O_2. An example of epoxidation proceeding via gold catalyst was studied by Haruta et al. [20] who presented an application of nano-gold catalyst immobilised on titania in presence of a mixture of H_2/O_2 to selectively oxidize propylene to propylene epoxide. Other catalysts such as Pt/TiO_2, Pd/TiO_2, Cu/TiO_2 and Ag/TiO_2 were investigated for comparison. The results suggested that Au and TiO_2 crucial for selective epoxidation of propylene. When the catalytic conditions were optimised the selectivity to epoxide reached the 90% and the formation of the major byproduct, CO_2, was 1-2%.

Aldehydes and ketones are used in the cosmetic industries for producing flavours, fragrances and biologically active compounds. A conventional methods to produce carbonyls is the oxidation of alcohols in presence of a stoichiometric amount of $K_2Cr_2O_7$ as an oxidising agent. Since salts of chromium (III) and (VI) are toxic, gold nanoparticles represent a safer alternative for oxidizing alcohols.

The first kind of catalytic system proposed for the oxidation process of alcohols consisted of gold nanoparticles on iron oxide. Such a system resulted effective for the selective oxidation of *o*-hydroxybenzylalcohol to *o*-hydeoxybenzadhyde but the conversion and selectivity were not very high. A better performance was found when gold nanoparticles were supported on ceria nanoparticles. This catalytic system gave more than 90% conversion and selectivity [21].

Many other chemical processes have been investigated by using gold as catalyst. Amongst many other reactions gold catalysis has been found useful in the chemical processes such as selective oxidation reactions of 1,4-diols [22], amines [23], silanes [24] and aldehydes [25] and so on.

One of the chemical processes which, in the last few decades, has attracted large interest in gold catalysis is the addition reaction of HCl to alkynes and in particular, the hydrochlorination of acetylene. The addition of the acid to the alkynes is an alternative process to produce vinyl chloride monomer (VCM). VCM is the precursor of polyvinyl

chloride (PVC) a plastic that has the third-highest global volume after polyethylene and polypropylene because of its excellent physical and chemical properties. PVC has many applications, such as water pipes, ceiling tiles, clothes, electric wires, portable electronic accessories, etc.

There are two possible methods for the industrial production of vinyl chloride monomer depending on the starting organic substrates. Two building blocks are ethylene and acetylene. Ethylene is produced from the cracking of hydrocarbon fractions obtained from distillation of natural gas and oil, it is manufactured to produce VCM in those countries where fossil oil is abundant. On the other hand, acetylene which is obtained from coal pyrolysis in hydrogen atmosphere is converted in VCM prevalently in those Countries where coal resources are vast.

Since VCM production is very relevant to this thesis work, it will be discussed in more details.

The industrial manufacturing of VCM through ethylene route is obtained by the balanced process which consists of four steps: direct chlorination, oxychlorination, pyrolysis and quench and vinyl chloride purification [26-28].

The chlorination of ethylene can be carried out by the direct use of chlorine according to the reaction:

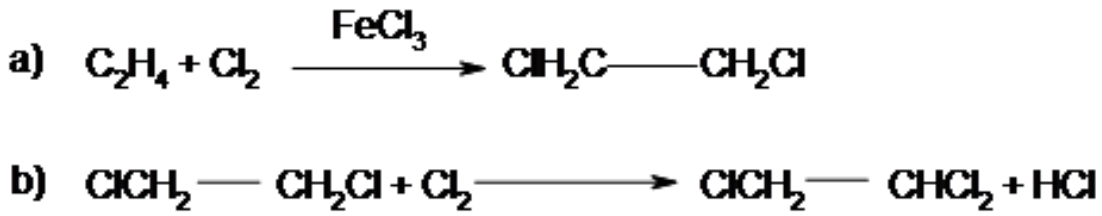

Fig. 4 a) Chlorination process of ethylene. b) The formation process of the 1,1,2-trichloroethane as reaction secondary product. The process has been adapted from references [26,27].

In the chlorination process, the reactants and the catalyst are dissolved in a solvent which is also the reaction product, 1,2-dichloroethane. With the aim to preserve the selectivity, the catalyst has to be used in diluted concentrations, usually between 0.1 and 0.5% wt.

Oxychlorination of ethylene is the other industrial process useful to convert the alkene in 1,2-dichloroethane. The industrial importance of this process consists mainly in avoiding corrosive degradation of the reactor which is due to the action hydrogen chloride.
The oxychlorination occurs in gas phase as liquid phase process has not industrial applications. In the industrial process, gaseous ethylene and oxygen react with hydrogen chloride coming from the vinyl chloride purification section in presence of the heterogeneous catalyst $CuCl_2$. Such a process is described in Fig. 5.

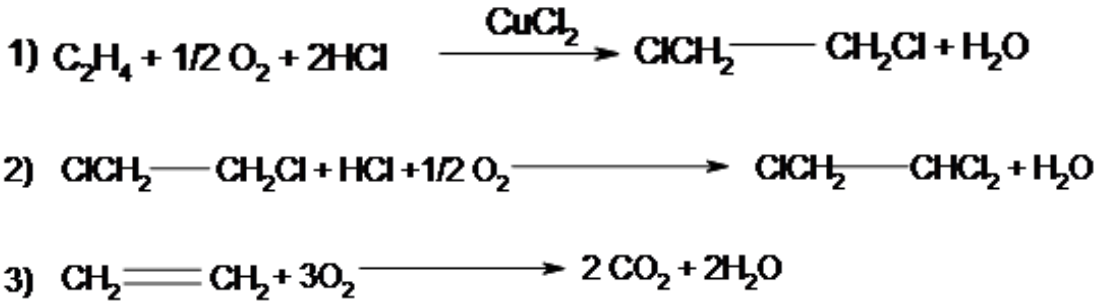

Fig. 5 Reaction 1): Oxychlorination process to convert ethylene in 1,1,2-trichloroethane.
Reaction 2): formation of the 1,1,2-trichloretane from 1,2-dichloroethane.
Reaction 3) oxidation of ethylene to carbon dioxide and water.
The processes have been adapted from references [27, 28].

In Fig. 5, the first reaction describes the process to obtain 1,1,2-trichloroethane by the oxychlorination reaction. The selectivity and conversion in the oxychlorination process is lower than in the direct chlorination process. The former varies from 90% to 96% whereas the latter usually spans in the range between 80% and 96%. The products of the reaction are: 1,1,2-dichloroethene which can be formed via direct oxychlorination of ethylene (Fig. 5, reaction 1)) or via further chlorination of 1,2-dichloroethane (Fig.5 reaction 2)). In addition, by complete combustion of ethylene, carbon dioxide is formed (Fig. 5 reaction 3)).
After production and purification of 1,2-dichloroethane, vinyl chloride is finally produced by thermal cracking according to the following reaction of Fig. 6.

Fig. 6 pyrolysis of 1,2-dichloroethane and vinyl chloride formation. The figure has been adapted from reference [26].

The reaction is highly endothermic and takes place in gas phase. This process can be quenched lowering the temperature of the reaction. Quenching is needed to avoid that vinyl chloride is decomposed or other byproducts are formed during the pyrolysis.

The last step of balanced process consists in the achievement of purified vinyl chloride and in recovering the dichloroethane and HCl which are formed during the oxychlorination and pyrolysis processes, respectively. The conversion of ethylene to vinyl chloride is an industrial process which was introduced in the second half of the 50's after the optimisation of the oxychlorination process by Dow chemicals. These process as already introduced above is one of the two possible routes for the production of vinyl chloride monomer.

The other alternative route for the manufacturing of VCM is the hydrochlorination of acetylene. This is the oldest method to produce VCM and is commonly manufactured via activated carbon-supported mercuric chloride catalyst.

Mercury containing salts have been found to be highly toxic and the Minamata convention on mercury in 2013 restricted the application of products containing such a heavy metal on a global scale in 2020 [29].

Consequently the industrial and scientific community are encouraged to explore a green non-mercury catalyst to replace mercury and its derivatives.

Since the 60's many investigations attempted to find an alternative to the mercury catalyst. In 1968, Smith et al. [30] suggested that the catalytic activity was related to the electronic affinity of the metal used as catalyst. In this study the authors investigated on a series of silica-supported metal chloride catalysts for the acetylene hydrochlorination. Successively, in 1975 Shinoda et al. [31] investigated on the acetylene hydrochlorination reaction considering 20 types of metal chloride salts as catalyst. A decade later, Hutchings [32-33] demonstrated how the activity of a metal could be correlated to the standard electrode potential of the metal used to carry out the hydrochlorination reaction and showed that the correlation predicts gold to be the most effective metal for the catalytic hydrogenation of acetylene.

The mechanism of gold catalysed acetylene hydrochlorination was proposed by Hutchings et al. [34] using density functional theory and is summarised in Fig. 7.

The surface energy profile of Fig. 7 suggests that the first reaction step consists in the formation of a complex where the acetylene coordinates on $AuCl_3$ catalyst. The coordination of acetylene at metallic centre activates the triple bond which undergoes to

the nucleophilic attack from the chlorine from HCl. The transition state (structure 7) shows the concerted formation of the bonds C-Cl and C-H and is found when the reactants overcome an energy barrier of 98 kJ mol^{-1}. The final product is formed after a barrierless proton transfer. The overall process leading to vinyl chloride is exothermic of 203 kJ mol^{-1}.

The second reaction pathway presents an energy barrier (structure 4 of Fig. 7) of 69 kJ mol^{-1} with respect to the reactants and 114 kJ mol^{-1} with respect to the products. At room temperature this barrier can be overcame easily and reactants and products can be considered in equilibrium. Finally, the coordination of HCl on gold is found at -105 kJ mol^{-1} (structure 2 of Fig. 7). This structure is higher, in energy, than structure 3 of Fig. 7 which is more stable and is preferentially formed.

In the same work, Hutching and collaborators used higher alkynes to investigate on the possible regioselectivity and stereoselectivity of the addition of HCl by gold catalyst. The addition reaction on hex-1-yne was found to display very high selectivity toward the Markovnikov products (only traces of the anti-Marcovnikov products were found). In addition, the NMR analysis of deuterated substrates confirmed that the HCl is added on alkyne by the *anti*-stereochemistry.

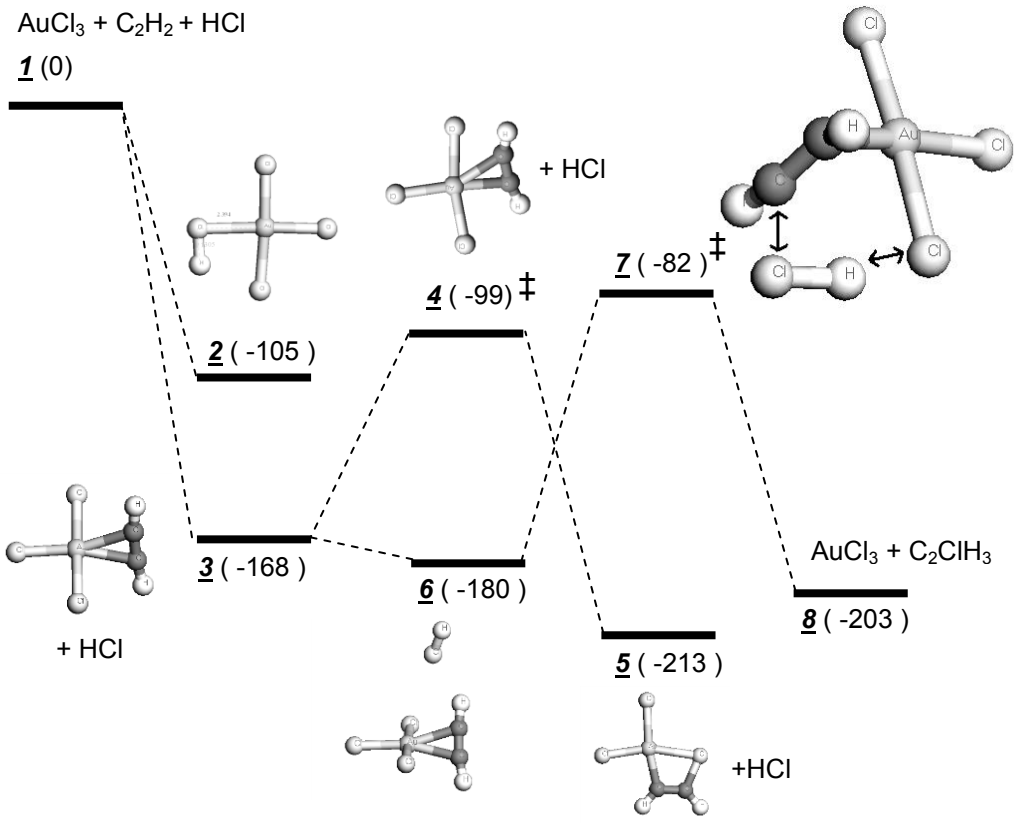

Fig. 7 Reaction energy profile for hydrochlorination of acetylene, all energies are in kJ mol^{-1}. The picture has been adapted from reference [34] by author permission.

Although gold can be considered the best catalyst in terms of initial activity, deactivation problems occur during the reaction. The most important deactivation pathways have been identified as the Au^{3+} reduction and oligomer formation over the surface of the catalyst. While the oligomer formation can be minimised by modification of the temperature conditions, the Au^{3+} reduction is inevitable.

3. Survey of gold catalyst preparation methods.

One of the distinctive advantages of gold catalysis over the other metal based catalysis such as Ni, Ru, Pt and Pd is mainly represented by the large variety of methods available to prepare the supported catalyst. Amongst these methods, the most conventional ones are: deposition-precipitation (DP), chemical vapour deposition (CVD), cation adsorption (CA), impregnation (IMP), anion adsorption (AA) and the deposition of colloidal gold onto support.

Because the choice of the preparation methods plays a crucial role in enhancing the activity of the catalyst, in this section, the main aspects of these methods are briefly described.

Au loading over reducible oxide supports is often accomplished by DP. Such a method consists in precipitating the metal as hydroxide on an oxide support. The preparation protocol requires the use of an aqueous solution of tetrachloroauric acid, $HAuCl_4$. When the support is added to the solution of the precursor, the pH is raised to a fixed value adding NaOH or Na_2CO_3. Under stirring, the solution is heated for about one hour at the temperature of about 350 K. To remove sodium and chlorine impurities, the product is washed with water and dried under vacuum at 373 K.

The influence of the solution pH has been reported only for few supports. Amongst them, the study on gold deposition over titania substrates has shown interesting results. In fact, it was observed that the pH range between the values of 7-8 gives a good compromise between gold loading and sizes of gold particles [35-37]. Higher pH values result in a decreasing of the gold loading which is due to an increasing of the $Au(OH)_3$ solubility. The influence of pH on the process of gold loading over titania support was explained considering that at pH values slightly higher than 6, a coordination complex between gold and the surface is formed. The process is described by the following equation:

Equation 1. Surface complex formation. The equation is adapted from reference [37].

To confirm the validity of the suggested deposition process which is described in (Eq. 1) an extended X-ray absorption fine structure spectroscopy (XAFS) study was carried out [38]. The investigation was conducted in an alkaline solution (pH = 8) and before washing the Au loaded substrate. Thus, under these conditions, the XAFS characterisation detected only the presence of oxygens in the first coordination sphere of gold.

There are several variants of the DP method where the values of pH, preparation and washing temperatures can be slightly different from those mentioned above. In some case, the alkaline reactants NaOH and Na_2CO_3 can be replaced by ammonia. A popular variation of the DP method makes use of urea [39]. The organic compound has the task to delay the hydrolysis which takes place only when the solution of the support and the aqueous gold salt is heated at 333 K. In fact, under such temperature conditions, the urea hydrolyses according to the following equation:

Equation 2. Dissociation reaction of urea in H_2O. Images adapted from reference [39]

leading to a gradual and homogenous releasing of hydroxyl ions and an increasing of the solution pH.

The chemical vapour deposition (CVD) is another widely used method to deposit gold on supports. The CVD involves the use of an organogold compound, dimethyl gold acetylacetonate ($Me_2Au(acac)$), which, reacting over the surface of a support, decomposes to neutral gold nanoparticles or, in the case of a support having a flat and regular surface, to a thin and coherent film.

The CVD method leads, after calcinations, to small gold particles but with a wider size distribution than is given by DP [40].

The advantage of this technique is mainly due to the absence of chlorine in the $Me_2Au(acac)$ precursor which is also commercially available. On the other hand, the

preparation of the supports with this method has the drawback to be conducted in complete absence of air.

The cation exchange and adsorption (CA) is another efficient way for introducing high dispersed gold nanoparticles into zeolites by cation exchange. The CA uses the *bis*-ethylenediamine Au(III) cation as precursor. The ion exchange by bis-ethylenediamine Au (III) cation works well not for depositing gold on zeolites or activated carbon fibres but also for depositing the metal on oxide supports by cation adsorption. For instance, by CA, it is possible to deposit gold on the TiO_2. In this case several precautions have to be taken. First of all, as the bis-ethylenediamine Au (III) cation decomposes at 333 K, the preparation of the support has to be made at room temperature. In addition, because cations are adsorbed through electrostatic interactions on the negatively charged surface of the support, the solution pH has to be higher than the point of zero charge. Thus, by CA, gold was deposited onto the TiO_2 surface at room temperature and pH 9 leading, after calcination at 573 K, to 2.5 nm particles [41].

Historically, the very first supported gold catalysts were obtained via impregnation method (IMP) which is the simplest known method to load gold over a given support and can be used with large variety of surfaces. The chloroauric acid ($HAuCl_4$), gold chloride and ethylenediammine complex ($[Au(en)_2]Cl_3$) are the widely used precursor in IMP. By impregnation, gold was loaded on oxide supports such as silica, alumina, titania, ferric oxide and magnesia. However, it was observed the presence of large gold particles responsible of the poor activity of the catalysts [42].

When the pH of the solution is lower than the point of the zero charge of the support, the support surface is positively charged. This circumstance allows the deposition of aqueous anionic gold complexes resulting from $HAuCl_4$. This method to deposit gold on the surface of a support material is known as anion adsorption (AA). The AA was investigated for preparing the gold catalyst on the TiO_2 support. Diverse temperature conditions and a fixed pH of 2 were used in this study but the gold loading was of about 1.5 wt.% and the diameter of the particles exceeded the 4 nm [43].

Small gold particles can also be deposited on a support by colloidal dispersions. Colloidal state of the gold has been largely investigated. The colloidal route for preparing supported gold catalysts has the main advantage to permit the manipulation of the preparation conditions which influence the size and size distribution of the particles. In fact, since the main factor governing the mean size and size distribution is the relative rate of nucleation and growth, to get a narrow size distribution of small particles, the necessary

conditions to obtain a rapid production of a large number of small nuclei have to be created and when larger nuclei are forming the growth process must be immediately terminated [44].

The initial work of J. Turkevich *et al*. [45] investigated on the nucleation of gold particles using the anion and sodium citrate as reducing agent . Large particles were obtained when a standard concentration of the anion was used. However, smaller particles of 1-2 nm range, resulting from a faster nucleation, were obtained when the anion concentration was doubled. Under these conditions, the nuclei are initially formed as chains of gold atoms or ions with reductant or its oxidation product.

A large variety of reducing agents can be used in combination with the anion to form small gold nanoparticles. Amongst them, white phosphorus in diethylether produces 5 nm particles. Small particles may be obtained by other reducing agents such as sodium thiocyanate, poly(ethylene-imine) and sodium borohydride. In addition, the reduction to atoms of metal ions can be achieved by generation of electrons resulting from X-rays irradiation or accelerated electron pulses. In this case, reduction of $HAuCl_4$ is obtained in presence of stabilising agents such as CN^- and EDTA or polymers capable to avoid the beginning of the reduction before the irradiation. Such a technique guarantees smaller particles and the size distribution is narrower as the rate of the irradiation dosage is increased [46].

The size of gold particles is a very important parameter in obtaining active catalysts for many reactions and, thus, it is required that several variables have to be considered when the metal is deposited onto the support. Most of the methods suitable to deposit gold involve $HAuCl_4$ which is a source of chlorine. Chlorine encourages the mobility of gold and particle aggregation that is detrimental to obtain small particles and the desired catalytic activity. A good strategy to reduce the chlorine amount in DP consists in maintaining the pH of the solution quite high. Under this conditions, the hydrolysis of the Au-Cl bonds takes place and by successive washing with water, at the end of the preparation, it is possible to remove chloride. On the other hand, when the gold deposition is performed by the anion adsorption technique, the pH of the solution has to be maintained low. At low pH values, the gold complexes still contains chlorine in their coordination sphere. An effective method to remove chloride after gold deposition consists in washing with a solution of ammonia which leads, after calcination, to gold nanoparticles which are smaller than those that were obtained by water washing. These results suggested to experiment other ways to obtain small metal particles leading to

some useful variants. For instance, if the catalyst precursor is washed with ammonia just after impregnation of the support, gold is not eliminated and, after calcination at 573 K, nanoparticles, of 3 nm in diameter, are obtained.

Although less popular, many other methods are suitable to deposit gold onto supports. Photochemical deposition [47], sol-gel method [48], spray [49] and sonochemical techniques [50] are just few examples of non-conventional deposition methods.

4. Influence of the preparation method on graphitic supports and thesis structure.

The preparation of the gold catalyst for the HCl addition to acetylene is usually carried out using an incipient wetness impregnation technique and aqua regia as a solvent. To remove impurities which can poison the catalyst the carbonaceous support has to be washed for 5 hours with diluted HCl which is kept warmed at 70 C. Carbon is then filtered and washed with distilled water and dried for 18 h at 140 C. Under stirring an aqueous solution of $HAuCl_4$ in aqua regia is added to the carbon. The obtained supported catalyst is dried for 18 h at 140 C [34]. The acid washing has the purpose of removing unwanted contaminants such as N, P, Si, Ca, Na, K, Al, Zn and Fe that accumulate on the carbonaceous surface during the preparation [51-53].

In addition, it is also though that by acid washing hydrophilic functional groups are introduced on the surface. These groups can modify the behaviour of carbonaceous materials toward the adsorption of active components and the reaction solvent. To better understand the effect of acid washing on the Au/C interface, a systematic investigation has been carried out by X-ray photoelectron spectroscopy (XPS), atomic force microscopy (AFM). The obtained results have been interpreted by the density functional theory study which is presented in this thesis work which is the result of a research aimed to investigate, understand and predict the experimental observations.

The work is organized as follows: Chapter 2 gives the key concepts in density functional theory and presents in some detail the modern approaches which are used to account for the dispersion interactions. Moreover, geometry optimisations and electron properties of graphite bulk and surface are also presented. In Chapter 3, the experimental results which have been obtained by AFM and XPS characterisations of hydrochloric acid washed graphite are discussed. Optimisations and calculated properties of pristine graphite surface and defected graphite surfaces and step edges are presented. Moreover, in this chapter the systematic investigation of the interaction between graphitic surfaces and water is also discussed. In Chapter 4, the treatment of graphite surfaces with diluted

HNO_3 is discussed. In this Chapter, interactions between gold clusters and functional groups at the surface sites are computationally investigated. Finally, Chapter 5 presents the conclusions and the agreements existing between experiments and computational investigations.

5. References

1. M. Haruta, T. Kobayashi, H. Sano and N. Yamada, Chem. Lett., 1987, 405.
2. G. C. Bond, C. Louis and D. T. Thompson, Catalysis by Gold. Imperial College Press, 2006.
3. M. Haruta, Chem. Rec., 2003, 3, 75.
4. G. J. Hutchings, Gold Bull., 2004, 37, 3.
5. R. Meyer, C. Lemire, S. K. Shaikhutdinov and H. Freund, Gold Bull., 2004, 37, 72.
6. Choudhary, V. R.; Dhar, A.; Jana, P.; Jha, R.; Uphade, B. S. Green Chem. 2005, 7, 768.
7. Protasova, L. N.; Rebrov, E. V.; Skelton, H. E.; Wheatley, A. E. H.; Schouten, J. C. Appl. Catal., A: Chem. 2011, 399, 12.
8. Chen, Y. Y.; Qiu, J. S.; Wang, X. K.; Xiu, J. H. J. Catal. 2006, 242, 227.
9. M. Conte, A. F. Carley, C. Heirene, D. J. Willock, P. Johnston, A. A. Herzing, C. J. Kiely and G. J. Hutchings, J. Catal. 2007, 250, 231-239.
10. Barbosa, S.; Agrawal, A.; Rodríguez-Lorenzo, L.; Pastoriza-Santos, I.; Alvarez-Puebla, A.R.; Kornowski, A.; Weller, H.; Liz-Marzán, L.-L. Langmuir 2010, 26, 14943–14950.

11. Ishida, T.; Haruta, M. ChemSusChem 2009, 2, 538.
12. Okumura, M.; Akita, T.; Haruta, M. Catal. Today 2002, 74, 2.
13. Hugon, A.; Delannoy, L.; Krafft, J.-M.; Louis, C. J. Phys. Chem. C 2010, 114, 10823.
14. Zhang, X.; Shi, H.; Xu, B. Q. Angew. Chem., Int. Ed. 2005, 44, 7132.
15. Bailie, J. E.; Abdullah, H. A.; Anderson, J. A.; Rochester, C. H.; Richardson, N. V.; Hodge, N.; Zhang, J.-G.; Burrows, A.; Kiely, C. J.; Hutchings, G. J. Phys. Chem. Chem. Phys. 2001, 3, 4113.
16. Liu, Z. P.; Wang, C. M.; Fan, K. N. Angew. Chem., Int. Ed. 2006, 45, 6865.
17. Chen, Y. Y.; Qiu, J. S.; Wang, X. K.; Xiu, J. H. J. Catal. 2006, 242, 227.
18. Budroni, G.; Corma, A. J. Catal. 2008, 257, 403.
19. Hughes, M. D.; Xu, Y. J.; Jenkins, P.; McMorn, P.; Landon, P.; Enache, D. I.; Carley, A. F.; Attard, G. A.; Hutchings, G. J.; King, F.; Stitt, E. H.; Johnston, P.; Griffin, K.; Kiely, C. J. Nature 2005, 437, 1132.
20. Hayashi, T.; Tanaka, K.; Haruta, M. J. Catal. 1998, 178, 566.
21. Milone, C.; Ingoglia, R.; Neri, G.; Pistone, A.; Galvagno, S. Appl. Catal., A: Chem. 2001, 211, 251.
22. Huang, J.; Dai, W. L.; Li, H. X.; Fan, K. J. Catal. 2007, 252, 69.
23. Aschwanden, L.; Mallat, T.; Grunwaldt, J. D.; Krumeich, F.; Baiker, A. J. Mol. Catal. A: Chem. 2009, 300, 111.
24. Mitsudome, T.; Noujima, A.; Mizugaki, T.; Jitsukawa, K.; Kaneda, K. Chem. Commun. 2009, 5302.
25. Biella, S.; Prati, L.; Rossi, M. J. Mol. Catal. A: Chem. 2003, 197, 207.
26. S. M. Al-Zahrani, A. M. Aljodai, and K. M. Wagialla, 56:621–626, 2001.
27. F. Benyahia. VCM process design. Chemical Engineering Education J., 39(1):62 67, 2005.
28. R. P. Arganbright and W. F. Yates.The Journal of Organic Chemistry 27:1205–1208, 1962.
29. Mackey, T.K.; Contreras, J.T.; Liang, B.A. The Minamata Convention on Mercury: Attempting to address the global controversy of dental amalgam use and mercury waste disposal. Sci. Total Environ. 2014, 472, 125–129.
30. Smith, D.M.;Walsh, P.M.; Slager, T.L. J. Catal. 1968, 11, 113–130.
31. Shinoda, K. Catal. Lett. 1975, 219–220.
32. Hutchings, G.J. J. Catal. 1985, 96, 292–295.

33. Conte, M.; Carley, A.; Attard, G.; Herzing, A.; Kiely, C.J.; Hutchings, G.J. J. Catal. 2008, 257, 190–198.
34. M. Conte, A. F. Carley, C. Heirene, D. J. Willock, P. Johnston, A. A. Herzing, C. J. Kiely and G. J. Hutchings, J. Catal., 2007, 250, 231–239.
35. F. Moreau, G.C. Bond and A.O. Taylor, Chem. Commun. (2004) 1642.
36. S. Tsubota, D.A.H. Cunningham, Y. Band o and M. Haruta, Stud. Surf. Sci. Catal. 91 (1995) 227.
37. F. Moreau, G.C. Bond and A.O. Taylor, J. Catal. 231 (2005) 105.
38. Y.A. Nechayev and N.V. Nikolenko, Geochem. Intern. 11 (1985) 1656.
39. M.A.P. Dekkers, M.J. Lippits and B.E. Nieuwenhuys, Catal. Lett. 56 (1998) 195.
40. P. Serp, P. Kalck and R. Fenner, Chem. Rev. 102 (2002) 3085.
41. D.A. Bulushev, I. Yuranov, E.I. Suvorova, P.A. BufFat and L. Kiwi-Minsker, J. Catal. 224 (2004) 8.
42. G.C. Bond and D.T. Thompson, Catal. Rev.-Sci. Eng. 41 (1999) 319.
43. P.A. Sermon, G.C. Bond and P.B. Wells, J. Chem. Soc. Faraday Trans. I 75 (1979) 385.
44. A.-Q. Wang, J.-H. Liu, S.D. Lin, H.-P. Lin and C.-Y. Mou, J. Catal. 233 (2005) 186.
45. G.C. Bond and J. Turkevich, Trans. Faraday Soc. 52 (1956) 1235.
46. J. Turkevich, Gold Bull. 18 (1985) 86, 123.
47. A. Fernandez, A. Caballero, A.R. Gonzalez-Elipe, J.-H. Herrmann, H. Dexpert and F. Villain, J. Phys. Chem. 99 (1995) 3303.
48. G.C. Bond and D.T. Thompson, Catal. Rev.-Sci. Eng. 41 (1999) 319.
49. L. Fan, N. Ichikuni, S. Shimazu and T. Uematsu, Appl. Catal. A: Gen. 246 (2003) 87.
50. A. Fasi, I. Palinko, J.W. Seo, Z. Konya, K. Hernadi and I. Klricsi, Chem. Phys. Lett. 372 (2003) 848.
51. Albers P, Deller K, Despeyroux BM, Prescher G, Schafer A, Seibold K. SIMS/XPS. J. Catal. 1994;150(2):368–75.
52. Wang S, Lu GQ. Carbon. 1998;36(3):283–92.

Chapter 2

In principle, the complete description of the quantum-mechanical behaviour of a molecular system of N interacting electrons is achieved by calculating the many-electron wavefunction which is the exact solution to the Schrödinger equation. However, due to the coupling between the motions of electrons and nuclei, the dynamics of a many-electron system is very complex and the exact solution to the Schrödinger equation cannot be found analytically. This chapter is meant to provide an introduction to the basic ideas behind theoretical methods which have been used throughout this work. Some of those, such as the Hartree-Fock method, are focused on calculating the many-body wavefunction. Others, the density functional formalism, for instance, attempt directly to solve the Schrödinger equation for the physical observable.

2.1 The many-body Schrödinger equation

The non-relativistic, time-independent Schrödinger equation (SE) describing the quantum mechanical behaviour of a molecular system of M nuclei and N interacting electrons in the state n can be written as follows

(2.1)

Where, the full Hamiltonian operator is

Here, r_i are the coordinates of electrons $(i = 1, 2, \ldots, N)$, R_A denotes the coordinates of nuclei $(R_A = 1, 2, \ldots, M)$, M_A and Z_A are mass and charge of the nucleus A, respectively. The first two terms, in 2.2, represent the kinetic energy operators for the N electrons and M nuclei, respectively. The third term is the external potential due to the M nuclei and, finally, the remaining two terms represent the electron-electron and nuclear-nuclear electrostatic potential operators, respectively. E_n is the total energy of the physical system in the n state and Ψ_n is the solution to the SE [1]. It is worth noting that, in the discussion of the molecular Hamiltonian, atomic units have been used. Employing the system of atomic units (au), as is done in the equation 2.2, is very useful for working with atoms and molecules because all equations appear in a very compact form without any fundamental physical constant. The au's relation to the corresponding SI units, which are used throughout this work, will be presented in more detail in the last part of this chapter.

In addition, because only the wavefunctions of ground state systems (n=0) are discussed, from now on, the subscript n, in Ψ_n and E_n, will be dropped.

In 2.1, Ψ is a function of the positions of electrons and nuclei and contains all the information about the molecular system under investigation. As the name suggests, in the context of the SE, the wavefunction is a description of a particle as a wave. In other words, it is a probabilistic description of the behaviour of those particles and evaluates their probability of being in a certain region of the space. This postulate places some constraints on the requirements for an acceptable wavefunction. For a bound particle, the normalised integral of over all the space has to be unity and this requires that Ψ has to be a continuous, single-valued and square-integrable function. Thus, by boundary conditions on the wavefunction, one can exactly solve the SE for some very simple physical systems such as the particle in a box, the harmonic oscillator, the particle on a ring, the particle on a sphere and the hydrogen atom but, for other simple physical systems presenting more than two particles, such as the ion (two nuclei and one

electron), for instance, the state of motion can be solved only in accordance with the Born-Oppenheimer approximation which is the topic of the next section.

2.2 The Born-Oppenheimer approximation

An attempt to reduce the many-body problem complexity in the SE is known as the Born-Oppenheimer (BO) or adiabatic approximation [2]. It consists of neglecting the coupling between nuclear and electron motions and is based on the large difference in electron and nuclear masses ($m_e << M_A$) [2]. Thus, considering the nuclear positions as fixed, the total wavefunction for a molecule can be simplified in a product of two wavefunctions, one for nuclei and the other for electrons:

. (2.3)

Thus, if the wavefunction Ψ_{tot}, in 2.3, replaces Ψ_n, in the equation 2.1, the SE can then be rewritten as

(nuclei)Ψ(electrons). (2.4)

It follows that, the total energy of the molecule, E_{tot}, can be expressed as sum of two contributions:

$$E_{tot.} = E_{elect.} + E_{nuclei} \quad (2.5)$$

where, $E_{elect.}$ and E_{nucei} are the electron and nuclear energies, respectively.

The solution to the electron problem requires the electron wavefunction to be found solving the electronic SE:

(2.6)

In 2.6, the wavefunction Ψ_{elect} describes the motion of electrons and depends explicitly on electron coordinates while accounts for the nuclear positions only parametrically. The electronic Hamiltonian is given by:

It comprises the kinetic and the potential operators for electrons moving in the electrostatic field of fixed nuclei and the electron-electron repulsion operator.

When the electronic problem has been solved, the total energy for clamped nuclei is obtained adding the constant term of the nuclear repulsion to the calculated electronic energy:

The evaluation of the total energy for a given molecular system is the main goal in computational chemistry and, by the BO approximation, it is possible to simplify the nuclear-electron coupling. The BO approximation has also proven effective for accurate determination of chemical reactions [3], molecular dynamics [4] and phonon frequencies in a wide range of metallic systems [5]. In spite of this, the BO approximation is not universally valid. It is well known, in fact, that it breaks down in some circumstances as, for example, when the energy gap between ground and excited electronic states is smaller than the energy scale of the nuclear motion.

In addition, the BO approximation is not, of course, relevant to polyelectronic systems with just one nucleus and thus, for such systems, approximate solutions to the SE have to be found following other ways.

2.3 Pauli's exclusion principle and Slater's determinants.

The total molecular Hamiltonian, as described above in 2.2, does not show any dependency on the electron spin, but to fully describe the electron behaviour in polyelectronic systems, one has to keep in mind that electrons are quantum particles with half-integer spin and, therefore, the intrinsic spin coordinate must be included in building up multi-electronic wavefunctions. In addition, electrons are indistinguishable and this means that the probability to find them in a given region of the space has not to change when position and spin coordinates of two electrons are switched:

$$|\Psi(\quad,\qquad\qquad)|^2 = |\Psi(\qquad\qquad\qquad)|^2. \qquad (2.9)$$

Here, $\Psi(\quad,\qquad\qquad)$ describes the N-electron wavefunction, whereas the represents the set of the space coordinates, and the spin variables, α and β.

Thus, in order to obtain a physically relevant solution to the SE, the many-electron wavefunction has to obey the antisymmetry principle. This principle is a restriction of a more general rule which is known as the Spin-Statistics theorem. Such a theorem was formulated by Wolfgang Pauli [6] and relates the spin of a particle to the particle statistics it obeys:

"...Systems of identical particles with half-integer spin (s = – –) have wavefunctions which are anti-symmetric under interchange of any pair of particle labels. The wave-function is said to obey Fermi-Dirac statistics ...."

In other words, the interchange of space and spin coordinates of any two fermions leads to a sign change in their wavefunction:

$$\Psi(\quad,\qquad\qquad) = -\,\Psi(\quad,\qquad\qquad). \qquad (2.10)$$

The Spin-Statistics theorem is supported by experimental evidence and represents the quantum-mechanical generalisation of Pauli's exclusion principle [6]:

No two identical fermions can be in the same quantum state. Once the form of a many-electron wavefunction has been determined, it is possible to look for the best ground state wavefunction by the application of variational principle. Such a principle allows one to judge the quality of the guessed wavefunction Φ_{guess} and can be expressed as follows:

Given a normalised wavefunction, Φ_{guess}, that satisfies the appropriate boundary conditions, then the expectation value of the Hamiltonian is an upper bound to the exact ground state energy:

$$E = \qquad \geq E_{guess} \qquad (2.11)$$

The equality, in 2.11, holds if and only if the approximate wavefunction Φ_{guess} is identical to the exact ground state wavefunction Ψ.

Since the energy of an approximate wavefunction is always too high, a measure of the quality of a wavefunction is its energy. The lower the energy, the better the wavefunction.

Usually, in computational quantum chemistry, the variational principle requires to alter the spin orbitals, $\chi_i(\mathbf{x}_i)$, under the constriction that they remain orthonormal.

The requirement that two or more spin orbitals are orthonormal is a mathematical device aimed to simplify the choice of computationally convenient wavefunctions.

An orbital is defined as a wavefunction for an electron. The term space orbital $\Psi(\mathbf{r})$ is referred to a function of the position vector, $\mathbf{r}$, which accounts for the distribution of the electron in the space such that $|\Psi(\mathbf{r})|^2 d\mathbf{r}$ is the probability of finding an electron in the small volume element $d\mathbf{r}$ surrounding r. Space orbitals are assumed to form an orthonormal set:

(2.12)

where, the Kronecker delta symbol, δ_{ij}, is a mathematical way for expressing that two functions are mutually orthogonal and normalized:

(2.13)

For computational convenience, the spin functions are often chosen to be orthonormal as well:

(2.14)

and

(2.15)

here, $\alpha(\sigma)$ and $\beta(\sigma)$, corresponding to spin up and spin down respectively, are functions of an unspecified spin variable, σ.

Since the N space orbitals and the two spin functions are orthonormal, it follows that the spin orbitals:

(2.16)

form a set of $2N$ functions which are also orthonormal:

(2.17)

To start obtaining *N*-electron wavefunctions, one can consider a very simple case that is given by an *N* non-interacting electron system. Neglecting the electron-electron repulsions, the *1*-electron Hamiltonian has the form

The operator, *h(i),* has a set of *N* eigenfunctions, the spin-orbitals $\{\chi_j(\mathbf{x}_i)\}$:

$$h(i)\chi_j(\mathbf{x}_i)=\varepsilon_i\chi_j(\mathbf{x}_i). \tag{2.19}$$

Because, in 2.18, is the sum of all *1*-electron Hamiltonians, a wavefunction, resulting from the product of spin orbitals for each electron, is known as Hartree product (HP), Ψ^{HP}, and has the form:

$$\Psi^{HP}(\mathbf{x}_1, \mathbf{x}_2, \ldots, \mathbf{x}_N)=\chi_i(\mathbf{x}_1)\chi_j(\mathbf{x}_2), \ldots, \chi_k(\mathbf{x}_N). \tag{2.20}$$

is an eigenfunction of :

$$=E$$

with eigenvalue *E*, which results from the sum of the spin orbital energies of each of the *1*-electron wavefunctions appearing in Ψ^{HP}. This method which is aimed to calculate the energy of a system considering its electrons as non-interacting is known as Hartree method.

While HP functional form is fairly convenient, it presents some shortcomings, amongst them, the HP gives an uncorrelated wavefunction and fails to satisfy the anti-symmetry principle.

For the simplest two-electron problem, one can correctly build up an anti-symmetrized wavefunction considering the only two possible Hartree products that can be obtained interchanging two electrons and two spin orbitals:

(2.22)

and

. (2.23)

At this point, one takes a linear combination of these two Hartree products to obtain

Ψ = . (2.24)

The quantity $2^{-1/2}$ is a normalisation factor. The negative sign guarantees that $\Psi(\boldsymbol{x}_1, \boldsymbol{x}_2)$ is anti-symmetric with respect to the interchange of coordinates of the two electrons. If both the electrons occupy the same spin orbital, the wavefunction vanishes. Thus, the anti-symmetry requirement has been met. Finally, the (2.24) can be expressed as determinant:

Ψ = (2.25)

The wavefunction 2.25 is an example of 2x2 Slater determinant, SD which, for an *N*-electron system, can be generalised as:

$$\Psi = \quad . \qquad (2.26)$$

Very often, the SD is written in the very convenient short-hand notation which shows only the diagonal elements:

From now on, this notation will be used to represent the SD.

In the SD, electrons are indistinguishable and the exchange effects have been introduced, namely, when the SD is used as wavefunction, the motion of two electrons with the parallel spin is correlated (exchange correlation). Unfortunately, single SD's cannot account for the correlation between the motions of two electrons with opposite spin and, for this reason, a single SD is known as an uncorrelated wavefunction.

2.4 The Hartree-Fock approximation.

To proceed any further with the discussion of theoretical methods attempting to solve the many-electron problem in molecules and crystals, the ideas underlying the Hartree-Fock (HF) approximation and *ab initio* HF calculations need to be illustrated. For the sake of brevity, the description that is reported here does not cover the HF theory in every detail but is limited to a short overview on some basic concepts such as the self-consistent field method, basis set, exchange and correlation effects etc. which are of fundamental importance in any discussion about modern *ab initio* methods.

In spite of its simplicity, the HF approximation has played an essential role in the development of computational quantum methods. In fact, with the only exception of the Extended Hückel semi-empirical method and the tight-binding approach to crystals which are examples of models with full absence of electron correlation in the wavefunction, the HF method is the natural precursor of all modern approximate theories that are explicitly based on the electronic Hamiltonian.

Besides, the HF approximation is not just one of the methods of mere theoretical interest but has also proven effective in elucidating the chemistry of various real systems.

With respect to the Hartree method, where the fictitious system under investigation consists of *N*-noninteracting electrons, the HF method tries to find an approximate solution to the problem of describing a realistic system consisting of *N*-interacting electrons. Thus, if in the first case the total energy of the system is simply calculated by the summation of the spin-orbital energies of every single electron, for a system with interacting electron the situation results to be slightly more complicated. Here, in fact, the Hamiltonian depends on the unknown *1*-electron wavefunctions which, at beginning of the calculation, have to be guessed in order to calculate the Coulomb and exchange parts. In the following steps, to improve quality of eigenstates and operators, the self-consistent field procedure is required. Thus, the central idea of the HF method, is that the problematic electron-electron repulsion is replaced by an average repulsion field.

The starting point of the HF method is the assumption that the anti-symmetrized Slater determinant (SD):

, (2.28)

is an acceptable wavefunction to describe an *N*-electron system.
For a closed shell ground state, the expression of the HF energy is obtained expanding the SD and constructing the individual terms with respect to the various components of the Hamiltonian operator:

The first term, in 2.29, comprises the contributions of the kinetic energy and potential energy for attraction to the nuclei of a single electron, *i*. The second term, called Coulomb integral, defines the potential that an electron at position $\mathbf{x}_i$ experiences in presence of the average charge distribution of another electron in the spin-orbital χ_j. Moreover, since the terms $|\chi_i(\boldsymbol{x}_i)|^2 d\boldsymbol{x}_i$ and $|\chi_j(\boldsymbol{x}_j)|^2 d\boldsymbol{x}_j$ determine the probabilities of finding the electrons $\boldsymbol{x}_i$ and $\boldsymbol{x}_j$ in the volume elements $d\boldsymbol{x}_i$ and $d\boldsymbol{x}_j$, respectively, the Coulomb integral is weighted by the probabilities that the electrons occupy the positions $\boldsymbol{x}_i$ and $\boldsymbol{x}_j$ at distance $\boldsymbol{r}_{ij}$.

The remaining term in 2.29 is the exchange contribution to the HF energy. The exchange potential has no classical equivalent and is entirely due to the anti-symmetrized nature of the SD. A consequence of choosing orthonormal spin-orbitals, the exchange contribution exists only for electrons with the same spin. In fact, since the $1/r_{ij}$ operator is spin independent, the integration over the spin coordinates can be separated so that one obtains an integral over the product of two different spin-orbitals depending on the same coordinate $\boldsymbol{x}_j$. The presence of electrons with unlike spins introduces the and factors which, being orthogonal, make vanishing the exchange integral. Finally, one should note that, since the Coulomb and exchange integrals appear with the opposite signs, the self-interaction problem, due to the particular case $i=j$, is elegantly solved by the cancellation of both the integrals.

The equation 2.29 is a functional of the spin-orbitals and, for obtaining the minimal SD, the spin-orbitals have to be chosen in accordance with the variational principle. These are adjusted throughout the minimisation, under the constraint that they must remain mutually orthonormal. This restriction requires the introduction of Lagrange multipliers, , into the equations determining the minimal spin-orbitals. These are known as Hartree-Fock equations and have the form:

(2.30)

In the set of the *N* eigenvalue equations, 2.30, is the Fock operator, a *1*-electron operator which is defined as

Where, the first two terms represent the kinetic and attractive potential energy operators, respectively. $_{HF}$(i) is the Hartree-Fock potential, namely, the average repulsive potential which is seen by *i*th electron and is due to the remaining *N*-1 electrons.

By $_{HF}$(i), the HF operator tackles the electron-electron repulsion in an average way replacing the complex *2*-electron repulsion operator, which appears in the Hamiltonian.

The potential $_{HF}$(i) consists of the sum between two components:

The Coulomb operator, , is defined as

—

and represents the average local potential at $\boldsymbol{x}_i$ due to an electron in χ_j while the nonlocal exchange operator, which has the form

—

is responsible of an exchange between electron *i* and electron *j* to the right of .

Finally, ε_i represents the orbital energy resulting from the action of the Fock operator on the orbital χ_i. The physical interpretation of the orbital energies ε_i is provided by the Koopmans' theorem. Such a theorem states that the Hartree-Fock orbital energy ε_i is an approximation of the ionization energy, *IE(i)* (taken with negative sign), and is due to the removal of an electron from the *ith* orbital, χ_i:

The system of HF equations 2.30 and 2.31 is nonlinear and, thus, it has to be solved iteratively.

In practice, an initial guess at the spin orbitals is made and in this way the average field $V_{HF,}$ seen by each electron, can be calculated. When the V_{HF} is known, the system of eigenvalue equations 2.30 is solved for a new set of spin orbitals which are requested to satisfy the orthonormality requirement during the minimization. Such new spin orbitals are now used to calculate a new field and the process is repeated until the field no longer changes and the spin orbitals which have been used to build up the Fock operator are identical to its eigenstates within the desired accuracy. In practice, one can also choose other convergence criteria to estimate the accuracy of the obtained solution amongst them the total energy and electron density are the most common examples.

Since the new spin orbitals are derived from their own effective potential, the procedure used to get them, is called self-consistent field (SCF).

The rate of convergence of the iterative procedure depends on the nature of the physical system as well as on the choice of the initial approximation.

One of the major problems that one encounters in solving iteratively the HF equations is obtaining the operator eigenstates at the *ith* iteration. In fact, this requires the evaluation of the exact HF exchange potential 2.34 which is a very complicated task to accomplish computationally. In this case, a simpler solution is adopted. It consists in replacing the nonlocal exchange potential by a local one. The local exchange potential has the form:

Here, $\rho($ is the electron density and α is an adjustable parameter which can assume values ranging from 2/3 and 1. The expression 2.36 is a clear example of how the exchange potential can be expressed as a functional of electron density. Since the HF approximation assumes that the many electron wavefunction can be written as one SD, it is defined as uncorrelated approximation. However, the electron motions are no longer completely independent.

2.5 Electron correlation problem.

In molecules and crystals, electrons repel each other. According to Coulomb's law, the repulsion energy depends on the inter-electron distance $1/r_{ij}$. This interaction generates a correlation hole around each electron. The presence of the correlation hole implies that the probability to find any pair of electrons at the same point in the space is zero. In the HF method, the many body wavefunction is represented by a single SD. In this case, electrons with different spins are uncorrelated and electrons with the same spin cannot be found at the same point in the space, they are correlated (a Fermi hole exists). Moreover, when a single SD is used to describe a system with an odd number of electron through the unrestricted HF scheme, the HF SD is no longer an eigenfunction of the total spin operator, S^2, and in the more dramatic situations, it is contaminated by functions corresponding to states with higher spin multiplicity. In such cases, the expectation values of the total spin operator, which is obtained by a single SD, is physically meaningless. Thus, even though the SD is a wavefunction capable of describing accurately several aspects of the many-electron system, it is just an approximated wavefunction which is never identical to the exact wavefunction of the many-electron system. It follows from the variational principle that, the expectation value of the HF energy, which is obtained using a single SD, is always larger than the exact ground state energy. In the modern computational chemistry, the difference between the exact ground state energy, E_0, and the HF energy, E_{HF}, in a complete basis (HF limit) is called HF correlation energy, :

(2.36)

Thus, the correlation energy is considered as the error which has been introduced through the HF method in calculating the exact energy of the ground state system.

Since, both E_0 and E_{HF} are negative quantities and the absolute value of E_0 is always greater than that one of E_{HF}, it follows that the correlation energy is always a negative quantity. As the exact energy is an unknown quantity, one has to use the experimental total energy which is given by the sum of the experimental cohesive energy and free-atom energies. Another way to get the exact total energy consists in calculating the exact

energy for a given one-electron basis set and defining the basis set correlation energy as the difference between the exact and HF energies calculated for the same one-electron basis set. In molecular systems, the correlation energy is about 1 eV per electron pair in a bond or lone pair. In the HF scheme, the correlation energy is mainly caused by the instantaneous electron-electron interactions. As it has been described in the previous section, the effective HF potential is not able to exactly account for the electron-electron repulsions but it treats such interactions in only average manner. Because the electron-electron interaction are directly connected to the term $1/r_{ij}$, when the electrons get too close to each other, the Coulomb integral increases and the HF energy becomes larger than the exact energy, E_0. Because it is intimately connected with the instantaneous electron motions, this kind of short range correlation is generally known as dynamic electron correlation. The other main contribution to the correlation HF energy is, instead, connected with the nature of the wavefunction which one employs to describe the energy of the ground state system. This contribution does not depend on the electron motion and is known as non-dynamical or static correlation. The effects of non-dynamical correlation are easily described through the dissociation energy of the H_2 molecule. This study [7] shows that the restricted HF method can approximate the exact total energy of the H_2 molecule at the equilibrium distance with a small correlation error. On the other hand, when the interatomic distance between the hydrogen atoms increases, the correlation error gets larger. Since at very large bond distances, the bond breaks to give two independent hydrogen atoms, the contribution from the term $1/r_{ij}$ is absent and there is no dynamical correlation contribution to the total HF energy. To illustrate the effects of the static correlation, one can start to consider that, at equilibrium distance, the HF ground state wavefunction is represented by a single SD, $\Psi_{GS,}$ wherein the bonding orbital, σ, is doubly occupied and can be approximated, using the basic quantum mechanics picture, as result of a linear combination of the two 1s atomic orbitals of each hydrogen atom:

$$= \quad (2.37)$$

and

$$= \quad (2.38)$$

If the SD, 2.37, is expanded in terms of the atomic orbitals, 2.38, one gets:

– (2.39)

The first two terms of the SD show that the electrons are shared between two protons occupying the bonding orbitals with paired spins. The last two terms take into account the alternative that the two electrons are located on just one nucleus giving rise, within the H_2 molecules, to a hydrogen anion and a proton. These two terms result in an adequate description of the interatomic bond at equilibrium distance but, at dissociation limit, when the two atoms are at large distance, the contribution of the ionic structures has to be zero in order to give the expected asymptotic behaviour of the relative energy consisting with the dissociation of the H_2 molecule in two hydrogen atoms. Thus, the presence of the ionic structures within the HF wavefunction is responsible for the large error in the dissociation energy.

Unlike the dynamical correlation, non-dynamical contributions, becomes more important when the bond is stretched, and is known to be a long range effect.

Since the measures the difference between the expectation value of the Hamiltonian operator on a single SD and the exact total energy resulting from the true wavefunction, the correlation energy is not only connected with inter-electronic interactions but can be also related to the kinetic energy or the nuclear-electron interactions. In fact, when in the HF scheme the average electron-electron distance becomes too small, the kinetic energy "increases", consequently and the nuclear-electron attraction becomes stronger leading to a decrease of the term accounting for the attractive potential in the equation 2.34.

The improvement of methods attempting to determine efficiently and accurately the correlation contributions is still an active area of the conventional theoretical chemistry. In the context of the wavefunction based *ab initio* theory several methods dealing with the electron correlation problem have been developed during the years. Amongst the most popular ones, the second order Møller-Plesset, MP2, considers the correlation effects as a small perturbation and as such, they are treated using the perturbation theory. In the MP2 method, only the second-order many-body perturbations are taken into account. Møller-Plesset perturbation theory to fourth order, MP4, is also often used

to deal with the electron correlation problem. This technique is more accurate but also considerably more expensive than MP2. In fact, the main disadvantage of the wavefunction based methods is the high scaling of the computational cost with the number N of the atoms in the molecules and crystals. While MP2 formally scales with the 5th power of the system size O(N^5), MP4 scales as O(N^7). Other popular post-HF methods such as configuration interaction (CI), multiple configuration SCF (MCSCF) and coupled-clusters (CC) theory account for the electron correlation problem in molecules considering wavefunctions consisting of the sum of several SD's. For the CC theory the computational cost scales as O(N^7). The high scaling wall of such methods restricts the application range of wavefunction based methods to molecular systems of rather small sizes.

2.6 **Density Functional Theory (DFT): introduction.**

Generically speaking, computational methods accounting for electron correlation in molecules and crystals are classified in two main categories: wavefunction-based methods and density functional theory methods. The former ones start from the electronic SE and try to solve it using increasingly more accurate approaches such as HF theory and post-HF methods. For the major part of systems of chemical interest, post-HF approaches lead to very accurate energies which are in good agreement with the experimental results and, for this reason, such approaches are often used as a benchmark in the determination of the accuracy of new computational methods. However, since post-HF methods have the drawback of being computationally very costly, limiting the size of the systems to which they can be applied and with a very limited application to the transition metals, it was soon clear that an alternative theoretical strategy to those computational methods had to be found to satisfy the continuous and ever more demanding requests of the physics and chemistry problems.
A possible way to tackle the many-electron problem and to reproduce with notable accuracy the interplay of a wide range of interactions in hundred-of-atoms systems while keeping within reasonably affordable limits the accompanying computational expenses was recognised in density functional theory (DFT) methods.
In fact, with respect to the wavefunction methods, the DFT formalism offers some important advantages. The most important of these is that, in DFT, the basic variable

describing an *N*-electron system is the one-body electron density, $\rho(\mathbf{r})$. This variable is only a function of three space variables, *x, y* and *z*, whereas, the *N*-electron wavefunction is a function depending on *3N* space coordinates and therefore the electron density is a simpler quantity to deal with either conceptually and practically than the wavefunction. The literature on DFT and its applications is very large. Here, only the basic formulations of time-independent DFT are given. It is an alternative, and complementary, approach to the traditional methods of quantum chemistry which are built in terms of many-electron wavefunction.

The Thomas-Fermi model, in particular, represents the first genuine attempt of using the electron density rather than the wavefunction for obtaining information about atomic or molecular systems. In fact, this model, which is dated back to 1927, permits the calculation of the atomic energy just combining the classical attractive and repulsive potentials with a very simple expression of the electron kinetic energy resulting from a uniform electron gas. The Thomas-Fermi energy has the form:

(2.40)

The first term, in 2.40, is the kinetic energy of the electron which is expressed as a model system of constant electron density. The latter two integrals account for the potentials of the nuclear-electron attraction and electron-electron repulsion, respectively.

The Thomas-Fermi approach was developed in the hopes that the energy could be written exclusively in terms of the electron density.

The early electron density model was very innovative for the time it was proposed, but the proof that this was the case came only thirty years later when, in 1964, Hohenberg-Kohn formulated and proved a theorem that set on solid mathematical ground the intuitions of Thomas and Fermi.

Since the 1970s, density functional theory (DFT) started to become very popular for calculations in solid state physics. In the context of the solid state, DFT with the local density approximation (LDA) and plane waves basis functions leads to low cost results (in comparison with quantum-mechanical methods) which, in many case, are in good agreement with the experimental data.

Since electron distribution in molecules cannot be considered uniform as in solids, DFT was not recognised accurate enough for calculations in molecular quantum chemistry until the 1990's when the DFT approximations were refined to better model the exchange and correlation interactions. Nowadays, the DFT based methods are the leading methods for the electron-structure calculations in both the solid state and molecular quantum chemistry fields.

2.7 **The First Hohenberg-Kohn's Theorem.**

Some of the core elements in DFT are represented by Hohenberg-Kohn (HK) theorems. The first HK theorem, which is mainly conceptual, demonstrates the existence of a one-to-one mapping between the ground state electron density and the ground-state wavefunction of a many-body system. In substance, it is only an existence theorem, stating that the mapping exists, but does not provide any exact form of such a mapping.

The second HK theorem, instead, establishes the variational principle.
In plain words, the HK theorems state that, the total energy, E, and the charge density, ρ, of N electrons in presence of an external potential, v_{ext}, are obtained minimising a universal functional i.e. a function of a function.

2.7.1 **First Hohenberg-Kohn theorem**

The external potential is uniquely determined by the electron density, besides a trivial additive constant.

For a given system of N-electrons and M-nuclei, in the BO and non-relativistic approximation, the Hamiltonian operator in the electron SE,

, (2.41)

can always be written as sum of three components:

(2.42)

The $\boldsymbol{x}_i$, in 2.41, denote the set of N space coordinates $\boldsymbol{r}_i$ and the spin variables of electrons. The kinetic and potential energy operators in the electron Hamiltonian have the following forms:

and

In the first HK theorem the one-to-one mapping relation between the electron density ρ:

and the external potential, (typically representing the electric field of nuclei and any applied electric field) is proven.
The direct correspondence,

(2.47)

is simple and straightforward. Each corresponds to a wavefunction Ψ by the solution to the SE 2.41 and the corresponding density ρ can be found by integrating the square of the wavefunction 2.46.

To prove the correspondence in the opposite direction, i.e., ρ determines ,

(2.48)

one can consider the following two steps:

i. If and differ by more than an additive constant c, they will not lead to the same wavefunction Ψ.
ii. If the ground state wavefunctions Ψ (corresponding to) and (corresponding to) are different, they will not lead to the same density ρ.

The proof of the statement (i) is achieved considering the effects of the two external potentials on the ground state wavefunctions in the SE:

( )

from the assumption that , it follows that:

, (2.51)

which obviously leads to contradicting what is stated in (i).

To prove the second part of the theorem, i.e. (ii), the Rayleigh-Ritz's variational principle is used:

Where, it has been taken into account that different Hamiltonians correspond to different ground states, $\Psi \neq \Psi'$.

If the roles of Ψ and Ψ' (and) are exchanged, a new relation between E_{gs} and is obtained:

If the (2.52) is added to the (2.53), it turns out that which is absurd.

Therefore, there cannot be corresponding to the same electron density for the ground state, unless they differ by an arbitrary additive constant.

Corollary *Since ρ(**r**) univocally determines , it also determines the ground state wavefunction Ψ, which is obtained by solving the many-body SE.*

Therefore the maps between ρ, and Ψ are bijective (one-to-one):

, (2.54)

and, as a consequence of the bijective map , every observable O of a given system is a unique functional of density:

(2.55)

Thus, the ground state density gives, in principle, all properties of interest. To be sure that a certain density corresponds to the ground state density, the second Hohenberg-Kohn theorem has to be considered. In fact, it is a formal prescription for obtaining the lowest energy corresponding to the ground state if the density satisfies some necessary conditions.

2.7.2 **The Second Hohenberg-Kohn Theorem.**

The electron density that minimizes the energy of the overall function is the true electron density corresponding to the full solution of the SE.

Let $\boldsymbol{(r)}$ be a non-negative trial electron density which is normalised to N and let the variational energy, E_v, be defined as:

where, from the first HK theorem, the variational energy E_v is a functional of the density and the part of the energy functional, $F_{HK}[\ ]$, is a universal density functional which does not depend explicitly on the external potential and has the following form:

(2.57)

In 2.56, is the ground state wavefunction of a potential having as its ground state density, and are the kinetic energy and electron-electron interaction operators, respectively.

If the true ground state energy is defined as $E_0 = E_v[\rho]$ and verifies the relation:

(2.58)

for any $\rho \neq$, then the proof of the second HK theorem is quite simple:

The inequality in (2.59) is due to the Rayleigh-Ritz variational principle considering the wavefunction, but is applied to the electron density.

Moreover, one has to keep in mind that, to give a realistic description of a physical system, the electron density has to correspond to an antisymmetric wavefunction. This condition is necessary for the true electron density ρ but is not the case for trial electron

densities, . In fact, if the variational search is not done carefully, unacceptable electron densities might be obtained. To guarantee that the electron density is originated by antisymmetric wavefunctions, in the 80's, Levy proposed the idea of the constrained search method which consists of redefining the universal functional, F[ρ], as follows:

(2.60)

where, the first minimisation (that one which is inside the round parentheses) guarantees that the search is done within a subset of all the antisymmetric wavefunctions Ψ_{anti}, that upon quadrature yield the corresponding electron density ρ_{anti}. The second minimisation, instead, ensures that the search of the wavefunctions determining the lowest energy is extended over all the densities. The result of this final step is the antisymmetric wavefunction delivering the lowest energy for the ground state.

Since the energy resulting from the external potential is simply determined by the density, it does not depends on the wavefunction which generates that density. Thus, since such an energy is the same for all wavefunctions integrating to that particular density, the external potential can be separated by the other two contributions as follows:

The universal functional $F_L[\rho]$ which is defined as:

(2.62)

can be introduced into the 2.61 to give:

In conclusion, the 2.63 shows that, given a density, the energy resulting from the quantity has to be minimised to yield the ground state density and the corresponding energy. It is also noteworthy that, since the universal functional $F_L[\rho]$, given in 2.62, is defined for a subset of all the densities which are originated from antisymmetric wavefunctions, it differs from the HK universal functional $F_{HK}[\rho]$ given in 2.57.

The HK theorems form the mathematical basis of the modern density functional theory. However, at the same time, these do not provide any guidance at all about how the functional delivering the ground state energy should be constructed. The practical scheme for performing the correspondence $\rho \rightarrow \Psi$ was provided some years later by the approach of Kohn and Sham which is illustrated in the next section.

2.8 **The Kohn and Sham's equations**

The HK theorems formally define the form of the universal functional, $F_{HK}[\rho(\mathbf{r})]$. This functional contains the individual contributions of kinetic, Hartree (or classical Coulomb energy) and the non-classical energy. It can also be schematised as:

Amongst these contributions, only the Hartree term, $H[\rho]$, is known:

The expression of kinetic energy, $T[\rho(\mathbf{r})]$, is not known in terms of electron density. In fact, the exact calculation of this term requires the knowledge of the Laplacian of the one-body density matrix. Moreover, the Thomas-Fermi model of kinetic energy (2.40), being dependent on the term, is local in density and therefore, responsible for severe limitations in the description of chemical systems. To derive an expression for the kinetic energy, Kohn and Sham used the idea of considering a system of non-interacting electrons. As it has already discussed in the section 2.3, the SD can be considered as the exact wavefunction for a fictitious system of N *non-interacting*

electrons. Thus, by analogy to the HF theory, for such a wavefunction, the kinetic energy can be easily obtained in terms of one-electron orbitals and be expressed as:

–

Where, the φ_i are the one-electron orbitals and is the Laplacian operator.

Thus, if one can find a system of non-interacting electrons that produces the same electron density as that of the interacting system, then the kinetic can be calculate by the 2.66.

For sure, the non-interacting kinetic energy is not equal to the true kinetic energy even if both the systems share the same density. The residual part of the true energy, T_C = , is accounted in the exchange-correlation energy, E_{xc}, which will be discussed later in this section.

The KS method can be easily illustrated by the following few steps. The first one permits to calculate the non-interacting kinetic energy from a fictitious *N*-particle system which is constructed in a way to satisfy the following requirements: the ground state of this system has to be described by a single SD and its density $\rho_{s,}$ has to be exactly the same density as the interacting system, ρ_0. In the second step, an effective potential,), is defined and the form of this potential has to be chosen for fulfilling the condition of $\rho_S=\rho_0$.

Such prescriptions lead to the SE for a non-interacting *N*-electron system:

where, is the one-particle Hamiltonian:

–

The true ground state wavefunction of the 2.67 is the single SD having the following form:

The N elements of the SD are usually known as Kohn-Sham orbitals, , and they are solutions to the N eigenvalue equations:

The one-electron KS operator in 2.70 is defined as

–

and the relation connecting the density of the non-interacting system to that one of the real system is

with occupations, n_p, equal to zero or one.

Going back to the kinetic energy problem, the KS scheme accounts for the residual part of the kinetic energy, T_C, in an approximate way introducing the separation of the functional $F[\rho]$:

. (2.74)

The last term in 2.74 is the xc energy:

The xc energy functional contains not only the residual part of the true kinetic energy, T_C, but also other contributions to the system total energy. Such contributions include

non-classical effects of self-interaction correction as well as the electron exchange and correlation. The xc functional, , which captures the missing energy contributions which are not contained in the other functionals is usually partitioned into an exchange part and a correlation functional:

The exchange contribution is defined as the difference between the classical electron-electron repulsion, $H[\rho]$, and the expectation value of the many-body electron-electron energy term:

As it has been mentioned above in the paragraph 2.4, for a 1-electron system, the exchange term would cancel exactly the spurious self-interaction of the electron with itself coming from the $H[\rho]$ term.

Hence, contains the energetic contribution resulting from the anti-symmetry requirement which is imposed on the many-body wavefunction and corrects for the double-counting electron in $H[\rho]$. The correlation energy, E_C, is defined as the missing energy necessary to make xc energy, E_{XC}, exact.

At this point, there is just one step which is left to consider, namely, the determination of the effective functional form.

According with the first HK theorem ($_{s,0}(\mathbf{r}) \leftrightarrow \Phi_s(\mathbf{r}) \leftrightarrow \rho(\mathbf{r})$), the effective potential has to be unique in the sense that it is a unique functional of density, $v_{s,0}[\rho](\mathbf{r})$. The expression of the energy of a real system of interacting electrons is given in term of the separation of the functional $F[\rho]$, seen in 2.67 and accounts for dependence on the KS orbitals of the kinetic energy term (see equations 2.64 and 2.66). It has the form:

At this point, the so-called xc energy is the only unknown contribution to the real system total energy. If the xc is ignored, the physical content of the 2.78 becomes identical to that of the Hartree approximation. Thus, there is no surprise that associating the Euler-Lagrange equation with the stationarity of leads to a new set of self-consistent equations, the Kohn Sham equations:

If the equation 2.79 is written in a more compact form, as:

after comparing the 2.80 with the 2.70 and 2.71, one finds immediately that:

The variational principle is now applied to the set of local equations 2.81. In order to minimise the energy, the relation between the KS orbitals and the electron density, $\rho(r)$:

and the xc potential:

have to be considered as well.

In other words, the KS equations 2.81, 2.82 and 2.83 are solved self-consistently calculating the KS orbitals, the density and the xc potential in each cycle starting from the 2.83 with an appropriate approximation for . In spite of its apparent simplicity, the KS equations are in principle exact if the exact xc potential is used in 2.83. The only error which has been introduced in KS theory is due to xc functional.

Here, briefly, some aspects of density functional theory are stressed to highlight the main differences between the electron density based methods and wavefunction methods.

First of all, traditional wavefunction based methods are preferable when dealing with few atom systems and when high accuracy is required whereas, DFT is preferable when the system under investigation contains a larger number of atoms and a more modest accuracy is acceptable.

Both the Thomas-Fermi and Hartree-Fock methods can be regarded as ancestors of modern DFT. While the former theories are intrinsically approximate, modern DFT is in principle exact.

In conclusion, when a wavefunction based method is used, in principle, an arbitrary level of accuracy can be achieved for every system and limitations are only due to the performance of the computational system carrying out the calculations. Since, DFT depends on the adequate knowledge of the xc energy functional, and although more and more accurate forms are constantly being developed, there is no known systematic way to achieve a high level of accuracy.

The next section will focus right on this topic, namely, on the strategies which have been adopted, during the years, to set the DFT theory to practical use by approximated forms of the xc energy functional.

2.9 **The local-density approximation (LDA)**

Most of the contributions to the electron energy of a physical system can be exactly calculated by KS formalism of DFT minimising the set of the self-consistent equations 2.81, 2.82 and 2.83. However, due to the presence of the unknown xc term, $E_{xc}[\rho]$, a small part of the system total energy is missing and has to be determined by an approximated functional. In this section, the first model system of local density approximation (LDA), on which several approximated xc functionals are based, is introduced. The core of LDA is a hypothetical uniform electron gas and, although such an idea was already present in the Thomas-Fermi model, the embryonic form of LDA was proposed for the first time in the seminal paper of Kohn and Sham and in spite of its simplicity, it has been for a long time the most widely used approximation to xc energy.

In the LDA, a real inhomogenous electron system is considered as locally homogeneous. In fact, the uniform electron gas is the only system for which the exchange energy can be derived exactly and the correlation energy can be calculated numerically. This approximation consists of a system wherein the electrons are placed in an environment positively charged and the entire ensemble results to be neutral. The number N of electrons as well as the gas volume V are considered approaching infinity, whereas the electronic density, $\rho=N/V$, remains finite and constant everywhere. Thus, the resulting xc energy, , is simply given by:

In this formulation of the xc energy, two kinds of densities are involved: the electron density which is a per unit volume density and the energy density which is, instead, a per particle density. Moreover, can be further split in its components as follows:

Here, , represents the exchange energy of an electron in a homogeneous electron gas of constant density and is exactly expressed by the Dirac's formulation:

Details of 2.85 have been already discussed above in the section 2.4.

For the correlation energy functional, the situation is more complicated and even for a homogeneous electron gas, is not known exactly and thus it has to be approximated.

Early approximations for correlation were based on the perturbation theory () but the most accurate results are based on Monte Carlo simulations for an electron liquid which forms the reference system for LDA []. On data resulting from the work of Ceperly and Alder [8], a new family of xc functionals were parametrised for free-electron gas leading to the correlation energy for homogeneous system. In this context, the most common LDA parametrizations are those of Vosko-Wilk-Nisair [10] Perdew-Zunger and Perdew-Wang [9] which are largely implemented in standard DFT computer codes carrying out calculations for both solids and molecules.

The extension of LDA to the unrestricted case leads to the local spin-density approximation (LSDA). Formally, the xc energy can be written in terms of two spin densities, and :

For many decades, LDA has been applied in calculations of band structures and total energies in solid state physics with satisfactory results. In fact, such an xc functional has proven successful especially in describing systems which are very close in resembling the electron gas and, in specific cases, metallic solids with delocalised electrons. On the other hand, there are well known problems in making use of LDA for other systems such as molecules, semiconductors and ionic solids in which the electron distribution is non-homogeneous. In this respect, LDA reveals the shortcomings of underestimating the bond distances overestimating the binding energies. Moreover, in

the case of superconductors, the main problem is due to calculation of the band gaps that are calculated too small.

2.10 **Generalised gradient approximation (GGA)**

To address the issue of inhomogeneity in the electronic density, in the early 1980s, some successful extensions of the purely local approximation were developed. The first step in this direction consisted in realising that the knowledge of the density $\rho(r)$ at each point, **r,** was not enough to account for the non-homogeneity of true electron density. Thus, it was suggested to supplement the density with information about the gradient of the charge density, . In practice, with the aim to account for the slowly varying charge density in the real systems, the LDA xc energy was interpreted as the first term of a Taylor expansion which was extended with the next lower term given by charge density gradient. The resulting form of this functional was termed the gradient expansion approximation (GEA). The GEA did not improve the LDA performance, on the contrary, in some situations, it gave results even worse than those of LDA.

It was a major breakthrough, when it was realised that better improvements could be achieved if, instead of making use of systematic gradient expansions, more general functions of $\rho(\mathbf{r})$ and were considered. Thus, a new family of xc functionals, known as generalised-gradient approximation (GGA), was generated. In short-form, the GGA xc functionals are represented by the following general expression:

The parametrization of GGA xc functionals depends on the choice of the function and, as consequence, this affects the results. Thus, two different GGAs lead to different values of the ground state total energy of the same system.

Due to the several possibilities to construct the function *f*, nowadays, many GGA-type xc functionals are available in the standard DFT software packages and new ones continue to appear. There are, amongst the GGA's, some xc functionals containing parameters which are calibrated against reference values rather than being derived from fundamental physical constants. Others are constructed without empirical fitting trying

to satisfy as many exact theoretical constrains as possible while providing satisfactory numerical predictions for real systems. In this respect, accordingly with the definition of [11], the density functional formalism is a non-empirical theory.
The GGA xc energy can be partitioned into exchange and correlation components as follows:

Where, in principle, each exchange functional might be combined with every correlation functional, but, in practice, just few combinations of them are considered as effective.

2.11 **The Perdew, Burke and Ernzerhof xc functional**.

Since there are many ways to get information from the gradient of electron density, many GGA xc functionals have been developed during the years. Nowadays, one of most popular GGA xc fuctionals, widely used in solid state and surface calculations, is the parametrisation of Perdew, Burke and Ernzerhof, PBE. Such a GGA xc functional considers as core element the LSD approximation. In fact, the PBE exchange and correlation functional consists of supplementary factors which are added to their corresponding LSD counterparts. Furthermore, in the PBE parametrization, the spurious oscillations in the Taylor-like expansion to the first order have been removed as they were considered energetically non relevant. Accordingly, when the reduced gradient (see eq. 2.92) vanishes at the position of the electron, the GGA holes reduce to LSD. With the aim of refining the PBE improving its performance for periodic systems, a new "large" family of GGA xc functionals which includes the PW86, PW91, RPBE, revPBE, PBEsol, opt-PBE, etc. has been created and recently some of those functionals have been modified to increase the accuracy for thermodynamic and electronic properties of molecules.
Since PBE has played an important role in the development of several GGA xc functionals, this paragraph is aimed to illustrate briefly some of the characteristics of its formulation focussing solely on those aspects which have been considered relevant to the scopes of this thesis work.

The model of the exchange hole, which the GGA PBE proposed, is given by the integration over the product of the LSDA exchange and the damping function $F_x(s)$:

with

where k is 0.804 and $\mu = \beta(\pi^2/3)$ is 0.21951. The constant β=0.066725 is related to the second order gradient expansion [Perdew Wang 1992]. The argument of the function $F_x(s)$ is the reduced density gradient for the spin σ and generally its form is developed to account for the local inhomogeneity in electron density:

and

Here, for core electrons and for valence electrons.

Equation 2.92 shows that, the reduced density gradient assumes large values not only in those regions of small electron density but also for large gradients. This guarantees that the exponential tails are located far away from nuclei. On the other hand, small gradients and large densities, which are characteristic of bonding regions, lead to small values of s_σ. Intermediate situations, namely large values of density, lead to values of the reduced density gradient which are in between these values which s_σ assumes in the bonding and tail regions. Obviously, for a homogeneous electron gas, the reduced

density gradient is zero everywhere. Moreover, due to the particular exponent to which the density is raised, s_σ results dimensionless.
The PBE correlation energy functional is expressed by the following integral:

The non-local contribution to the correlation energy is due the term *H:*

while $\gamma = 0.03191$ is just a numerical constant, t is parameter including the density gradient via the function s_σ (see the 2.96):

where,

is a function of the relative spin polarisation:

Finally,

For a system with uniform electron density, the PBE xc functional reduces to LSD. The term H is able to account for limits of GGA namely for very small and very large gradients ($t \to 0$ and $t \to \infty$, respectively). The PBE xc functional satisfies the Lieb-Oxford bound [11]:

In conclusion, several benefits are obtained with the PBE xc functional as it has proven useful for a large number of investigations on solid, surface and molecular systems which have been reported so far in literature. These works point out that with respect to LDA and LSDA, the PBE xc functional is able to improve the binding energy as well as the atomisation energies. In addition, the bond lengths and angles of many solids and molecular systems are better described by the PBE xc functional. In good agreement with experimental data, the PBE xc functional is the best choice to investigate on energetics, geometries and dynamical properties of water, ice and water clusters. In fact, the description of hydrogen-bonded systems is very much improved.

Although, LDA performs better in the descriptions of semiconductor materials, the calculated binding energies are consistent with experimental data if they are evaluated by PBE.

Density functional theory with LSDA or GGA xc functionals have the drawback that they include self-exchange and self-correlation, both of which are unphysical.

Because in DFT there is not the rigid requirement of the antisymmetric wavefunction as in HF, electron-electron interactions can be overcounted or undercounted leading to the unphysical problem of the electrons which interact with themselves. The most popular example of self-interaction error takes places in the hydrogen atom for which, since the $E_{xc}[\rho]$ contribution and many-body electron-electron energy term, $H[\rho]$ In this case, most DFT functionals fail to find the ground state energy due to the functions tend to predict small a HOMO-LUMO gap, in molecules, or small a band gap in solids. In DFT, when GGA and LDA functionals are used, an electron interacts with its own charge density leading to an increase of the energy of localized states. As consequence of this, DFT produces excessively delocalised charge distributions and incorrectly predicts some materials as metals rather than insulators.

In conclusion, the PBE xc functional adequately describes many properties of solids, surfaces and interfaces and is largely used by the physics community for its very satisfactory results. However, like other GGA, LDA and LSDA standard xc functionals, the main limitation of PBE consists in the inability to capture the contributions to inter- and intra-molecular binding energies which are due to the dispersion forces.

2.12 **Hybrid HF-KS functionals.**

The development of approximations which combine HF and DFT formalisms has been influenced by the observation that LDA and GGA trends are opposite to those of the HF theory. In 1993, Becke suggested [13] that a way to go beyond the accuracy of GGAs was that of considering the exchange contribution as a combination of the exact exchange functional and that of the DFT approximation for the exchange functional. Such an idea is put in practice by the adiabatic connection method (ACM). ACM permits, in fact, the connection between the non-interacting electron KS reference system and the fully interacting electron real system. Thus, the ACM functionals established a new class of xc functionals: the so-called hybrid functionals which made the DFT so effective and popular. From the computational chemistry point of view, hybrid functionals have represented an incredible success because they embodied for the first time the ideal quantum-mechanic method which holds the very desirable characteristics of being accurate, reliable and at the same time computationally affordable.

The basic expression representing an xc hybrid functional is given by the following general form:

where and are the semilocal approximations for the exchange and correlation functionals, respectively. The universal parameter α, which is responsible of mixing HF and KS exchange, is determined by an empirical fit such that the equality 2.99 is capable to reproduce data resulting from experimental determinations such as atomisation energies, exact nonrelativistic energies, reaction barriers and so on. In particular, the mixing fraction has to obey to the restriction $0 \leq \alpha \leq 1$. The basic requirements $\alpha = 0$ and $\alpha = 1$ are imposed to the two extremes representing non-

interacting and interacting electron systems, respectively. A values of $\alpha \approx 0.2$ is obtained from atomisation energies and is used in several hybrid GGAs, whereas, a value of $\alpha \approx 0.5$ is found fitting the 2.99 to the reaction barrier heights.
Since the mixing factor shows system-dependent variations, turning it into a function of the electron position $\mathbf{r}(x, y, z)$, such as:

leads to an expression of the xc energy which is adapted to the local chemical environment.
An example of the most successful hybrid functionals is represented by the B3LYP which is widely used in computational chemistry. The B3LYP xc energy is given by:

Here, the correlation part is that suggested by Lee-Yang-Parr. The three parameters, α, β and γ are optimised to fit general experimental data and they do not depend on the molecules under investigation.
Although, the B3LYP xc functional has demonstrated of being reliable and accurate in describing the geometrical parameters, atomisation energies and reaction barriers for molecular systems containing only main-group atoms, it fails to give the correct predictions for compounds containing transition metals. In this respect, Paier *et. al* published a study entitled "Why does the B3LYP hybrid functional fail for metals?", In such a contribution, some xc functionals such as the PBE, B3PW91, B3LYP, PBE0, and HSE were tested to reproduce lattice constants, bulk moduli, and cohesive energies of some metallic systems. Transition metals such as Rh, Pd, Cu, and Ag bulk were investigated and some aspects of the conclusions can be extended to the whole block of the transition metals. In substance, the authors pointed out that B3LYP fails in describing the transition from localised electrons, which is typical of single atoms, to that one of delocalised electrons, which is instead a characteristic of the metal bulk. Moreover, the authors attributed the poor performance mainly to the LYP correlation than to the B88 exchange contribution.

A formally parameter-free hybrid with the PBE xc part is known as PBE0 functional (PBE1PBE appears in the literature quite frequently). The PBE0, that uses a quarter of the exact exchange (α=0.25), is very competitive with the most reliable and empirically parametrized functionals. The exchange energy in the PBE0 hybrid functional has the form:

which can also split in short-range (sr) and long-range (lr) components to give:

.

Here, ω is an adjustable parameter accounting for the extension of short-range interaction and, for the specific case of PBE0, $\omega = 0$. The separation of the exchange components, as it has been done in the 2.102, is an arbitrary choice since the short range and long range components recombine themselves to the original Coulomb operator.
PBE0 has proven to be very successful in calculations of molecular systems. In this respect, Zhao *et al.* applied 23 density functionals to relative energies of different structures, ionization potentials, bond distances, and vibrational frequencies of neutral and ionic clusters containing up to four transition metal atoms. PBE0 was found to be the most satisfactory functional. On the other hand, due to the high computational cost that the exact exchange involves, the use of hybrid functionals is not a common practice in solid state calculations.

2.13 DFT approach to the dispersion energy problems.

The KS formalism of DFT is exact in principle but, in practice, to fully describe how the electrons interact with each other, approximations are required via so-called xc functionals. Much of the popularity of the DFT stems from the fact that xc functionals lead to very accurate results in spite of their simplicity. The development of new xc functionals, which is still a very active research area, has provided enhanced accuracy in predicting many chemical-relevant properties such as thermochemistry, reaction barriers, atomisation energy, and so on at modest computational costs. Standard xc

functionals are, nowadays, considered very reliable in capturing most of the properties of molecules, surfaces and interfaces as proven by the comparison between calculated and experimental data. However, despite the bright story of success, some DFT limitations were already known since the early 90's. In fact, it was noted that common xc functionals overestimate the interactions in strongly bond species while underestimate weaker interactions. The most popular example of this trend was found in many published works on hydrogen binding interactions which, during the last three decades, have been carried out with a large variety of xc functionals. In general, these studies have shown that there is a good conformity between the several functionals in calculating the hydrogen binding energies below the 2 kcal/mol. Since typical hydrogen-bonds are of 5 kcal/mol in strength, the missing energy revealed the inability of modern functionals to describe those contributions to intermolecular binding energies which stem from dispersion forces. Dispersions are long-range attractive interactions occurring between otherwise non-interacting systems (atoms, molecules, surfaces and so on) even in absence of charges or permanent electric moments. The nature of these forces, is purely quantum mechanical because such interactions take place from an interplay between electrons belonging to the densities of different systems; in fact, due to the identical electric charges, the electron densities of both the systems repel each other when they come too close. Surprisingly, at intermediate distances, the motion of the electrons of one system slightly perturbs the otherwise evenly distributed electron density of the other system. Thus, the electron motion correlation generates a temporary dipole moment on the second system. In turn, the presence of an induced dipole moment on the second system perturbs the first one, inducing a charge polarisation which originates an attractive force between the two systems. Such an induced-dipole induced-dipole attraction decays with the inverse of the six power of the intramolecular distance. At molecular scale, dispersion interactions play a crucial role: for example, they are responsible for deviation from ideal gas behaviour of most real gasses. Friction and wetting phenomena are also connected to the dispersion forces. The attraction of molecules to a surface can be due to dispersions and such a phenomenon, often referred to as physisorption, may precede important chemical events like catalytic steps of chemical reactions or surface modifications. Since dispersion forces are entirely due to the electron correlation, the HF method cannot be used to describe the potential energy surfaces of such systems. In fact, because of its lack of correlation, it predicts a purely repulsive potential energy curve.

Thus, when the post-HF methods cannot cope with the description of dispersion interactions occurring in large molecular systems, because this would result in a prohibitive computational cost, DFT is desirable. Common xc functionals, which are based on the local approximation, consider only the local electron density of the molecular system. Thus, if two systems are distant and there is no overlap of the densities, the local electron density of one system is not affected by the density of the other one and, consequently, there is no lowering of the energy. Thus, since local xc functionals cannot describe such nonlocal correlation effects by design, in order to capture dispersion forces, a nonlocal xc functional is required. In this respect, while some standard xc functionals are capable of describing correctly the short-range repulsions, they fail completely in capturing the attractive interactions. Accordingly, the simplest way to account for the missing energy is to consider that DFT is approximately capable to capture some other noncovalent interactions while the dispersion forces are accounted separately adding the supplementary dispersion term:

E_{disp} is dispersion correction to the DFT functional and not only contains the missing dispersion contribution to the total energy but has also the task to correct the uncontrolled effects on the binding energies due to the standard DFT functionals. Many forms of dispersion corrections have been suggested in the last two decades. Amongst them, the simplest is the pairwise correction which is briefly presented in this paragraph with the aim to give an introduction to the DFT-D2 method that has been extensively used throughout this thesis work. As it has already been discussed above, for two neutral molecular systems, which are sufficiently separated, the dispersion energy is already attractive and decays as the six power of the intersystem distance and this can be proven using simple arguments such as the interaction of two coupled harmonic oscillators or the second-order perturbation theory. It follows that the asymptotic behaviour of the dispersion energy is described by a simple expression:

At the heart of all pairwise dispersion corrections is the determination of the interatomic interaction coefficients, , and with the aim of obtaining these coefficients in the best agreement with experimental data, a large number of methods has been proposed during the years.

Usually, the dispersion coefficients are determined by the Casimir-Polder's formula:

–

This formula, involving the atomic frequency polarisations , is consistent with the familiar concept that the dispersion forces arise from induced-dipole interactions on the atoms A and B. The London's formula, on the other hand, is less accurate and contains only qualitative information about the dispersion coefficients. Here, it is illustrated because the DFT-D2 method [14], which is discussed below, uses such a procedure to calculate the homo-atomic coefficients. The London's formula is given by:

– ———

The I and α are the ionisations and the polarizabilities of the atoms A and B, respectively.

Amongst the most popular methods to calculate the dispersion interactions by the pairwise energy expressions, there is the DFT-D approach [14]. The DFT-D functionals have been proposed by Grimme and collaborators for the first time in 2004 and, due to their relative accuracy, simplicity and, in particular way, the widespread implementation in the most popular software packages, nowadays, they are considered the most widely-used dispersion corrections. In general, all DFT-D approaches are based on pairwise dispersion methods but they differ by increasing levels of accuracy and complexity leading these functcionals to be classified in three generations.

The original DFT-D approach uses the pairwise corrections which involve the C_6 coefficients which are calculated by experimental atomic polarizabilities. Such coefficients are constant for different hybridisation states of the atoms and do not

account for different chemical environments. Within the DFT-D approach, the total energy is calculated as:

—

K is the number of atoms in the system, denotes the dispersion coefficients for atom pair ij, s_6 is a global scaling factor, a fitted functional-dependent parameter which assumes several values for different xc functionals. The scaling factor values serve to correct the overrepulsive or overattractive behaviours of the used exchange functional. It is noteworthy the presence of the double summation running over all atoms which extends the equation 2.104 to the interactions between molecules or distant fragments of the same molecule so that all atoms in the system interact with one another. The damping function $f_{damp}(R_{ij})$ is given by

—

Such a function of the interatomic distance R_{ij} goes to zero in the limit $R_{AB} \rightarrow 0$ and to one if $R_{AB} \rightarrow \infty$ so that the dispersion contributions are deactivated at very short distances and infinitely separated atoms are not considered as interacting. Finally, the numerical constant ϑ fitted to the value of 23 and the R_0 is the atomic distance, in term of van der Waals radii, for a particular pair of atoms. Among the limitations of DFT-D, there is the lack of C_6 coefficients for general atomic pairs, the presence of systematic errors in molecules involving heavy metals and in the treatments of thermochemical data. However, the DFT-D results, which have been reported in the original paper for a collection of molecules, showed that, although the description of hydrogen bonds was not fully satisfactory, an improvement, upon the MP2 method, was achieved in capturing the π-π stacked interactions. Despite its limited success, the DFT-D method has proven that a simple formulation, such as the pairwise energy expression, when coupled with a standard xc functional, represents a valid supplement in capturing the dispersion contributions which, otherwise, would be inaccessible by common DFT methods.

The next development in the Grimme's series of the dispersion corrections led to the popular DFT-D2 functional. Such a new method, which was developed with the purpose of being more general than its predecessor, makes use of both the atomic polarizabilities and the ionisation potentials. In DFT-D2, the total energy expression is the same of DFT-D (see equation 2.107) but with some minor differences involving the reduction of the scaling factor in the van der Waals radius from an initial value of 1.22 to 1.10 as well as the ϑ parameter in the dumping function which is reduced from 23 to 20. The combination rule to obtain heteroatomic coefficients in DFT-D2 is given by:

(2.109)

while the homoatomic coefficients are obtained by the London's formula (see equation 2.106). As the authors claimed DFT-D2 contains less empirical parameters than DFT-D and fewer other methods and provides a functional which in principle is valid for all elements. The improvements of DFT-D2 upon the accuracy of DFT-D did not included some shortcomings such as the C_6 coefficients which are fixed and independent on the chemical environment and this limits the accuracy of DFT-D2. Moreover, high-order dispersions which are responsible of non-negligible contributions to the dispersion forces are not considered. Recently, the new DFT-D3 functional has been implemented in most popular software packages and is rapidly replacing the DFT-D2. The main feature of the new Grimme's functional is that the chemical environment is accounted considering that the interaction coefficients depend on the molecular geometry rather than on the electron density. Moreover, in DFT-D3 high-order dispersion contributions are considered by the high-order coefficients, C_8. These coefficients account for interaction of higher order electric moments such as quadrupole-dipole interactions which vary as $1/r^8$. Because the corrections become unstable, other high-order terms such as the three body interactions, C_9, C_{10}, etc. are absent. In conclusion, DFT-D3 has been extensively benchmarked and proved satisfactory results in many applications.

2.14 Basis sets in the electron-structure calculations of molecular and solid systems.

In order to solve the electronic structure problem in practice, either with DFT or within HF and post-HF approaches one has to choose a mathematical representation for the

one-electron orbitals. In this respect, a possible strategy would consist in representing the orbitals on a set of grid points in real space and solving the partial differential equations by the finite difference method. However, more efficient alternatives that make use of specific characteristics of the system under investigation are possible and, in this paragraph, some different types of ideas that, during the years, have been proposed and adopted for electron structure calculations, will be presented emphasising the particular importance role which is played by the choice of basis set when treating physical systems where a large variety of chemical bonding can be found. All electron structure calculations use a basis set expansion to express the unknown orbitals in terms of known functions. In principle, every type of function can be used as basis but, in practice, one should prefer those basis functions having a behaviour that agrees with the physics of the problem in order to get a reasonably rapid convergence of the results. In addition, the chosen basis function should simplify the calculation of all required integrals.

The simplest basis functions are the exponential functions since they are known to be the exact solutions to SE for the hydrogen atom. Unfortunately, such functions are numerically difficult to handle. A popular example of exponential basis functions is given by the Slater-type orbitals (STO). These basis functions, as their name suggests, are used to approximate the shapes of one-electron orbitals. The mathematical form of the normalised Slater-type wavefunction in atom-centred polar coordinates is:

Thus, the Slater-type wavefunctions can be written as the product of two normalised functions, the radial function, and the spherical harmonic, .

The radial part of the STO's depends on the orbital exponent $\zeta =$—, the principal and angular momentum quantum numbers n and l, respectively. Moreover, due to screening of the nuclear charge Z by the inner shell electrons, the effective quantum number n^* and the screening constant s have to be accounted in polyelectronic atoms. These last two parameters can be obtained by the Slater's rules considering the total number of electrons as well as the nuclear charge. Since contains the exponential term, , the STO basis functions are expected to represent the orbitals quite well in the

regions wherein r is large. Since the STOs functions do not present nodes, except for the lowest-lying states of the various angular momenta (1s, 2p, 3d, etc.), linear combinations of several STOs are required to reproduce the nodal structure in the electron structure of atoms and molecules. In practice, similar linear combinations are also required to represent accurately the lowest-lying atomic orbitals without nodes. The STOs were the first to be used in molecular quantum chemistry semiempirical calculations. Although, Slater functions were proposed in 1930 by Slater, they are still used today. Unfortunately, the analytic expressions which are involved in the computation of three and four centre Coulomb integrals are too complicate and the STOs are not the best choice for fast *ab initio* calculations. To remedy such an inconvenience, in 1950 Boys [16] proposed an alternative approach for replacing the exponential functions introducing the wide popular Gaussian-type orbitals (GTOs). In fact, within this new type of functions all the integrals, even the most complex such as the four centre Coulomb integrals, can be solved analytically. Although the natural representation for the GTOs is in polar coordinates, for the sake of brevity, the Cartesian Gaussian type functions (GTF), which is the most convenient form for the computation of the Hamiltonian matrix elements, is here discussed:

where

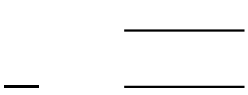

and similar expressions are given for and . Since the product of the Cartesian coordinates appears to the same power l of the radii coordinate in polar Gaussian, then the sum of the indexes has to satisfy the following equality: $i+j+k = l$. The advantage of using Gaussian type functions is that molecular integrals factorise into three Cartesian variables. Moreover, the product of two Gaussian primitives with different centres can also be written as one single Gaussian function with different centres and exponents. The behaviour of Gaussian functions is qualitatively useless at nuclei and in long-distance limit for a Hamiltonian of point charges and Coulomb

interactions. In this circumstance, the Slater-type function are preferred. Thus, in the so-called Pople's basis sets, each Slater type function is represented by a linear combination of Gaussian primitives:

N is the number of Gaussian primitives which have been used to represent a particular STF and the C_i are coefficients. The summation 2.113 is referred to as contracted Gaussian. The benefits of representing the STF's by linear combination of GTF's are now more obvious: in correspondence of nuclei the STF's present a cusp while the GTF's does not, but if linear combinations of GTFs are taken, the cusp is well reproduced. Besides, the contractions of GTF's improve the description of the electron density at very short distances from the nuclei. In molecular quantum chemistry, Gaussian-type basis functions are instead expanded as linear combinations of normalised Gaussian primitives having in common the same centre and quantum numbers but not the exponents. Such a contraction is expressed as:

and

where N, ζ_j and d_j are the contraction length, exponents and, coefficients, respectively. Since the ζ_j are fixed, contracted basis functions are very useful to represent core orbitals. A proper choice of N, ζ_j and d_j allows to the contracted Gaussian to assume any wanted functional form with desired properties which depend only on the used primitive functions. Generally, for molecular basis sets of Gaussian-type functions acronyms and notations are used: a minimal basis set is constructed by the minimum number of functions possible, in other words, the smallest number of functions which are employed to contain all the electrons of the neutral atoms. Thus for example, if there

is at least an occupied *p*-type, *d*-type or *f*-type orbital, then the complete set (3 for the *p-,* 5 for the *d*- and 7 for the *f*-type orbital) of functions has to be included in the basis sets generating minimal basis sets such as STO-3G, STO-5G and so on. The simplest of such basis sets is represented the by STO-3G. Such an acronym means that three Gaussian primitives have been added together to simulate *Slater-type-orbitals*. In general, the innermost primitives which represent the core states are contracted, while the more diffuse ones are left uncontracted. Minimal basis sets can be remarkably accurate for isolated atoms, but they are not flexible enough for describing molecular systems wherein the orbitals, being involved in chemical bonds, become polarised. In such a situation additional basis functions of the same type of those already present are required to improve the accuracy.

When each basis functions is doubled, the minimal basis set become a double-ζ (DZ) type basis (such a name is due the presence of two different ζ (zeta) exponents). The DZ basis uses two *s*-functions for hydrogen (1s and 1s′), four functions (1s, 1s′, 2s and 2s′) and two set of *p*-functions for the first row elements. The importance of a DZ over a minimum basis set is that the DZ permits a better description of electrons allowing for different bonds in different directions. Since the core state do not participate to bond formation, a modification of the DZ type basis set only affects the valence orbitals which are doubled producing a split valence double basis (VDZ).

To better describe the deformation of orbitals due to the presence of neighbour atoms, more functions of the same symmetry may be added. In the triple zeta-type (TZ) basis set, the number of functions is three times that of the minimal basis. As it has been seen for the VDZ, in triple split valence VTZ some core orbitals can be saved splitting only the valence orbitals. In TZ basis set there are six *s*-functions and three *p*-functions for the elements of the first row. Further increases of the number of symmetric orbitals leads to larger basis sets such as quadruple zeta (QT), quintuple zeta (5T) and next level of basis sets which are explicitly expressed in terms of the number of basis functions of each type. In general, multiple splits of basis functions improve the description of outer valence region. Usually, in computational chemistry, the Pople's notation 3-21G (or STO-3-21G) is used to designate a Slater-type orbital which is described by a split valence basis set. In particular, the 3-21G abbreviation means that the core electrons are represented by three Gaussians, the inner and the outer valence electrons are described by two Gaussians and one Gaussian function, respectively. Analogously, the notation 6-311G describes a split TZ basis set wherein six Gaussians represent the core

orbitals, three Gaussians describe the innermost valence orbitals whereas the middle and outermost orbitals are described as single Gaussians.

Further improvements of the basis set may be achieved considering functions of higher angular momentum and this is done introducing the polarisation functions into the basis set. Polarisation effects are accounted by functions of different angular momenta. In this respect, the perturbation theory indicates that the most important contributions are given by angular momenta $l=\pm 1$. The rule of thumb to improve the basis set requires that the doubling of the basis set has to precede the polarisation. In presence of negatively charged molecular fragments, the enhanced Coulomb repulsion between the electrons is responsible of the spreading of the atomic orbitals. Since the standard basis functions are not enough to describe such atomic orbitals, additional basis functions with small exponents need to be included. Such complementary basis functions are called diffuse functions and, in the Pople's notation, they are indicated by a plus sign, "+". It also possible to increase the number of diffuse functions. In general, diffuse functions are requested for improving the description of non-bonding interactions. Dunning-Huzinaga (DH) correlation-consistent (cc) basis sets represent one of the several alternatives to the Pople's basis set style that nowadays are available to represent orbitals in electron structure calculations. Such basis set are due to the Huzinaga idea of determining uncontracted energy-optimised basis sets for the first row elements[16]. Successively, Dunning used the Huzinaga primitive GTO's to derive various contraction schemes and the resulting basis sets are successively optimised using correlated wavefunctions. Since the basis sets are optimised at HF level, as Dunning pointed out [17], they might not be the best choice for correlated calculations. The acronym cc-pVXZ is used to indicate a DH correlation-consistent, polarised valence, X-ζ basis; where X=D, T, Q, 5, 6, 7. In particular case of the carbon atom, the cc-pVDZ consists of *3s2p1d* while the cc-pVTZ would be *4s3p2d1f* and so on. The popularity of the Pople and DH style basis sets is due to large number of calculations which have been reported in literature during the years. In fact, the more results are published with that given basis sets, the more the knowledge of the level of accuracy attainable with that basis set increases. This favours the growth in popularity of that particular basis set which is mainly due to an extensive calibration.

Besides, since the Dunning-Huzinaga type basis set have not the restriction of the Pople's style basis set of equal exponents for the *s*- and *p*- coefficients, they are somewhat more flexible. In conclusion, high quality wavefunctions are required in

calculations involving the effects of electron correlation. This requires very large basis sets and, in particular, wavefunctions with complex nodal structures (large polarisations) which lead to very demanding computational tasks. Thus, one of the thumb rules for choosing a basis set: the bigger the better finds its limitation in the compromise between the desired accuracy of the results and the computational time which has to be spent to obtain them. One of the most important shortcoming which is connected with the use of basis set is known as basis set superposition error (BSSE). The simplest way to explain the BSSE is that of considering a practical situation which consists in calculating the energy of a dimer with respect to the isolated monomers. In the dimer, the basis functions from one monomer can compensate the basis set incompleteness on the other monomer, and vice versa. In this situation, the dimer is found lowered in energy and the bond between the monomers overestimated. In the limit of a complete basis set, the BSSE error would be zero and adding more basis functions does not yield any improvement. Unfortunately, this means to use large basis sets and it result in a computationally expensive task. An approximate way of assessing the BBE is the counterpoise correction. In the counterpoise correction the BSSE is estimated as the difference between monomer energies with regular basis and the energies calculated with the full set of the basis functions for the whole complex.

To see how this approach works, let's consider two components A and B forming a molecular complex AB having individually regular basis sets: *a* (for the component A), *b* (for the component B) and *ab* (for the complex AB). After optimising the geometry of each molecular structure, it is found that the geometry of A and B in the molecular complex are slightly different from isolated species A and B. In general, for a complexation reaction

the complexation energy is given by

To estimate how much of this complexation energy is due to the BSSE, one needs to calculate the energy of the fragment A in same geometry that it had in the complex using the basis set *a*. Then, one has to repeat the same procedure for the fragment B

using the basis set *b*. At this point, the energy of the fragment A and B with the geometry they had in the complex AB has to be separately (A with *ab* and B with *ab*) calculated with the full *ab* basis set. This means that the energy of the A fragment is calculated in presence of both the normal *a* basis function and with the b basis function of the fragment B which is located at the corresponding nuclear position but without the B nuclei present, and vice versa. The basis functions which are located at fixed points in space are often referred to as ghost orbitals. Since the basis becomes more complete, the energy of the individual A and B fragments will be lowered and for the complexation reaction of A and B, the counterpoise correction is defined as:

where is the energy of the fragment A which is calculated in the geometry of the complex AB with the full basis set *ab* etc.

2.15 Effective core potentials, ECP's.

Chemical experience suggests that most of the properties of molecules and crystals are mainly determined by the valence electrons of constituent atoms while core electrons are weakly influenced by chemical events such as bond formation, electron cloud polarisation, ionisation etc. However, since the innermost electrons play a crucial role in determining the electronic structure of the periodic table elements, they have not to be completely neglected. In fact, core electrons shield the nuclear charge and provide an effective potential for the valence electrons. In addition, due to synergic contributions of the strong binding of the core electrons to the nucleus and the reduced nuclear charge experienced by the valence electrons, there is a space/energy separation between the innermost and valence electrons. Such a separation is more pronounced for light elements than for transition metals. The effect of the space/energy separation between core and valence electrons is seen, for examples, considering the energies of the occupied orbitals for the ground state of an isolated oxygen atom. Such energies were calculated at HF level and resulted: -20.66 a.u for the *1s*, -1.24 a.u for the *2s* and, -0.63 a.u for the *2p.* As it can be easily seen, there is a marked separation in energy which allows the precise distinction between the core and valence states. However, the

decomposition of electrons into core and valence becomes more complicated when the energy separation between shells is very small. This is, for example, the case of the isolated Ti atom in its ground state but, such a situation is quite common to many other transition metals. The Ti orbital energies resulting from HF calculation are: -2.87 a.u for the *3s*, -1.79 a.u for the *3p*, -0.44 a.u for the *3d* and -0.22 for the *4s*. Accordingly, the *4s* and *3d* states are very close in energy and this fact determine the chemistry of Ti. Nevertheless, also the 3*s* and *3p* orbitals are very close in energy. Since, the overlap of the *3d* (or 3*s* and *3p*) with the orbitals of neighbour atoms is too large to be ignored, the large and small effective potentials have to be introduced. The difference between these two is that the large effective potential also include the *3s* and *3p* core orbitals. The basic idea behind the effective core potentials (ECP's) is that to consider the core electrons as responsible of an effective averaged potential rather than distinct quantum mechanical particles. ECP's are based on the frozen-core approximation and since the number of coefficients in the one-electron wavefunctions results largely decreased, in some cases, the use of ECP's leads to significant savings in the SCF part and consequently in the CPU time. This is the case of heavy-element atoms which are involved in many chemical and physical phenomena and the ECP's result of particular importance especially in the description of molecular and crystal systems containing atoms with a nuclear charge $Z \geq 50$ for which the relativistic effects appearing in the core atomic region play a crucial role in the total nature of the electronic structure and the full treatment of these effects by the Dirac's Hamiltonian would request severe computational efforts. ECP's and their relative basis sets make use of parameters which are determined experimentally not only for the ground state but also for excited states. Due to their semiempirical nature the ECP's can perform remarkably well for some systems but if they are used for other environments, their performance can be poor. Phillips and Kleinman showed that ECP's could also be found nonempirically [473]. Since the first formulation of ECP's of Fock, Veselow and Petrashen [101], many other parametrisations have been proposed during the years. Amongst them, the Hay and Wadt ECP's which are of general form [483] and the large-core semilocal ECP's of Durand-Barthelat [484]. One of the most recent developments of ECP's and relativistic ECP's (RECP's) is that of Stoll and Preuss or Stuttgart-Dresden (SD) ECP's as they are largely known. Since in this thesis work the SD ECP's for gold have been used, a brief overview on the SD ECP's will conclude this paragraph. The SD semilocal ECP's have the following form:

—

where the first term is the Coulomb contribution considering the effective charge, Z_N, namely, the total nuclear charge minus the number of electrons which are represented by the ECP. The second summation is a local term involving the product between polynomial radial functions and Gaussian radial functions. In the third summation the polynomial radial functions and the Gaussian radial functions are multiplied by the angular momentum operator . The most recent ECP parameters and optimised valence-electron basis sets for the GAUSSIAN and other software packages can be found online at: http://www.theochem.uni-stuttgart.de (last access on 07/08/2016). The database also includes relativistic ECP's which have been obtained solving the Dirac-Fock equation for atoms.

2.16 Plane-wave Basis sets

In order to describe systems with periodically arranged atoms, one has to choose basis functions satisfying the Bloch's theorem [18]. Such a theorem prescribes that a wavefunction must be composed of a periodic part, so that, the following equality:

is always valid for any lattice vector, $\boldsymbol{a}_i$. Thus, for periodic systems, the SE solutions are expressed as a sum of terms having the form:

Where φ_k is the one-electron wavefunction in the unit cell. The imaginary phase factor, comprising the space coordinates **r** and the reciprocal space vector **k**, is called plane wave. Thus, the Bloch's theorem indicates that the crystalline orbital for the *n*th band in the unit cell can be written as a wave-like part and a cell periodic part or, equivalently, the wavefunction for an electron in a periodic potential is a periodic function which is modulated by a plane wave whose wavelength is

Due to its periodicity, the Block orbital, u_k, can be expanded as a set of plane waves, namely:

Here, the sum runs over the reciprocal space vectors, **G**. It follows that, the 2.120 allows to write the one-electron wavefunction as a linear combination of plane waves:

In principle, an infinite number of **G** vectors is required to represent the wavefunction with an infinite accuracy. In practice, since the wavefunction Fourier coefficients , decreases with the increasing of the term | , the plane wave expansion can be effectively truncated at a finite number of terms so that only the waves with kinetic energy lower than some energy cutoff E_{cut} are considered.

In atomic units $\hbar = m = 1$. It is quite common to specify the energy cutoff in Rydberg; 1 Ry = 13.6 eV = 0.5 a. u. or hartree.
The use of plane waves permits to the KS equations to assume a very simple form:

where, the first term is the kinetic energy, and,

are the Fourier transforms of the electron-nuclei, electron-electron and xc potentials. Plane waves offer several advantages. They are universal: do not depend on the atomic positions nor their nature. Since, the plane waves do not move together with atoms, they represent all the space of the unit cell with the same accuracy and calculations of the energy and its derivatives is analytic and quite simple to obtain. This yields to an advantage with respect to the basis sets especially in molecular mechanics calculations. Another benefit which is obtained when plane waves are used rather than basis sets is that calculations do not suffer of basis set superposition error (BSSE).

2.17 Pseudopotential methods.

In the previous section, it has been seen that for free electrons in a periodic system, the wavefunction can be expanded in plane waves. In the ideal situation, when the atomic potential can be neglected, the plane waves are the exact solution to the SE. On the other hand, if the potential is smoot, it can be considered as a perturbation. However, in the real systems, the potential generated by atoms is far from being smoot. For example, in the simplest case that is represented by the hydrogen atom, the potential is given by which diverges at the origin. On the contrary, the 1s wavefunction has a cusp at the origin and decays exponentially with the distance. For heavier atoms the associated wavefunctions are steepest. The problem of describing core electrons is that they are characterised by fast oscillations and large number of plane waves would be required at very costly computational expenses. In the 1937, a possible solution to this problem was suggested by Slater [19] that proposed an expansion of plane waves which were augmented with the solution to the problem in a spherical region around the nuclei while the potential was assumed as spherically symmetric within the spheres and zero outside (Augmented plane wave method APW). In order to overcome the shape approximation of the potential, few years later, it was suggested an alternative method that consisted in constructing the valence wavefunctions as a linear combination of plane waves and core waves functions. Since these plane functions are orthogonal to the core states, this method is known as orthogonalized plane waves (OPW). A step beyond the OPW approach consists in replacing the core states with an effective potential or pseudopotential. The most common pseudopotential approach consists in not allowing the relaxation of core electrons according to environment. This approach which is largely known as frozen core approximation is based on the observation that cores states are not fundamental for the description of chemical bonding and a detailed

description of the valence wavefunction within the core region is not strictly necessary. Moreover, there is no loss of crucial information if the inner solution is replaced by pseudo-wavefunction which is not the solution to the original atomic problem but nothing less than a smoot and nodeless function. The origin of modern pseudopotential approach stems from the OPW method and in the 1959, Philips and Kleinman were the first to show how to construct a smoot valence wavefunction which is not orthogonalised to the core states by a combination of the core state and the true valence wavefunction :

where, . Such a wavefunction is solution to the modified SE:

here, — which leads to the pseudo-Hamiltonian:

which has the same eigenvalues of the original Hamiltonian but the eigenstate is smooter and nodeless. Finally the associated potential

—

is known as pseudopotential.

There is a large freedom in building pseudopotentials. Empirical pseudopotentials that were determined by fitting experimental energy bands have been very popular in the past. However, they lack of transferability, namely, pseudopotentials built for a specific environment could not be used for the same atomic species within a diverse environment. The construction of a pseudopotential requires initially to choose the

reference configuration, namely, the electron configuration in the isolated atoms. States of angular momenta that are unoccupied in the neutral atom hybridise with the occupied states in the presence of a different environment becoming partially occupied. Hence, these angular momenta have to be incorporated as non-local component of the pseudopotential. Finally, in performing DFT calculations one faces different types of pseudopotentials such as norm-conserving or ultrasoft. The choice of the right pseudopotential depends on the basis set. If plane waves are used, then ultrasoft pseudopotentials are the most efficient. For atom centred basis sets, the softness of pseudopotential does not present a big issue since the basis functions are tailored to reproduce atomic orbitals. In this case, norm-conserving and ultrasoft pseudopotentials result being equivalent.

2.18 Generalities about carbon allotropes and their applications in science and technology.

The most intriguing element of periodic table is, surely, carbon. It plays a unique role in nature being the key element of life on planet Earth. Carbon is synthetized through the triple α-process in stars where allows the formation of other elements as well. Besides, due to its ability to react also in relatively mild conditions with other carbons, hydrogen, oxygen and other elements, it gives rise to an extraordinary number of chemical compounds and isomers which are found in most facets of everyday life. The compounds of carbon with hydrogen and their derivatives are object of study of large branches of chemistry such as organic chemistry, bio-chemistry, organometallic chemistry and, so on.

Even elemental carbon shows unusually complicated behaviour. In fact, a number of different allotropes having diverse dimensionalities are known today. In this regard, carbon is found in two stable three-dimensional forms such as graphite and diamond which exist in nature and were known since ancient times while, zero-, one- and two-dimensional allotropes which are better represented by the most popular polymorphs such as fullerenes, nanotubes and graphene, respectively, derive from carbonaceous precursors and have been recently isolated by chemical or physical processes. The properties of these allotropes can vary widely. For instance, comparing the physical characteristics of three-dimensional allotropes, one finds that, while diamond with the highest Young's modulus is the hardest-known material, graphite is one of the softest. Diamond is transparent. Graphite is opaque. Diamond is an electrical insulator.

Graphite is a conductor. These striking disparities between these two allotropes show that physical and chemical properties are deeply influenced only by the arrangement of carbon atoms in the crystals. In diamond, all bonds between carbons are sigma type and can be described as formed by the overlap of sp^3 orbitals. The atoms in diamond are arranged in a tetrahedral geometry which is responsible for the crystal isotropy. By contrast, in graphite where the carbon atoms.

The wide variety of mechanical, electrical, optical and tribological properties of carbon-derived materials has witnessed a strongly increased interest from both scientific and industrial communities which have seen in these materials an enormous upside potential suitable for an almost limitless number of applications. Here, few examples of the state of art in the research fields

Diamond, for instance, being characterised by a high refractive index and a noble gloss is mainly popular as precious gems which are largely used in jewellery, but in the last few decades some its properties have been discovered and have led this material into the focus of scientific and technological interest. It is an insulator in its natural form but, the discovery of superconductivity in some of the diamond forms has opened the possibility to combine outstanding mechanical properties with superconductivity. In fact, when diamond (a super-hard material) is doped with boron, it can be turned in a superconductor at low temperatures. At micrometre and nanometre scale, boron-doped diamonds have a wide range of applications spanning from the production of microelectrodes to that of nanomechanical devices in superconducting circuits allowing the fabrication of very powerful technological micro devices.

Other carbonaceous materials that, in last few decades, have seen an increasingly interest in science and technologies are the fullerenes. The fullerene molecules are considered the third form of carbon and although, initially, were used in the industry, mostly in cosmetics, where they play an important role as antioxidants, nowadays they are the key topics in medicine after that water-soluble functionalised fullerenes revealed their biological activity. In particular, fullerenes molecules are investigated as anti-HIV and anti-cancer agents. Within the fullerene molecules, carbon atoms have both sp^2 and sp^3 hybridised orbitals which are responsible for the unique molecular geometry as well as for the unusual physical and chemical properties. In fact, the delocalised pi electrons are responsible of providing exceptional large nonlinear optical responses. Fullerenes have a LUMO which is very low in energy and endows the molecules an electron affinity relatively high to many organic electron donor materials. Such a

requisite makes fullerenes good materials for the productions of solar cells. Fullerenes have also other technological applications such as in hydrogen gas storage and are used in the production of sensors.

At this point, with the aim of simplifying the following description of nanotube and graphitic materials, some characteristic of the graphene structure need to be discussed. In fact, graphene can be considered as the basic building block of all other dimensionalities and the following discussion on graphite and nanotubes is largely simplified with the graphene structure in mind. Graphene (or more precisely, monolayer graphene) is the first known example of two-dimensional crystal. For this reason and for its outstanding physical properties, it has been rightfully termed as the "ultimate flatland" [20]. Graphene is a one-atom thick sheet of carbon atoms that are arranged in a honeycomb lattice. The sp^2 hybridisation of the orbitals in the atoms allows the formation of chemical bonds that are stronger than those of diamond. In graphene, each carbon atom is bonded to three others, forming a series of continuous hexagons which may be considered as an infinite two-dimensional crystal. Although, graphene-planar, hexagonal arrangement of carbon atoms has been the starting point of theoretical investigations on the graphite structure since the late 40's, the first graphene crystal has been experimentally isolated for the first time in 2004 by a technique known as micromechanical cleavage. Graphene's unique properties depend on its crystal structure which presents two equivalent carbon sublattices, A and B (in bilayer graphene). The quantum mechanical hopping of quasiparticles (Dirac fermions) taking place between the A and B carbons lead to the formation of two energy bands and the intersection of these, near the edges of the Brilluin zone, yields the conical energy spectrum in proximity of the Dirac points.

In the graphene crystal, quasiparticles show the linear dispersion relation $E=\hbar k v_F$ behaving as massless relativistic particles moving at the Fermi velocity v_F (v_F is related to the speed of light c by the relation $v_F=c/100$). Thus, since its discovery, graphene is attracting tremendous attention from scientific and technological communities aiming to provide insight into this carbonaceous material and exploring the large spectrum of technological applications which are based on its unique and remarkable properties.

For example graphene is a metallic-like zero band gap which makes it a promising candidate for future electronic applications.

Graphene can absorb gas molecules from the surrounding atmosphere, resulting in doping of the graphene layer with electrons or holes depending on the nature of the

adsorbed gas. Changes in monitored resistivity permit of detecting the presence of minute gas concentrations in the environment. Different types of carbon materials, such as activated carbon, graphite and carbon black, have been successfully used over the last centuries as catalysts or catalyst supports in the chemical industry.

2.19 Graphite

In graphite, the sp^2 hybridisation leads to a covalently bound lattice of graphitic planes which are stacked one on each other and weakly bound by residual forces arising from non-hybridised $2p_z$ orbitals extending perpendicularly to such planes. The cohesive forces between layers determine diverse stacking order of the graphene planes that can be classified in hexagonal, orthorhombic and rhombohedral sequences. The ideal hexagonal graphite structure which is also known as Bernal phase is composed by a theoretically infinite number basal graphene planes with a perfect stacking that leads to two atomic environments. The first environment includes the α atoms, namely, all those carbons having directly above and below them other carbon atoms in the contiguous layers. The β atoms, instead, are carbon atoms which are placed above or below the empty centres of the hexagonal rings in adjacent planes. In the orthorhombic sequence, the plane stacking allows each carbon atom to be always superimposed by other atoms and finally, in the rhombohedral or type graphite, the staking sequence does not allow any direct superposition between the atoms in adjacent layers.

Experimental investigations have shown that a given graphite sample usually contains the 80% of the hexagonal structure, 14% of rhombohedral structure and only 6% of orthorhombic graphite and, no rhombohedral structure has been detected in the isolated form without the hexagonal component. Since the Bernal phase is more abundant in nature, it is the only subject of this computational investigation. From a theoretically stand point

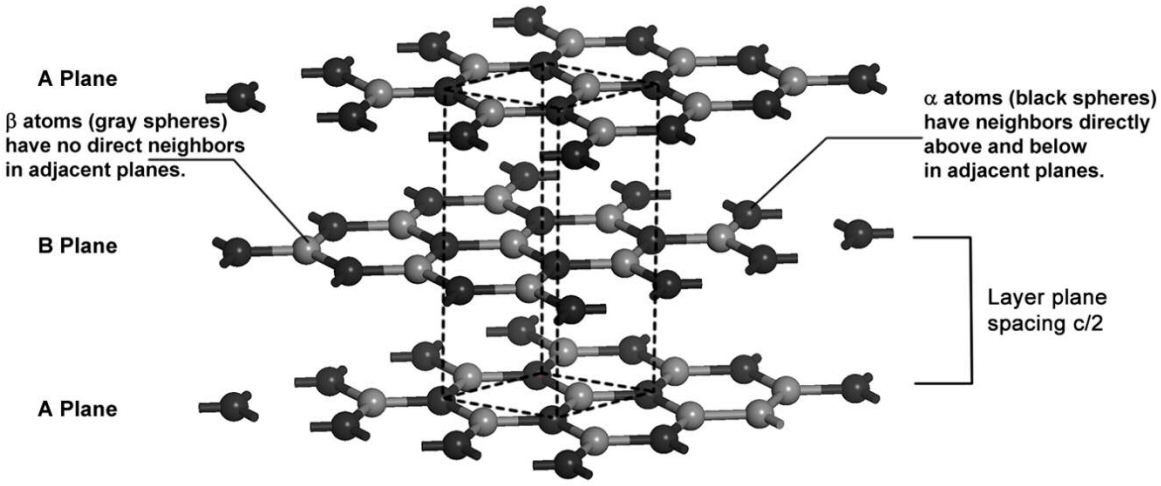

Figure 1. Example of graphite surface. In the picture only three layers have been shown. The dotted black line represent the unit cell.

This work has been additionally aimed to a preliminary understanding to the role played by dispersion forces, and to acquiring the ability to describe these purely quantum mechanical interactions at high level of accuracy.

2.20 Computational Methodology

All results that will be discussed in the rest of this chapter have been obtained by periodic Kohn-Sham DFT calculations using the plane-wave basis set code Vienna Ab initio Software Package (VASP 5.3) [21]. Electron ground state energies of equilibrium geometries were obtained within the generalised gradient approximation (GGA) by the Perdew, Burke and, Ernzerorf (PBE) [22] parametrisation of the xc energy functional and, adding the Grimme's D2 [23] empirical dispersion corrections to the DFT energies (PBE-D2) in order to give a more accurate treatment of the dispersion forces. Carbon core electrons, $1s^2$, were accounted by the projector augmented plane wave method (PAW) and a cut-off energy of 500 eV is used for limiting the number of plane waves. A Monkhoster-Pack [24] Γ-centred 5 5 3 k-point mesh was used for the geometry relaxations and single point calculations. A finer grid of 16 16 5 k-points was used, instead, for density of states (DOS) calculations. The relaxation cycle was stopped when the Hellmann-Feynman Forces was smaller than $5 \cdot 10^{-3}$ eV/Å and a Gaussian smearing with a width of $\sigma = 0.05$ eV was used for the occupation of the electronic levels.

2.21 A preliminary computational investigation on graphite bulk.

It is well accepted that, in graphite, carbon atoms are covalently bonded within the layers but the nature of the interlayer bonding is still poorly understood. To our knowledge, at present, no direct measurements of interlayer binding energy have been published. The only available physical quantities are estimates of the binding energy which are based on theoretical models using experimental data for the exfoliation, namely, the necessary energy that permits to remove a graphene plane from the surface of a graphite crystal.

Three experimental works have been performed in synergy with molecular mechanics measuring the exfoliation energy in graphite by different approaches. Girifalco and Lad [25] used a Lennard-Jones potential to estimate the exfoliation energy in relation to the cleavage energy. They reported a value of the exfoliation energy of 43±5 meV/atom and estimated that the difference between exfoliation and cleavage energy was of about 18% but the exact difference is unknown.

Benedict *et al.* [26], using a force field to model the elastic properties of nanotubes, have extrapolated a graphite layer interaction energy of 33.3 eV/atom from measures on collapsed nanotubes.

More recently, Zacharia *et al*. [27] derived the graphite exfoliation energy by extrapolating, as a function of the number of atoms, the energy of aromatic molecules which were desorbed from the graphite surface, doing so, they obtained a value of 52±5 meV/atom. This investigation also permitted a better estimation of the cleavage energy which was found to be of 62 meV/atom.

From a practical standpoint, understanding the dispersion forces underlying the interlayer interactions in graphite is relevant to the comprehension of carbonaceous materials including carbon based systems for hydrogen storage, graphite intercalation compounds and novel technological components which are relevant for many applications. On the other hand, the ability to describe accurately those interactions represents a challenge for theoretical approaches which are based on density functional theory. This motivates the intense interest of the theoretical community in understanding the role of dispersion forces and acquiring the ability to describe such purely quantum mechanics interactions at a high level of accuracy. Many computational works with aim to improve the description of dispersion forces in graphite are appeared in literature since the early 90's. Amongst them, Girifalco et al. [28] suggested that, in

the graphite crystal, in plane C-C bond lengths and the interlayer binding which are responsible for the lattice constants are well reproduced by LDA. Although, LDA reproduces the interlayer distance (3.31 Å), in good agreement with experiment, it underestimates the binding energy (-20 eV/atom). In this respect, Graziano *et al*. [29] pointed out that, by the LDA, the energy decays incorrectly as the separation of graphene layers increases. Thus, since the limits of the local correlation are fully understood, it is interesting, at this stage, to investigate on the possible improvements that might be obtained employing the GGA correlation in the treatment of dispersion forces. It is largely recognised that GGA fails in reproducing any significant interlayer bonding. Thus, in order to improve upon the standard GGA xc functional in the form of PBE, this is coupled with the Grimme D2 corrections. A preliminary test that at first glance is capable to give an idea of the performances of pure PBE and DFT-D2 methods, consists in calculating the potential energy surfaces as function of the interlayer distances.

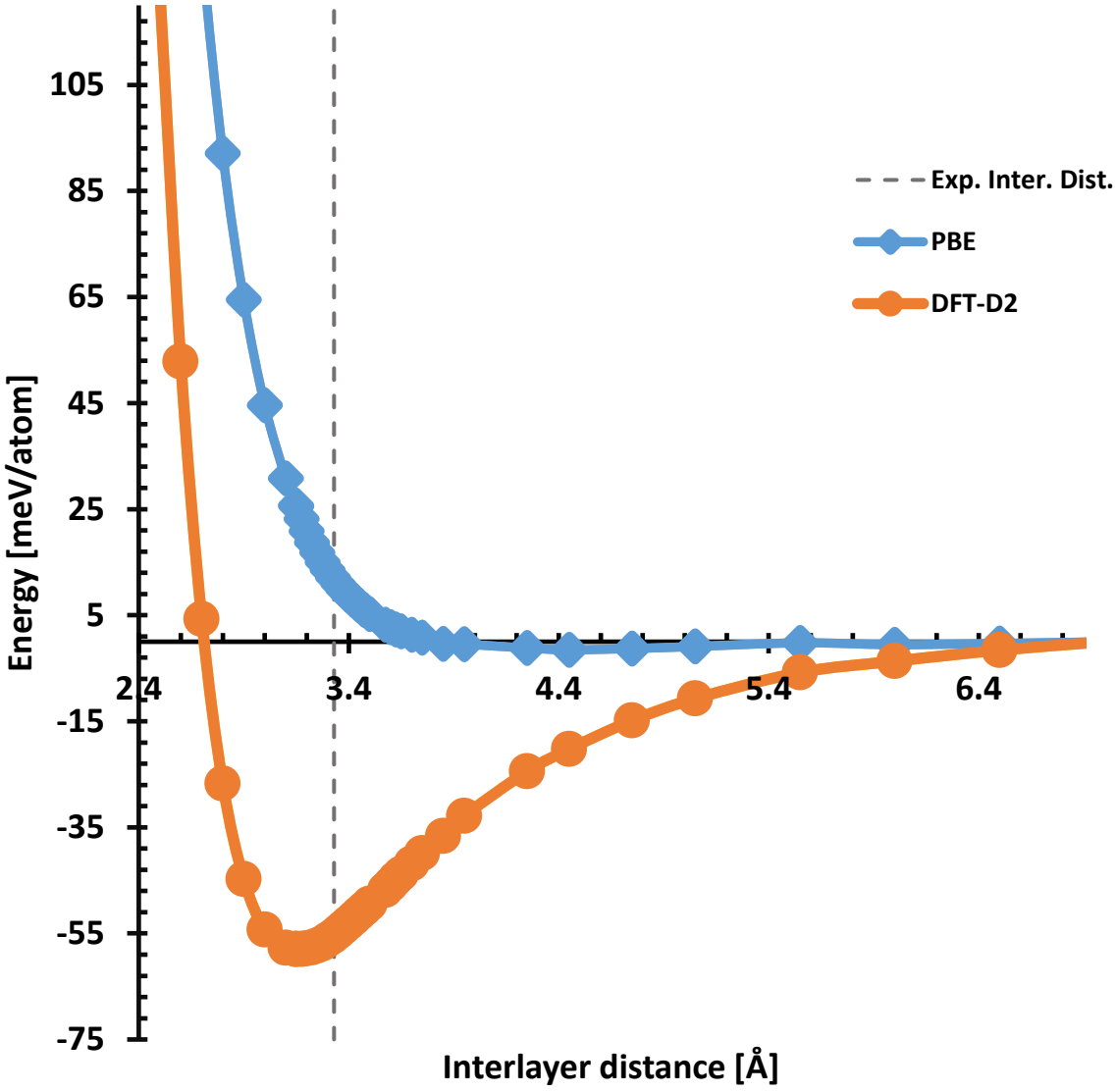

Fig. 2 Binding energies as function of interlayer distances in graphite bulk. The experimental value of the interlayer distance is taken from [29] and is indicated by the vertical dashed line.

As it can be seen from Fig. 2, the PBE xc functional produces a potential energy surface (blue line) that is uniquely repulsive and essentially does not present any binding between the graphene planes except for the small minimum occurring at 4.45 Å of interlayer separation. Such an equilibrium distance corresponds to a very low binding energy of -1.52 meV/atom which might be attributed to small (semilocal) correlation effects.

The overestimation of the interlayer binding as well as the underestimation of the binding energy resulting from GGA-PBE calculations, are not surprisingly. In fact,

GGA is a semilocal approximation and by a completely non-overlapping electron density is not capable, by design, to account for dispersion forces that are long range interactions.

The orange line, in Fig. 2, represents the binding energy curve of GGA-PBE xc functional incorporating the dispersion corrections which, from now on, is simply referred to as DFT-D2. The performance of DFT-D2 is notably superior to that of PBE. In DFT-D2, the semilocal (gradient) part of the GGA correlation functional has been supplemented with a semiempirical correction terms allowing to obtain a curve which shows both the attractive and repulsive behaviours as it is expected in a system where most of the stabilisation comes from dispersion interactions. The energy minimum is located at 0.14 Å of interlayer separation below the experimental value showing that DFT-D2 gives a satisfactory interlayer binding within about the 5% of the experimental value [29] (in Fig. 2, the experimental interlayer separation is represented by the vertical dashed line). Although DFT-D2 gives interlayer separation in good agreement with the experimental value, the binding energy is calculated about ~6 eV/atom below the exfoliation energy of Zacharia *et al*, [26] that has been chosen as indirect reference. However, PBE completely fails to predict the magnitude of the binding energy while DFT-D2 gives a good estimation of the interlayer binding energy.

The structure of graphite has been widely investigated during the years not only theoretically but also from the experimental standpoint [21-24]. Thus, in order to choose the computational method that is capable to reproduce more accurately the graphite bulk properties, experimental measurements are used as direct benchmark in the geometrical optimisation of graphite bulk.

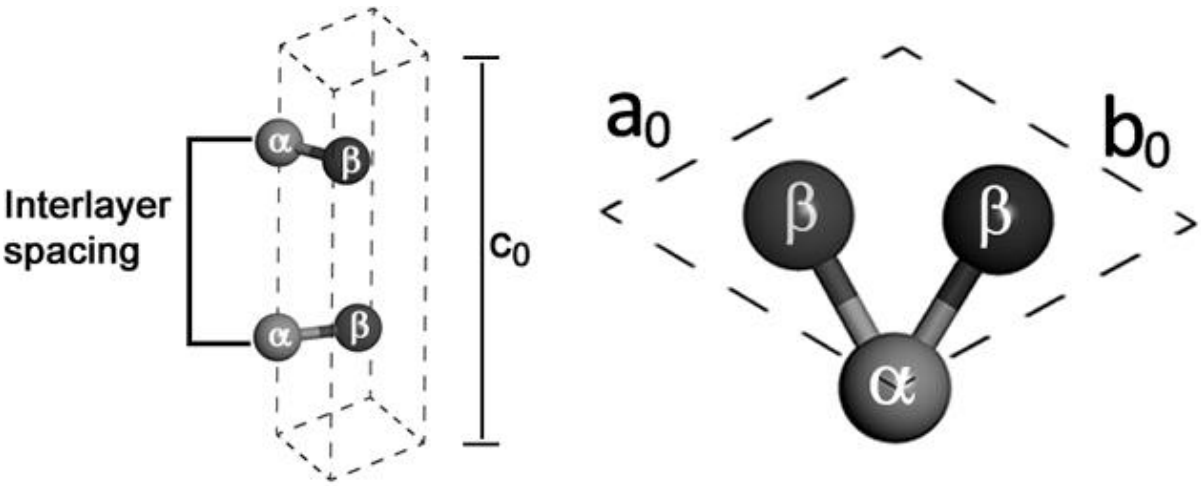

The Bernal's structure unit cell, which is pictured in Fig. contains four carbon atoms. The experimental lattice constants are $a_0 = b_0 = 2.462$ Å, $c_0 = 6.711$ Å [25]. Such lattice parameters has been used for the geometry optimisations of the bulk structure using both the selected DFT methods, PBE and DFT-D2.

Some geometrical parameters are collected in Table 1 which contains also other theoretical and computational works.

	PBE	**DFT-D2**	**Comp.[a]**	**Exp.[a]**	**Exp.[b]**
	2.472	2.462	2.448 [17]	2.462 [21]	
	8.000	6.299	2.443 [17]	6.711 [22]	
C-C (1)	1.425	1.423		1.421 [23]	
C-C (2)	4.451	3.148	3.24, 3.35	3.33[24-25]	
$\mathbf{E}_{\text{atomisation}}$	-7.44	-7.50		-7.53 [29]	-7.37 [29]
Cell Vol.	42.34	33.14		35.28 [29]	35.12 [29]
$\mathbf{E}_{\text{exfoliation}}$	-1.52	-57.95		33, 43 [29]	52 ±5 [26]

Table 1. Selected bond lengths (Å)

In graphite bulk, the in-plane bond lengths [C-C (1)] between carbon atoms are shorter than sp^3 bond lengths in diamond (1.54 Å) and larger than a pure double bound (1.334 Å) in alkenes. Not surprisingly, they result very close to the sp^2 hybridised bonding lengths of aromatic condensed rings ranging from 1.39 Å in benzene to 1.427 Å for the innermost coronene ring. Although, both the DFT methods calculated the in-plane C-C bond lengths in good agreement with the experiments, DFT-D2 gives a bond length that is a slightly more accurate than that one of PBE though it might not be van der Waals bonding. Accordingly, experimental lattice constants a_0 and b_0 are properly reproduced by DFT-D2 which also performs better than LDA calculations.

2.22 Electron properties in graphite bulk

Another way to find the computational method which better describes graphite properties closer to the experiment, is that of considering the bulk electronic structure. There have been many published simulations on the electron structures of graphite since the early day of quantum chemistry [10-11]. More recently, the experimental work showed the presence of interlayer states in graphite. This experimental work was performed using the NEXAFS with the aid of band structure calculations. Natural graphite presents a mixture of crystallites with three diverse stacking sequences: AB (Bernal), ABC (rhombohedral) and AAA (orthorhombic) the band structures of each of these allotropes were studied by Charlier *et al.* [45]. This study was aimed to understand the differences to resolve the discrepancies in experimentally measured graphite band structures. A step forward in the understanding the electronic structure of graphite was made when Wang *et al.* [45], using pseudo-potential calculations, investigated on the inter-plane and intra-plane carbon binding in graphite and in graphitic silicon. The authors observed, plotting the charge densities resulting from the analysis of diverse bands, that in graphite the role of the p_z orbitals of carbons is twofold. Firstly, the p_z orbitals contribute to the intra-layer carbon binding, providing a carbon-carbon bond which is stronger than a carbon-carbon bond that is obtained by the mere combination of sp^2 hybridised orbitals. Secondly, there is an additional contribution to the interlayer binding in the form of an overlap of p_z orbitals.

In this work, DOS diagrams have been obtained using the graphite bulk unit cells which were previously optimised with PBE and DFT-D2. A preliminary single point calculation, using 24 24 1 *k*-mesh of 156 irreducible points gave the charge density and the wavefunction which were used as input to a subsequent calculation. In both the calculations, a Gaussian smearing of 0.1 eV was chosen. Finally, the projected DOS were calculated within Wigner-Seitz sphere of radius 0.863 Å (such a value was obtained from carbon pseudopotential file which is provided by VASP).

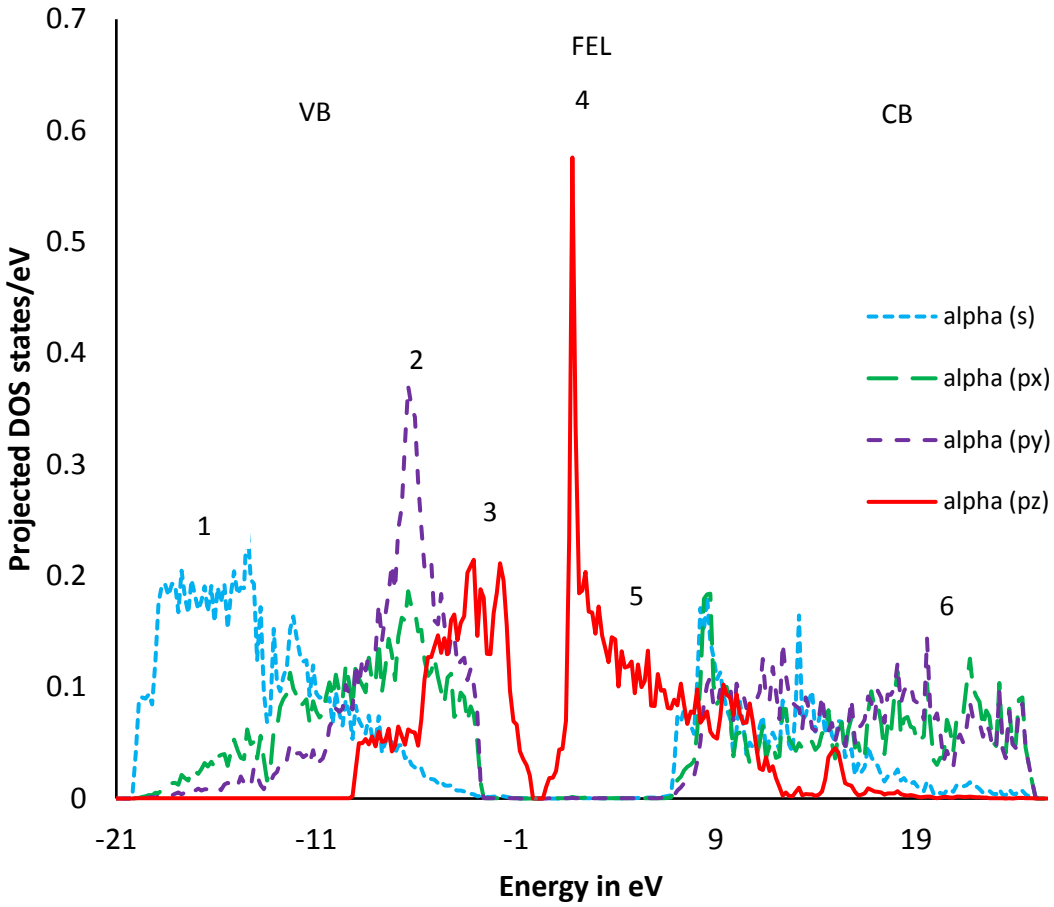

Fig. 5 - *lm* decomposed DOS diagram of α-carbon atoms in bulk graphite. The optimised unit cell and DOS diagram have been obtained by PBE xc functional. The dotted grey line represents the Fermi energy level (FEL) and is placed at 0 eV.

Fig. 4 reports the *lm* decomposed DOS structure of α-carbons within the graphite bulk. It was obtained considering the previously optimised unit cell by PBE xc functional. In the diagram, the highest features resulting from the contribution of each angular momentum are labelled with numbers in order to simplify the following discussion. In the VB, the 1s core orbitals extend in the lowest energy range which goes from -20.19 to -13.12 eV. The 1s peak is found at -14.44 eV and, in Fig. 4, is labelled with 1 (1). The largest peak (2) within the VB is at -6.39 eV. This peak is located in an energy range extending from -13.12 to -2.77 eV. This energy range mainly consists of the contributions of 2s, $2p_x$ and $2p_y$ atomic orbitals and the sum of the projections on these orbitals is usually referred to as σ band. The pure π band, which indicates the projection on the carbon $2p_z$ orbital, overlaps the σ band from -9.18 to -4.42 eV. Finally, the last

sequence of peak (3) is associated to the pure π band and occurs at -1.79 eV while the range of the pure π band extends from -4.42 to 0 eV. In the CB, the main π* peak (4) is at 1.82 eV. The π* peaks extend up to 12.6 eV overlapping with the σ* band from 7.08 to 12.66 eV. Finally the σ* band extends from 7.08 to 27.15 eV. The energy difference between π* and the σ* features is of 6.57 eV which is in good agreement with the experimental values found in literature. The high resolution electron energy loss spectroscopy (HREELS) value places such a difference in the range of 6-7 eV [45] while the carbon K near-edge spectroscopy X-ray-adsorption spectra (NEXAFS) yield a distance of 7 eV [42]. Finally, the experimental and theoretical work published by Titantah *et al*. reports a different value of 6.4 eV [16].

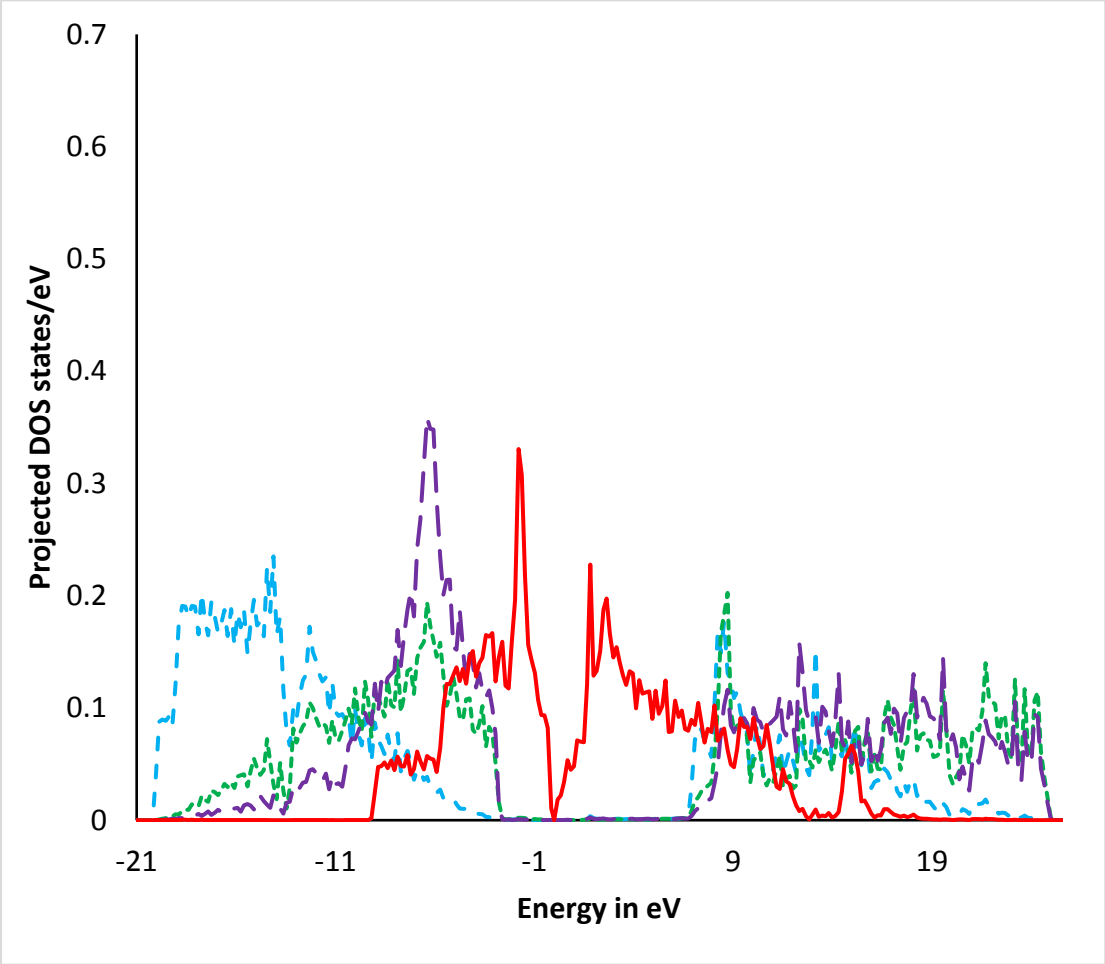

Fig. 6 shows the *lm* decomposed DOS of the β-carbons. As above the PBE xc functional was used to optimise the unit cell.

In the VB, the first sequence of peaks (1), which is found between -20.19 and -13.29 eV, belongs to the1s core orbitals. The pure σ band (2s, $2p_x$ and $2p_z$) is from -12.80 to 2.77 eV and, in this range of energy, the highest peak (2) is found at -6.06 eV. The π band is from -9.18 to 0 eV. The pure π band overlaps with the σ band in the energy range from -9.18 to -3.82 eV while the pure π band is from 2.44 to 0 eV. The large features in this energy region are from 2.77 to 0 eV and belong to the pure π band. In the CB, the pure π* band is from 0 to 7.08 eV and the highest peaks are found in this energy range. The pure π* band overlaps with the σ* band from 7.24 to 13.49 eV. The energy difference between the highest features of the pure π* and σ* bands are of 6.57 eV. Finally, the σ* band is from 6.75 to 25.15 eV while, the pure σ* band is 15.45 to 24.42 eV. In this last energy range is found the sequence of pure σ* features (6).

The main difference between the two DOS diagrams is already visible at this point and is unequivocally associated to the intensity of the peaks of the pure π and pure π* bands in both the α- and β-carbon atoms.

In this regard, Alluche and Ferro [35] suggested that the differences in length of the features are due to those parts of DOS that cannot be projected on higher angular momentum localised orbitals. Therefore, these electronic states are associated to polarisation and diffuse contributions. They are generally due to the interlayer electron density. Such an observation was also supported by the experimental work of Fisher *et al.* [32] where, the interlayer states were assigned to those peaks situated approximatively 4eV above the π* peak in the C K NEXAFS spectra of polycrystalline graphite. The authors likened those peaks in the same domain of the theoretical DOS they took as a reference.

Fig. 7 shows the DOS diagram of the α-carbon in the graphite unit cell which was optimised by DFT-D2 method.

In the VB, the 1s core orbital energies (1) are from -21.68 to -19.38 eV. The σ band is from -19.5 to -2.78 eV and, the highest peak (2) is at -6.40 eV. The σ band overlaps with the π band at -9.03 eV. The pure π is from -2.78 to 0 eV and the highest peak is at -1.80 eV. In the CB, largest peak (4) is found at 1.81 eV. It belongs to the π* band which extends from 0 to 12.65 eV. The pure π* band is from 0 to 7.08 eV and the features associate to the interlayer interactions (5) are located from 2.47 to 4.27 eV. The pure π* band overlaps with the σ* band at 5.26 eV. The σ* band is from 5.10 to 24.8 eV and the largest features (6) are located in the energy range from 6.41 to 11.34 eV. Finally, the pure σ* band extends from 18.73 to 24.80 eV.

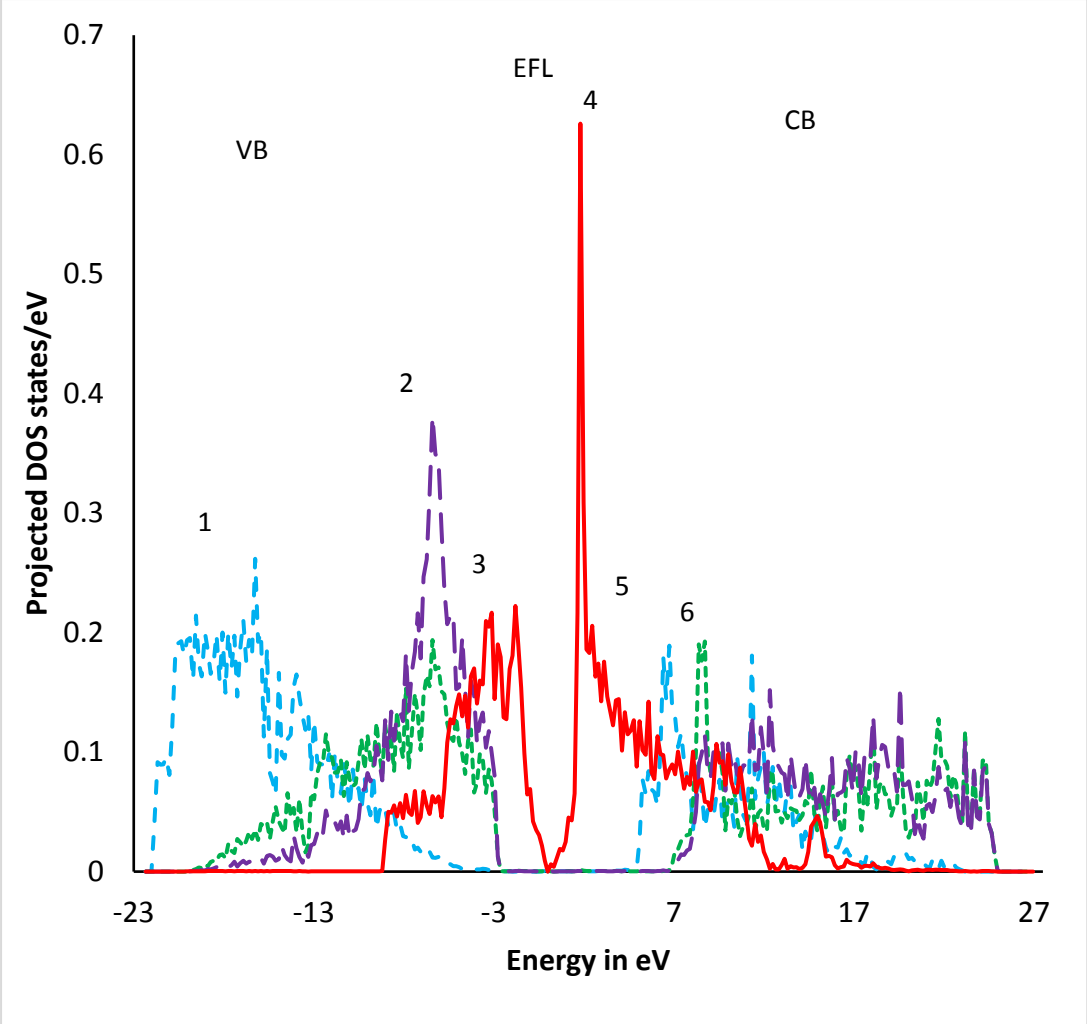

Fig. 7 *lm* decomposed DOS diagram for the alpha atom in the graphite bulk unit cell which was previously optimised by DFT-D2. The numerical labels refers to features which are considered more relevant to the interpretation of the graphite electronic structure. The Fermi energy level has been placed to 0 eV.

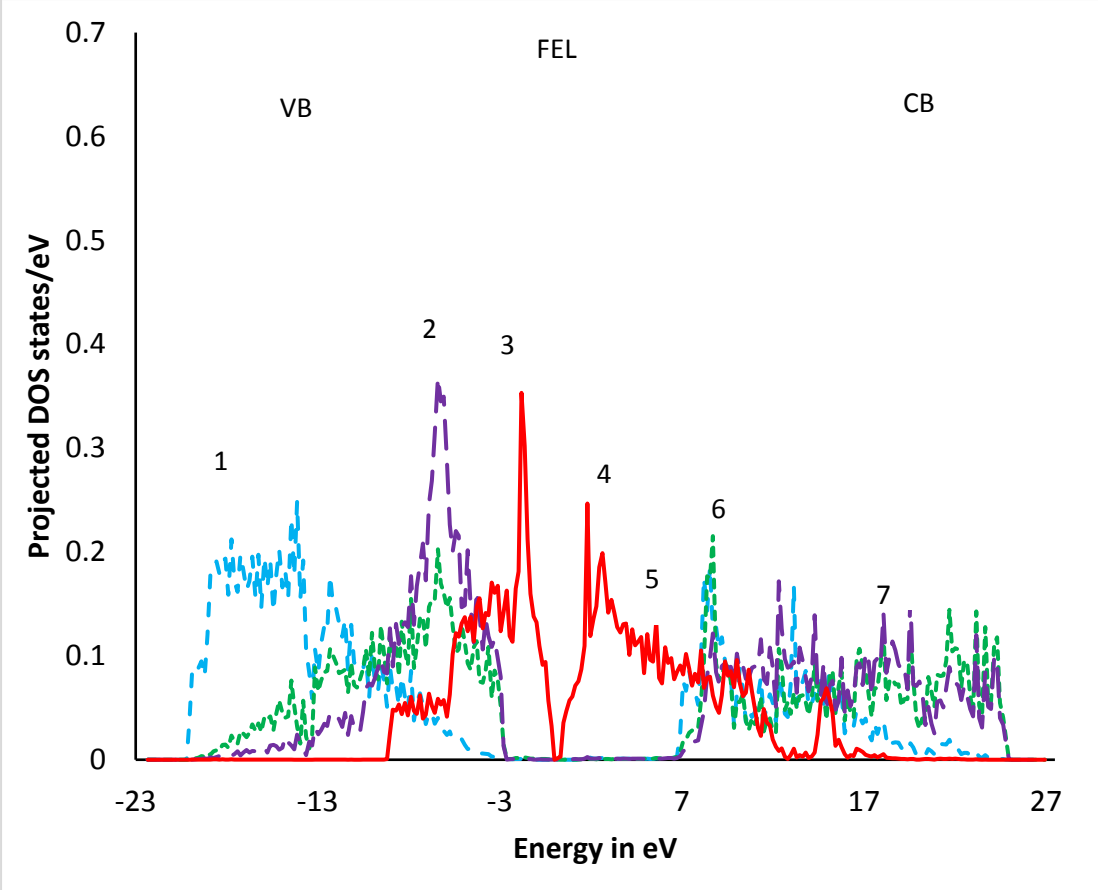

Fig. 8 *lm* decomposed DOS on the β-carbon atoms of graphite bulk unit cell which was optimised by the DFT-D2 method. The Fermi energy level (FEL) has been placed at 0 eV and is graphically represented by the dotted grey line. The pure s, p_x, p_y and p_z orbitals are represented by blue dashed, green dotted, purple dashed and finally red solid line, respectively. The numerical labels have the purpose to identify easily the positions of the larger features which are discussed in the text.

Fig. 8 shows the *lm* decomposed DOS of the β-carbons within the unit cell which was previously optimised by the DFT-D2 method.

In VB, the 1s core orbitals (1) are found in the energy range from -20.04 to -13.6 eV. The σ band is from -20. 04 to 2.7 eV and the largest σ peaks (2) are found from -8.86 to -4.26 eV. The σ band overlaps the π band in the energy range from -9.19 to -2.78 eV. The pure π band is from -2.78 to 0 eV and a large feature (3) is found at -1.80 eV. The largest peak (4) in the CB is at 1.81 eV and belong to the pure π* band. The features (4), which are experimentally ascribed to the interlayer forces, extend from 2.63 to 4.27

eV. The pure π* band overlaps the σ* band at 8.71 eV. The σ* band is from 7.07 to 24.65 eV.

In general, the four DOS structures show many similarities such the feature positions, their lengths and the orbital energy ranges. This should not surprise if one considers that, because of the absence of dispersions arising from the σ band [33], both PBE and DFT-D2 methods give for the in-plane C-C bond a description which is in excellent agreement with experiments.

As it was mentioned above, in hexagonal graphite, the α-carbons have neighbours atoms in the immediately adjacent layers that give different contributions to the interplanar binding if compared to the β-carbons which are in juxtaposition. DOS structures reproduce very well these discrepancies. In fact, comparing the PBE DOS structures of the α- and β-carbons (Fig. 5 and 6, respectively) the only noticeably discrepancy concerns the larger features (3 and 4) in the pure π and π* bands. A partial filling of carbon π* band leads to an increasing of length of the corresponding feature (4) while the partial decreasing in electron charge is responsible for shortening of the feature (3). In this light, α-carbons of Fig. 5 show a peak (5) in of pure π* band which is larger than peak (4) of the pure σ band indicating that such atoms are interacting with the nearest neighbours in next layer.

On the other hand, the β-carbon DOS in Fig. 6 show a peak (5) that is shorter than peak (4) suggesting that such atoms are not interacting with carbons in adjacent planes. Analogously to the PBE DOS structures, in DFT-D2 DOS structures of Fig. 7, the peak (5) is larger than peak (4) showing that inter-plane interactions occur between the α-carbons while, in the β-carbons which are described by the DOS of Fig. 8., there are no relevant interlayer interactions.

Accordingly, after comparing the length of peak5 (5) in the α-carbon DOS structures of Fig. 5 (PBE) and Fig. 7 (DFT-D2), one finds that, in DFT-D2, the feature (5) results larger than the same peak in PBE. On contrary, the feature (4) is calculated by DFT-D2 a slightly shorter than peak (4) in PBE. In conclusion, the DFT-D2 describes the interlayer interaction states better than PBE. Once DOS structure of graphite bulk have been fully understood, in order to validate the accuracy of the computational methods which have been used so far, the experimental data are considered. In Fig. 8, graphite unit cell total DOS, resulting by incorporating dispersion corrections, is directly compared with available experimental and theoretical data available in literature. Amongst the diverse experimental techniques which are used for electronic structure

studies, photoemission electron spectroscopy (PES) and Auger electron spectroscopy (AES) are the most commonly used. However, the energies of photons which are typically employed by the standard spectroscopic techniques such as X-ray and ultraviolet photoemission spectroscopies yield to a very poor photoemission cross-section for the 2s and 2p orbital of carbon atom [34]. Besides, in the range of energies of XPS, the presence of contaminants like O, N, and Ar, leads to larger cross-sections overlapping carbon signals [35]. A reliable method which has been demonstrated very useful for obtaining information about s- and p- orbitals is the analysis of carbon by K V V Auger spectroscopy [36] which provides intrinsic information about the valence electrons. A detailed description of such a technique is not the aim of this work. However, technical details can be found in the following sources [36,37]. Fig X shows the second derivative with opposite sign of experimental C KVV Auger spectrum of graphite (a) and the calculated DOS (b) [38] which was obtained by LDA xc functional and that was taken from Ref. [39]. Finally, in (c) is reported the total DOS which was calculated by DFT-D2 xc correlation method. Firstly, it can be noted that both LDA and DFT-D2 are in qualitative agreement with the experimental measurement. However, some quantitative discrepancies could be mentioned: first, the experimental valence bandwidth determined by Auger photoemission spectroscopy is 22 eV, namely, it is stretched by ~16% with respect to the LDA bandwidth and by ~10% with respect to DFT-D2 bandwidth.

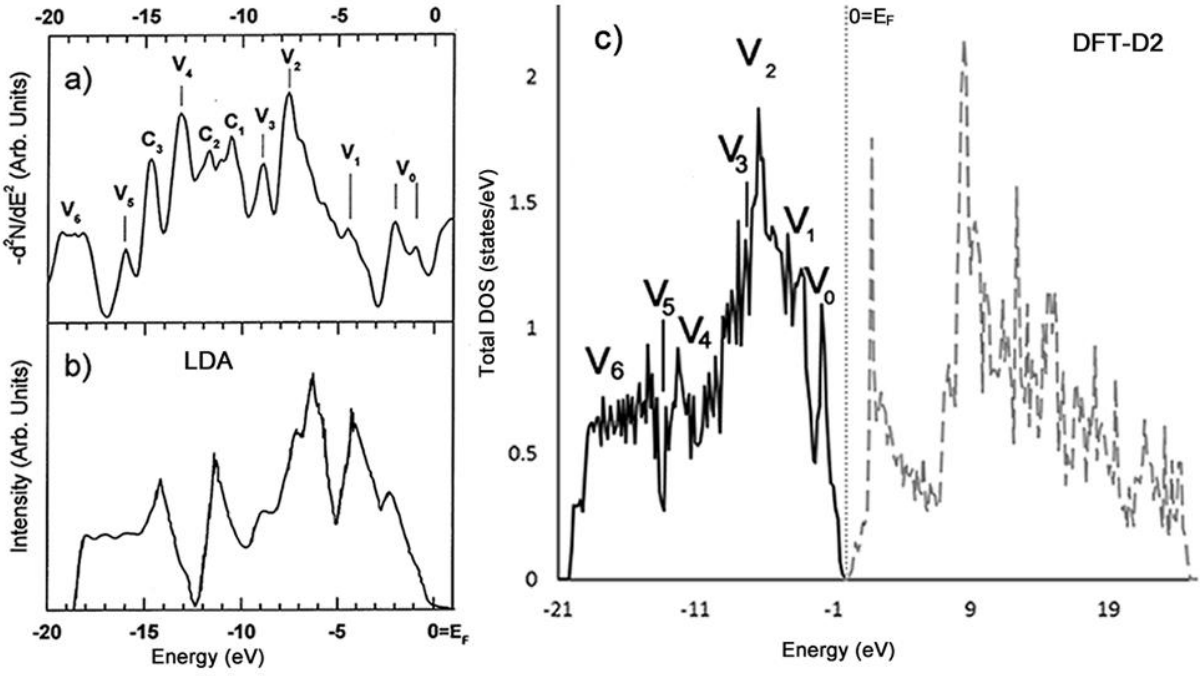

Fig. 9 comparison of the experimental and theoretical graphite DOS. On the left there is the work described in ref. [35] on the right the DOS which have been calculated in this work. The picture has been adapted by permission of the authors.

Second, the Auger spectrum is expected to show features reflecting DOS structures, but the extra features coming from cross-terms (C_1-C_3) do not belong to the DOS. Generally, the amplitude of the double- and cross-terms are accounted during the analysis of the instrumental data and several authors have reported that cross-sections tend to accumulate in the central region of the spectrum [40].

Of course, the Kohn-Sham eigenvalues are not intended to reproduce exactly the experimental photoemission data, and these differences do not imply that all quantities resulting from expressions involving the Kohn-Sham eigenvalues are necessarily affected by large errors.

In the previous discussion about projected DOS, the most relevant information about the type of bonding, especially those occurring between the graphitic planes, were found in the first half of the valence band. In the total DOS (c), the largest feature of the π band are found at 1.8 eV below the Fermi Energy level (which is placed at 0 eV) in good agreement with the experiment which assigns the doublet V_0 at 0.9 and 2 eV (a) while LDA (b) places this feature slightly above 2 eV. The next critical points, which are labelled as V_1, V_2 and V_3, correspond to the features of σ band and were experimentally located at 4.4, 7.6 and 8.9 eV (a), respectively. In this work, the corresponding peaks are found at 4.26, 6.40 and 7.38 eV (c) while LDA (b) placed this features at 3.6, 6.9 and 9 eV, respectively. At lower energy range, the V_4, V_5, and V_6 (broad peak) critical points are experimentally (a) found at 13.2, 14.7 and 19 eV. In this work (c), these features are placed at 12.31, 13.14 and 18.76 eV. Finally, the DFT-LDA yields this features at 12.7, 15.1 eV while the peak which is associated to core s-orbital is located at 17.5 eV (b). Thus, the accuracy of DFT-D2 in reproducing the experimental features is slightly better than LDA.

In Tab. 2 some experimental and theoretical DOS features are collected. A comparison is made with electron spectroscopy methods and other theoretical works mentioned in Lascovich *et al.* [41]. The following table has been adapted from the report of Lascovich et al. and also includes data resulting from this work.

	V0	V1	V2	V3	V4	V5	V6
Experiment							
Ugolini et al. (UPS data)[a]	2.8	4.8	8.2		12.8		
Bianconi et al. [54] (synchrotron data at 200 eV photon energy)	0.7/3	5.7	8		13.6		~19[b]
Carlisle et al. (X-ray emission data at 400 eV photon energy)a	~2.5	~4.5	~8		~14		
McFeely et al. (XPS data)	~3–4[b]	~5	8		13.8		17–19[b]
Lascovich (XAES)	0.9/2	4.4	7.6	8.9	13.2	14.7	~19b
Theory							
This Work (DFT-D2)	**1.80**	**4.26**	**6.40**	**7.38**	**12.31**	**13.14**	**18.76**
Willis et al.	2.3b	4.5	7.8	9.2	12.5	15.4	17/19.2
Charlier et al.	2.3	3.6 (4)	6.9	9 (8)	13.1 (12.7)	15.1	
Fahy et al. (DFT-LDA calculation)[a]	0.95/2.4	4.2	6.2	8.8	11.4	14.3	17.4[b]

Tab. 2 Experimental and theoretical DOS feature data for graphite. Energies are referred to Fermi level. The experimental values were found tabulated in the cited references or taken from tabulated plots. The superscripts (a) and (b) refer to extracted from plotted data and broad peak respectively. Tab. 2 has been adapted from Lascovich *et al*. [45]

The Kohn-Sham band structure which has been calculated along highest symmetry Brillouin zone (Fig.) by DFT-D2 method is shown in Fig. XY. The qualitative facet of the obtained structure is very similar to earlier pseudopotential [1, 2] and all-electron DFT calculations [43,44]. In Fig. XY also the character of the bands has been denoted. The major features of the band structure are also in qualitative agreement with experimental measurements by photoemission. From the band structure, it is possible to extract some information which are not available analysing the DOS diagrams. For example, the lowest orbital energies are found at Γ point in the reciprocal space. At K

point, the energy of HOMO and LUMO equal the Fermi energy that means the band gap enables the thermal excitation which can be achieved even at low temperature. The degeneracy does not appear experimentally due to interlayer interactions which splitting the valence from the conduction band create a very small band gap. Thus, graphite is a semimetal with a very high electrical conductivity along the direction parallel the graphitic planes but an insulator along the direction perpendicular to these planes.

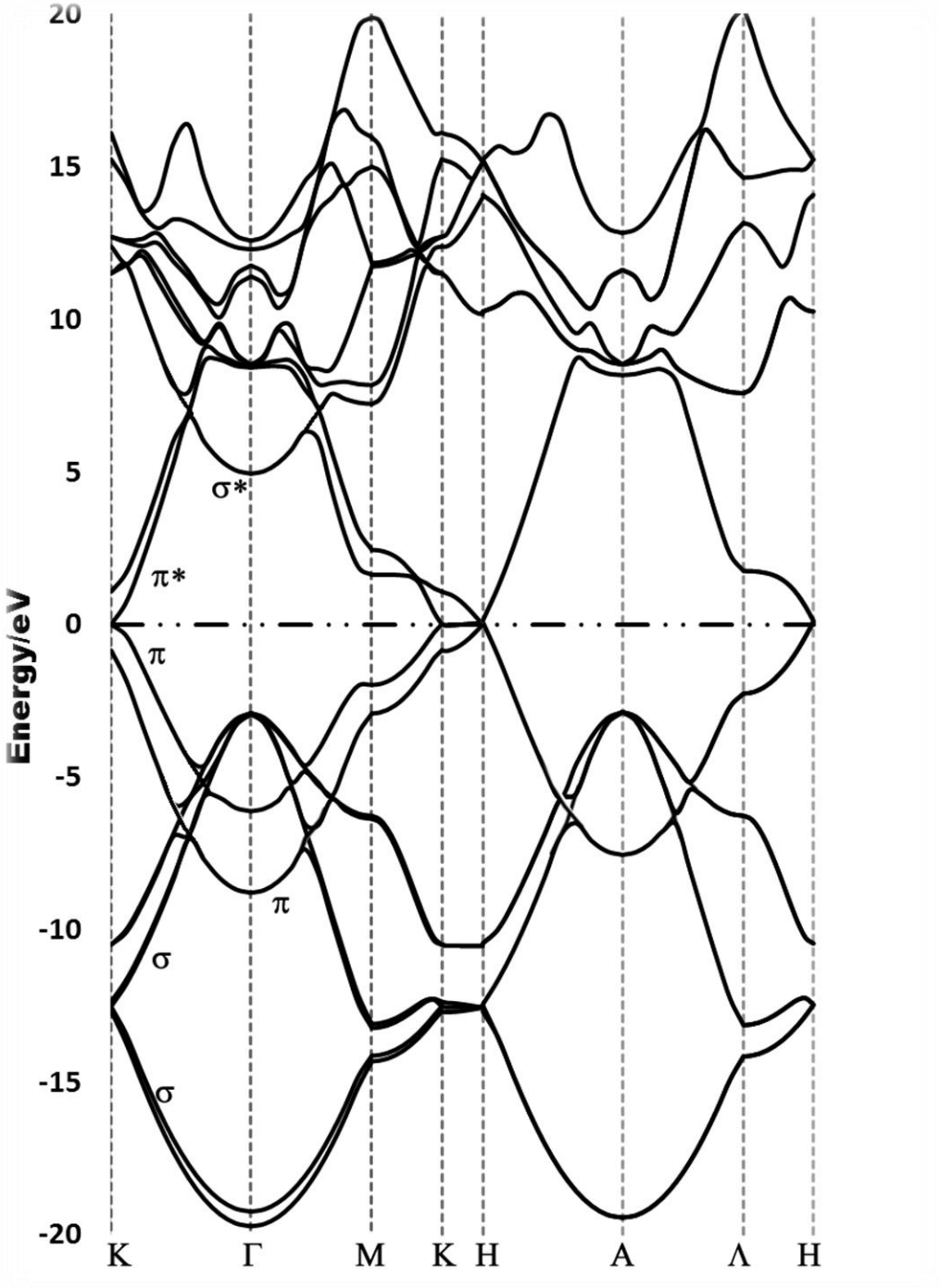

Fig. 10 Electronic band dispersion curves of graphite.

The energy gap between valence and conduction band is of fundamental importance for the properties of solids. Most of a material behaviour, such as intrinsic conductivity, optical transitions, or electronic transitions, depend on it. Any change of the gap may significantly alter the material physical and chemical properties.
The unique characteristic of graphite band gap has motivating an intensive research in making electrical conductivity of this material comparable to those of metal by doping of intercalation compounds.

2.23 References

1. E. Schrödinger, Phys. Rev. 28, 6, 1048 (1926).
2. M. Born and J. R. Oppenheimer, Ann. Phys. 84, 457 (1927).
3. G. J. Kroes, A. Groß, E. J. Baerends, M. Scheffler, D. A. McCormack. Acc. Chem. Res. 35, 193 (2002).
4. B.G. Walker, C. Molteni, N. Marzari. J. Phys.: Condens. Matter 16, S2575 (2004).
5. D. Y. Savrasov. Phys. Rev. B 54, 16487 (1996).
6. W. Pauli, Phys. Rev. 58, 716–722 (1940).
7. Cook, M. Karplus, M. 1987, J. Physic Chem. 91, 31.
8. D. M. Ceperley and B. J. Alder, Phys. Rev. Lett., 45 (1980) 566.
9. J. P. Perdew and Y. Wang, Phys. Rev. B45 (1992) 13244.
10. S. J. Vosko, L. Wilk and M. Nusair, Can. J. Phys., 58 (1980) 1200.
11. J.P.Perdew et al. Chem. Phys. 123, 062201, 2005
12. E.H.Lieb and S.Oxford, Int. J. Quantum Chem. 19, 427 (1981).
13. A. D. Becke, Phys. Rev. A33 (1988) 3098
14. S. Grimme, J. Comput. Chem., 2006, 27, 1787–1799.
15. S.F. Boys, Rev. Mod. Phys. 32 (1960) 296.
16. S. Huzinaga, C. Arnau, Phys. Rev. A 1 (1970) 1285; S. Huzinaga, C. Arnau, J. Chem. Phys. 54 (1971) 1948.
17. R.A. Bair and T.H. Dunning, Jr, J. Chem. Phys. 82 (1985) 2280.
18. F. Bloch, Z. Phyzik 57 (1929) 545.
19. J. C. Slater, Phys. Rev. 81(1951) 385.

20. C. Elias, R. R. Nair, T. M. G. Mohiuddin, S.V. Morozov, P. Blake, M. P. Halsall, A. C. Ferrari, D. W. Boukhvalov, M. I. Katsnelson, A. K. Geim, and K. S. Novoselov, Science 323, 610 (2009).
21. G. Kresse and J. Hafner, Phys. Rev. B: Condens. Matter Mater. Phys., 1994, 49, 14251–14269.
22. J. P. Perdew, K. Burke and M. Ernzerhof, Phys. Rev. Lett., 1996, 77, 3865–3868.
23. S. Grimme, J. Comput. Chem., 2006, 27, 1787–1799.
24. H. J. Monkhorst and J. D. Pack, Phys. Rev. B: Solid State, 1976, 13, 5188–5192.
25. L. Girifalco and R. Lad, J. Chem. Phys. 25, 693 (1956).
26. R. Zacharia, H. Ulbricht, and T. Hertel, Phys. Rev. B. 69, 155406 (2004).
27. L. Benedict et al., Chem. Phys. Lett. 286, 490 (1998).
28. L. Girifalco and Hodak, Phys. Rev B 2002; 65(12):125404-8.
29. G. Graziano et al. J. Phys.: Condens. Matter 24 (2012) 424216-24.
30 P. R. Wallace, Phys. Rev. 71, 662 (1947).
31 C. A. Coulson and R. Taylor, Proc. Phys. Soc. London Sect. A 65, 85 (1952).
32 D. A. Fisher, R. M. Wentzcovitch, R. G. Carr et al., Phys. Rev. B 44, 3 (1991).
33 J. C. Charlier, X. Gonze and J. P. Micheneaud Carbon 32(2):289-99 (1994).
34 Y. Wang, K. Sheerschmidt, U. Gosele. Phys. Rev. B. 61 (19):12864-70 (2000).
35 A. Allouche, Y. Ferro et al. Chem. Phys. 123 124701 (2005).
36 J. T. Titantah and D. Lamoen, Phys. Rev. B 70, 075115 (2004).
37 A. Rairkar, J. B. Adam and N. Ooi. Carbon 44 231 (2005).
38 H. O. Pierson. Handbook of carbon, graphite, diamond and fullerenes. USA: Noyes.
40. P. Oelhafen, D. Ugolini, in: E-MRS Meeting, June Vol. XVII, Les Editions de Physique, Paris, 1987 .267.
41. A. Mansour, G. Indlekofer, P. Oelhafen, Appl. Surf. Sci. (1991) 312.
42. S. Iacobucci, P. Letardi, M. Montagnoli, P. Nataletti, G. Stefani, J. Electron Spectrosc. Relat. Phenom. 67 (1994) 48/49 479.
43. M. Cini, Solid State Commun. 20 (1976) 605, Solid State Commun. 20 (1976) 681, Phys. Rev. B 17 (1978) 2788.
44. M. C. Schabel and J. L. Martins, Phys. Rev. B 46 7185 (1992).
45. J. C. Charlier, X. Gonze, and J. P. Michenaud, Phys. Rev. B 43 4579 (1991).
46. L. G. Johnson and G. Dresselhaus, Phys. Rev. B 7, 2275 (1973)
47. R. Ahuja, S. Auluck, J. M. Wills, M. Alouani, B. Johansson and O. Eriksson, Phys. Rev. B 55, 4999 (1997).

Chapter 3

It is known on theoretical grounds that the electronic structure of first atomic layer of a clean surface is different from that of the bulk. Surface atoms are undercoordinated with respect to the atoms in the bulk, and therefore chemically different from them. At the surface, the periodic pattern of chemical bonds in the crystal is interrupted leading to dramatic modifications of physical and chemical properties which are observed in bulk materials: dangling bonds can rearrange themselves or can be saturated by a layer of adatoms which may completely change the nature of the electronic structure of the surface with respect to that of the bulk. Thus, quantifying and understanding the structure of surfaces, and their interactions with adsorbates, are crucial steps to understand the large variety of aspects which are connected with the surface behaviour including chemical properties. Thus, in the first part of this chapter, after introducing some of the aspects of heterogeneous catalysis involving carbonaceous materials, the DFT-D2 method is applied for studying the properties of pristine and defective graphite surfaces. In the second part, water and graphitic surface interactions are investigated. The observations resulting from the theoretical study of the interactions between carbonyl groups on graphite, hydroxylated graphite surfaces and gold nanoparticles are discussed in the last part. All the calculations account for long-range dispersion forces which play crucial role in surface science especially when the interactions between adsorbates and surfaces are considered.

3.1 Introduction

Carbon plays a well-established important role in heterogeneous catalysis for a wide variety of reactions, not only as support material but also as catalyst. Carbonaceous materials, in fact, possess unique characteristics which are useful for many catalytic applications and some of them have been discovered in the last few decades. In fact, these materials are characterised by large specific surface area, high porosity, and excellent electron conductivity. Advantageously, carbon supports have been proved to have a better stability than metal oxides in catalytic processes that take place in liquid phase under extreme conditions such as acid or alkaline environments. Moreover, carbon materials show superior stability also at high temperatures and, in comparison with other materials, they can be easily prepared in diverse physical forms, such as fibres, pellets and granules. Other practical benefits stem from the fact that the active phase can be easily removed from carbon supports and their cost is very low if compared to that of other support materials. In the last few decades, the explosive development of new carbon nanostructures has enabled the controlled applications of carbonaceous materials at multiple scales introducing new approaches to some aspects such as their synthesis, control of size and the morphology. In the next section, a brief overview on the applications of carbon in heterogeneous catalysis is given.

Compounds containing carbon are, in most catalytic applications, the substrates of the process under consideration but deposits and polymers of carbon often occur as poisons on catalysts. In particular the deposition of carbon is the most severe problem in zeolite applications whereas in hydrogenation reactions carbon deposits act as modifiers of the catalyst activity and provide selectivity controlling the hydrogenation-dehydrogenation activity of the catalyst.

Carbon is also a catalyst in its own right and is of fundamental importance in homogeneous catalysis where is the main constituent of the organic ligands that coordinate a metallic centre. The influences of organic ligands on a metal catalyst can be diverse and lead to several desirable effects. In fact, depending on the nature of ligands, the catalyst becomes specific toward some reactants leading to selected products. There are metal complex catalysts which possess unique characteristics such as chemoselectivity, regio-selectivity, stereo-selectivity enantio-selectivity and so on. Although carbon compounds are essential to the homogeneous catalysis, the few

following sections will introduce the applications of carbonaceous materials which are only limited to the heterogeneous catalysis applications.

3.2 Carbonaceous materials as catalysts.

The treatment of waste water and gas with active carbon may be considered as one of the first applications of carbon as catalyst which was largely used in the past years due to the good catalytic performance. The modern use of carbon based catalysts, instead, involves more complex chemical reactions.

The process for oxidizing the sulphur dioxide to sulphur trioxides is just one of the contemporary industrial processes in which carbon catalyst has been used to replace the more expensive conventional vanadia catalyst. The product of this reaction is a strong acid, H_2SO_4, which is removed from the catalyst surfaces by organic solvents [1].

Other popular industrial oxidation-reduction processes, using carbon as catalyst, are the reaction of nitrogen oxide and molecular oxygen that leads to nitrogen dioxide [2] and the reaction of sulphur with water for the production of H_2S [3]. Carbon catalysis literature is large and many other industrial processes are reported where carbon is successfully used as catalyst, for example, in dehydrohalogenations [4] and decomposition reactions [5]. Emerging applications where carbon catalysts show potential applications include oxygen reduction reaction in fuel cells [6-8], carbon molecular sieves for shape selectivity reactions [9], catalytic wet air oxidation of organic pollutants [10], methylamines synthesis [11], etc.

Carbon catalysts are known to degrade during the reactions. The re-activation of carbon is a practice that can be accomplished easily. Generally the industrial process consists in a high temperature (up to 800℃) treatment which takes place in large furnaces where carbon is cleaned and reactivated. The pollutants with exhaust gas are eliminated in to the waste gas treatment systems and then the re-activated carbon is cooled down, analysed and sieved. If mercury, sulphur and other pollutants are present, they are removed by distillation. Sulphur, in particular, is usually converted in gypsum.

The presence of these elements in carbonaceous materials may be due to another important industrial application of carbon catalysis which consists in fuel cleaning. The dry desulfurization, denitrification and air toxic removal processes using activated carbon

were originally researched and developed during the 1960s by Bergbau Forschung in Germany. In these processes, the active carbon acts simultaneously as an adsorbent and as a catalyst in the temperature range 383–443 K, i.e., under conditions where the material is stable in the presence of oxygen [12].

Due to its "green" characteristics, carbon is largely employed as catalyst in gasification of organics and biomass [13] and CO_2 reforming of methane [14]. Another use of catalyst for environmental cleaning is the removal of halogen from organic compounds. This can be achieved following two different ways. The first one is the catalysed oxidation of the halogenated compounds in CO_2 and the corresponding formation of halogenated acid [15]. The second method is catalytic dehalogenation [16].

Finally, it is noteworthy to mention the catalytic role of carbon in the synthesis of styrene because such a process has influenced the major part of the carbonaceous catalysis based literature of the last few decades. The oxidative dehydrogenation of ethylbenzene which yields styrene is an exothermic process which presents the advantage of not being limited by equilibrium and can be carried out a low temperatures.

In the past, some catalysts such as alumina and various metal oxides and phosphates have shown improved activity and selectivity comparable or better than iron catalyst. Gradually, the results of many investigations accumulated evidence that the active sites were not located on the catalyst surface but on the over-layer of carbonaceous nature. The time which is necessary to form such an over-layer on the metal surface, is the reason for which the catalyst exhibited induction periods in its activity. This finding has motivated an intense interest in studying a large variety of carbon and graphite materials for potential application to oxidation of ethylbenzene [17-21]. These few examples evidence that activated carbon and its derivatives display good catalytic performances and are largely used industrially. The next section will briefly survey the role which is played by the surface chemistry of supports in promoting the activity and other properties of the supported catalysts.

3.3 The chemistry of carbon catalysts

Amongst their many industrial applications, carbonaceous and graphitic materials have been considered for their utilisation in several processes in the field of heterogeneous

catalysis. The catalytic activity and selectivity of carbonaceous materials have been related to their surface chemistry and their electric properties [22]. In this regard, carbonaceous materials may exhibit a wide range of behaviours from being conductors, semi-conductors or insulators and such characteristics depend on the methods of pre-treatment and preparation. In fact, it has been observed that thermal graphitisation treatments favour the metallic behaviour whereas treatments resulting in oxidation of the material and disordered carbon lead to semi-conductivity and insulator-type behaviours, respectively. In addition, the anisotropy in electron property of graphitic materials is responsible for broad spectrum of crystalline properties which may been seen in carbonaceous materials and explains the low selectivity which is observed when such materials are used as catalysts. Understanding the electron properties for catalytic application of carbon materials has stimulated the interest of many research groups. The investigations on the insertion of heteroatoms (N, P, B, O, S) on a carbon catalysts have been investigated and the results were interpreted in term of semiconductor properties [23]. In fact, it was observed that the insertion of nitrogen atoms in graphite lattice reduces the band gap and increases the electron mobility. In addition, the work function at the carbon/fluid interface results decreased in energy. Doping carbon with nitrogen enhances the catalytic activity of graphitic compounds reaching the same performances of semiconducting metal oxide catalysts in electron transfer reactions. Moreover, N-doped carbon gave the possibility to understand that the catalytic properties are due to the synergic action of two effects: the first one consists in basic surface sites and the other one in electron donation. Due to the positive results which were obtained by N-doping graphite, more recently, hetero-atoms were introduced in carbon nanomaterials such as carbon nanotubes (CNTs) and graphene with the aim to introduce intramolecular charge transfer for the development of metal-free carbonaceous electrocatalysts [24-26]. The relations between chemical properties and catalytic activity of carbon have been investigated extensively in past decades. Historically, two diverse approaches can be identified in the surface chemistry of carbon. The first one considers mainly the morphology of the crystal, namely, crystal features including defects on the surface and the edge sites which are proven to be more reactive while, the basal planes are to be considered as nearly inert. Thus, one can aspect to find active sites at the edges of graphitic planes where the unsaturated carbons can chemisorb heteroatoms such as oxygen, nitrogen or sulphur originating surface groups. Such groups can act as active sites in various acid-base or redox reactions. The concentration of these active sites is

largely correlated to the crystal structure of the carbonaceous materials. In fact, crystals of small dimensions expose more edges whereas more surface groups can be formed whereas in large crystallites, it is important the role which is played by basal planes and π electrons. Thus, as it has been experimentally proven the orientations of graphitic layers and the ratio between the prismatic and basal plane areas are responsible for the reactivity [27-29]. The other approach which is used to explain the catalytic activity of carbonaceous materials deals with the nature and the chemistry of oxygen and other heteroatoms which are chemisorbed at the edges and surface defects. For example, no activity for dehydration and dehydrogenation of alcohols is exhibited by active carbon which is annealed in hydrogen atmosphere. On the contrary, an oxidation treatment by nitric acid increases the activity of the material suggesting that this improvement should be attributed to the functionalisation of the active carbon surface [30]. An important point concerns the influence that heat-treatment may have on functionalised surface stability and the effects of the concentration of functional groups on the catalytic activity should be also accounted.

In conclusion, from this brief overview on the use of carbonaceous materials as catalysts, it appears that the main properties that control the catalytic activity of these material are deeply related to the electronic properties of the surface and the ability to tune by the introduction of hetero atoms. Their surface chemistry which accounts for the presence of active sites such as dangling atoms at vacancy defects and edges which, in general, exhibit higher reactivity compared to saturated atoms in the basal plane. Undercoordinated atoms are very reactive and may undergo oxidation and be terminated by oxygen atoms. Besides, thermal stability plays an important role, for example, acidic group have experimentally shown to decrease the hydrophobic character of carbonaceous surfaces. However, it has been observed that thermal stability of carboxylic group is limited to temperatures quite close to 673 K. Such temperatures are often used for the decomposition and reduction of metallic precursors. Finally, the porosity of the surface which allows the access to active sites and is determined by the pore sizes. This aspect of the surfaces is particularly important in case of microporous materials which are employed in catalysed reactions occurring in solid/liquid and solid/gas interfaces. Finally, the pore size distribution can be adjusted to suit the requirements of several reactions.

3.4 Carbon supports

This paragraph is a brief panoramic on the industrial use of activated carbon, carbon black as well as graphitic surfaces as support material for the preparation of commercially available precious metal catalysts. The main industrial applications of carbon supported metal catalysts will be briefly presented with the aim to illustrate the properties of the supports. Most of catalytic applications use powder based or metal nanoparticles and the role of the support is mainly indented to allow the fine dispersion and the stabilisation of small particles of the catalyst. However, it has been observed that carbon supports can accomplish several other tasks among them charge transferring and influencing the more stable geometries of nanoparticles are just some examples of the support properties which have large effects on the catalytic activities of the supported materials.

One of the greatest advantages resulting from using carbonaceous materials consist in recovery, refining, and recycling precious metals. In fact, in the case of carbonaceous supports this procedure results to be largely simplified if it is considered that such material can be burnt and the resulting ashes permit an economic recovery of precious materials [33-34]. Since they do not produce a large amount of solid wastes, from an ecological standpoint, the use carbonaceous materials represents a very important advantage. Carbons are chemically considered stable as support material, activated carbons are nearly inert in both acidic and basic media which is not true for other commonly used supports such as alumina and silica which are attacked at low pH's and easily dissolved at high pH's [31-32]. The surface chemistry of carbon materials influences their performance as catalyst support. Carbon material are normally hydrophobic and usually they show low affinity towards polar solvents such as water, alcohol and higher affinity towards solvents such as acetone, ethers. Although the hydrophobic nature may affect the active phase dispersion over the carbon support, the surface chemistry of carbon material can be easily modified. One of the methods which is often used to reduce hydrophobicity of carbonaceous surfaces is the oxidation which favours the ionic exchange. The insertion of oxygen of acidic groups on the surface, for example, has been proven to decrease the hydrophobic character and increasing the metal dispersion providing anchoring sites. This observation was largely documented in the works of Richard [35] and Prado-Burguete [36]. The authors reported that the presence of oxygen on carbon black surface favour the dispersion and resistance to sintering of platinum supported catalyst. In addition, they observed that increasing the concentration

of the acidic groups the surface resulted more accessible to aqueous solution of metal precursor which was prepared by the impregnation method. Thus, an increasing of oxygen concentration resulted in a better dispersion of the catalyst. It was also found that decreasing the amount of acidic groups on the surface at high temperatures, thermally more stable groups favoured the interaction between catalyst and support reducing the metal sintering. Acid treatment is generally used to introduce functional group on activated carbon surface, the effects of acids on these surfaces has been studied by Lu *et al.* [37] who, investigating on the N_2O reduction over Ni/C catalyst, found that HNO_3 treatment leads to high concentrations of acidic surface groups. On the other hand, HCl treatment of active carbon surfaces decreases the number of the acidic groups increasing the concentration of inactive groups. The authors pointed out the opposite behaviours showed by the support after these treatments: only after HNO_3 treatment, the dispersion of Ni particles resulted uniform on the surface. Good support should be characterised by a surface which prevents excessive catalyst mobility. Dispersion and sintering of some metals over carbonaceous surfaces have been found to be a function of the number of functional groups containing oxygen, and in this regard, carbonyls appear to be quite effective [38]. Nitrogen surface groups have been less studied than oxygen. The presence of nitrogen on carbonaceous surfaces also influences the dispersion and the catalytic activity. The effects of nitrogen functionalities can be diverse and depend on the system under investigation. As can be seen from the following selected examples the presence of nitrogen groups on carbon supports results useful for increasing the catalytic activity of Mo catalyst for thiophene hydrodesulfurization [39] and other metals such as Co [40] and Fe [41], which were deposited on nitrogen-doped carbon showing a better dispersion and higher activity for fuel cell electrocatalysis. It is noteworthy that in the case of Pt clusters on HOPG with nitrogen defects, a computation investigation showed, initially, that nitrogen doping at high concentrations tends to form nitrogenous agglomerates at defective sites. For Pt clusters which were deposited on HOPG with nitrogen defects, the theoretical investigation gave also a description of the nucleation and the anchoring of Pt particles on the nitrogen decorated aromatic rings. Besides, the intrinsic enhancement of activity by chemical doping of the catalyst support is attributed to a down-shift in the Pt *d*-band because of charge donation from the dopant to platinum [42]. An important consideration about the presence of heteroatoms on the carbonaceous surfaces is that often it has a positive impact on the metal dispersion but some studies have also proven the contrary [43]. Some possible explanations can be given in the case a support is

predicted theoretically effective for some purposes but in practice it results to be inefficient. On microporous supports, for example, a fast nucleation could hinder the precursor from penetrating the porous network of the support. In addition, it can also happen, on functionalised surfaces that during the catalyst activation, anchoring sites, which are due to functional groups, may decompose. Finally, to mention an example where the functionalisation of the carbonaceous surface leads to unwanted effects, the role of surface chemistry on the catalytic activity of Au/C in the glycerol oxidation reaction is considered. In this reaction, it has been observed that Au nanoparticles with similar average sizes show diverse performances depending on the concentration of functional groups containing oxygen on the surface support. It was also observed that the activity of the catalyst was low at high concentrations of oxygen and improved when by thermal treatments oxygenated groups were removed. The highest catalytic activity was found for the oxygen-free surface which is characterised by a high density of free π-electrons. Thus the role of the carbonaceous surface was interpreted by considering that the absence of oxygen atoms promoted the electron mobility from and to gold nanoparticles promoting both the adsorption of OH^- ions from the solvent which allow the oxidation [44]. In this paragraph, the useful properties arising by modification of surface chemistry of carbon supports has been described in some details. In conclusion the surface chemistry of a carbonaceous support has large influences on the catalyst manufacture and on its performances. Most of the desired properties of the support can be obtained by functionalising the surface with oxygen or some other heteroatom during the preparation of the support. Most popular functional groups which are inserted on these surfaces consist in carboxylic, phenolic, lactonic and etheric groups and they are responsible for both acid/base and the redox properties of activated carbon. These surface groups not only act as anchoring sites but also as nucleation centre for the generation of highly dispersed metal crystallites. Depending on the nature of functional groups two important mechanisms are observed. The first one consists in the adsorption of ions at acid or basic sites while the other one is the deposition of metallic species by a redox reaction with carbon. Although the two mechanisms can operate in synergy, to avoid acid base interactions with the surface, charge neutrality of the support is very important especially if the first mechanism is exclusively desired [45-46]. Functional groups on the surface can include heteroatoms such as nitrogen, sulphur and so on which, like oxygen, play an important role on the surface chemistry and the identification of heteroatoms requires accurate instrumental analyses. This is partially due to the presence of impurities

such as calcium, potassium, alumina, silica, sulphur, iron and other transition metals that can drastically modify the acid/base and redox properties of the support [47-48].

3.5 Physical and chemical treatments of the catalyst supports.

The choice of the best catalyst, amongst those which are indicated for a given chemical reaction, is one of the most delicate process. Since several contrasting parameters have to be considered at same time, such a choice has to be made only after that all the possible circumstances have been accurately evaluated. For example, finely divided powders of catalysts are easy to suspend in the reaction medium causing a low diffusion in the porous support. In addition, these suspended powders may be difficult to separate by filtration from the final product. If during the catalytic process no mass transfer is expected, uniformly impregnated catalysts are preferentially used. There are many other methods which are commonly used for the preparation of carbon supported catalysts, amongst these methods, one finds the chemical vapour deposition, precipitation, dip-coating, hydrothermal, sol-gel and egg-shell technique. The selection process of suitable deposition method largely depends on several variables such as the catalyst support, the type of pollutants to be degraded and the degradation phase, be it a liquid or a gas-phase. Later on in this paragraph, the impregnation method is discussed in more details because this is the preferred method which has been experimentally used for depositing gold nanoparticles on carbon support for the acetylene hydrochlorination reaction which is the centre of interest of this work. In order to proceed gradually and systematically in the illustration of the steps which are required for the preparation of the catalyst support, the processes for the manufacture of carbonaceous supports will be considered.

Many forms of carbon are largely used as supports for precious metal catalysts such as carbon nanotubes, nanofibers, nanodiamonds, carbon onions, fullerenes, graphene, multi-layered graphene and so on. Since it is not possible a complete description of all these materials, some generalities on how these forms of carbon find their application in catalysis will be given in the next paragraph while, here, only the three forms of carbon largely used in catalysis are illustrated in more details. They are activate carbon, carbon blacks and graphite. At first glance, carbon blacks and graphite materials on the one side and activated carbons on the other side are very similar, even if one has to take care not

to confuse them [49]. However, three major differences exist between activated carbon and the other carbons and they will be explained here.

Using the term activated carbon or activate charcoal as it is often made in literature, one refers to a group of materials with highly developed internal surface area and porosity to which is due the large capacity to adsorb ions, atoms or molecules from gas and liquid phases [50]. In these carbonaceous materials, London dispersion forces play an important role in the adsorption of chemicals on the surface. Since the dispersion forces are uniquely of quantum-mechanical character, they do not depend on external parameters such as pressure or temperature. In addition, these forces are strictly correlated to the electron density and, because of this, adsorbed molecules will be strongly held where the concentration of carbon atoms (and their electrons) is larger. High temperature treatments (>1500 K) have proven increasing the π-state density on partially graphitised structures leads to a better adsorption [50-51]. This type of carbon can be obtained in several ways and from diverse materials. The most important raw materials for the production of activated carbons are wood, coal, lignite, coconut shell and peat although other materials such as fruit pits, synthetic polymers or petroleum processing residues can also be used. The final products show different properties, e.g. pore structure and surface area, depending on the nature of the precursor, the nature of the activating agent and the conditions of the activation process [52-56]. The first step to obtain activated carbon is the carbonisation process which consists in a thermal treatment of the raw material and is expressed by the following chemical equation:

In the range of temperatures from 673 to 1123 K, most of non-carbonaceous elements such as dust and volatile substances are eliminated by heating the source under anaerobic conditions. The carbonisation process takes place when the temperatures are increased up to 1123 K. Such extreme conditions are used to burn the raw material which starts to assume the carbonaceous structure [57].

In fact, it has been observed that in this high temperature process, carbon atoms rearrange themselves to form rigid and dense clusters of microcrystals. These microcrystals

consists of several layers of graphitic planes. It is noteworthy at this point that undercoordinated carbon atoms at the edges of the crystal planes have a high adsorption potential available.

Concerning with the nature of active sites which are formed on the microcrystals, it is found that the basal planes are not very reactive whereas the unsaturated carbons at the edges may chemisorb oxygen, nitrogen or sulphur from the atmosphere originating surface groups.

After the carbonisation, the activation process takes place. The activation may be achieved by several methods which can be classified as belonging to two distinct classes: physical and chemical activation. The choice of which one of these processes has to be used depends on the starting materials and whether a low or high density powdered or granulated carbon is desired.

Since the objective of the activation is that to enhance the pore structure, during the physical activation the char is treat with steam, carbon dioxide and air at temperatures around 1000-1500 K. This process is also useful to eliminate superfluous material and makes the char more accessible to the active phase.

In order to increase the pore volume, the crystallites are treated with activate agents which consist in oxidizing gases such as steam or CO_2. The oxidizing agents also remove volatile impurities from the solid.

In comparison with the physical activation, the chemical activation is a one-step process where the carbonisation and activation take place simultaneously. In fact, the raw material is initially impregnated with chemical agents such as H_3PO_4, H_2SO_4, HNO_3, KOH or $ZnCl_2$ and then it is decomposed at high temperatures.

This process yields a carbonised product which also possesses the desired porosity. The resulting activated carbon shows some properties which are directly related to the impregnation conditions. For example, the presence of dehydrating agents favours the formation of carbon while inhibits the tar formation. The ratio between the activating agent and carbon precursor as well as amount of time of impregnated material pre-drying and, pyrolysis conditions have large influence on the porosity of the material.

In addition, since the porous structure of the produced carbon depends on the temperature, the chemical activation, which uses lower temperatures, produces carbon with better porosity than the physical activation process.

Although the chemical activation presents the advantages to require only one step for carbonisation and activation, it presents the drawback to wash the final product for removing the residual organic materials.

Finally after activation, carbon has a certain degree of porosity and an internal surface area which commonly is found in the range of 700–1200 $m^2\ g^{-1}$ (these values depend on the processing conditions).

In comparison with activated carbon, graphite materials present a lower surface area which generally can be placed in the range from 10 to 50 $m^2\ g^{-1}$. In addition, due to the low reactivity toward the activation agents, some problems can be experienced during the preparation of porous supports. In spite of its chemical inertness, graphite shows a property which is typical of layered materials and is very useful in catalysis. In fact, graphite has ability of intercalating metals or other chemical species in between the graphitic planes. Investigations on graphite intercalated compounds have proven that these materials may expand their volume along the crystallographic *c*-axis after a high temperature treatments [58].

As a consequence of the volume expansion, the graphite surface area increases reaching values of 100-300 m^2g^{-1} which is a good requisite to use the intercalated graphite compounds as catalyst supports [58-62]. There are other methods to obtain high surface area in graphite, amongst them, the high-energy ball-milling may increase the surface area from 10 to 600 $m^2\ g^{-1}$ [63]. When graphite materials are obtained with high surface area, they consist of crystalline graphite structures of small sizes. The basal plane area in these small crystals is reduced. Small crystallites may expose more edges; therefore more active sites of unsaturated carbons are available. High surface area graphite has been used as catalyst support in many reactions such as oxygen reduction reaction in fuel cells [64], NO reduction [65], wet air oxidation [66], hydrogenations [67], hydrodechlorination [68] and decomposition of NH_3 [69].

Carbon blacks are a group of materials which are agglomerated together to form spherical particles of colloidal sizes. These materials may be considered as a very pure form of coal and commonly are produced by four processes. In furnace black process, aromatic

oils are burned producing carbon blacks and gas. The system containing the products of the combustion is refrigerated to permit the separation of the carbon blacks from the densified gas which is separately processed into pellets. In the same fashion acetylene and natural gas can be burnt to produce carbon blacks in processes which are known as thermal black process and acetylene black process. Finally, the Lampblack process uses a coal tar derived aromatic oil which is heated in to produce carbon blacks. The main differences between carbon black materials consist in the particle sizes, their aggregation and agglomeration but also to the type of impurities which may be introduced during the manufacture process. In addition, the finesses, the structure, porosity and surface chemistry are the key properties which make this materials the right support for a selected catalyst in a given reaction. The average primary particle diameter of commercial carbon blacks ranges from 10 to 100 nm while the average size of the agglomerates is in the range 100-800 nm or above. Graphitized carbon black is another support material of interest to catalyst manufactures. This high surface material is obtained by recrystallization of the spherical carbon black particles at 2773–3273 K.

After discussing how the most common carbon supports are manufactured, it appears clear that the main difference comparing the properties of these materials is the specific surface area which is higher in activated carbon than carbon blacks and graphite. Another important difference consist in the porosity of the materials. The porosity of carbon blacks and graphite result very different for that of carbon blacks. Finally, concerning the surface chemistry of graphite, the high temperature treatment, surface oxide groups only play a minor role and the material is hydrophobic. On the other hand, surface functionalities of carbon blacks and activated carbon are principally the same. These three aspects have large influences on catalytic activity, for example they may affect the dispersion of the catalyst particles on the support, may guarantee the presence of anchoring sites for ionic species and modify the hydrophobic nature of the surface.

3.6 Other carbonaceous materials

Carbons such as activated carbon, carbon blacks and graphite have been, over the last centuries, the predominant carbonaceous forms which played a very important role as catalysts or catalyst supports in the industry or for energy and environmental applications but the last decades have seen a rapid advance in the manufacture of nanoscale materials

which has introduced many innovative carbonaceous forms. These novel materials present unique characteristics which have proven to be very effective for catalytic applications. Although these materials present interesting properties which are relevant to catalytic applications, it is not possible in this work, for the sake of brevity, to cover the singular material in all details.

Nowadays, the most investigated carbonaceous material, which had demonstrated to possess unique properties also for catalysis applications is graphene. From the theoretical point of view, it provides the first example of a 2-dimension catalyst support although, in our knowledge, the experimental use of a single layer graphene, in catalysis, has not been reported yet. However, some promising results have been already obtained with few layers graphene [70]. Due to its redox properties graphene has large potential as catalyst as it has been shown by many investigations [71-73]. The dispersion of catalyst particle on graphene show a good distribution and can provide great versatility in carrying out catalytic processes. In addition, DFT calculations have shown that the active catalytic sites on single nitrogen doped graphene have either high positive spin density or high positive atomic charge density. The nitrogen doping introduces asymmetry spin density and atomic charge density, making it possible for N-graphene to show high electrocatalytic activities for the oxygen reduction reaction [74]. Based on first principles method, the catalytic property of nitrogen-doped graphene has been investigated for the oxygen reduction reaction [75] where it has been observed that nitrogen clusters are most efficient catalytic sites for oxygen reduction.

If one imagines to roll up a single graphene sheet, the nanotube structure is obtained. In practice, rolling up a graphene sheet in the nanotube geometry has a large effect on the electronic structure of carbons which results deeply altered. In fact, in the nanotube arrangement the bond lengths and angles results to be modified respect their original values measured in the flat graphene. In particular, because of the curvature, σ and π orbital planes are not perfectly perpendicular to each other and the geometric arrangement of the atoms in nanotubes enforces the overlap of π orbitals which have to arrange (to minimise the electron repulsions) in a way that the outer contribution is larger than the inner one. The curvature of nanotubes leads to a mixed state of σ and π molecular orbitals which is known as rehybridisation. The rehybridisation of the orbitals can be also interpreted in terms of the simpler mixing of the sp^2 and sp^3 hybridized orbitals. Accordingly, if saturated sp^3 orbitals are mixed to saturated sp^2 orbitals, an unsaturated

orbital is available for free binding. This model is used to interpret the reactivity of nanotubes. In fact, higher is the ratio of sp^3 contribution the more free electrons are available to form bonds, or in other words, the higher is the reactivity of the nanotube structure. An index of the reactivity is represented by the pyramidalisation angle θ. The comparison between the different pyramidalisation angles allows the comparison of reactivity, where a higher angle results in a larger reactivity. Due to their defined surfaces carbon nanotubes as well as graphene, have been by far the most studied materials. The adsorption of various species on nanostructured carbon surface has been studied by first principles calculations [76]. In addition, it has been shown that air oxidation may result in the motion of metal atoms confined in carbon nanotubes. Oxidized nanotubes are used as supports in metal catalysed reactions which often show better performances than their counterparts which use other carbonaceous material as support [77]. One of the examples where carbon nanotubes are used as catalyst support is found in hydrogenation of benzene. In fact, it has been observed that carbon nanotube supported Rh nanoparticles are highly active and reusable catalysts for hydrogenation of benzene and its derivatives at room temperature [78]. In addition, Pd nanoparticles were stabilised on nitrogen doped nanotubes and were used as metal catalyst in the hydrogenation of benzene and in these conditions, Pd clusters exhibited higher activity than other supports such as activated carbons [79]. Instead, a high performance Pd catalyst has been for selective olefin hydrogenation has been obtained by supporting the metal on nitrogen doped nanotubes [79]. In conclusion, carbon nanotube can be used as catalyst support for a wide range of catalysed reactions such as hydrogenation of carbonyls, alcohol and nitro groups [80-82]. A common factor in carbon nanotubes, graphene, fullerenes, carbon onions, nanodiamonds and other novel materials consists in unique advantageous characteristics which might not be found in the other support materials such as graphite, carbon blacks and activated carbon. For example, novel materials can be obtained with high purity which is a good requisite to avoid the poisoning of the catalyst. Some of these supports present a mesoporous nature which may be advantageous for liquid-phase processes. A common characteristic of carbonaceous materials which results of large importance when these materials are employed as catalyst support is due to high thermal capacity. In fact the event of formation of hot-spots is rare, thus the risk to damage the catalyst results minimal. In addition, novel materials are characterised by a rich surface chemistry permits the functionalisation allowing the adsorption and fine dispersion of the active phase. Finally, the specific metal support interactions, due to high electrical conductivity

of the support and to the tunable orientation of the graphene layers, that exist and that can directly affect catalytic activity and selectivity.

3.6 **Functionalisation of graphite by acid treatments**.

As discussed above, the application of carbons in catalysis is mainly as support for active phases in various reactions. Besides, a wide variety of noble metal-carbon systems for hydrogenation reactions and fuel cell applications, the largescale application in the synthesis of vinyl acetate [83] and vinyl chloride are important technical applications [84-86]. The mercury-free process of the vinyl chloride production takes place via gold catalyst which is dispersed on a carbonaceous support. With the aim to shed light on the role that functionalised carbon supports play in this reaction, the identity of functionalities which acid treatment introduces on the support surface as well as the effects that thermal treatment have on the deposition of gold nanoparticles were explored [87]. In this study, high ordered pyrolytic graphite (HOPG) has been used instead of amorphous carbon support. The use of HOPG is manifold: This material is characterised by a flat surface that is ideal for studies employing spectroscopic methods such as scanning tunnelling (STM), atomic force (AFM) and X-ray photoelectron spectroscopies. The HOPG surface is, in fact, characterised by large planar area and reduced number of edges. Such a characteristic gives the advantage of using a material with a surface which is easily reproducible not only experimentally but also computationally. Finally, HOPG is commercially available, easy to shape and does not need particular storage precautions because the material is mostly inert to ambient conditions. Before to employ the support in any catalytic activity, possible impurities which are accumulated on the surface during the manufacture of the material, have to be eliminated. According to the usual procedure, in the experimental work, the HOPG samples were cleaned, before each experiment, by removing mechanically few graphene layers from the top. Fresh diluted HCl was used to wash the support and remove traces of Na, Fe and Cu which are poison for the hydrochlorination reaction [88]. The HOPG sample is, then, left to stand for 30 minutes before drying under a pure helium stream. The AFM analysis of the HOPG acid treated sample shows the presence of features protruding out from the surface as it can be seen from Fig. 1. These features of circular shape are 50-100 nm in diameter and ~15-20 nm

in height above the planar surface. The presence of these feature was already detected in previous experiment in which the same operative conditions were used except for the concentration of the HCl. The HOPG samples which were treated with acid at diverse concentrations have shown that the features are due to the delamination of planes. The delamination of graphitic planes might be due to the functionalisation of surface defects which lead to a reduction of interlayer bonding. In addition, this preliminary experiment suggested that the size of protrusions on HOPG surface are related to the acid concentration [89].

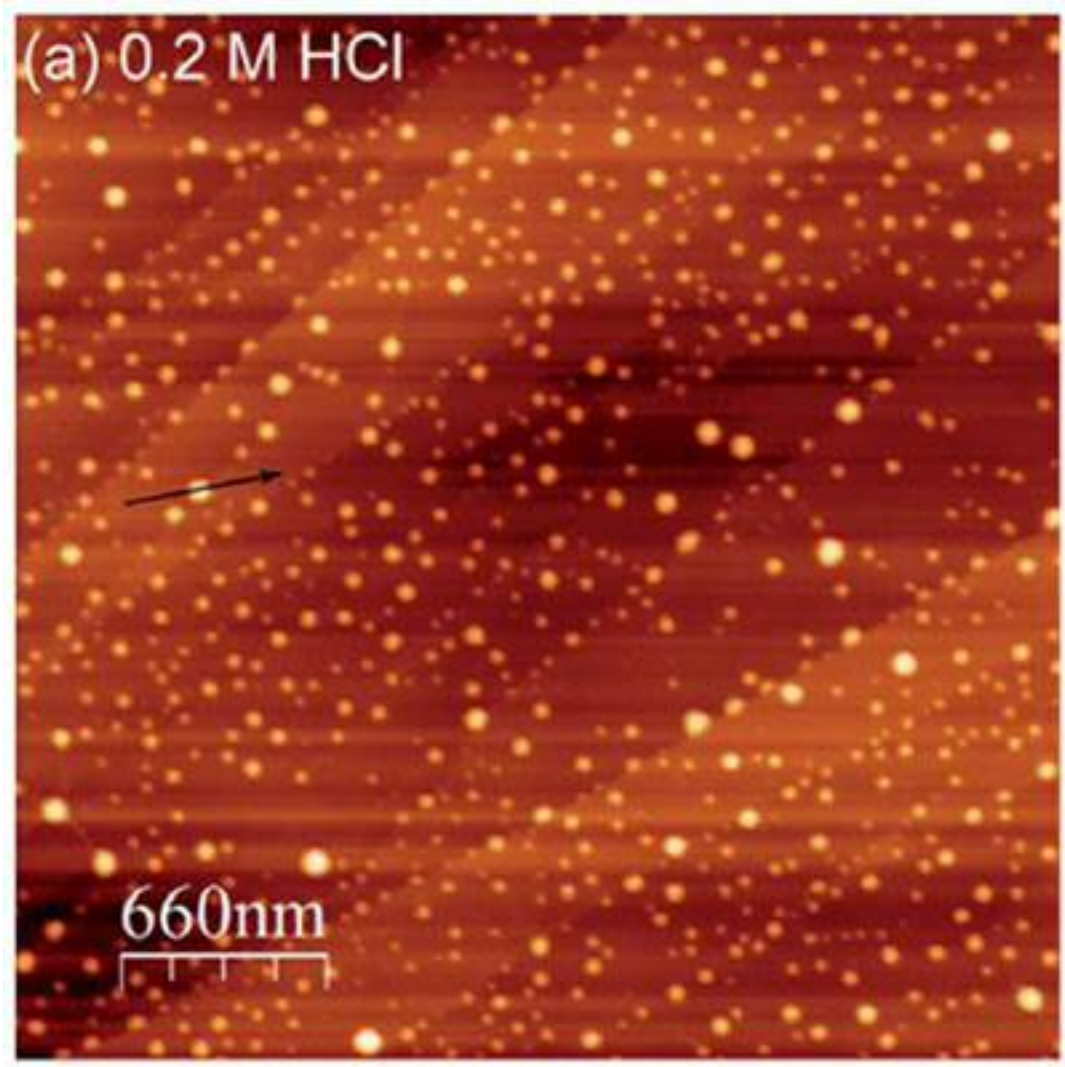

Fig. 1 Atomic force microscopy image of HOPG surface treated with 0.2 M HCl for 30 minutes. This picture has been adapted from one of our previously published works [87]

The XPS analysis, which is reported in Fig 2, detects the presence of oxygen which is identified by the peak at 532 eV while chlorine is found at 198 eV and some traces of nitrogen a 400.2 eV.

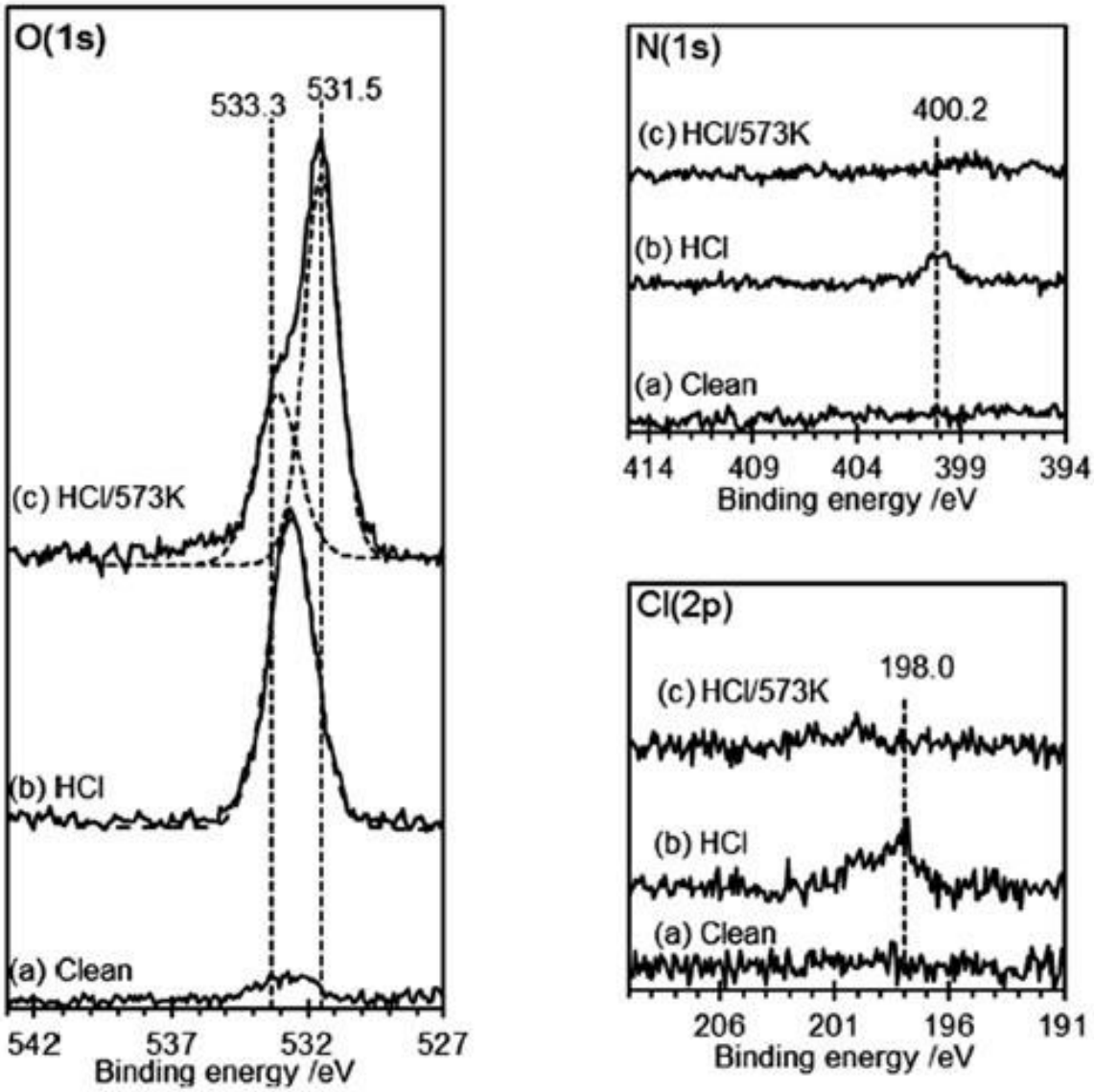

Fig. 2 O(1s), N(1s) and Cl(2p) XPS regions of the HOPG sample after 0.2 M HCl treatment and successive heating at 573 K. In each figure, at bottom there is the spectrum of the clean surface, in the middle, after acid treatment for 30 minutes and, finally at the top after heating for one hour at 573 K and cooling at room temperature. More detailed information about spectral data are available in reference [87].

As it can be seen from the spectral data of Fig. 2, heating the HOPG sample at 573 K leads to a split of the oxygen peak in two other peak which are located at 531.5 and 533.3

eV. Besides, the spectral features in the nitrogen and chlorine regions result scarcely detectable. The AFM image of Fig 3 supports the XP data showing that after heating the HOPG sample, the features which were formed by acid treatment, results no longer visible on the surface.

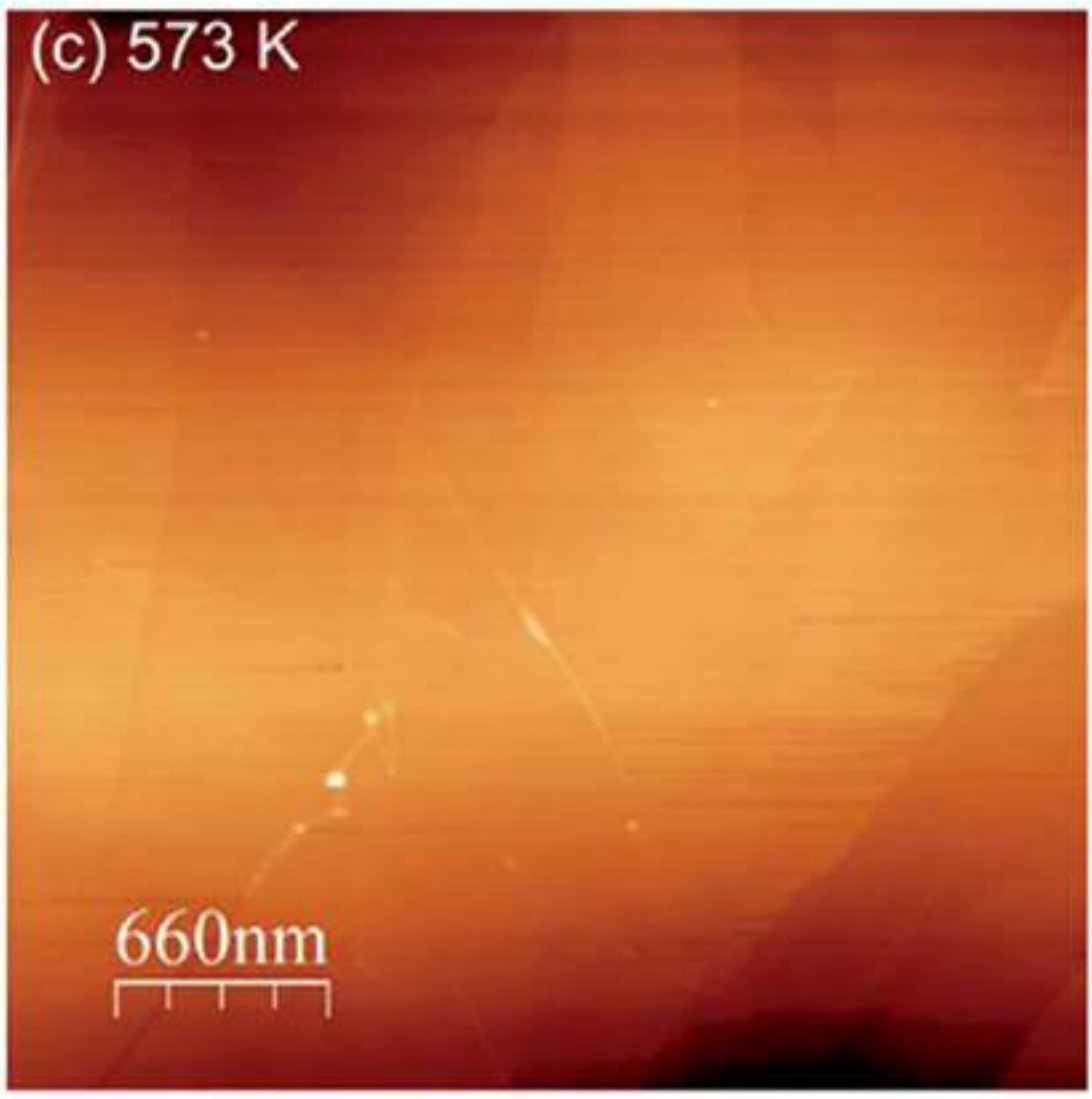

Fig. 3 AFM imaging of HCl treated HOPG sample after heating for one hour at 573 K. In this image, the feature which were formed on the surface are no more visible.

Interestingly, experiments consisting in heating the acid treated HOPG samples showed that in the temperature range from 290 to 573 K, only small variations of the oxygen concentration were observed. This was also supported by the AFM image of Fig. 4 that was acquired at 423 K and shows that at this temperature, features are still persistent on

the HOPG surface. In addition the AFM line profile of Fig. 5 shows that an increasing in temperature determines a reduction of the average sizes of the features.

Since the XP spectra show two large peaks in the oxygen region (Fig. 2), further investigations were conducted with the aim to resolve these peaks identifying the corresponding chemical nature.

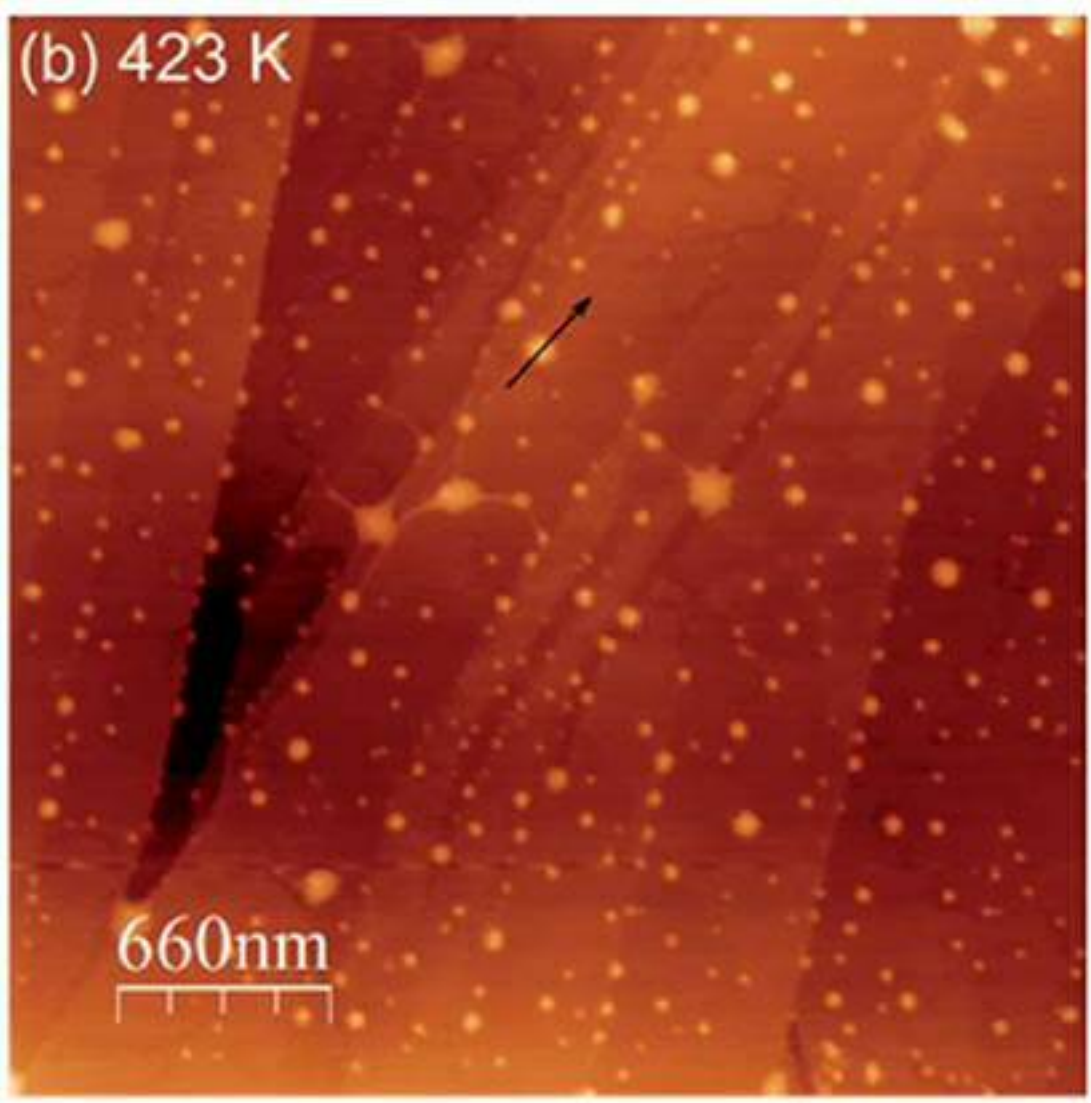

Fig. 4 AFM image of HOPG sample after heating for 1 h at 423 K and cooling at room temperature.

Generally, by the technique of the XP spectroscopy, the distribution of oxygen-containing functional groups is often characterised by deconvoluting the C(1s) spectral envelop to obtain quantitative information which are based on differences in binding

energy. However, such a spectral envelope is typically broad and featureless in the C(1s) spectral region and several other factors play a role to complicate the peak-fitting leading to misleading and ambiguous results in terms of the calculated distribution of oxygen-containing functional groups. Amongst the limitation inherent to the peak-fitting, the main complication is due to the proximity of the binding energies which are associated with different oxygen-containing functional groups. Often, the peak-fitting results

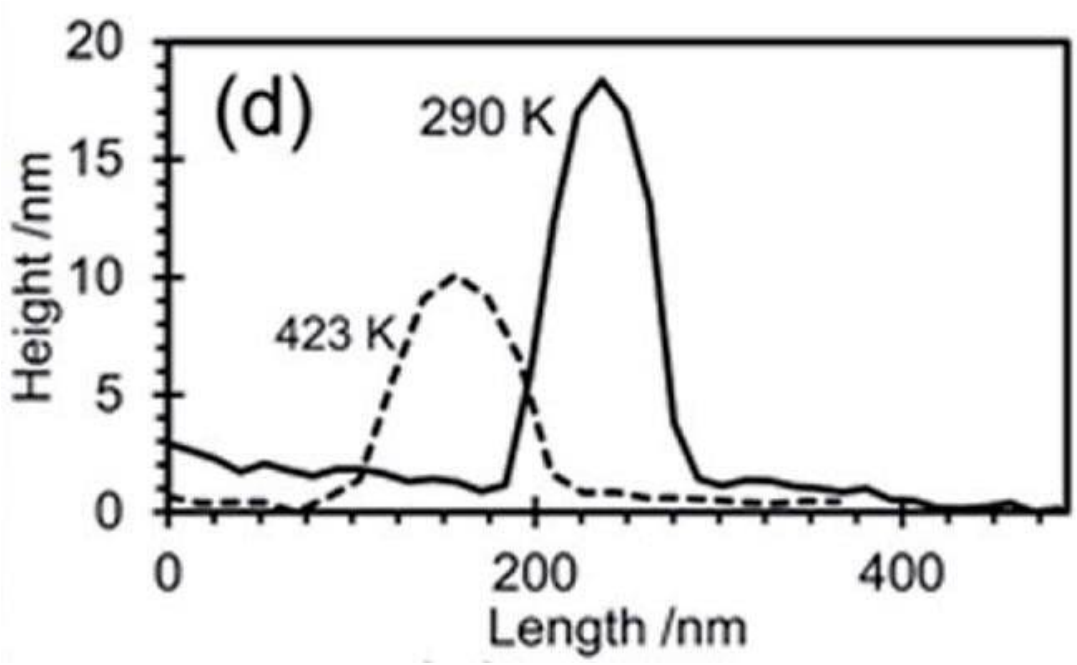

Fig. 5 Line profile of the AFM image showing the average sizes of the surface feature as a function of heating temperature.

problematic because of limited resolution of typical energy analysers [92, 93]. In addition, in systems with delocalised π electrons such as in graphitic materials, the presence of π-π* shake-up feature determines further congestion in the C(1s) region [92]. Thus, derivatisation methods have been developed to overcome the limitations inherent to the peak-fitting permitting the characterisation of key oxygen-containing groups on carbonaceous surfaces [94, 95]. In the applications of chemical derivatisation, a targeted oxygen-containing functional group reacts selectively with a specific derivatisation reactant that contains a unique chemical tag (in this work fluorine atoms). When the reaction has completed, the presence of the chemical tags is indicated by a well-defined peak allowing directly to determine the presence of the targeted functional group.

In order to detect hydroxyl groups (C-OH) on the acid treated surface, the 2,2,2-trifluoroacetic anhydride (TFAA) is used as derivatizing reagent. As shown in (3.2), TFAA reacts selectively with hydroxyl group to form a trifluoromethyl ester group and

trifluoroacetic acid as a byproduct. When HOPG surfaces are cleaved in air the presence of small oxygen concentration is always detected and identified by a peak at 532.6 eV. Accordingly, when the clean surface is exposed at TFAA, a weak peak is found in the F(1s) XPS region. On the other hand, when the acid treated HOPG surface is exposed to TFAA a large peak at 532.7 eV in O(1s) XPS spectral region is broadened and presents a shoulder at higher binding energy as can be seen in Fig. 6.

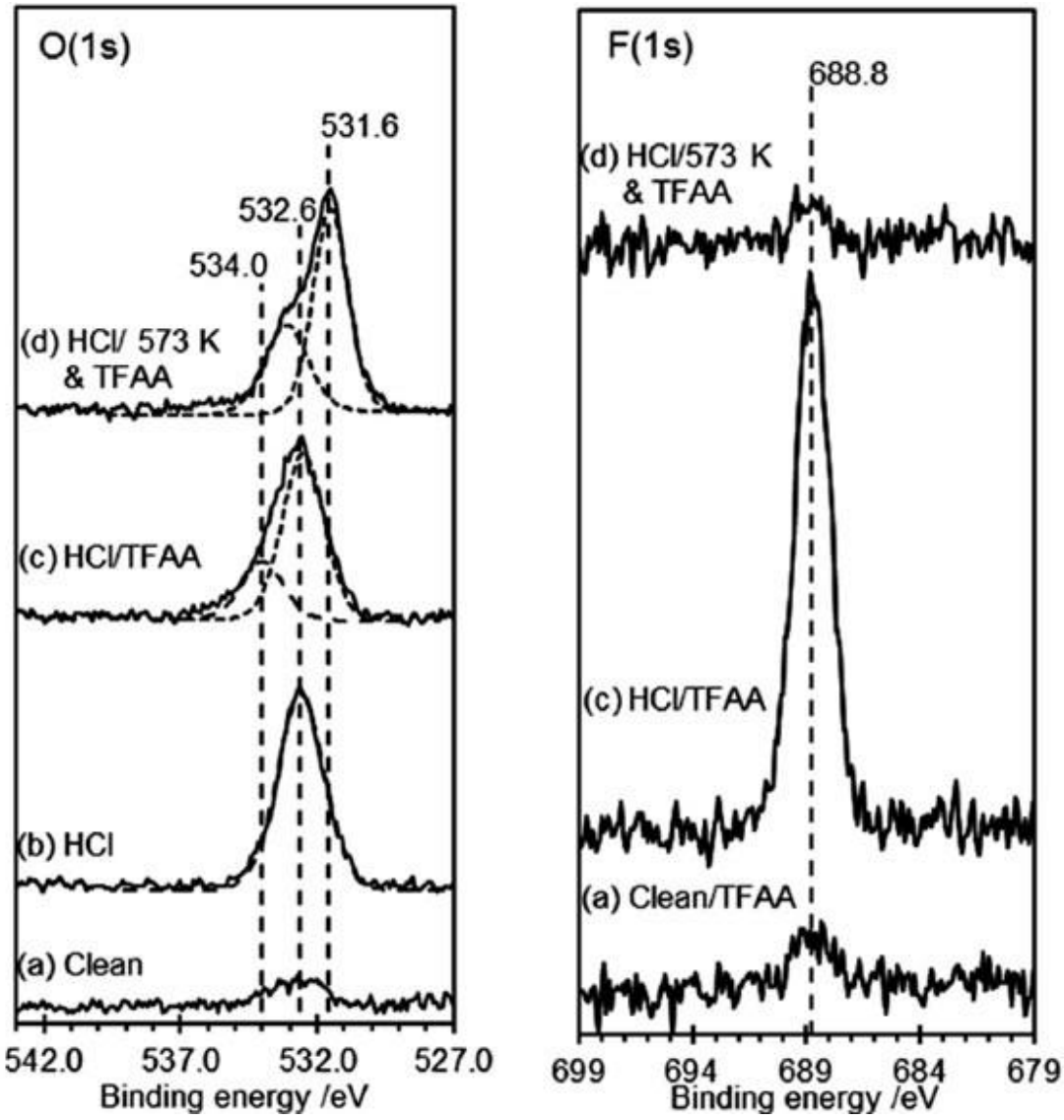

Fig. 6 O(1s) and F(1s) XPS regions of HOPG surface after a) being exposure to atmospheric air, b) treatment with 0.5 M HCl, c) treatment with 0.5 M HCl and successive exposure to TFAA d) treatment with 0.5 M HCl, heating at 573K and exposure to TFAA.

The deconvolution by peak-fitting permits to identify the contribution of peaks at 532.6 and 534.0 eV which have been found in the area ratios of about 3:1. In the F(1s) region, an intense peak is found at 688.8 eV.

The spectral data obtained by TFAA suggested that the acid treatment introduces hydroxyl groups on the surfaces.

The identification of carboxylic acid (COOH) groups on the treated HOPG is obtained using the derivatisation reagent 2,2,2-trifluoroethanol (TFE) and *N*,*N*'-di-*ter*-butyl-

carbodiimide (DTBC). The reaction of TFE with carboxylic acids in presence of DTBC may form two products as it is pictured in Fig. 7. One is a trifluoroethyl ester **4** and the volatile 1,3-di-*ter*-butyl-*N*-acyl urea containing two nitrogen atom. The other reaction product is a surface bound di-*ter*-butyl-*N*-acyl urea **3**.

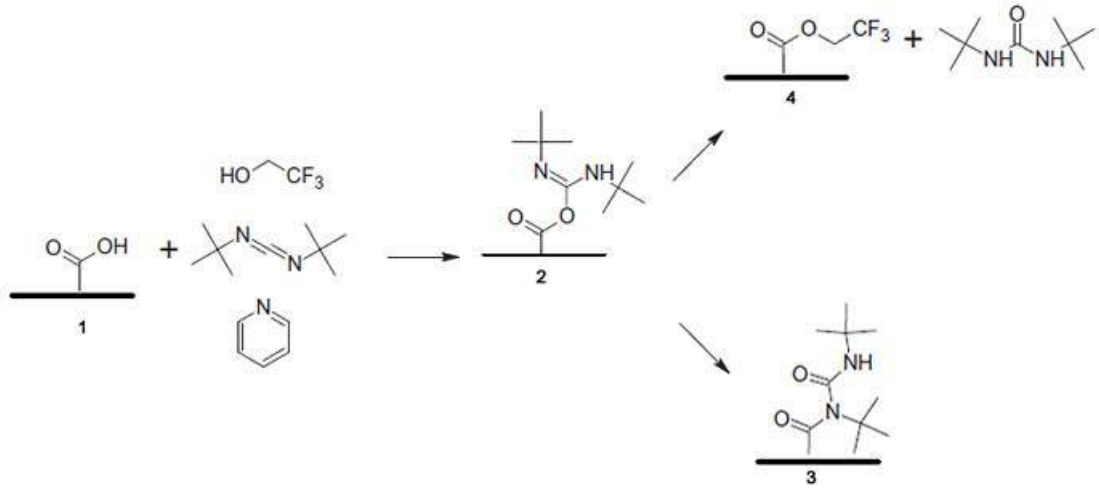

Fig. 7 derivatisation reaction of TFE with carbossilic acid 1 (on HOPG surface) in presence of DTBC forming, initially, the activated complex O-acyl isourea and formation of the final products: di-*ter*-butyl-*N*-acyl urea **3** and trifluoroethyl ester **4**.

It is noteworthy, in the reactions of carbodimmides with carboxylic acids in presence of DTBC both the **3** and **4** are possible [96, 97]. Thus, the observed N(1s) signal is a result of the TFE/DTBC reaction with the carboxylic acid and is principally due to the formation of an *N*-acyl urea. Fig. 8 shows the XP spectra of the O(1s) and F(1s).

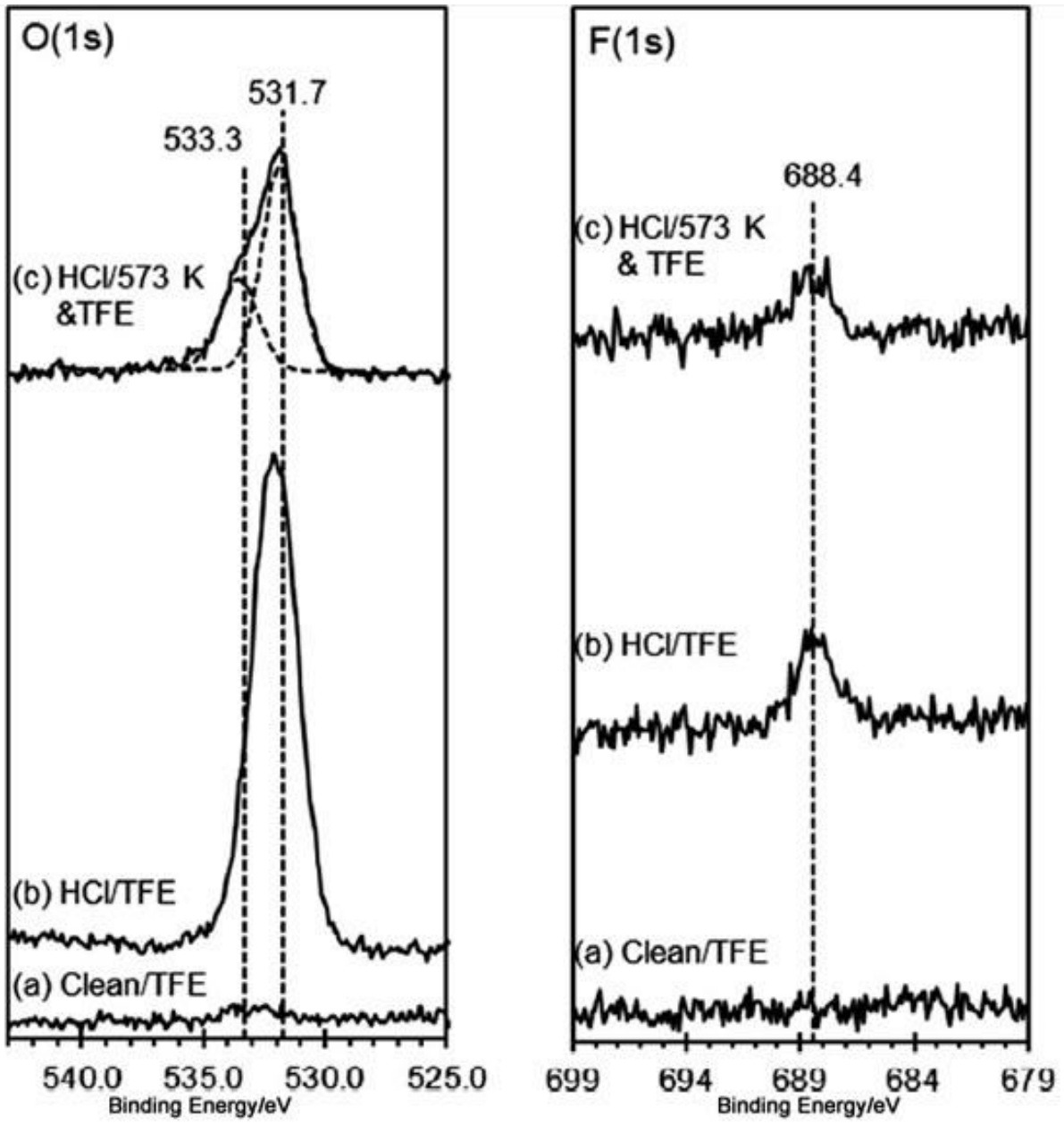

Fig. 8. O(1s) and F(1s) XPS regions of HOPG after a) cleavage at atmospheric air, b) 0.5 M HCl and exposure to TFE/DTBC c) 0.5 M HCl, heating at 573K and exposure to TFE/DTBC.

Three HOPG samples, namely, a clean surface, a 0.5M HCl treated surface a high temperature treated sample were exposed to TFE in presence of DTBC for 24 hours. The XP spectra of these three samples are represented in Fig. 8. In either O(1s) and F(1s) regions the absence of features in the spectra of the clean HOPG suggests that no reaction

occurred between the derivatising reactants and the surface functional groups. In addition, while in the O(1s) spectral region, the HCl/TFE treated surface show a large peak at 532.0 eV, in the F(1s) region the corresponding peak is very small indicating that only traces of the derivatising species were involved in the reaction. Analogously, for the heated surface no reaction was detected. Thus, the analysis of the XP spectra suggests that the two the peaks at 531 and 533.3 eV may not be associate to carboxylic acid group.

The identification of oxygen in ketones is based on the derivatisation reaction of the carbonyl group **1** with 2,2,2-trifluoroethylhydrazine (TFH) which produces one exclusive surface product, a trifluorinated hydrazone **2** where the terminal nitrogen group in TFH form a double bound with the carbonyl (C=O) carbon and the oxygen atom is expelled as H_2O. This reaction proceeds with high efficiency and selectivity towards the carbonyl group. The derivatisation reaction is sketched in Fig. 9.

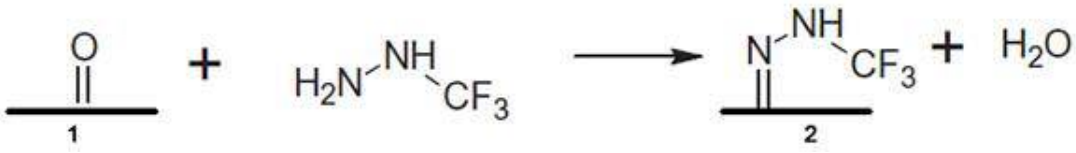

Fig. 9 The selective reaction of carbonyl group **1** with trifluoroethylhydrazine (TFH) to form a fluorinated hydrazone **2**.

As above, three samples of HOPG were prepared to investigate if functional groups were already present after exposure to air or they were introduced by dilute acid treatment and to observe the effects of the high temperature heating on the functionalised surface. The results of XP spectra are shown in Fig. 10.

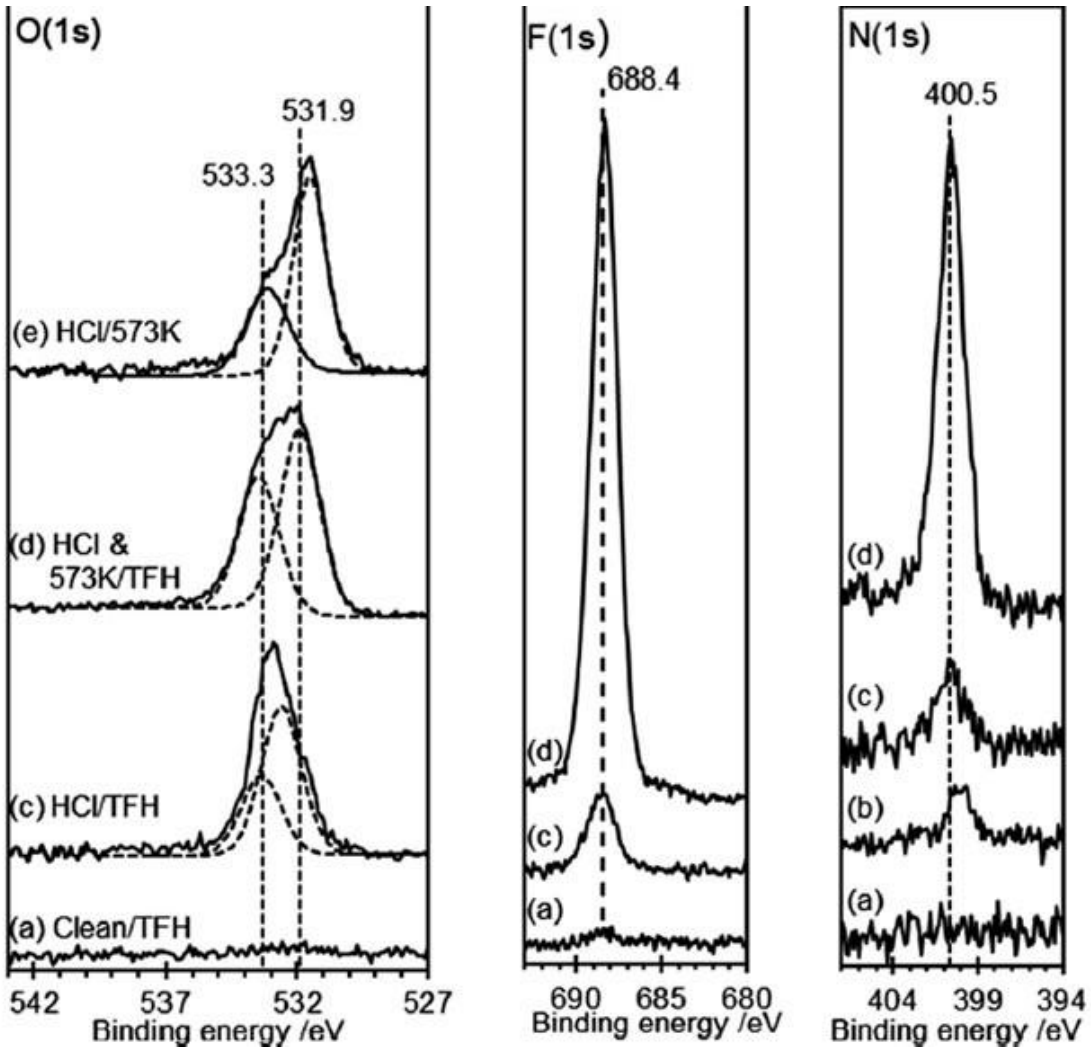

Fig. 10 O(1s), F(1s) and N(1s) XP spectral regions of four HOPG samples. The spectra were obtained after: a) cleaving the surface of HOPG in atmospheric air and successive exposure to TFH, b) 0.5 M HCl treatment on the HOPG surface c) after 0.5 M HCl treatment and exposure to TFH d) after 0.5 M HCl treatment, thermal treatments at 573 K before exposure to TFH. In the O(1s) region

The analysis of the spectral results of Fig. 10 suggest that there is no reaction between the clean surface and the derivatising reactant. This appears clear in the F(1s) spectral region where a small peak indicating that only a very reduced number of functional groups reacted with TFH. The peak in the F(1s) region shows that the exposure of acid treated HOPG is not able to generate a large quantity of carbonyl groups as the exposure to TFH still returns small peak. Interestingly, after the HOPG is acid washed, heated at

573 K and exposed to TFH, the XP spectrum in the region F(1s) show a large peak at 688.4 eV. In addition, also in the N(1s) region the spectrum of the acid washed and heated surface show a large peak in correspondence of 400.5 eV. Thus the XP spectral investigation on the carbonyl groups suggests that heating the surface at 573K play an important role in the formations of carbonyls may be associated to the peak at 531.6 eV.

Considering all the XP spectra results, it is possible to summarise what they suggest. An initial XP spectra on clean HOPG surface show a small peak at 532 eV in the O(1s) region Fig. 2 spectrum a). After washing the HOPG sample with diluted acid a prominent peak is detected at 533 eV and AFM images of this sample reveal the formation of spherical features on surface. Heating at 573 K the acid washed surface leads to a broadening of the peak which splits generating a shoulder as shown in Fig. 2, spectrum c) in the O(1s) region. The AFM images of this sample shows that the features are disappeared. The chemical derivatisation of the functional groups permits to shed more light on the nature of the prominent uncharacterised peak which is detected in O(1s) region at 532 eV.

The derivation reaction with TFAA (Fig. 6) permits to identify hydroxyls on the surface and the XP spectrum detects a large concentration of OH groups reacting with TFAA only after the surface is washed with diluted acid. Although a small concentration of OH is detected on the clean surface, after heating the acid treated sample, the prominent peak observed in c) in the F(1s) region, disappears in d) suggesting that heating the surface removes nearly the totality of the OH groups on the surface. Derivatisation reaction with TFE/DTBC reveals in the XP spectra of Fig. 8 that carboxylic groups were not detected on the considered HOPG surfaces. Finally, the derivatisation reaction of carbonyl groups with TFH permits to detect by the XP spectra of Fig. 10 the presence of carbonyl groups only after the thermal treatment of the acid washed surface.

These data suggest that the diluted acid wash of the HOPG introduces hydroxyl functionality almost exclusively whereas other functional groups such as carboxyl acids and carbonyl groups where not detected at this stage. Thermal treatment at high temperatures of the hydroxyl functionalised surface leads to oxygens in higher oxidation state. By the derivation method one of these oxygens has been identified as belonging to ketone compound while the other type of oxygen is presumable to be an ether group.

Deposition of gold nanoparticles on HOPG surface was also investigated by AFM and XP spectroscopy.

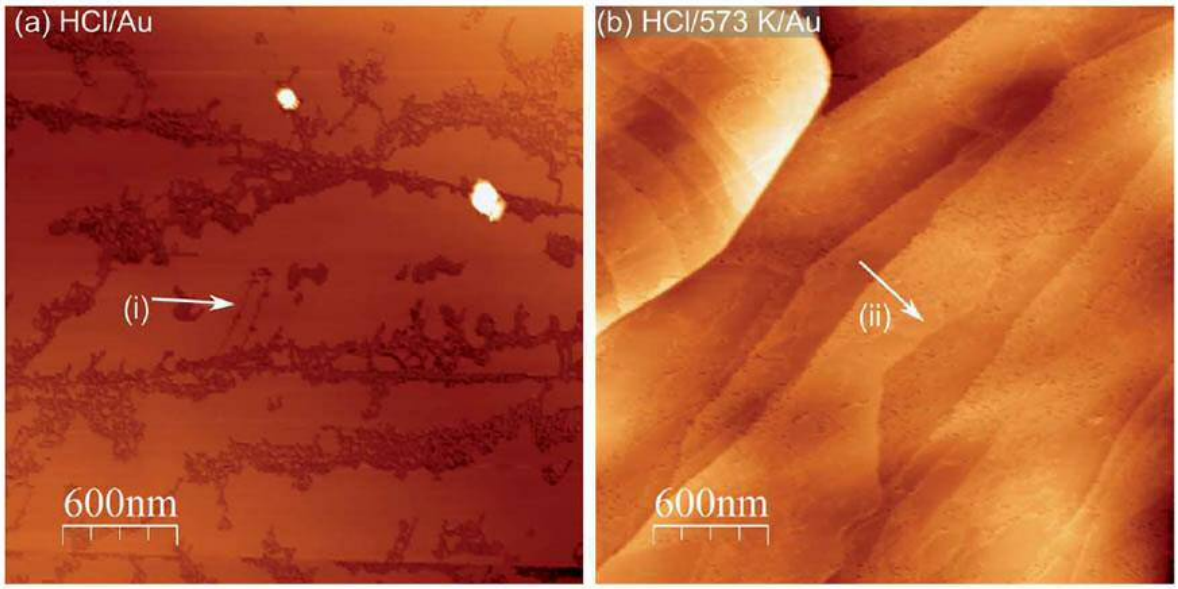

Fig. 11 AFM images of HOPG surface after gold deposition from a solution of chloroauric acid ($HAuCl_4$). (a) HOPG surface after treatment with 0.5 M HCl, dried and then exposed to a $6x10^{-6}$M solution of $HAuCl_4$.

Surprisingly, when gold was deposited on heated and non-heated HCl treated HOPG graphite, the spherical features protruding from the surfaces which were visible in the AMF images of Fig.1 and Fig. 4 have not been found. In fact, how Fig. 11 shows, gold deposition prevent the formation of features and delamination. The AFM image Fig. 11 picture a) which was obtained for deposited gold on HCl treated surface evidences the formation of a discontinuous film of adsorbed particles which resulted to be 2 nm thick. On the other hand. the layer of gold which was formed on the heated HCl surface appeared more uniform as can be seen from Fig. 11 in the picture b). To shed light on these findings, the XP spectra were considered. The experimental details of wet chemical treatments were based upon the established procedure which is accurately described in reference [87]. As Fig. 12 shows, in the Au(4f) spectral region, the acid treated surface as well as the heated surface show two prominent peaks at 84.0 and at 86.5 eV which can be assigned to Au^0 and Au^{3+}. Peak-fitting of data suggest also the presence of another

specie which is mostly likely the Au^{+}. In fact, chlorine binding energy of 198.0 and 199.7 eV have been previously reported for chlorine bound to the Au^{3+} and Au^{+} species after exposure of gold metal to chlorine gas [98]. These experimental findings stimulated a computational investigation which was aimed to shed light on the stability characteristics of functional groups which are formed at the reactive sites of graphite surface and the role they play in Au particle anchoring.

3.8 Computational methods

The results of electronic structure calculations, which will be discussed in following paragraphs, were based on the Kohn-Sham approach of DFT and performed within the periodic plane-wave basis set code VASP 5.3 [99-100]. Projector augmented waves (PAW) potentials were used to describe the ion cores leaving valence electron configurations $C(2s^2 2p^2)$, $O(2s^2 2p^4)$, and $Au(6s^1 5d^{10})$ to be explicitly calculated whilst the ultrasoft pseudopotential was used for representing the electronic structure of the H atoms. Exchange-correlation interaction was treated by generalised gradient approximation (GGA) in the parametrisation of Perdew, Burke, and Ernzerhof (PBE) [103]. The weak van der Waals interactions operating between the graphitic planes were accounted by the semi-empirical method of Grimme et al. DFT-D2 [101], as is implemented in VASP. The dispersion coefficients C_6, and the van der Waals radius, R_0, for gold were taken to be 40.62 J $nm^6 mol^{-1}$ and 1.772 Å, respectively as reported in a previous work of Amft *et al*. [102]. For supercell calculations of the surface a Monkhorst-Pack grid was used for *k*-point sampling [104-105]. The plane-wave basis set was by a 500 eV cutoff for all calculations. The width of Gaussian smearing for the occupation of electronic levels was 0.01 eV and dipole corrections along the three directions of the unit cell vectors were included. All structures were optimised until a convergence of 10^{-5} eV was reached and the Hellmann-Feynman forces on each relaxed ion were smaller than 10^{-4} $eVÅ^{-1}$. In order to model graphite surface, the slab model was used. For calculations using a slab model, the surface energy is calculated by the classical energy equation:

Where is the surface energy, A is the surface area which in the case of a hexagonal unit cell is and a_o is the length of the lattice vector. is the energy of the slab containing n formula units (carbon layers), and is the energy formula unit in the bulk material. The surface energy convergence was reached when the slab thickness consisted of five graphene layers. Such energy was calculated using a unit cell where a vacuum gap of 15 Å in thickness was added to suppress the spurious interactions between the unit cells which are periodically repeated. Finally, a supercell was optimised. This supercell contains a large number of carbon atoms (165) and, in order to reduce the computational costs, after geometry optimisation, the layers at the bottom of the slab, namely, those which represent the graphite bulk were kept fixed while the last two layers, representing the surface, were allowed to relax.

3.9 Pristine graphite surface.

Two types of surfaces can be found in graphite, the basal plane (0001) and the prismatic planes (zig-zag face (1010) and armchair face (1121)). The basal plane is the less reactive surface and the reason is that the graphite crystal exhibits large difference in surface energy in the different crystallographic directions; such energies have been found higher in the prismatic planes 5 J/m^2 than in the basal plane 0.11 J/m^2 and these discrepancies account for the different rate of reaction, namely, slow at the basal plane and rapid at the prismatic surfaces which are located at the terminations of the basal planes or at defect sites within the basal plane [106]. Accordingly, graphite material with large crystals and no defects have the higher chemical resistance.

The structure which have been used to model the HOPG, is the pristine graphite surface, where no defects are present, is shown in Fig. 12.

The C-C distances are of 1.420 Å and the bond angles of 120.0 degrees which are the same values which were calculated in the graphite bulk. Interestingly, in the slab structure where all carbon atoms were allowed to relax, the interlayer distances gradually increase. Moving from the bottom layers to top, the largest distance is found between the top two layers and is of 3.271 Å.

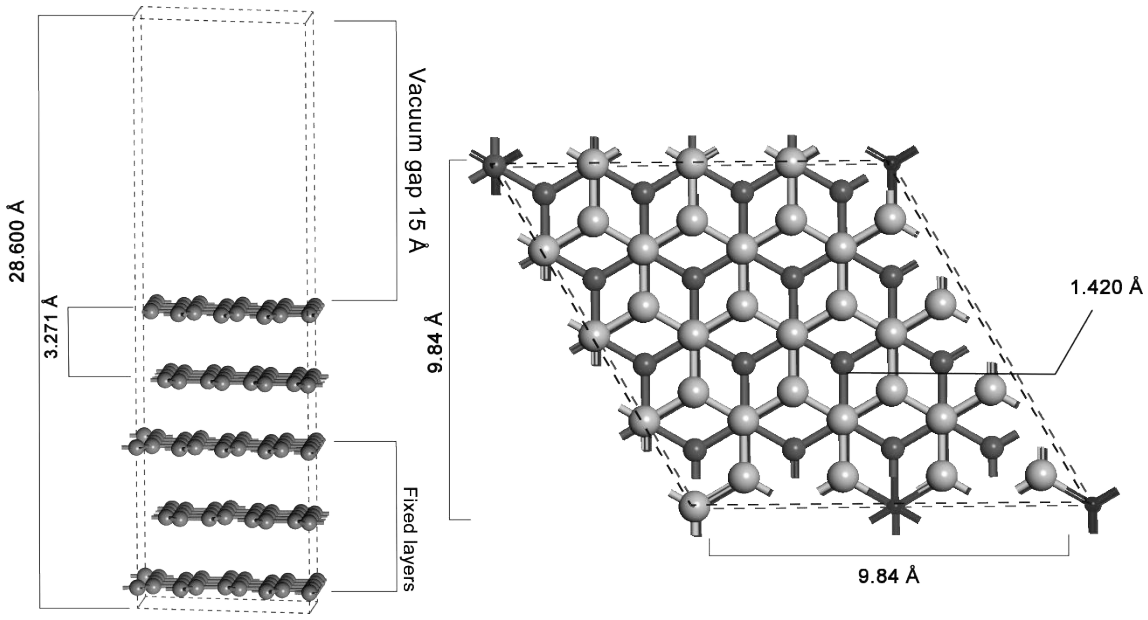

Fig. 12 Side view of the graphite supercell containing 165 carbon atoms. The slab is formed by five graphene planes. The first three graphene planes at the bottom of the slab are kept fixed during the geometry optimisations whereas the last two carbon layers are allowed to relax. The vacuum gap is 15Å and length of the lattice vector c is of 28.600Å. In the planar view of the 000 surface, the top layer of carbon atoms is light grey coloured. The lattice parameters $a_0 = b_0$ are of 9.84 Å in length.

The material HOPG is not of single crystalline quality and contains an uncharacterized amount of surface defects. Thus, before to discuss the results of surface topological defects, a brief introduction is given on this topic.

3.10 Topological defects in graphite.

So far, it has been assumed that the graphite 000 surface is infinite, perfect and uniform but the real surfaces containing steps, defects and impurities are more complicated to control in experiments. Thus, the sample heterogeneity is a significant problem especially when the comparison between theory and experiment is attempted.

The second law of thermodynamics dictates the presence of a certain amount of disorder in crystalline materials. However, it is also due to the imperfection of production process or particular material treatments that impurities and defects are always introduced in crystals. In three-dimensional crystals, defects are referred to as intrinsic when the crystalline order is perturbed without the presence of foreign atoms which are called impurities. The impurities are called extrinsic defects. Intrinsic defects are characterized by having diverse dimensionalities. For example, point defects such as vacancies or interstitial atoms are zero-dimensional. Extrinsic defects may exist as zero-dimension defect, namely, when foreign atoms substitute individual atoms of the crystal or are located in interstitial sites. Dislocations are considered as one-dimensional defects while the class of two-dimensional defects includes grain boundaries or stacking faults. Moreover, inclusions and voids are representative of the remaining three-dimensional class. Finally, agglomerated of foreign atoms can extend to more dimensions (two or three-dimensions). Since in graphite the role of defects on the electronic structure represents an essential tool for understanding carbon nanostructures, the last two decades have seen an increased interest in understanding the properties of defective surface. In fact, defects play a fundamental role in several fields. Examples are the postulation of specific electric properties that would arise from the broken bonds at surfaces of semiconductors and the high chemical activity that might be associated with defects on the surface. The invention of the scanning tunneling microscope (STM) and the subsequent development of other scanning microprobes changed that situation completely. Not only that line and point defects have become visible objects, one can even track their motion as they migrate across the surface, in the course of thermal fluctuations, catalytic reactions, epitaxial growth, or abrasion. Graphite is one of the most extensively studied materials in STM. However, there are still phenomena observed on graphite surfaces with STM, which are not well understood. Graphite shows superperiodical features often in STM experiments, which are not related to the topography of graphite. These features are often called superlattices in literature [107]. Graphite superlattices have been observed by many groups over the last two decades. Superperiodic hexagonal structures on a graphite surface arise during crystal growth or cleavage. Their formation is due to intrinsic defects of the substrate crystal. [108-110]. Moreover, due to its unique characteristics of material with an excellent thermal stability and strength at high temperature together with its ultrahigh purity, graphite is largely used as both moderator and a reflector material in nuclear reactors. In addition, graphite

has good thermal shock resistance and stability under nuclear radiation. In the nuclear reactor, the moderator acts in order to decreases the velocity of fast moving free neutrons which are created by fission. The resulting decrease in kinetic energy has been estimated to be from 2MeV for fast neutrons down to 1eV (thermal neutrons) so that the fissile nuclei, capturing the neutron, are capable to sustain the fission reaction reducing the size of the reacting pile. A greater advantage is obtained when graphite is used as both moderator and a reflector which result be safer and less expensive than other materials such as beryllium or if it is compared with heavy water can be also used as structural material. For these roles, most graphite has sufficient strength, density, and offer also other important advantages but to be used as moderator the most severe constraint is placed in purity. In fact, some impurities possess the ability to capture neutrons and in order to achieve the purest material, the manufacturing process requires that graphite is treated at much higher temperature and for longer periods of time. In the same year that Fermi prosed to use graphite as nuclear moderator [111], Wigner theorised that under the influence of the very fast and energetic neutron flux, graphite could, over time, undergo serious changes to its structure and properties [112]. This behaviour has been confirmed by a significant experimental program [113]. The response of graphite to damaging radiation is extremely complex, owing to its anisotropic structure, and the ability of carbon atoms to adopt a great variety of metastable configurations, yet the material can remain recognisably graphitic (with modified properties) even after exposure. Under the radiation process a chaotic cascade then follows, which eventually settles into a population of defects and defect complexes, accompanied by the formation of dislocation loops [114]. These defects affect the properties of the irradiated material compared with the pristine state. Insight into the nature of defects created by radiation damage at the atomic scale has in recent times been facilitated by the discovery of graphene, and by progress in atomic resolution imaging techniques.

3.11 Point defects: single vacancy.

The simplest point defect in a crystal is the vacancy. Vacancies arise when lattice sites are unoccupied by atoms. They may be formed when the energy E_f (eq. 3.3) which is required to remove atoms from the internal sites and place them onto the surface is not particularly high. This low energy coupled with the statistical entropy of mixing

vacancies among lattice sites, gives rise to a thermodynamic probability that an appreciable number of vacancies will exist at high temperatures. Vacancies play an important role in processes related to the solid-state diffusion recrystallization, grain growth, sintering, and phase transformations. In catalysis, defects are the anchoring sites for metal nanoparticles. Potentially, the dispersion of metal catalyst is monitored or regulated controlling the density of defects. In the Bernal structure of graphite, two types of atoms are found, α and β. Removing an α- type atom generates an α-vacancy (α-V1) whereas removing an atom of the other type results in a β-vacancy (β-V1). When an atom is removed from the lattices leaves a vacant space with three dangling carbon bonds in the network. The triplet state is slightly more stable than the single state [116]. These three dangling bonds are unstable and undergo recombination to make a chemical bond between two of them forming a pentagon ring and one remaining dangling bond in a polygonal ring with nine bonds (nonagon) [117].

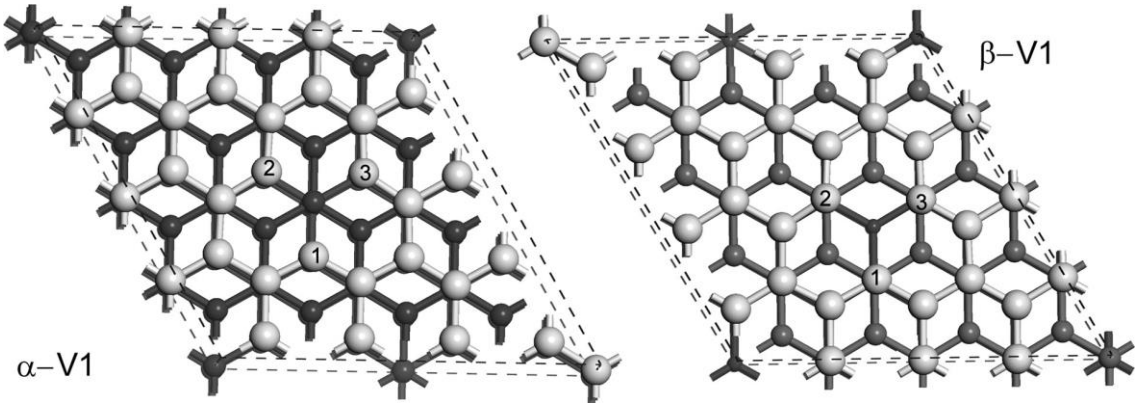

Fig. 13 Single vacancy defects: alpha-vacancy (α-V1) on the left, beta-vacancy (β-V1) on the right.

The optimised geometries of α-V_1 and β-V_1 are represented in Fig. 13. The planar view does not allow to see that the undercoordinated atoms, which in the figures are labelled with numbers, extrude out from the graphitic plane. Thus, the lowering of the symmetry of the defects from D_{3h} to C_{3v} characterises the Jahn-Teller distortion on both the α and β sites. Such a nonlinear arrangement in which atoms of a degenerate ground state undergo a geometric distortion is used to remove the degeneracy and stabilise the system. This is noteworthy owing to the fact that such an effect has quantum-mechanical origin.

The formation energies E_f for both the α and β vacancies were obtained from the total energies using the following expression [118]:

where, E_d is the total energy of the defected surface and E_{bulk} is the total energy of perfect graphite, which was calculated for the supercell identical to that one which was used to optimise the defected surfaces. The chemical potential of carbon is represented by μ while n is the number of carbon atoms which have to be added or removed from the pristine surface to obtain the defective surface under investigation. The α-V_1 was found 0.39 eV more stable than β-V_1. The formation energy, E_f, for the α-V_1, is of 7.65 eV whereas E_f for the β-V_1, is 8.04 eV. These values show a good agreement with the formation energies of α-V_1 and β-V_1 of 7.6 and 8 eV, respectively, which was reported within the GGA by Li *et al*. [120]. In the computational works of Kaxiras *et al.* [121] and El-Barbary [122], the formation energies of the α-V_1 were found of 7.8 and 7.4 eV, respectively. In the atomic configuration of the α-V_1 which is shown in Fig. 13, the bond distance between the carbons 1 and 2 is of 2.545 Å, the atomic distance between the carbons 1 and 3 is 2.556 Å while the interatomic distance between the atoms 2 and 3 is of 2.405 Å. The atom 1 rises above the carbon plane of 0.25 Å. The interlayer distance between the last two carbon layers at the top of the slab is found to be nearly the same (only 0.07Å shorter in the defective surfaces) of interlayer distance that was measured in the pristine surface. The bond angle which is formed between the two nearest neighbours to the carbon 1 is widened 3.20 degrees with respect to the average angles measured in the graphitic plane which were found of 120.00 degrees. Similar results have been found in the optimised geometry of the β-V_1 but in this geometry the carbon 1 extrudes out of the plane of 0.301 Å which effects the bond lengths which have found to be of 2.562 Å between the atoms 1 and 2. The interatomic distance between the atoms 1 and 3 is of 2.583 Å and that between the carbons 2 and 3 is the 2.405 Å. The angle that carbon 1 forms with its nearest neighbours is of 123.302 degrees.

It is well known that defects are not always stationary and that migration can have an important influence on properties of a defective crystal. In graphite, each defect has a certain mobility which is parallel to the other graphitic planes. Migration of single

vacancies has been described on carbon nanotubes, [123] showing an anisotropic behaviour of the migration mechanism and an increasing of migration barrier compared to graphite. The migration is generally governed by an activation barrier which depends on the defect type and increases exponentially with the temperature. The barrier calculated for the migration of the α-carbon in the α-V_1 toward the β-site leading to a β-V_1 was calculated to 1.22 eV which means that the process will be thermally activated above about 100 C. The energy profile of the monovacancy diffusion is reported in Fig. 14

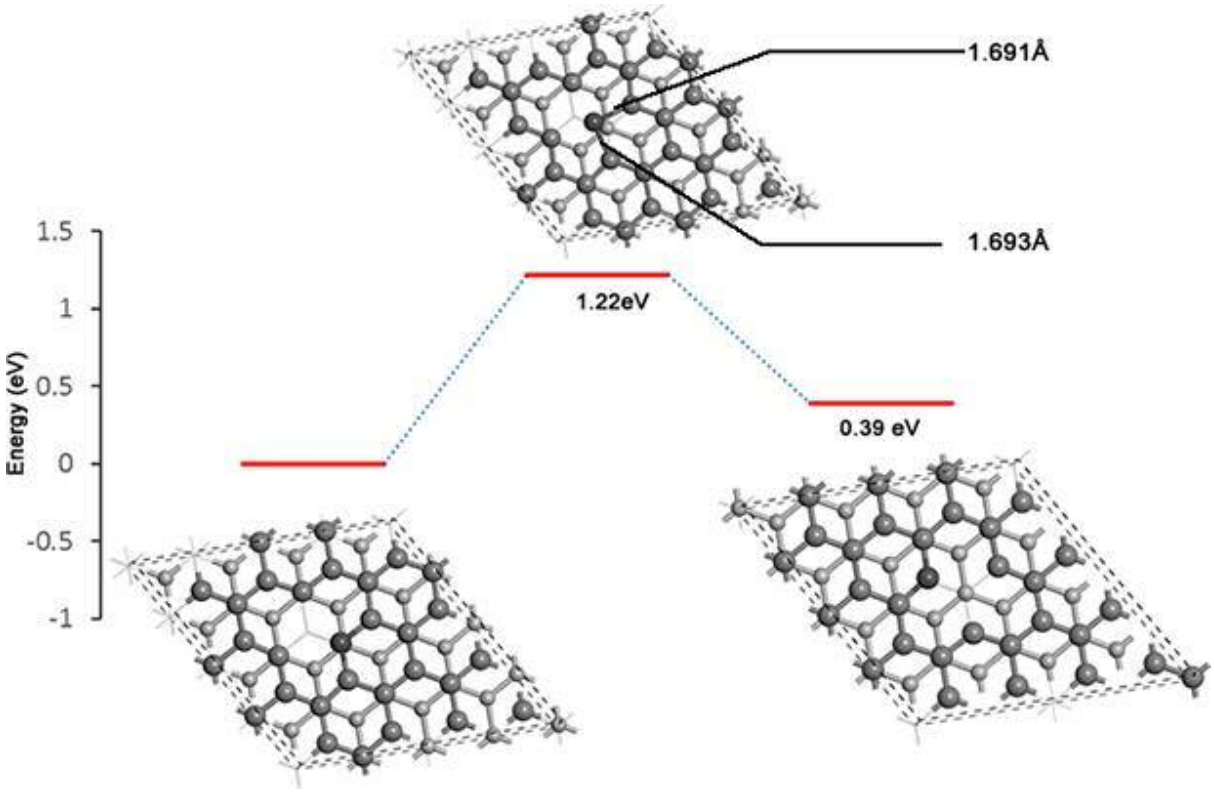

Fig. 14 energy profile for the diffusion of a mono-vacancy on the graphite surface. The optimised structure on the left side is α-V_1, the transition state is located at 1.22 eV. The β-V_1, is represented on the right side of the picture.

The determination of the diffusion barrier height required the nudged elastic band method (NEB) [124]. Starting from the optimised α-V_1, for allowing to the α-atom of reaching the β-position in the optimised geometry of β-V_1, the wanted path was represented by a

chain of three images, namely the reactant, α-V_1, the guessed transition state and final product, β-V_1.

To the best of our knowledge, there are no calculations aimed to determine the diffusion barrier of a monovacancy within a graphite structure which is described by a slab of many layers. However, some authors reported diffusion barrier which were calculated on non-interacting graphene layer. On graphene, the calculated energy barrier for the monovacancy diffusion is of 1.6 eV [125] and 1.3 eV [121]. In the optimised geometry of the transition state, the bond lengths between the carbon atom which is transferred from the α-ring and the two nearest neighbours carbons is increased of 0.271 and 0.273 Å with respect to the equilibrium values which are found in the α- and β- vacancies.

3.12 Point defect: Divacancy.

Divacancy is one of the simplest form of multi-vacancy defects. It is obtained removing two adjacent carbons from the pristine graphitic plane. The removal of two atoms generates unsaturated valences on the carbons which are in the neighbourhood of divacancy (V_2). Thus, in order to saturate the dangling bonds, four carbons move close to each other forming two new bonds. The reconstruction of this defect yields a structure with flattened eightfold ring and two fivefold rings on each side. For this reason the V_2 is often known as 5-8-5 defect or inverse Stone-Wales. The optimised geometry of the V_2 is reported in Fig. 15.

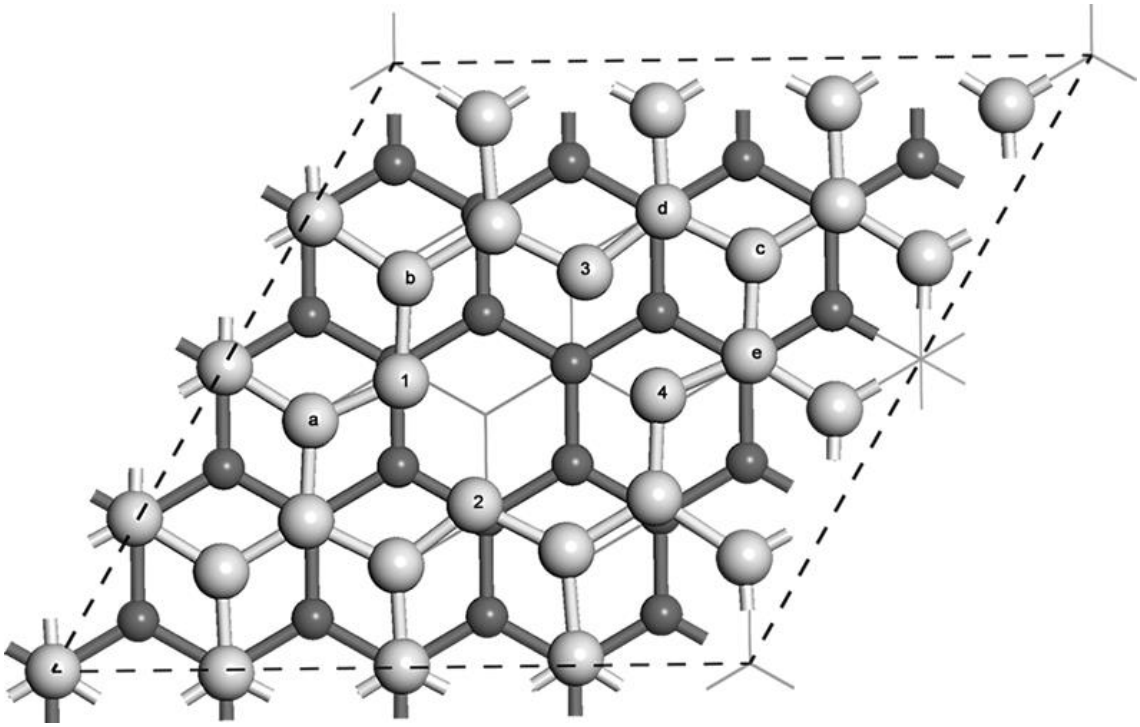

Fig. 15 Equilibrium geometry of a divacancy in graphite.

The formation energy of the V_2 was calculated by the expression (3.3) which returned an E_f value of 7.52 eV. This value is also in good agreement with the formation energy calculated in other works which reported formation energy values of 7.5 eV [126] and 7.6 eV [127].

The formation energy E_f suggests a divacancy is more likely than α-V_1 which instead requires 7.65 eV. In the optimised geometry of the V_2, the distance between the dangling carbons 1 and 2 is of 2.037 Å which is very similar to the bond length between the atoms 3 and 4 which is of 2.035 Å. The bond angle between the labelled atoms e-c-d is of 113.02 degrees while the bond angle a-1-b is of 116.85 degrees. Finally, a V_2 can be formed, not only by the collision reaction between the incident atoms and graphite under irradiation conditions, which removes two adjacent atoms from the lattice but also by coalescence reaction between two mono-vacancies.

3.13 Point defects: Stone-Wales.

In the discussions about vacancy defects, it has been pointed out that one of the unique properties of graphitic materials consists in their ability to reconstruct forming non hexagonal rings. The representative example of reconstruction is given by the Stone-Wales defect (SW). In the SW defect, no atom is added or removed from the lattice, two adjacent atoms, formerly, belonging to two adjacent hexagons are rotated of 90 degrees forming two pentagons and two heptagon rings which are opposite each other around the rotated C-C bond. For this reason, the SW defects are also known as 5-7-7-5 defects. The formation energy which was obtained by equation 3.3 for this defect is of 5.92 eV which is higher than the calculated value of Li *et. al* which is of 4.8 eV [120]. In addition, the formation of this defect from pristine surfaces of graphite and graphene is characterised by a potential energy barrier which is represented in Fig. 18 and it will be discussed below. In Fig 16, the optimised geometry of the SW defect shows some of interesting geometrical parameters. The interatomic distance between two carbon atoms which are represented in red is shortened of 0.145 Å while the two distances between carbons that are also involved in the formation of the pentagon rings are stretched of 0.05 Å with respect to the initial bond length in graphite. Interestingly, the interlayer distance between the two top layers has been found increased. The larger distance is found in correspondence of the two red atoms and is of 0.442 Å. The decreasing of the interlayer distances moving from the two atom in red toward the peripheral ring is consistent with the nature of the formation of SW defect which introduces a curvature into the surface. The surface curvature is better visible in Fig. 17.

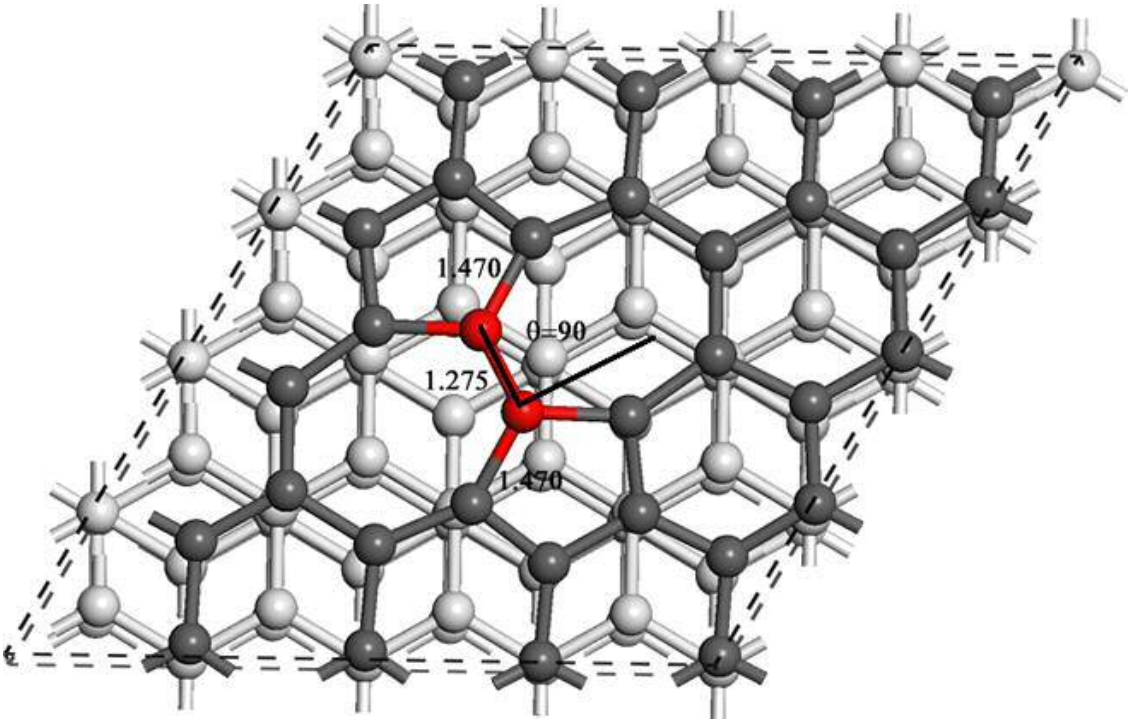

Fig. 16 The planar view of the point defect SW which shows the two pentagons and heptagons.

Fig. 18 reports the energy profile of the graphite surface as function of the rotation of the atom pair in the SW defect. The potential energy surface has been obtained scanning the bond angle by a 2.72 degrees maintaining only the x and y coordinates of one carbon as fixed while all other atoms were allowed to relax. Fig 19 shows the bond distances which have been found on the pristine graphite before the rotation of the atom pair takes place. On the pristine surface the interatomic distance between the atom pair (in red) is of 1.423 Å which is the same bond length which was found between these atoms and their nearest neighbours (in grey). The total energy of the graphite surface has been taken as reference. Thus the potential curve reports the relative energies of the barrier with respect to the pristine surface.

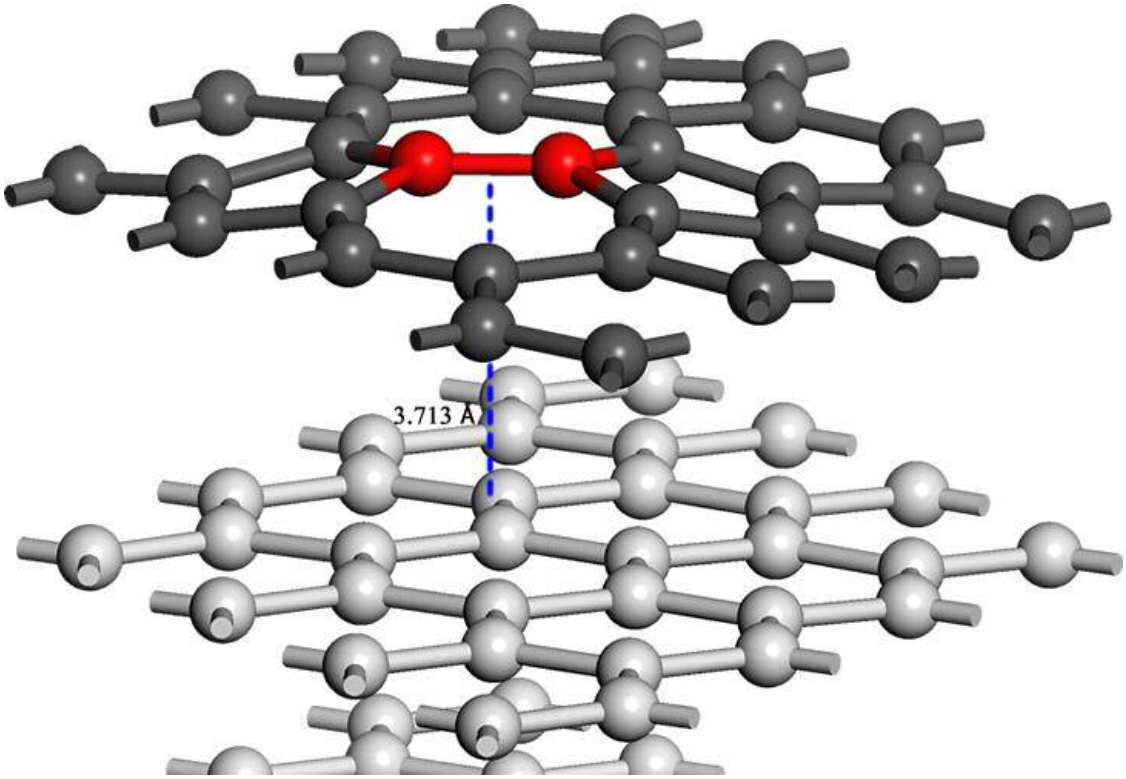

Fig. 17 side view of the SW defect showing the decreasing of the interlayer distance between the top graphitic planes.

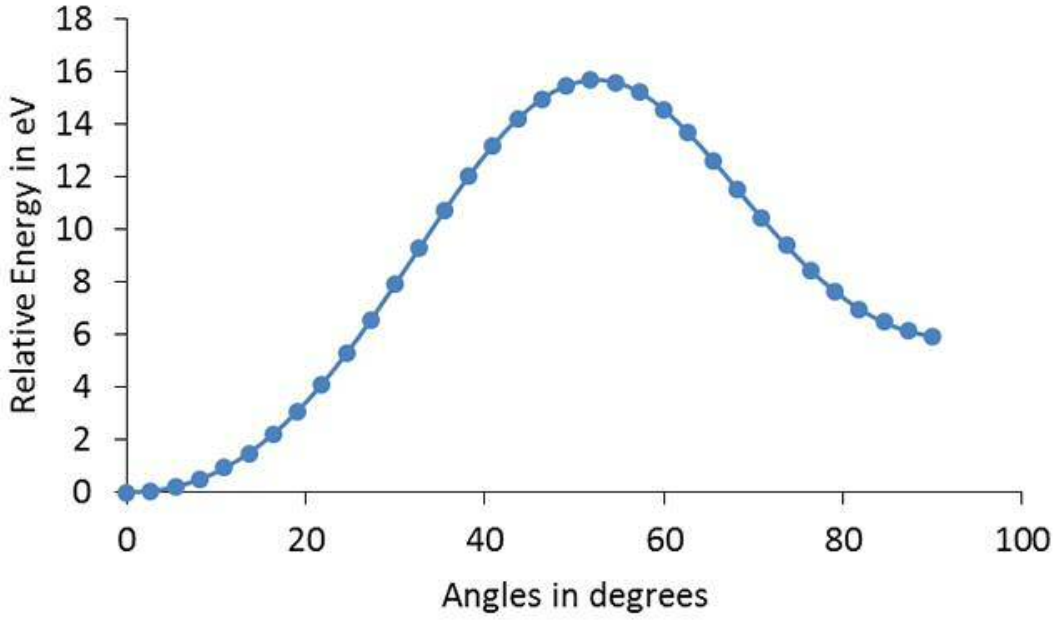

Fig. 18 Potential energy surface as function of rotation angle of the atom pair of the SW defect.

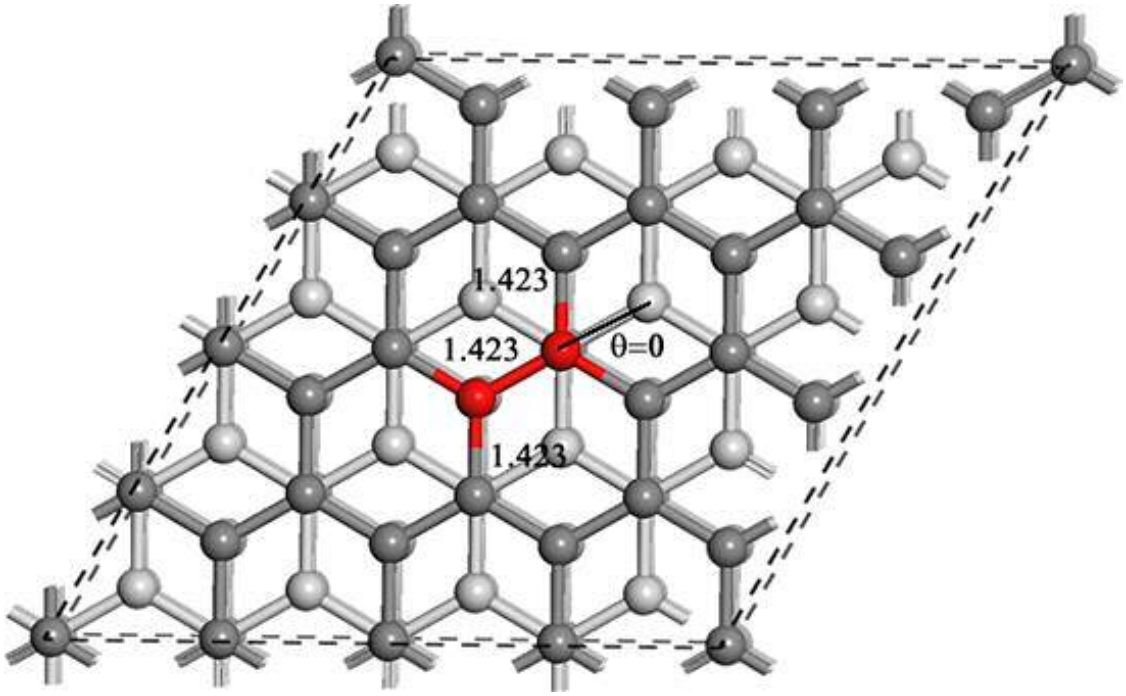

Fig. 19 Pristine graphite surface, selected bond distances in Å and rotation angle of the atom pair in degrees are reported as reference to the discussion. The total energy of this system has been taken as reference.

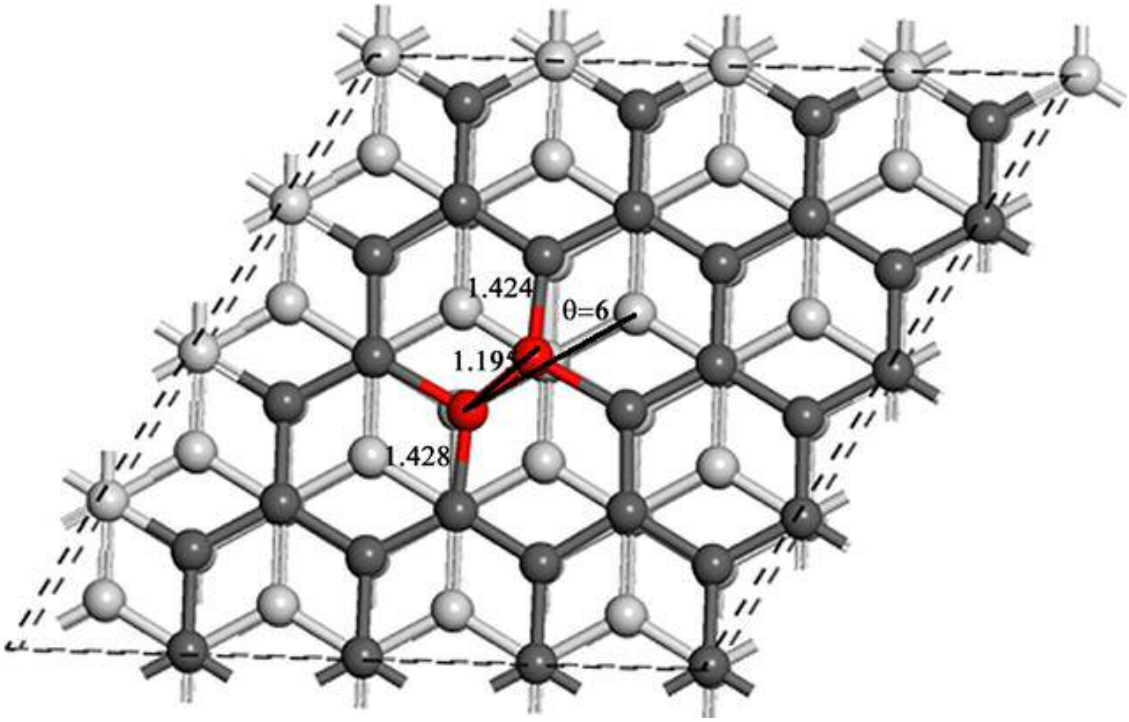

Fig. 19 Pristine graphite surface after a rotation of 6.00 degrees. Selected bond distances in Å and rotation angle of the atom pair in degrees are reported as reference to the discussion.

Fig. 19 show the graphite surface when a rotation of the 6 degrees has took place. The bond length between the atoms in red is notably reduced of 0.228 Å. The interlayer distance is increased by 0.05 Å. This the energy of this system is found 2.20 eV above the reference energy.

Fig. 20 Shows the effects on the surface when the atom pair has been rotated of 46.3 degrees. With respect to the pristine graphite surface, the bond distance of atom pair is shortened of 0.455 Å. The other two bond distances between the atoms in the defect neighbourhood and those forming the atom pair are also found slightly shortened. The interlayer distance is increased of about 0.3 Å. The relative energy for this atom arrangement is found of 14.96 eV.

Fig. 21 shows the atomic arrangement of the pristine graphite surface after a rotation of 51.81 degrees. The interatomic distance of the carbons in the atom pair is now shortened of 0.485 Å. The interlayer distance is found of about 0.47 Å. The relative energy of this system is of 15.67 eV which correspond to the height of the potential energy barrier.

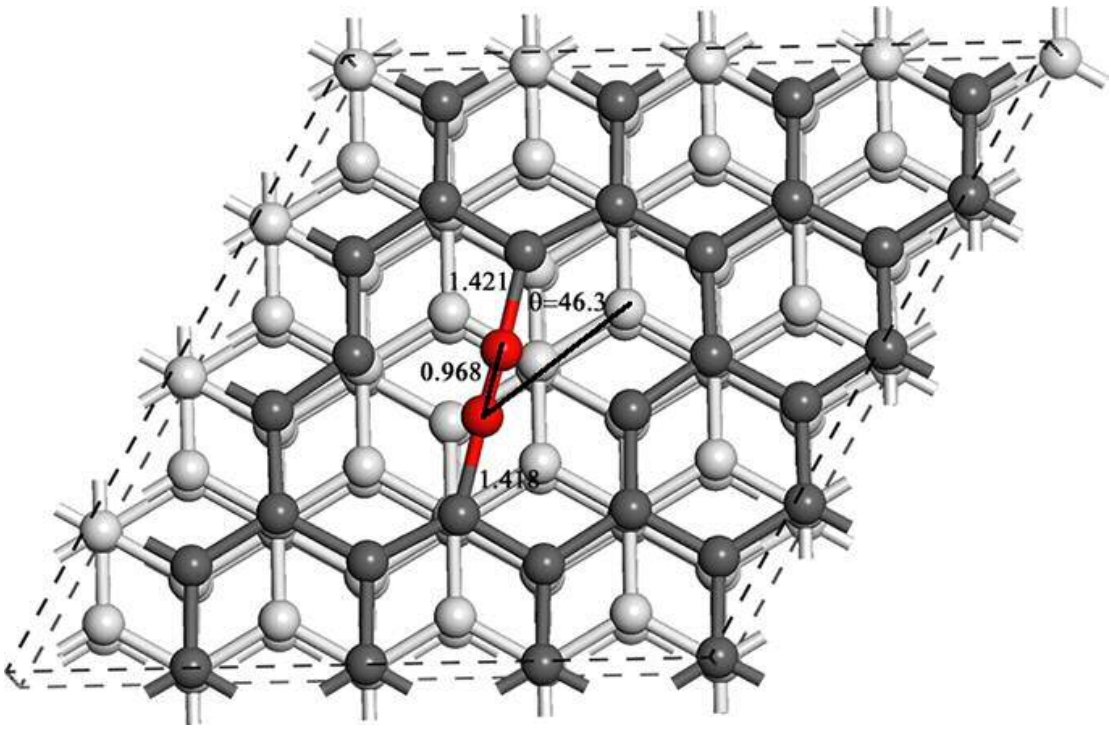

Fig. 20 pristine graphite surface after a rotation of the atom pair of 46.3 degrees.

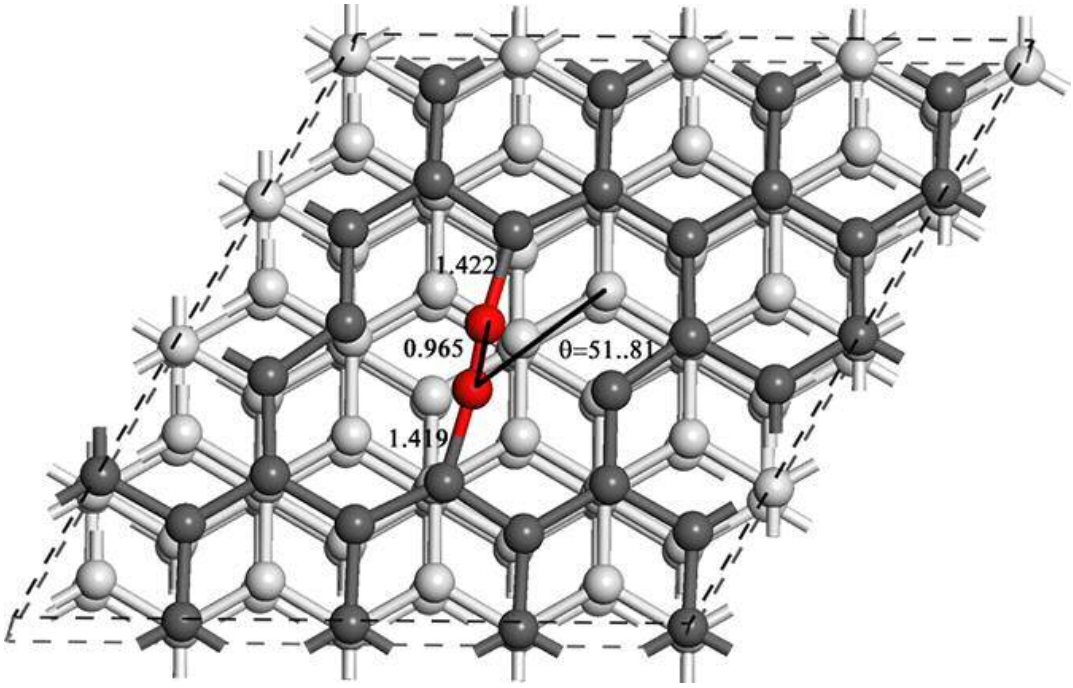

Fig. 21 Atomic arrangement of the pristine graphite surface after a rotation of 51.81 degrees of the atomic pair. The relative energy which is associated to this system corresponds to the top of the energy barrier.

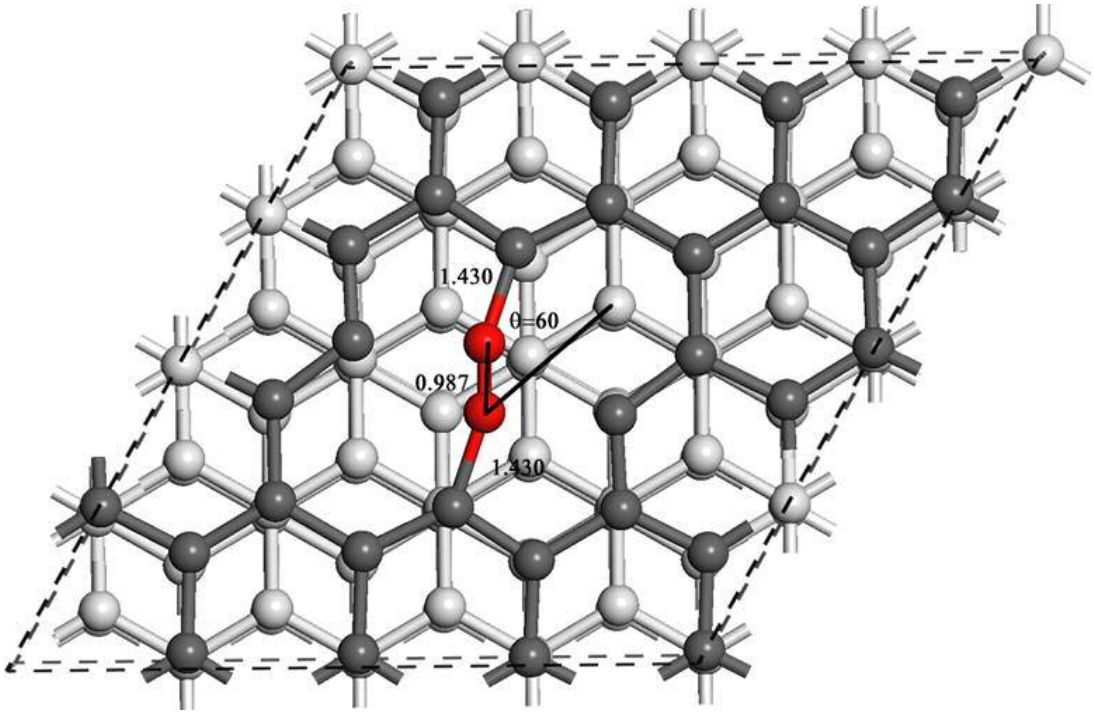

Fig. 22 Atomic arrangement of the pristine graphite surface after that the atom pair has been rotated of 60.0 degrees.

Fig. 22 shows the arrangement of the atoms in the top layer after a rotation of 60.0 degrees. In this arrangement the bond distance between the carbons in the atomic pair is shortened of 0.433 Å whereas the bond length between the atom pair and their nearest neighbours is stretched of about 0.01 Å. The interlayer distance between the top layers is of 0.445 Å. The relative energy of this atomic arrangement of 14.54 eV.

In the SW defect, the pairs of pentagon and heptagon rings create a local electron density, namely, the electrons result more concentrated in the double bounds of the defect rather than participating in the delocalised cloud which spreads on all the atoms of the graphitic plane. Such a localised electron density serves as a reactive centre for adsorption of various atoms, nanoparticles, or molecules [128-129].

3.14 Carbon Adatoms.

Interstitial atoms in the three-dimensional crystals are common defects but in graphite, placing an atom to any in-plain position, for example, at the centre of a hexagon would require prohibitively high energy. When a carbon atom is bond to another carbon belonging to a pristine graphite plane, the hybridisation of the latter is changed. Some degree of sp^3 hybridisation can appear locally so that the new covalent bonds can be formed between the adatom and the underlying atoms in the carbon plane. In this work, the energies of a single additional carbon atom on the graphite surface have been calculated. Since these defects are common on high energy irradiated surfaces and generally are not relevant is catalysis. Thus, in this work, they are just introduced for a validation of the computational method which has been used.

Figure 23, shows the bridge adatom. In this atomic configuration a carbon atoms is adsorbed by two carbon atoms of the graphitic layer.

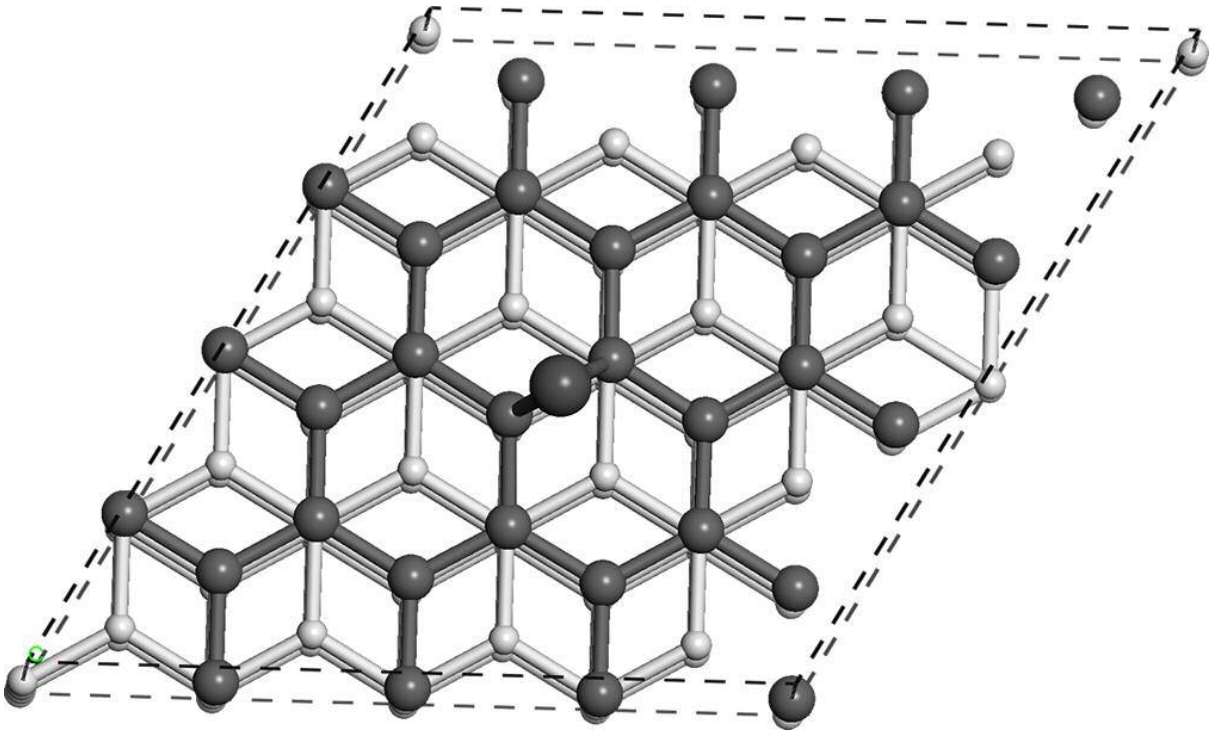

Fig. 23. Atomic arrangement of carbon atom which has been adsorbed in bridge position.

The interatomic distances between the adsorbed atom and the underlying carbons is of 1.662 Å while the bond distance of the two atoms within the layer is of 1.485 Å, namely, this bond is stretched of 0.058 Å with respects the bond length of other carbon within the plane which do not form any bond with the foreign atom. In addition, the two carbons involved in the new bond, extrude from the plane of 0.05 Å. Finally, the bond angle that these two carbons form with the nearest neighbour is widened of 0.5 degrees. These observation support the fact that the two carbons have modified the hybridisation of their orbitals from sp^2 to sp^3. The formation energy was obtained by the equation 3.3 and yield a value of 6.58 eV which shows a good agreement with the GGA values that was calculated by Li of 6.6 eV [120].

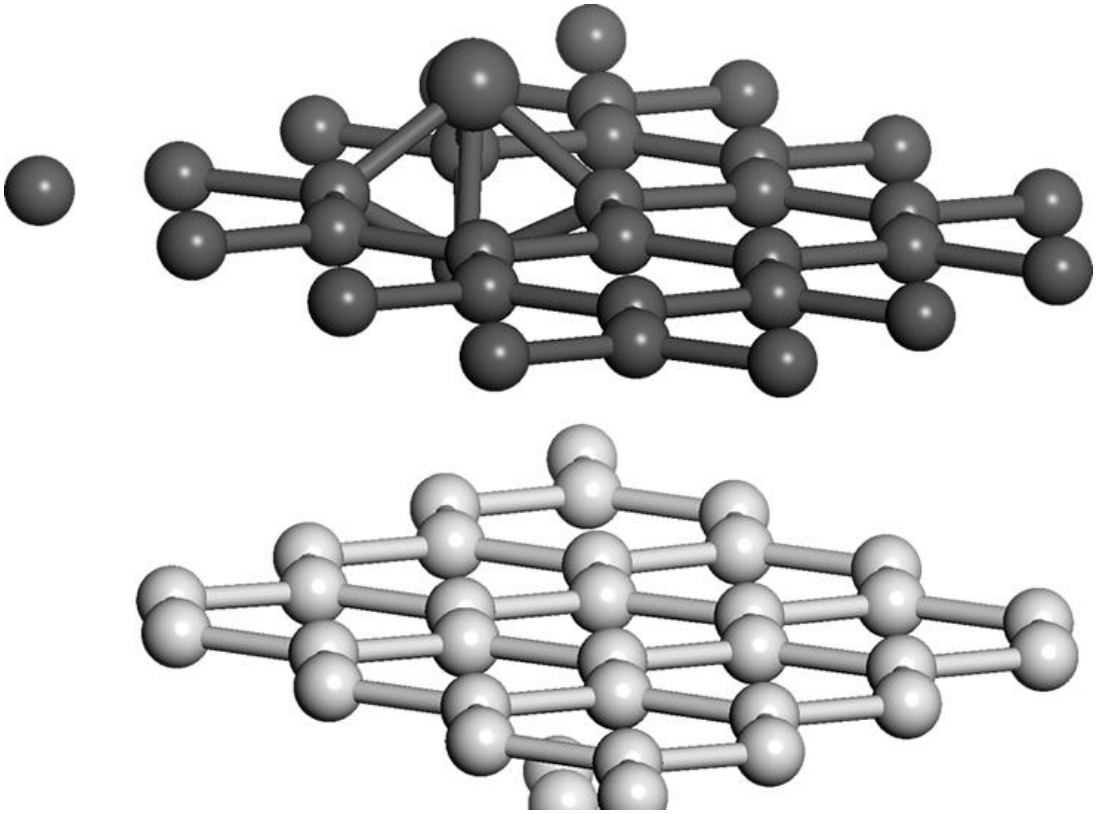

Fig. 24 shows a carbon atom that is adsorbed directly on the top of a plane atom.

The adsorption of a carbon atom in atop position is graphically represented in Fig. 24. The adatom, which lies 1.657 Å above the plane, induces a carbon of the plane to move into the interlayer space. The calculated formation energy for this atomic arrangement is of 7.78 eV which is in good agreement with the formation energy of 7.8 eV which has been reported by Li [120]. The bond distance between the adatom and the underlying carbon is of 1.571 Å while the interatomic distance between the in-plane atoms and the adatom are of 1.593 Å. On the other hand, the interatomic distances between the in-plane atoms and the carbon which lies under the plane are of 1.530 Å.

3.15 Graphite edges

The prismatic surfaces of graphite are also of great interest for adsorption. The morphology of the edges significantly effects the chemical reactivity and also the edge stability. Graphite edges can be configured either as a zig-zag face (10 0) and armchair face (11 1). They are often defined as open or closed depending on whether they are

decorated with fully coordinate bonds or not. In the zig-zag face, carbon atoms at the edges have an unpaired electron which is very active to combine with other reactants. On the other hand, the armchair edges are less reactive because of a triple covalent bond between the two open edge carbon atoms of each edge hexagonal ring. Therefore, the chemically reactive sites in graphitic material have been proposed to be an isolated carbene-type zig-zag carbon atom and carbene-armchair atoms. Energetically, the armchair edges are more stable than zig-zag edges [87]. Thus, the interconversion of zig-zag edges to armchair configuration requires a large amount of energy. Oxygen decorated armchair edges have been considered below in this work to investigate on the interactions between gold nanoparticles and functionalised edges.

3.16 Interaction between water and graphitic surfaces.

The physisorption of water on carbonaceous materials is one of the most largely studied topic. The formation of hydrogen bonds makes the interactions between water molecules much stronger than that between water molecules and carbon atoms. However, at molecular level, understanding this behaviour is quite complicated and far from being complete. The adsorption of water on the graphene surface stimulated the largest interest of several research groups after that Novoselov *et al.* [130] reported that traces of adsorbed water dramatically alter the electron mobility of the material. The interaction of water with graphite was calculated by *Jenness et al.* [131] to be of -0.095 eV but the authors assumed the geometrical structure with one hydrogen atom pointing down toward the hexagonal ring. Moreover, the structure with two hydrogens pointing down is predicted to be more stable with an interaction energy of -0.117 eV which was obtained by Fedorov *et al*. [132]. The investigation on the interaction between a water molecules and graphitic systems stems from the experimental data which clearly show the oxidation of the HOPG surface acid treatment. Thus, to shed light on the role that water molecules play when in contact with graphitic surface, a computational study has been performed considering the pristine graphite surface, the graphite surface presenting the vacancy defects, and finally the SW defect. The adsorption energies of water on the surface were calculated by the following expression:

where, is the total energy of the relaxed water-surface system, is the calculated energy for an isolated water molecule and is the total energy of the relaxed surface. The supercell is large enough to eliminate significant water-water interaction between neighbouring periodic images. Moreover, to avoid a large computational cost, the three graphite layers at the bottom of the slabs were kept fixed while the last two top layers were allowed to relax. The adsorption of a single water molecule on the model substrates is then investigated considering four the possible geometrical arrangements of the water molecules with respect to the basal surface plane. The discussion of adsorption of a water molecule start considering the interaction between water and pristine graphite surface.

3.17 Interaction between water and graphite surface.

For a defect-free graphite surface (GS), the three different adsorption sites can be referred to as atop (A), when the adsorbate is on the top of a carbon atom; bridge (B) when the adsorbate is above the C-C bond and, hollow (H) when the adsorbate is above the centre of hexagons. In this work, the adsorption of a water molecule has been investigated assuming that water molecules adopt one of the following configurations which, here, are referred to as one hydrogen (1H) when one of the hydrogen of the molecule points toward the surface; two hydrogens (2H) when both of the hydrogen atoms are pointing toward the surface; flat (F) when the molecular plane is parallel to surface plane and, finally oxygen (V) when the oxygen atom points toward the surface. In Figure 25 shows the optimised geometry of the free standing reactants namely, the pristine graphite surface and the water molecule.

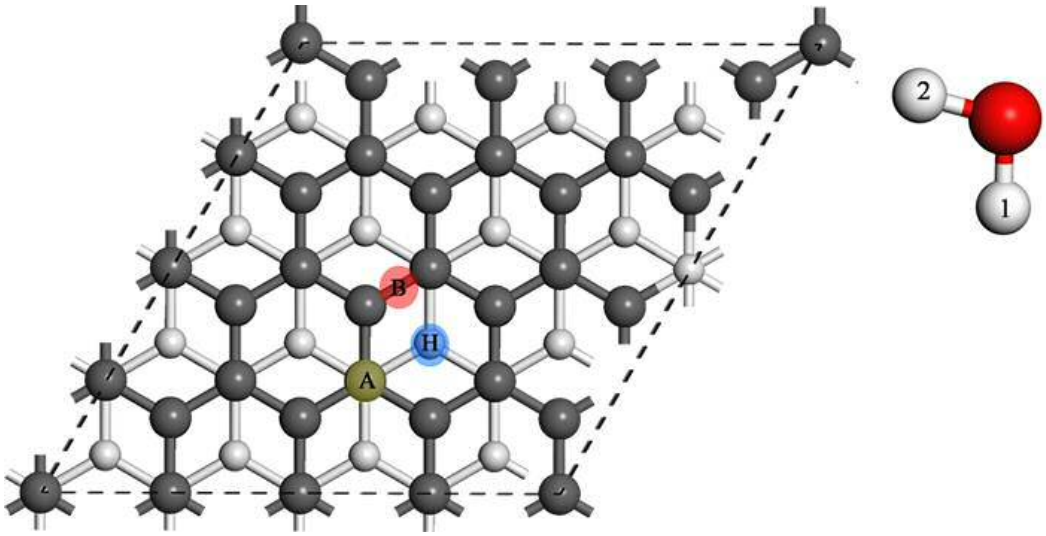

Fig. 25 – On the left, free standing graphite surface. The adsorption sites are (A) for atop, (B) for bridge and, (H) for hollow. On the right side, the free standing water molecule. In the text, 1H is referred to the hydrogen pointing toward the surface. Some geometrical parameters are collected in Table 3.1.

	Interlayer distance C-C (Å)	In-plane C-C dist. (Å)	C-H dist. (Å)	O-H_1 dist. (Å)	O-H_2 (Å)	H-O-H Bond ang. (deg.)	E_{ads}
Free Graphite	3.194	1.420	-	-	-	-	-
Free water	-	-	-	0.972	0.972	104.66	-

Tab. 3.1 Selected geometrical parameters of the optimised free standing reactants: pristine graphite surface and water molecule. These parameter will be used as reference for the following discussion.

Fig. 26 collects the optimised geometries of a water molecule assuming the 1H geometrical structure while Tab 3.2 collects the results which were obtained from the optimised arrangements of the atoms.

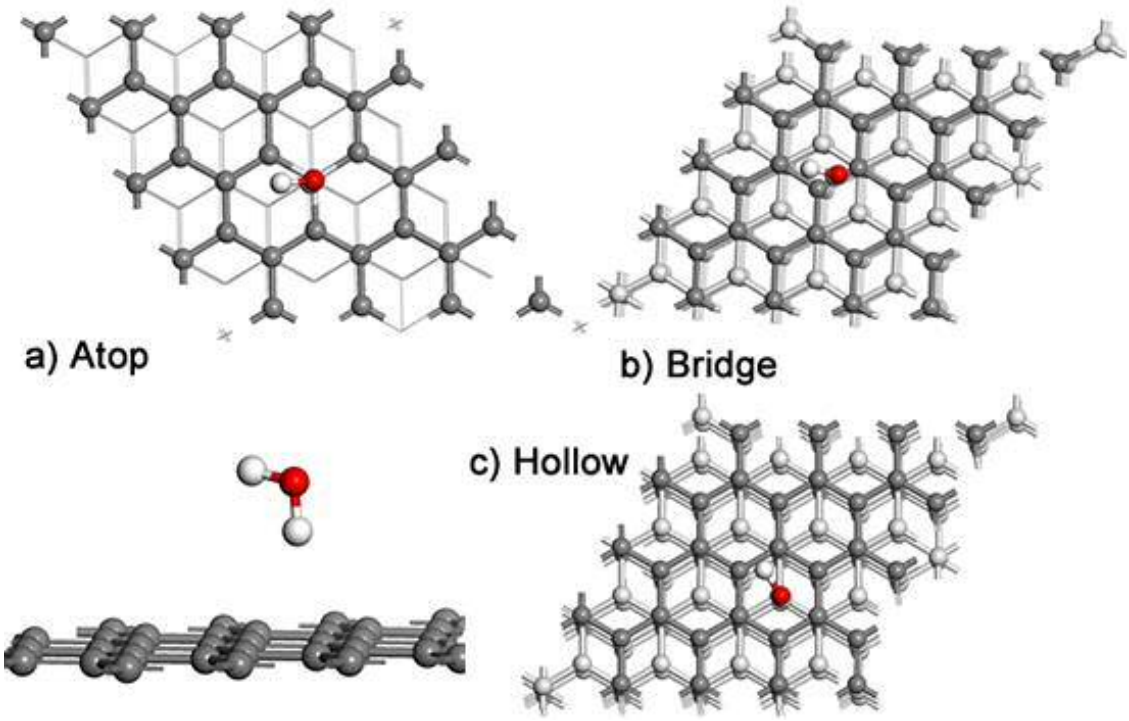

Fig. 26 Top view of the water molecules adsorbed on a pristine graphite surface: a) in atop position, b) in bridge position and c) hollow position.

	Interlayer distance C-C (Å)	In-plane C-C dist. (Å)	C-H dist. (Å)	$O\text{-}H_1$ dist. (Å)	$O\text{-}H_2$ (Å)	H-O-H Bond ang. (deg.)	E_{ads} (eV)
Free Graphite	3.194	1.420	-	-	-	-	-
Free water	-	-	-	0.972	0.972	104.66	-
1H-A	3.280	1.423	2.450	0.973	0.972	104.53	-0.167
1H-B	3.269	1.422	2.490	0.974	0.972	104.57	-0.159
1H-H	3.278	1.420	2.656	0.974	0.974	105.53	-0.145

Tab. 3.2 - Some representative data which are relevant to the description of the system consisting in a water molecule which is adsorbed on the pristine graphite surface. These data refer to a water molecule with one hydrogen pointing toward the surface (1H) which is adsorbed in atop (A), bridge (B) and (H) sites.

When the water molecule is physisorbed in A position, the system releases 167 meV. With respect to the free standing reactants, the interlayer distance is increased of 0.086 Å, the bond length between the interacting carbon and its nearest neighbour is of 1.423 Å. The interatomic distance between the surface carbon and the hydrogen of water is 0.973 Å while, the bond length between the hydrogen 1 and oxygen is stretched of 0.001 Å. Finally, the bond angle is reduced of 0.13 degrees.

When the water molecule is adsorbed in B position, the energy that the system releases of 159 meV. The interlayer distance results to be increased of 0.075 Å while the bond length between the two carbons near the hydrogen 1 is stretched of 0.002 Å. The interatomic distance between the hydrogen and its nearest surface carbon is of 2.490 Å. In this atomic arrangement the H1-O bond length is stretched of 0.002 Å while the bond angle is reduced of 0.13 degrees. Finally, when the water molecule is adsorbed in H position the amount of released energy is of 145 meV. The interlayer distance is increased of 0.084 Å while the C-C bond lengths, in the neighbourhood of water, are not modified. The interatomic distance between hydrogen 1 and the nearest carbon atom is 2.656 Å. The bond distance between hydrogen 1 and oxygen is stretched of 0.002 Å while the bond angle in water is decrease of 0.13 degrees.

In conclusion, the interaction of a water molecule having the 1H geometry occurs in three possible adsorption sites A, B, H and the stability order which is suggested by our calculation is B, A, H.

Fig. 27 shows the atomic arrangements of a water molecule which is adsorbed on the graphite surface. In this case, both hydrogens of water point toward the surface (2H). Tab. 3.3 collects some geometrical parameters of the optimised arrangement of the atoms.

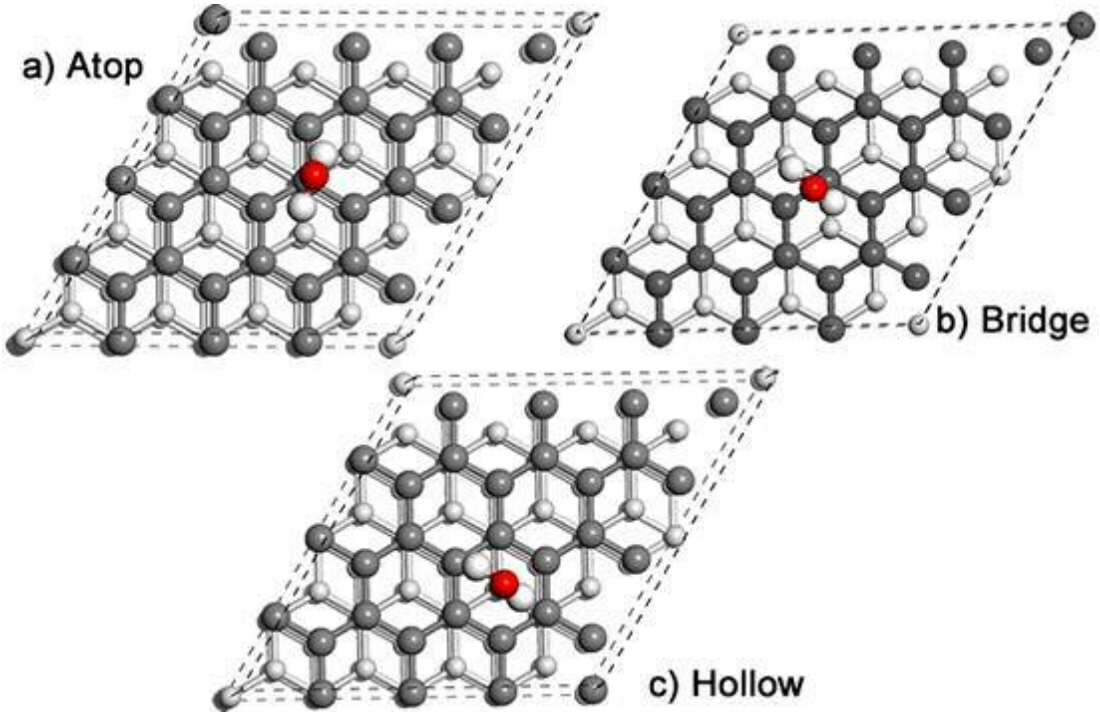

Fig. 27 Optimised geometry of the water molecule with two hydrogen pointing toward the graphite surface. Geometrical parameters of these structures are collected in Tab. 3.3.

	Interlayer distance C-C (Å)	In-plane C-C dist. (Å)	C-H dist. (Å)	O-H_1 dist. (Å)	O-H_2 (Å)	H-O-H Bond ang. (deg.)	E_{ads} (eV)
Free Graphite	3.194	1.420	-	-	-	-	-
Free water	-	-	-	0.972	0.972	104.66	-
2H-A	3.268	1.421	5.065	0.972	0.972	104.75	-0.054
2H-B	3.269	1.421	2.645	0.974	0.973	103.58	-0.170
2H-H	3.215	1.421	2.584	0.974	0.972	103.279	-0.168

Tab. 3.3 Selected geometrical parameter for the water molecule with two hydrogen pointing toward the graphite surface.

The geometry of a water molecule with two hydrogens pointing toward the surface is indicated with 2H. The 2H was initially placed at a short distance with respect the carbon atom but, after geometry optimisation, it was found in B position. The optimisation was repeated and the 2H was placed at larger distances from the carbon atom but, at equilibrium, the water molecule is found in different geometrical arrangements such as flat, tilted in the 1H geometry, and so on. The optimisation which returned the water molecule with the desired orientation of the hydrogen atoms, places such a molecule at more than 5 Å above the surface. Since, the geometry optimisation of 2H in bridge position led the same result, it has been assumed a relative minimum of potential energy exists in correspondence of the B position for the 2H molecule which is initially placed in both atop and bridge positions. As above, the geometrical parameters are compared with the geometrical parameters of the free standing reactants, these parameter are collected in Tab. 3.1. When the 2H molecule is in A position, Fig 27 (a), the system releases an amount of energy of 54 meV, the interlayer distance is increased of 0.074 Å and the C-C in-plane bond also is stretched of 0.001 Å. The C-H interatomic distance is of 5.065 Å and the O-H bond distances are the same of those which were found in the isolated water molecule. Finally, the bond angle is broadened of 0.09 degrees. The optimised structure of the water molecule in the 2H orientation is represented in Fig. 27 b), the adsorption of the 2H molecule at B site is an exothermic process and 170 meV are released. With respect to the free-standing surface, the interlayer distance is augmented of 0.075 Å. The planar C-C bond length between the two atoms nearest the 2H molecule is stretched of 0.001 Å and the interatomic distance between hydrogen and its nearest neighbour carbon atom is of 2.645 Å. The bond distance between H_1-O is stretched of 0.002 Å while the O-H_2 bond length is found to be the same of that in the free standing water molecule. The bond angle between H_1-O-H_2 is decreased of 1.08 degrees. Finally, the adsorption of 2H molecule in H position is exothermic of 168 meV. The interlayer distance is increased of 0.021 Å and the in-plane C-C bond lengths are stretched of 0.001 Å. The interatomic distance between the 2H and the graphitic plane is taken considering the nearest neighbour carbon atom and is of 2.584 Å. The H_1-O bond length is stretched of 0.002 Å whereas the H_2-O bond length is unchanged. Finally, the bond angle of water results decreased of 1.381 degrees. In conclusion the order of stability of the water molecule in 2H geometry is the following: B, H, A.

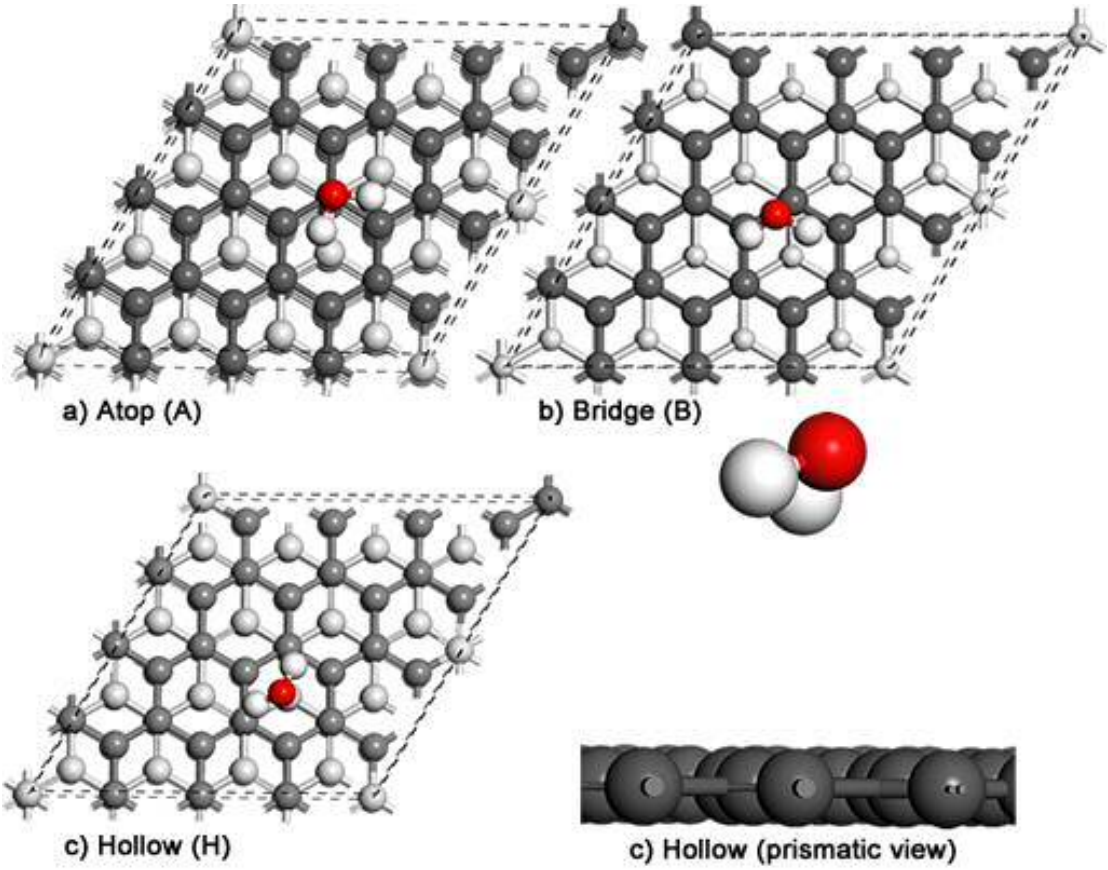

Fig. 28. Optimised geometries of a water molecule having its molecular plane parallel to that of the surface planes of graphite. In this work, a water molecule in this geometrical arrangement has been referred as to flat (F) and in the picture, one can see the equilibrium structures of F in a) atop (A) position, b) bridge position (B) and c) Hollow position (H).

	Interlayer distance C-C (Å)	In-plane C-C dist. (Å)	C-O dist. (Å)	O-H_1 dist. (Å)	O-H_2 (Å)	H-O-H Bond ang. (deg.)	E_{ads} (eV)
Free Graphite	3.194	1.420	-	-	-	-	-
Free water	-	-	-	0.972	0.972	104.66	-
F-A	3.322	1.421	3.410	0.972	0.972	104.216	-0.103

F-B	3.324	1.420	3.439	0.972	0.973	104.212	-0.110
F-H	3.286	1.421	2.965	0.972	0.974	103.95	-0.148

Tab 3.4 Selected geometrical parameters of optimised geometries of free standing reactants and a water molecule which is adsorbed on pristine graphite. The molecular plane of water is parallel to the planar surface and the molecule is this geometry is referred to as flat (F).

The discussion of the equilibrium atom arrangements resulting when a water molecule is adsorbed on the graphite surface in 1H and 2H geometries was presented in a certain detail. This permitted to compare the results which have been obtained in this work with those, previously, published by Jenness *et. al.* [132] and Freitas *et al.* [133]. Jenness reported an interaction energy for the water-graphite system of -95 meV assuming the 1H geometry. On the other hand, Freitas found a more stable structure when a water molecule is in 2H geometry. The results obtained in this work support those of Freitas, in fact, the interaction of a 2H is more stable than the interaction of a 1H of 3 meV.

In the following discussions of the water-graphite interaction, for the sake of brevity, only the geometrical parameters of most stable structure will be presented in detail. As Tab. 3.4 reports, the lowest calculated adsorption energy is of -148 meV and is found for F in H site. As can been seen from the prismatic view of Fig. 28, in this optimised atomic arrangement, the water molecular plane is not parallel to graphitic planes but it results bended. The two hydrogen atoms are not perpendicular to the graphitic plane and so, this structure cannot be considered as a 2H. With respect to the isolated reactants, the interlayer distance is increased of 0.092 Å, the in-plane C-C bond in proximity of the water molecule is stretched of 0.001 Å and bond distance between the water oxygen and nearest carbon atom is of 2.965 Å. In water, the OH_2 bond length is stretched of 0.002 Å. Finally, the bond angle is enlarged of 0.71 degrees.

The equilibrium structure of water in the horizontal geometry in the hollow site is 22 meV less stable than the equilibrium structure of 2H which was adsorbed in the bridge site.

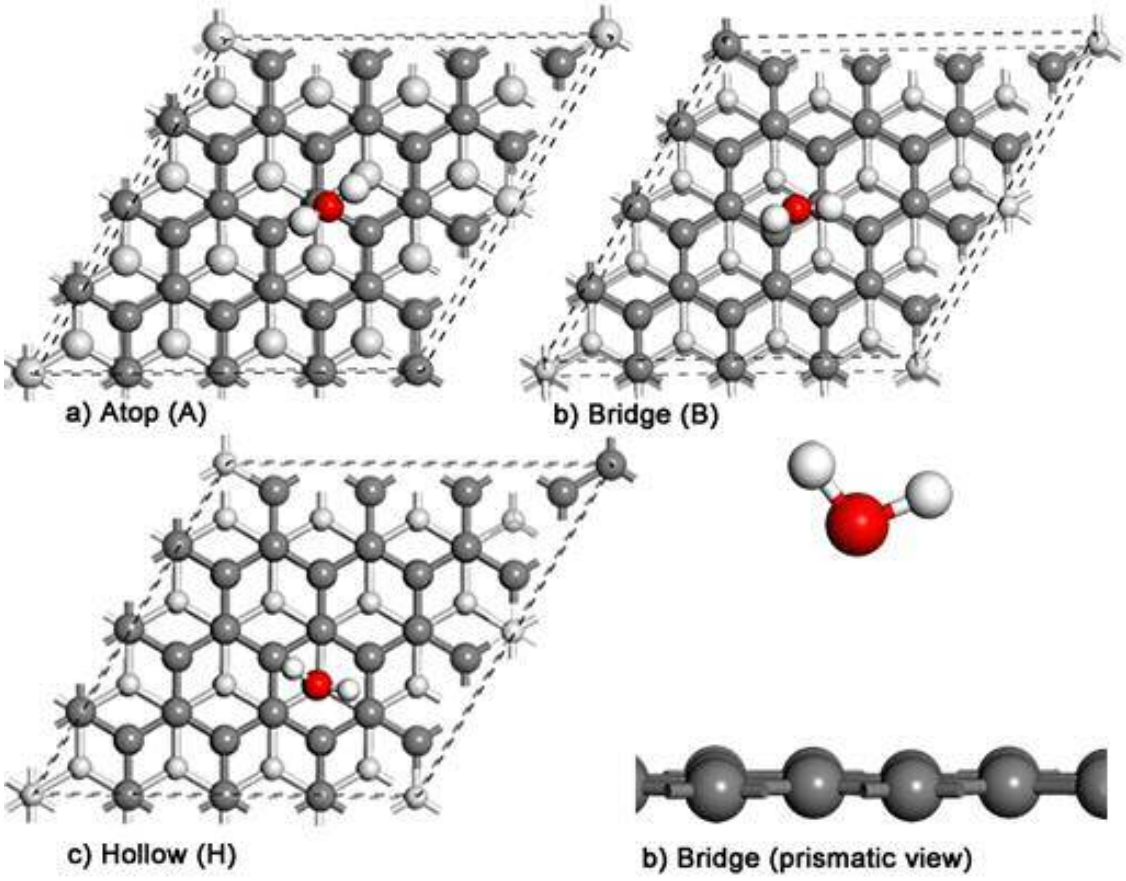

Fig. 29 Equilibrium geometries of a water molecule that is adsorbed on the graphite surface. The molecule is placed above the surface with the hydrogen atom pointing toward the surface. Thus, the water molecule in such geometrical configuration is referred to as V structure.

	Interlayer distance C-C (Å)	In-plane C-C dist. (Å)	C-O dist. (Å)	$O\text{-}H_1$ dist. (Å)	$O\text{-}H_2$ (Å)	H-O-H Bond ang. (deg.)	E_{ads} (eV)
Isolated Graphite	3.194	1.420	-	-	-	-	-
Free water	-	-	-	0.972	0.972	104.66	-
V-A	3.299	1.423	3.295	0.974	0.972	105.32	-0.099

V-B	3.275	1.420	3.314	0.973	0.972	105.27	-0.104
V-H	3.279	1.420	3.321	0.972	0.972	103.95	-0.097

Tab 3.5 Selected geometrical parameter of the equilibrium structures consisting in a water molecule which interacts with the pristine surface by its oxygen atom.

When a water molecule assumes the V geometry and is adsorbed into the bridge site, the system releases an amount of energy of 104 meV. In this atomic arrangement, the interlayer distance is increased of 0.081 Å and the interatomic distance between the nearest carbon and the oxygen is of 3.314 Å. The OH_1 bond length is stretched of 0.001 Å and the bond angle is widened of 0.61 degrees.

Since the presence of large vacancy defects as well as step edges allows water molecule to diffuse into the graphite interlayer space, in this work, the effects of water which is intercalated between the graphite layers has been investigated.

As above, the water molecule can be placed in between the layers in one of the four orientations which in this work are referred to as 1H for water molecule with one hydrogen atom pointing toward the surface; 2H when both hydrogens of water are pointing toward the graphitic planes; F, if the molecular plane is parallel to those of the surface and, finally, when water oxygen points toward the surface, the molecule is referred to as V.

Geometry optimisations of all these structures yield only atomic arrangements having water in F orientation. In addition, the presence of intercalated water induces distortions into the surface which show the presence of curvatures.

In the following part of this paragraph only the most stable arrangements of the intercalated water molecule will be discussed. They are represented in Fig. 30 while Tab. 3.5 collects some selected geometrical parameters.

When a water molecule is intercalated in between the first two graphite layers in atop position, the endothermal process requires 1.377 eV. The interlayer distance was measured in the points where the curvatures are more pronounced, namely, in proximity of the water molecule. The largest distance between the layers is of 5.350 Å, namely

2.156 Å larger than the equilibrium separation of the layers in the isolated surface. The C-C bond length is found stretched only of 0.001 Å and the interatomic distance between the hydrogen atom and its nearest carbon is 2.564 Å.

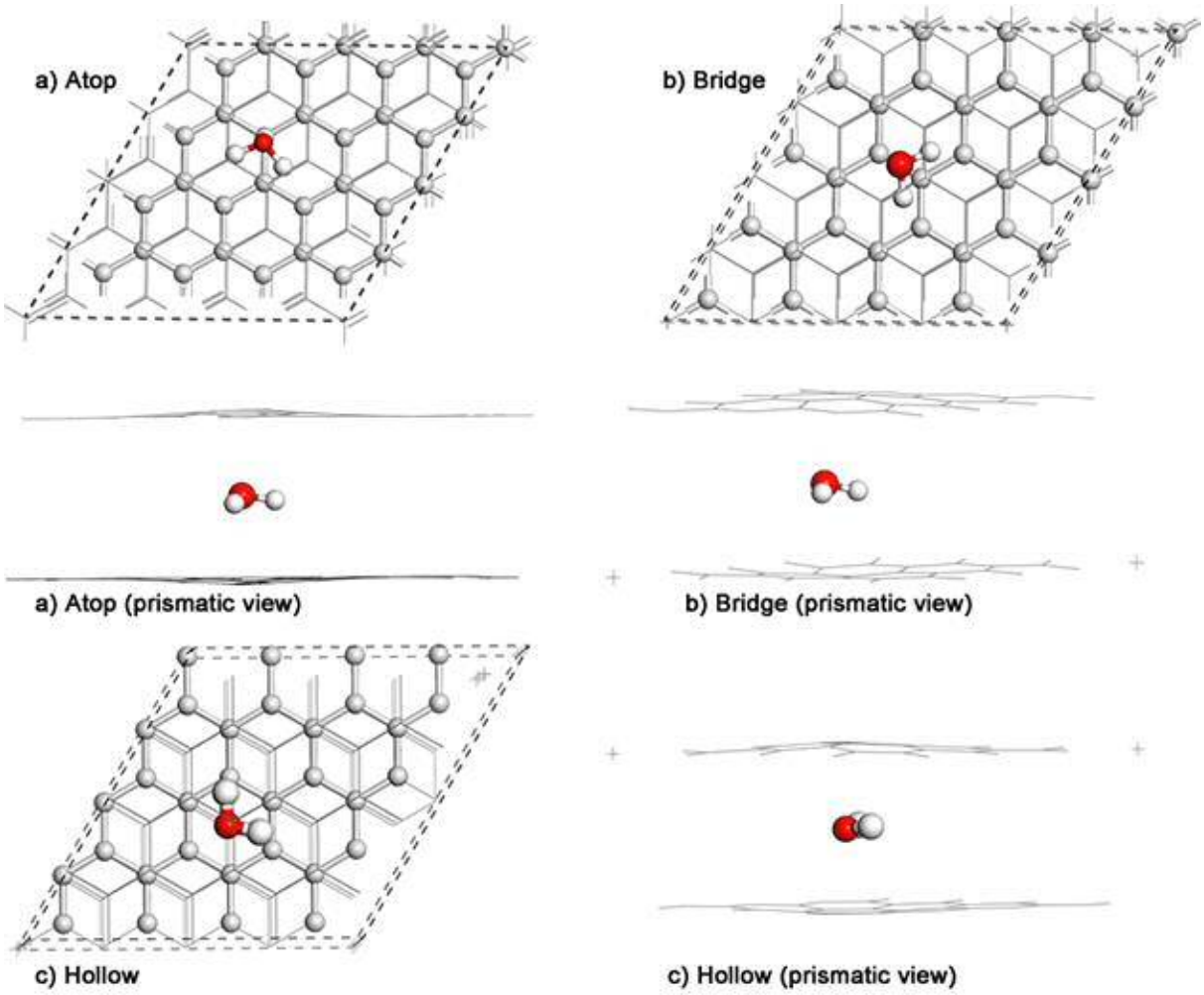

Fig. 30 Optimised atomic arrangements of a water molecule which is intercalated into the first two graphite layers in the following adsorption sites: a) atop position (A), b) bridge position (B) and c) hollow position (H). Prismatic views of the structure are reported to show the curvature of the surfaces. In order to facilitate the visualisation of the curvatures, the atomic layers are represented by lines.

In the water molecule, the O-H_2 bond length is stretched of 0.001 Å while the bond angle is decreased of 0.677 degrees.

	Interlayer distance C-C (Å)	In-plane C-C dist. (Å)	C-H_1 dist. (Å)	O-H_1 dist. (Å)	O-H_2 (Å)	H-O-H Bond ang. (deg.)	E_{ads} (eV)
Isolated Graphite	3.194	1.420	-	-	-	-	-
Free water	-	-	-	0.972	0.972	104.66	-
F-A	5.350	1.421	2.564	0.972	0.973	103.983	1.377
F-B	5.362	1.420	2.571	0.972	0.972	103.958	1.379
F-H	5.421	1.420	2.621	0.972	0.973	104.125	1.405

Tab 3.6 Selected geometrical parameters of an intercalated water molecule. These data are referred to the atomic arrangement which have been shown in Fig. 30.

Interaction between water and graphite has been investigated not only because it is present in the process of acid treatment of the substrate and it is present in innumerable industrial processes but also because it is a prototypical hydrogen-bond system. The water molecule is small enough to allow theoretical investigations. The process of intercalation of water between the graphitic planes is still unclear. The computational results of this work agree with the hydrophobic nature of graphite surface. In fact, the water molecule has been found weakly physisorbed on the surface in an exothermal process involving 170 meV. These results show a good agreement with those of Jenness [131] and Fedorov [132]. These authors found that when the water molecule is physisorbed on the surface, the minimum energy is found when one hydrogen points toward the surface and Jenness has found that this atomic arrangement is exothermic of 95 meV. In this work for the 1H orientation, the process releases 167 meV. Fedorov calculated an exothermic process involving 117 meV for the water molecule two hydrogens pointing toward the surface. For the same process, in this work, it has been obtained an exothermic process of 170 meV.

It is noteworthy, when the molecule is close to surface shows a strong preference to bend hydrogens down rather than through the lone pair electrons on the oxygen. The

optimisation results have also shown that when the water molecule is placed with the molecular plane parallel to the surface or with the oxygen atom pointing toward the surface, the molecule flips over to orient hydrogens toward carbons. However, after several attempts, it has been found that the orientations in which the water molecule does not point the hydrogen toward the surface correspond to higher energies. In addition, when water is placed above the surface, it moves away from the surface from at least 2.5 Å leaving behind a perfectly flat surface. Whilst, above the surface, the water molecule is clearly physisorbed, the situation is more complicated to be described when it is placed between two graphene planes. Although many attempts were done to obtain an optimised system where water orients hydrogen or oxygen toward both the two carbonic planes, namely, when the molecular plane of water and the graphitic planes are each other perpendicular, the only geometrical arrangement which was obtained at the equilibrium was the flat (F) geometry. Surprisingly, the presence of intercalated molecules dramatically modifies the geometry of the two nearest layers which are no more perfectly flat but present some curvatures in correspondence of the water molecule. The interatomic distance between the last two layers is largely increased whereas the interlayer distance between the bottom layer and its neighbour (third and fourth layer) decreases and it has been found of 3.07 Å in the most stable structure. In good agreement with the experimental results, the presence of intercalated compounds can modify the surface morphology. Thus, by a computational investigation, it is possible to support the hypothesis that the presence of the rising features, which were experimentally detected by the AFM (Fig. 1 and 4) [87], are generated by intercalated compounds. The intercalation of a water molecule is an endothermic process and requires an amount of energy of 1.377 eV and computationally the intercalation is accompanied by a large increasing of the inter-planes distance which, in this work, has been estimated to be larger than 2.156 Å.

3.18 Interaction between water and defected graphite: monovacancy (V_1).

The behaviour of a water molecule on a defected graphite surface was also investigated to understand which role is played by the unsaturated carbon atoms. As above, four possible orientations of the hydrogen atoms were considered, namely, 1H, 2H, V and F. In a mono-vacancy defect, V_1, the removal of a carbon atom generates another adsorption

site which here is referred to vacancy and indicated by the abbreviation Vac. The other possible adsorption sites on the defected surface are atop (A), bridge (B) and Hollow (H). Moreover, since the α-V_1 is more stable than β-V_1, it is described in the following discussion.

In Fig. 31, the optimised geometries of a α-V_1 and a water molecule are represented. As above the free standing reactants are used as reference to calculate the energy of the interacting systems. Tab. 3.7 collects some selected geometrical parameters which are used for comparison.

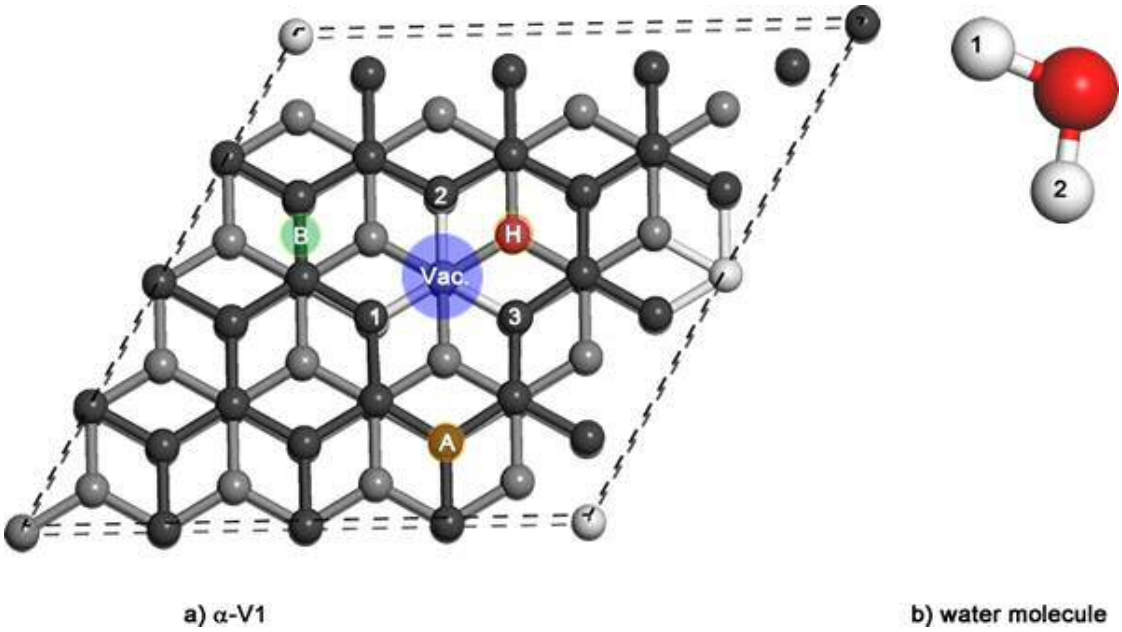

Fig. 31 Top view of the optimised atomic arrangement of a monovacancy on graphite surface. In the figure are also indicated the four adsorption site which during the discussion will be referred to as a) atop (A), b) bridge (B) c) hollow (H) and finally, vacancy (Vac.)

	Interlayer distance C-C (Å)	In-plane C_1-C_2 dist. (Å)	C-H_1 dist. (Å)	O-H_1 dist. (Å)	O-H_2 (Å)	H-O-H Bond ang. (deg.)	E_{ads} (eV)
Isolated V_1	3.291	2.517	-	-	-	-	-
Free water	-	-	-	0.972	0.972	104.66	-
1H-A	3.286	2.536	3.125	0.974	0.972	104.86	-0.178
1H-B	3.291	2.541	3.248	0.972	0.972	104.25	-0.145
1H-H	3.280	2.537	3.246	0.973	0.973	104.34	-0.150
1H-Vac	3.276	2.538	2.099	0.974	0.972	105.03	-0.214
2H-A	3.275	2.540	3.295	0.972	0.972	104.16	-0.142
2H-B	3.277	2.542	3.262	0.972	0.973	104.38	-0.098
2H-H	3.278	2.539	3.366	0.972	0.972	104.25	-0.095
2H-Vac	3.281	2.538	3.312	0.973	0.973	104.46	-0.102
F-A	3.279	2.534	3.325	0.972	0.972	104.24	-0.086
F-B	3.290	2.537	3.258	0.973	0.972	104.13	-0.089
F-H	3.286	2.535	3.356	0.972	0.972	104.25	-0.092
F-Vac	3.288	2.542	3.342	0.972	0.973	104.23	-0.085
V-A	3.287	2.539	3.358	0.972	0.972	104.49	-0.086
V-B	3.279	2.536	3.387	0.973	0.972	104.48	-0.089
V-H	3.281	2.533	3.291	0.972	0.973	104.44	-0.094
V-Vac	3.276	2.540	3.529	0.972	0.972	104.45	-0.082

Tab. 3.7 Selected parameters of the optimised geometries of a water molecules physisorbed on the graphite surface containing a monovacancy V_1.

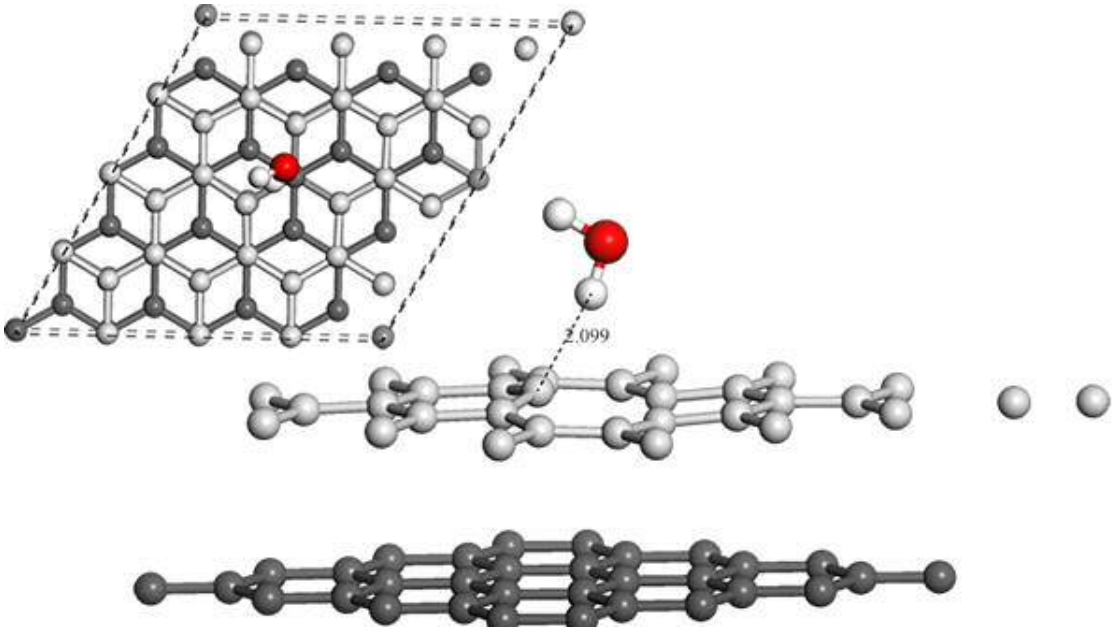

Fig. 32 Planar view and prismatic view of a water molecule strongly physisorbed at a vacancy. From the planar view, it is possible to see that the interacting carbon extrudes from the graphitic plane.

The process of physisorption of a water molecule in correspondence of the vacancy is exothermic of ~214 meV. If this adsorption energy is compared with that obtained for the most stable water adsorption on graphite which was of 170 meV, it is possible to say that water is strongly physisorbed at the vacancy. This is due to the interaction with unsaturated bonds at defect. The interaction between the hydrogen and carbon can be considered quite strong as the carbon atom is pulled out of the surface plane by ~0.52 Å. However, such an interaction is not strong enough to modify the triplet state of the dangling bond at the vacancy which remains spin-polarised.

Thus, if the difference in energy between water-pristine graphite and water-defected graphited are compared, one can aspect that, at ambient conditions, a water molecule may easily move on the graphite surface until it found a vacancy where it gets strongly physisorbed. The binding energy at the vacancy site is still very low if it is compared with a hydrogen bond, but this site could provide a nucleus for the growth of ice.

Water sits at ~3.07Å above the graphitic plane, the interatomic distance between the hydrogen and the carbon atom is only of 2.099Å. The interlayer distance of the defected

surface is increased of 0.015Å with respect the free standing defected surface. The C_1-C_2 bond length is stretched of 0.021Å. The bond angle in water is widened of 0.37 Å and the bond length O-H_1 is stretched of 0.02Å.

During the geometry of optimisation it was noted that some water molecules were chemisorbed when they were placed too close to the undercoordinated atoms. The chemisorption of water molecules on this vacancy was not investigated.

To study the dissociation path, the nudged elastic band (NEB) method was employed. Starting at the physisorption minimum, the product was reached by a path of seven images. The problem that was experienced using the NEB method to find the activation barriers is due to the horizontal movements of the last two layers which cannot be kept fixed. For this reason the energy of the system never converged.

The chemisorption of water at vacancy carbons was frequently observed at equilibrium geometries when the molecule of the adsorbate was placed too close to the undercoordinated carbons. Six different atom arrangements are possible when water is chemisorbed at defect vacancy.

These arrangement differ each other by the position of two hydrogens which can be placed both above or below the graphitic plane or alternatively one hydrogen is placed above the plane whereas the other one is below the plane. In the same way also oxygen can be found above and below the graphitic plane.

The presence of oxygen below the graphitic plane was obtained when the water molecule was placed in the interlayer space. In fact, in this situation the system is more stable if water is chemisorbed rather than physisorbed.

Fig. 33 shows the optimised geometries of a chemisorbed water molecule at monovacancy site.

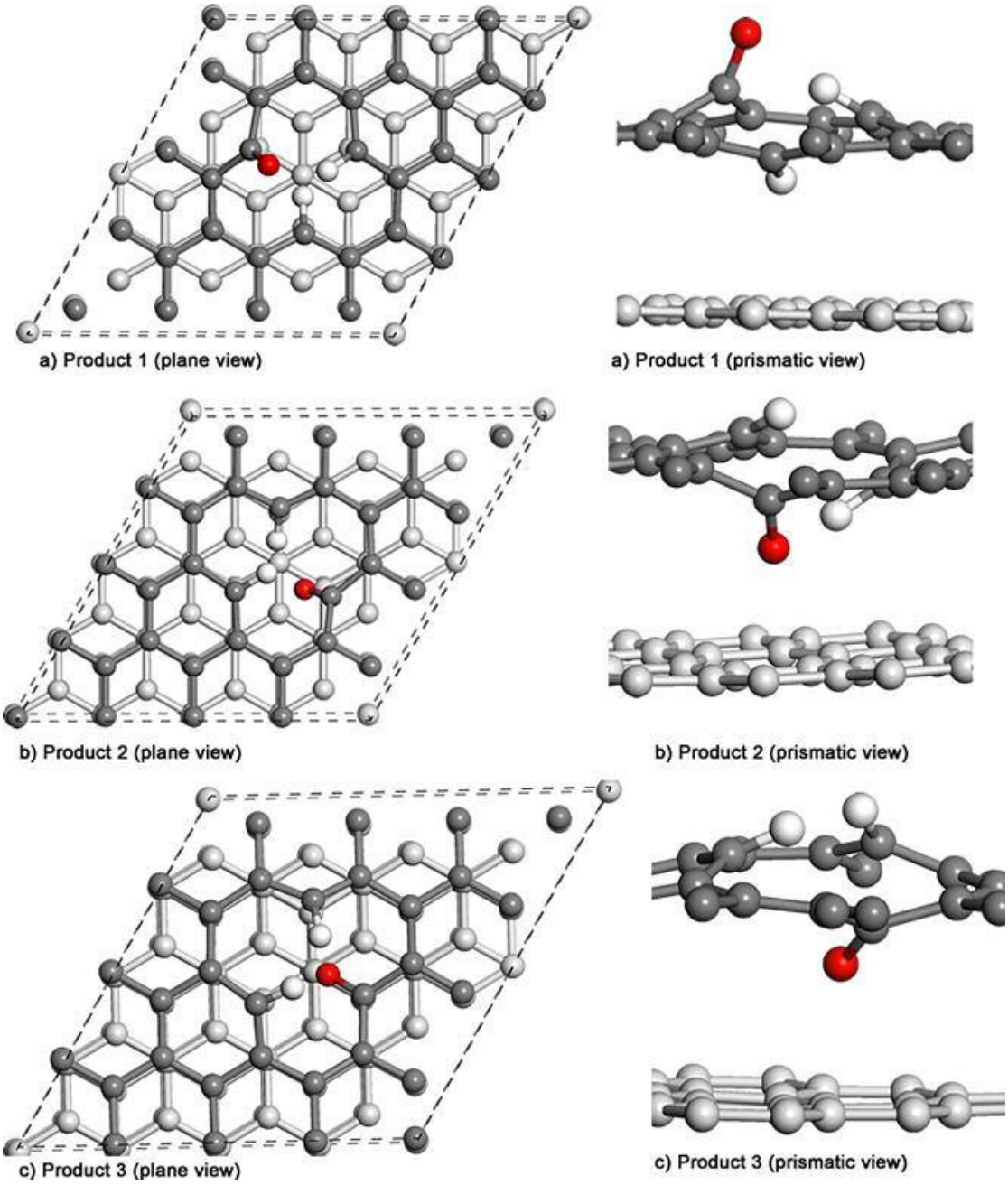

Fig. 33. The lowest energy arrangements of hydrogens and oxygen atoms which have been calculated for a chemisorbed water molecule at monovacancy site.

	Interlayer distance C-C (Å)	In-plane C_1-C_2 dist. (Å)	C-H_1 dist. (Å)	O-H_1 dist. (Å)	O-H_2 (Å)	H-O-H Bond ang. (deg.)	E_{ads} (eV)

Isolated V_1	3.291	2.517	-	-	-	-	-
Free water	-	-	-	0.972	0.972	104.66	-
Product 1	3.514	1.388	1.089	3.011	1.883	39.630	-3.568
Product 2	3.923	1.407	1.091	1.641	2.646	53.977	-2.725
Product 3	3.411	1.380	1.091	1.076	1.069	53.991	-2.660

Tab. 3.8 Some selected geometrical parameters of the optimised atomic arrangements of the most stable structures resulting from the chemisorption of water at monovacancy defect.

The most stable structure resulting from the chemisorption of water at V_1 defect is Product 1 in Figure 33 and Tab. 3.1. This product is formed by an exothermic process of ~3.57 eV. In this structure the interlayer distance is increased of 0.223 Å with respect to the free standing reactant surface. The carbon atom, which is involved in the bond with oxygen is pulled out of the plane of 0.967 Å. The shortest interatomic distance between the carbon atoms at the vacancy is of 2.786 Å whereas the largest is of 2.967 Å. With respect to the isolated surface, these interatomic distances are stretched of 0.230 and 0.422 Å, respectively. The C-O bond length is of 1.239 Å whereas the C-H interatomic distances are of 1.076 Å for the hydrogen above the plane and 1.089 Å for the other one. The interatomic distance between the oxygen and the hydrogen above the plane is stretched of 0.861 Å whereas the distance between oxygen and the other hydrogen is stretched of about ~2 Å. The angle bond between two hydrogen and oxygen is reduced of 50.68 degrees.

The other two optimised products will briefly discussed to understand which role plays the oxygen atom when is placed into the interlayer space.

The chemisorption of water in Product 2 is exothermic of -2.72 eV, the interlayer distance is increased of 0.632 Å. In the neighbourhood of the vacancy the planar C-C distances variate from 1.392 to 1.430 Å. The carbon which is bonded to oxygen is pushed into the interlayer space of 0.493 Å. The interatomic distance between oxygen and nearest neighbour in the underlying layer is of 2.570 Å. In addition, the C-O bond length is of 1.234 Å namely 0.05 Å shorter than that of Product 1. The two C-H bond lengths are of

1.091 and 1.081 Å. The interatomic distances between the top hydrogen and oxygen is of 2.646 Å whereas that between the bottom hydrogen and oxygen is of 1.641 Å. The bond angle between two hydrogens and oxygen of 50.67 Å.

Finally, in Product 3, the energy released during the chemisorption of water at the mono-vacancy is of -2.660 eV. The interlayer distance is increased of 0.103 Å and the carbon which is bonded to the oxygen is pushed into the interlayer space of 0.346 Å. The C-O bond length is of 1.234 Å, the same values that was found in Product 2. The O-H bond lengths are of 1.069 and 1.076 Å and the bond angle between hydrogens and oxygen is reduced of 71.85 degrees.

At this point, it is possible to say that in the most favoured adsorption configuration, one the hydrogen atom is oriented above the graphitic plane whereas the other one points down to the underlying planes. This arrangement minimises the repulsions arising when three atoms: oxygen and two hydrogens are located at the same side of the plane.

The saturation of the three dangling bonds around the vacancy quenches the dangling bonds. Thus, the oxygen and hydrogen decorated vacancy is more stable energetically.

Finally, comparing the results which have been obtained with those which have been reported in literature, a good agreement is found between the physisorption energy of a water molecule at the vacancy site. In this work, the lowest energy which was calculated for the physisorption was of -214 eV and corresponded to a water molecule placed at 2.099 Å far from a vacancy carbon. In the work of Carbrera-Sanfelix *et al.* [132], the dissociative adsorption of a water molecule was investigated on a monolayer of graphene. Using the GGA PBE xc functional, they found that water is physisorbed at the vacancy releasing an amount of energy of 210 meV, the H-C distance they calculated is of 2.14 Å. For the chemisorption of water at vacancy, they calculated an exothermic process of ~3.21 eV while in this work, the calculated energy for the chemisorbed intermediate is of -3.568 eV. These small differences can be attributed to the following fact, in the work of Cabrera-Sanfelix, only a graphene monolayer was used whereas in this work the graphite surface is modelled by using five graphene layers. In addition, Carbrera-Sanfelix did not account for the van der Waals forces which play a very important role in processes such as molecule adsorption on surfaces. Incorporating the dispersion corrections results in a lowering of the system total energy which explain nature of the small differences in distance and energy values.

3.19 Interaction between water and defected graphite: Divacancy (V_2).

In this section the interaction between water and a divacancy is considered. As in the case of the V_1, four possible adsorption sites can be found when the dispersion correction are used to describe the interaction between the water molecule and the graphite surface. In Fig. 34

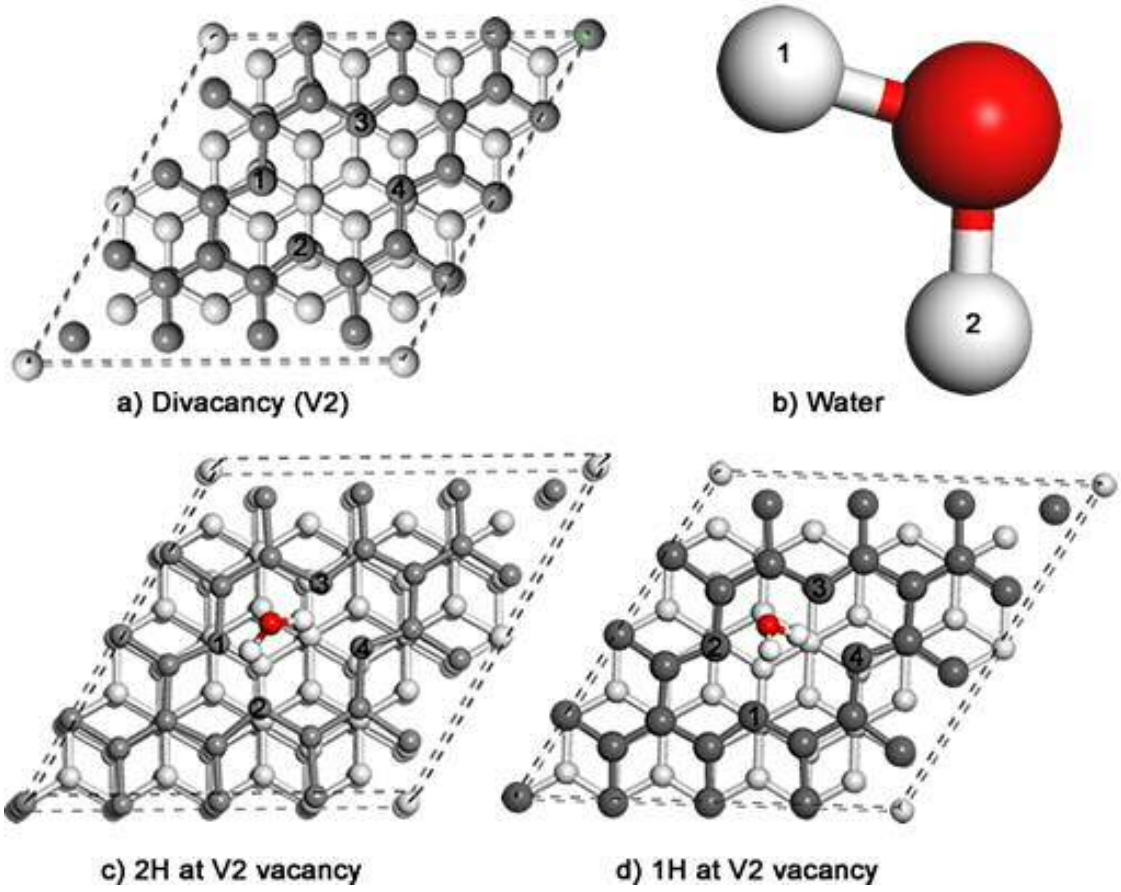

Fig. 34 Optimised atomic arrangement of a) V_2 vacancy defect, b) water, c) a water molecule with both hydrogens pointing down toward the surface (2H) and d) water molecule with a hydrogen pointing down toward the surface (1H).

	Interlayer distance C-C (Å)	In-plane C_1-C_2 dist. (Å)	C-H_1 dist. (Å)	O-H_1 dist. (Å)	O-H_2 (Å)	H-O-H	E_{ads} (eV)

						Bond ang. (deg.)	
Isolated V_2	3.285	1.520	-	-	-	-	-
Free water	-	-	-	0.972	0.972	104.66	-
1H	3.246	1.525	2.193	0.974	0.972	104.49	-0.198
2H	3.497	1.495	2.217	0.974	0.973	104.52	-0.186

Tab. 3.9 Selected parameters of the lowest energy optimised structures. These structure refer to the physisorption of a water molecule at the divacancy defect. The label 1H refers to water with 1H pointing toward the surface whereas 2H describes the orientation of a molecule which has both hydrogens pointing toward the surface.

The adsorption of water in 1H orientation is an exothermic process which releases 198 meV. The interlayer distance is decreased of 0.039 Å. Due to the rearrangement of the atoms near the vacancy the bond distance in the first layer result dramatically modified; with respect to the free standing reactants, the interatomic distance between two atoms forming a hexagonal ring is increased of 0.005 Å. The carbon atom (4 in Fig. 34 d)) is out of the plane of 0.235 Å. The interatomic distance between the atoms 4 and 3 is increased of 0.021 Å. The separation between carbon 4 and hydrogen is of 2.193 Å and the interatomic distance between the latter and oxygen is stretched of 0.002 Å. Oxygen and the other hydrogen atom are found at 0.972 Å. The bond angle is HOH is reduced of 0.17 degrees.

The water molecule in a 2H orientation is physisorbed at V_2 vacancy by an exothermal process which involves 186 meV. The interlayer distance is increased of 0.062 Å. The inter plane C-C distance is diminished of 0.095 Å. Carbons 2 and 4 are found above the plane of 0.051 and 0.034 Å, respectively whereas the interatomic distances between the carbons 2-1 and 3-4 are stretched of 0.012 and 0.009 Å, respectively. The interatomic distances between carbon 4 and the nearest hydrogen atom is found of 2.328 Å whereas

the interatomic distance between carbon 2 and hydrogen is 2.217 Å. The bond length between oxygen and hydrogens stretched of 0.001 and 0.002 Å.

Surprisingly, the water molecule with orientation 1H is found to better stabilise the total system. In a divacancy the unpaired electrons are unstable and extremely reactive. Thus, unsaturated carbon atoms react with each other forming two pentagons. This situation is at lower energy. The interaction with one hydrogen atom yield two unpaired electrons, one on carbon 4 and the other one on carbon 3. The interaction with two hydrogens generates four dangling bonds and the system is less stabilised. In the work,

In analogy with monovacancy, the divacancy can chemisorb water. The dissociation of a water molecule at the divacancy is shown in Fig. 35. As in the previous cases, for the sake of brevity, only the most stable structure is discussed.

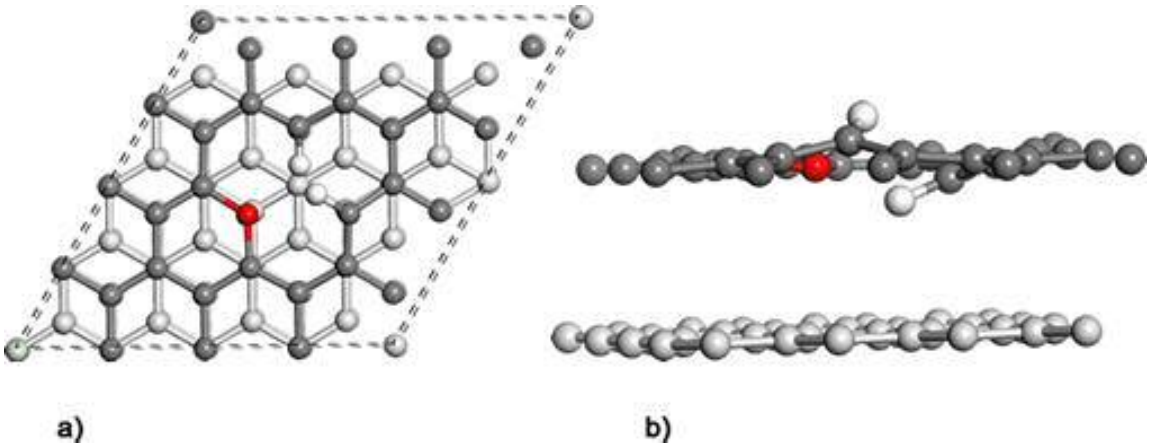

Fig. 3.35 Optimised atomic arrangement of a water molecule adsorbed at divacancy. In the figure, planar view a) and a prismatic view b) are shown

	Interlayer distance C-C (Å)	In-plane C_1-C_2 dist. (Å)	C-H_1 dist. (Å)	O-H_1 dist. (Å)	O-H_2 (Å)	H-O-H Bond ang. (deg.)	E_{ads} (eV)
Isolated V_2	3.285	1.520	-	-	-	-	-

Free water	-	-	-	0.972	0.972	104.66	-
Product 1	3.247	1.413	1.073	2.111	2.006	54.016	-4.956

Tab. 3.10 Selected geometrical parameter of the equilibrium atomic arrangement of a water molecule adsorbed at V_2.

When water molecule is chemisorbed at the divacancy the energy released is of ~5 eV. The dissociation of water is characterised by an energy barrier. Unluckily, due to the horizontal movement of the free layers during the search of the transition state by the NEB method, the convergence of energy was not obtained. In the final product of the chemisorption of water on V2, the interlayer distance is shortened of 0.038 Å. The in-plane C-C distance is decreased of 0.107 Å. To bind the hydrogen atom above the plane, the carbon atom extrudes from the graphitic plane of 0.756 Å whereas the other carbon if found 0.842 Å below the plane. The bond length between carbon and hydrogen are both of 1.073 Å. In contrast with the monovacancy, the oxygen atom lies into graphitic plane and form a bond with each of the two carbon which is of 1.384 Å in length. Finally, the HOH bond is reduced of 50.64 degrees. The large stabilisation which is obtained by the chemisorption of water on V_2 is mainly due to the quenching of the unpaired electrons. In addition, the oxygen atom lies in the carbon plane at large distance from hydrogen. In this position there are not repulsive interaction with hydrogen and the total geometry of the divacancy is less distorted with respect to the V_1. To the best of our knowledge, there are not published work on chemisorption of water on graphite divacancy. In the work of Xu et. al. [135], dissociation of water at divacancy was studied on graphene and the author discussing the dissociative process on many types of surface reported the dissociative barrier height of the dissociation of water molecule at divacancy which results to be of 0.35 eV while the calculated energy for the final product was below -5.84 eV. Cabrera-Sanfelix *et. al.* [134] reported that the barrier height for the dissociation of water on V1, such a barrier is of 0.47 eV. Considering that the energy of the barriers in both the chemisorption is quite low and the whole process of dissociation of water is exothermic, the dissociation of water at graphitic vacancy is a process which might occur at ambient temperature.

Finally, it is interesting to discuss the last case wich is represented by the physisorbtion of a water molecule on the Stone-Wales defect. The atomic arrangement is reported in figure 3.36.

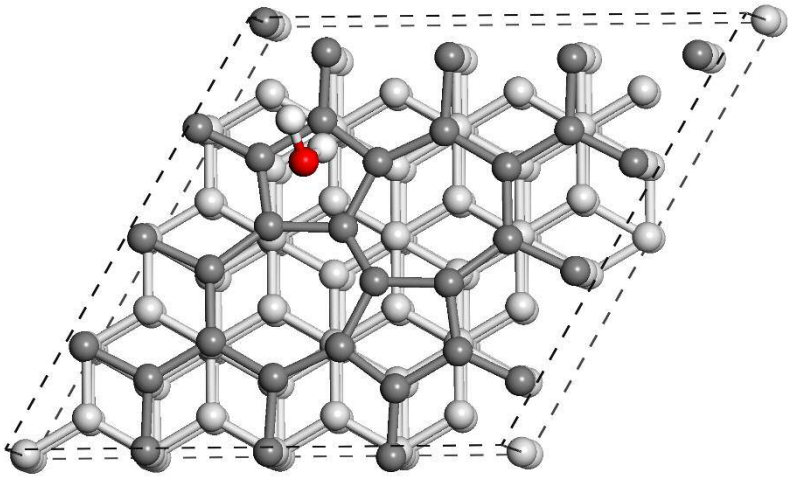

Fig. 3.36 A water molecule is physisorbed in hollow position in the pentagonal ring.

	Interlayer distance C-C (Å)	In-plane C_1-C_2 dist. (Å)	C-H_1 dist. (Å)	O-H_1 dist. (Å)	O-H_2 (Å)	H-O-H Bond ang. (deg.)	E_{ads} (eV)
Isolated SW	3.455	1.312	-	-	-	-	-
Free water	-	-	-	0.972	0.972	104.66	-
1H-SW	3.356	1.420	2.40	0.974	0.972	104.38	-0.180

Tab. 3.11 Selected parameters of the optimised atomic arrangement of a water molecule adsorbed on Stone-Wales defect.

Although the Stone-Wales defect does not present any unsaturated carbon, its ability to adsorb water molecules is better than that of the pristine graphite surface. In fact when a water molecule is adsorbed at SW defect, the system releases an energy amount of 180

meV. The interlayer distance decreases of 0.099 Å. The planar C-C distance between the two carbons forming the opposite pentagon rings is stretched of 0.005 Å. The C-H_1 bond length of 2.513 Å suggests that water is physisorbed on the surface. The O-H_1 bond length is stretched of 0.002 eV and the bond angle is diminished of 0.28 degrees.

3.20 References

[1] P. L. Silveston, R. R. Hudging, R. V. Vladea int. PCT Patent Publication WO 995915 (1999).

[2] I. Mochida, Y. Kawabuchi, S. Kawano, Y. Matsumura and M. Yoshikawa, *Fuel*, 1997, 76, 543–548.

[3] F. Adib, A. Bagreev and T. J. Bandosz, *Langmuir*, 1999, 16, 1980–1986.

[4] C. Sotowa, Y. Watanabe, S. Yatsunami, Y. Korai and I. Mochida, *Appl. Catal., A*, 1999, 180, 317–323.

[5] K. Miura, J. i. Hayashi, T. Kawaguchi and K. Hashimoto, *Carbon,* 1993, 31, 667–674.

[6] Y. Shao, J. Sui, G. Yin and Y. Gao, *Appl. Catal., B*, 2008, 79, 89–99.

[7] L. Feng, Y. Yan, Y. Chen and L. Wang, *Energy Environ. Sci.*, 2011, 4, 1892–1899.

[8] M. Zhang and L. Dai, *Nano Energy*, 2012, 1, 514–517.

[9] D. Lafyatis, R. Mariwala, E. Lowenthal and H. Foley, Expanded Clays and Other *Microporous Solids*, ed. M. Occelli and H. Robson, Springer US, 1992, pp. 318–332.

[10] F. Stüber, J. Font, A. Fortuny, C. Bengoa, A. Eftaxias and A. Fabregat, *Top. Catal*., 2005, 33, 3–50.

[11] M. Pérez-Mendoza, M. Domingo-Garcia and F. J. López-Garzón, *Appl. Catal., A*, 2002, 224, 239–253.

[12] H. Kühl. H. Jüntgen, in *Chemistry & Physics of Carbon*, ed. T. P. A. Kruck, Marcel Dekker, New York, 1989, vol. 22, pp. 145–195.

[13] D. C. Elliott, *Biofuels., Bioprod. Biorefin*., 2008, 2, 254–265.

[14] Q. Song, R. Xiao, Y. Li and L. Shen, Ind. Eng. Chem. Res., 2008, 47, 4349–4357.

[15] S. C. Petrosius and R. S. Drago, *J. Chem. Soc*., Chem. Commun., 1992, 344–345.

[16] M. Farcasiu, S. C. Petrosius and E. P. Ladner, *J. Catal*., 1994, 146, 313–316.

[17] H. Marsh, F. Rodríguez-Reinoso, *Activated Carbons*, Elsevier, Oxford, 2006.

[18] J. F. H. Peter, L. Zheng and S. Kazu, *J. Phys.: Condens. Matter*, 2008, 20, 362201.

[19] Y. Yang, K. Chiang and N. Burke, *Catal. Today*, 2011, 178, 197–205.

[20] E. Antolini, *Appl. Catal., B*, 2009, 88, 1–24.

[21] J. Pyun, *Angew. Chem*., Int. Ed., 2011, 50, 46–48.

[22] R. W. Coughlin, *Prod. Res. Dev*., 1969, 8, 12–23.

[23] V. V. Strelko, V. S. Kuts and P. A. Thrower, *Carbon*, 2000, 38, 1499–1503.

[24] 105. S. Chen, J. Bi, Y. Zhao, L. Yang, C. Zhang, Y. Ma, Q. Wu, X. Wang and Z. Hu, *Adv. Mater*., 2012, 24, 5593–5597.

[25] K. Ai, Y. Liu, C. Ruan, L. Lu and G. Lu, *Adv. Mater*., 2013, 25, 998–1003.

[26] L. Qu, Y. Liu, J.-B. Baek and L. Dai, ACS Nano., 2010, 4, 1321–1326.

[27] T.-J. Zhao, W.-Z. Sun, X.-Y. Gu, M. Rønning, D. Chen, Y.-C. Dai, W.-K. Yuan and A. Holmen, *Appl. Catal*., A, 2007, 323, 135–146.

[28] B. F. Machado, M. Oubenali, M. Rosa Axet, T. Trang Nguyen, M. Tunckol, M. Girleanu, O. Ersen, I. C. Gerber and P. Serp, *J. Catal*., 2014, 309, 185–198.

[29] J. Zhu, A. Holmen and D. Chen, *ChemCatChem*., 2013, 5, 378–401.

[30] F. Carrasco-Marín, A. Mueden and C. Moreno-Castilla, *J. Phys. Chem. B*, 1998, 102, 9239–9244.

[31] P. Roisson, J.-P. Brunelle, P. Nortier, in: A.B. Stiles (Ed.), *Catalyst Supports and Supported Catalysts*, Butterworth, Boston, 1987, p. 11.

[32] A. B. Stiles (Ed.), *Catalyst Supports and Supported Catalysts*, Butterworths, Boston, 1987, p. 57.

[33] T. D. Tran, S. H. Langer*, Electrochim. Acta* 38 (1993) 1551.

[34] A. Giroir-Fendler, D. Richard, P. Gallezot, *Faraday Discuss*. 92 (1992) 69.

[35] D. Richard and P. Gallezot, in Studies in Surface Science and Catalysis, ed. P. Grange, P. A. Jacobs, B.Delmon and G. Poncelet, Elsevier, 1987, vol. 31, pp. 71–81.

[36] C. Prado-Burguete, A. Linares-Solano, F. Rodriguez-Reinoso and C. S.-M. De Lecea, J. Catal., 1991, 128, 397–404.

[37] Z. H. Zhu, S. Wang, G. Q. Lu and D. K. Zhang, Catal. Today, 1999, 53, 669–681.

[38] F. Coloma, A. Sepulveda-Escribano, J. L. G. Fierro and F. Rodriguez-Reinoso, Langmuir, 1994, 10, 750–755.

[39] F. J. Derbyshire, V. H. J. de Beer, G. M. K. Abotsi, A. W. Scaroni, J. M. Solar and D. J. Skrovanek, Appl. Catal., 1986, 27, 117–131.

[40] H. T. Chung, J. H. Won and P. Zelenay, Nat. Commun., 2013, 4, 1922.

[41] K. Parvez, S. Yang, Y. Hernandez, A. Winter, A. Turchanin, X. Feng and K. Müllen, ACS Nano., 2012, 6, 9541–9550.

[42] T. Holme, Y. Zhou, R. Pasquarelli and R. O'Hayre, Phys. Chem. Chem. Phys., 2010, 12, 9461–9468.

[43] M. C. Román-Martínez, D. Cazorla-Amorós, A. Linares-Solano, C. S. M. N. De Lecea, H. Yamashita and M. Anpo, Carbon, 1995, 33, 3–13.

[44] E. G. Rodrigues, M. F. R. Pereira, X. Chen, J. J. Delgado and J. J. M. Órfão, J. Catal., 2011, 281, 119–127.

[45] K. Schick, F.J. Carduck, G. Goebel, H. Rollberg, German Patent DE 4209832 (1993), to Henkel KgaA.

[46] R.L. Seagraves, British Patent GB 2024643 (1979), to Du Pond De Nemours and Company.

[47] H. P. Boehm, C. Morterra, A. Zecchina, G. Costa (Eds.), Elsevier, Amsterdam, 1989, p. 145.

[48] H.P. Boehm, Carbon 32 (1994) 759.

[49] L.R. RadovõÂc, F. RodrõÂguez-Reinoso, in: P.A. Thrower (Ed.), Chemistry and Physics and Carbon, Vol. 25, Marcel Dekker, New York, 1997, p. 243.

[50] H. Marsh, F. Rodríguez-Reinoso, Activated Carbons, Elsevier, Oxford, 2006.

[51] J. F. H. Peter, L. Zheng and S. Kazu, J. Phys.: Condens. Matter, 2008, 20,

362201. [52] Y. Chen, Y. Zhu, Z. Wang, Y. Li, L. Wang, L. Ding, X. Gao, Y. Ma and Y. Guo, Adv. Colloid Interface Sci., 2011, 163, 39–52.

[52] Suhas, P. J. M. Carrott and M. M. L. Ribeiro Carrott, Bioresour. Technol., 2007, 98, 2301–2312.

[53] E. L. K. Mui, D. C. K. Ko and G. McKay, Carbon, 2004, 42, 2789–2805.

[54] J. M. Dias, M. C. M. Alvim-Ferraz, M. F. Almeida, J. Rivera-Utrilla and M. Sánchez-Polo, J. Environ. Manage., 2007, 85, 833–846

[55] O. Ioannidou and A. Zabaniotou, Renewable Sustainable Energy Rev., 2007, 11, 1966–2005.

[56] Y. Chen, Y. Zhu, Z. Wang, Y. Li, L. Wang, L. Ding, X. Gao, Y. Ma and Y. Guo, Adv. Colloid Interface Sci., 2011, 163, 39–52.

[57] F. Rodrõ Âguez-Reinoso, M. Molina-Sabio, Carbon 30 (1992) 1111.

[58] D. D. L. Chung, J. Mater. Sci., 1987, 22, 4190–4198.

[59] W. Li, C. Han, W. Liu, M. Zhang and K. Tao, Catal. Today, 2007, 125, 278–281.

[60] P. Shi, S. Zhu, H. Zheng, D. Li and S. Xu, Desalin. Water Treat., 2013, 1–8.

[61] J. Bian, M. Xiao, S. J. Wang, Y. X. Lu and Y. Z. Meng, J. Colloid Interface Sci., 2009, 334, 50–57.

[62] I. M. Afanasov, O. N. Shornikova, V. V. Avdeev, O. I. Lebedev, G. V. Tendeloo and A. T. Matveev, Carbon, 2009, 47, 513–518.

[63] H.-Q. Li, Y.-G. Wang, C.-X. Wang and Y.-Y. Xia, J. Power Sources, 2008, 185, 1557–1562.

[64] P. Ferreira-Aparicio, M. A. Folgado and L. Daza, J. Power Sources, 2009, 192, 57–62.

[65] C. Marquez-Alvarez, I. Rodriguez-Ramos and A. Guerrero-Ruiz, Carbon, 1996, 34, 339–346.

[66] P. Gallezot, S. Chaumet, A. Perrard and P. Isnard, J. Catal., 1997, 168, 104–109.

[68] B. Bachiller-Baeza, A. Guerrero-Ruiz, P. Wang and I. RodrÍguez-Ramos, J. Catal., 2001, 204, 450–459.

[69] E. Díaz, S. Ordóñez, R. F. Bueres, E. Asedegbega-Nieto and H. Sastre, Appl. Catal., B, 2010, 99, 181–190.

[70] B. F. Machado and P. Serp, Catal. Sci. Technol., 2012, 2, 54–75.

[71] E. Castillejos and P. Serp, Carbon Nanotubes and Related Structures, Wiley-VCH Verlag GmbH & Co. KGaA, 2010, pp. 321–347.

[72] A. K. Mark, Dekker Encyclopedia of Nanoscience and Nanotechnology, Taylor

& Francis, 2nd edn, 2009, pp. 2723–2736.

[73] B. F. Machado and P. Serp, Catal. Sci. Technol., 2012, 2, 54–75.

[74] L. Zhang and Z. Xia, J. Phys. Chem. C, 2011, 115, 11170–11176.

[75] Y. Feng, F. Li, Z. Hu, X. Luo, L. Zhang, X.-F. Zhou, H.-T. Wang, J.-J. Xu and E. G. Wang, Phys. Rev. B, 2012, 85, 155454.

[76] J. Zhou, H. Song, X. Chen and J. Huo, J. Am. Chem. Soc., 2010, 132, 11402–11405.

[77] P. Serp, in Carbon Materials for Catalysis, John Wiley & Sons, Inc., 2008, pp. 309–372.

[78] A. M. Zhang, J. L. Dong, Q. H. Xu, H. K. Rhee and X. L. Li, Catal. Today, 2004, 93–95, 347–352.

[79] F. Coloma, A. Sepulvedaescribano and F. Rodriguezreinoso, *J. Catal.*, 1995, 154, 299–305.

[80] J. K. Lee and M.-J. Kim, Tetrahedron Lett., 2011, 52, 499–501.

[81] M. Gopiraman, S. G. Babu, Z. Khatri, K. Wei, M. Endo, R. Karvembu and I. S. Kim, Catal. Sci. Technol., 2013, 3, 1485–1489.

[82] M. Gopiraman, S. Ganesh Babu, Z. Khatri, W. Kai, Y. A. Kim, M. Endo, R. Karvembu and I. S. Kim, J. Phys. Chem. C, 2013, 117, 23582–23596.

[83] H Juntgen, Fuel 1986, 65, 1436-1446.

[84] M. Conte, C. J. Davies, D. J. Morgan, T. E. Davies, D. J. Elias, A. F. Carley, P. Johnston and G. J. Hutchings, J. Catal., 2013, 297, 128–136.

[85] M. Conte, A. F. Carley, C. Heirene, D. J. Willock, P. Johnston, A. A. Herzing, C. J. Kiely and G. J. Hutchings, J. Catal., 2007, 250, 231–239.

[86] J. K. Edwards, B. Solsona, E. N. N., A. F. Carley, A. A. Herzing, C. J. Kiely and G. J. Hutchings, Science, 2009, 323, 1037–1041.

[87] C. Buono, P. R. Davies, R. J. Davies, T. Jones, J. Kulhavy, Ryan Lewis, David J. Morgan, Neil Robinson and David J. Willock. *Faraday Discuss.*

[88] V.E. Popov, V.I. Lazukin, T. Skaya, I.N. Novikov, M.N. Yakumova, A. Yu,

Kinet. Katal. 17 (1979) 60.

[89] E. Bouleghlimat, P. R. Davies, R. J. Davies, R. Howarth, J. Kulhavy and D. J. Morgan, Carbon, 2013, 61, 124–133.

[90] F. Pippig, S. Sarghini, A. Holl¨ander, S. Paulussen and H. Terryn, Surf. Interface Anal., 2009, 41, 421–429.

[91] C. D. Batich, Appl. Surf. Sci., 1988, 32, 57–73.

[92] K. Wepasnick, B. Smith, J. Bitter, D. H. Fairbrother. *Anal Bioanal Chem* 2010;396(3):1003–14.

[93] L. A. Langley, D. E. Villanueva, D. H. Fairbrother. Chem Mater 2006;18(1):169–78.

[94] N. P. Zschoerper, V. Katzenmaier, U. Vohrer, M. Haupt, C. Oehr,

T. Hirth. *Carbon* 2009;47:2174–85.

[95] H-H Cho, K. Wepasnick, B. A. Smith, F. K. Bangash, D. H. Fairbrother, W. P. Ball. *Langmuir* 2009;26(2):967–81.

[96] N. Nakajima, Y. Ikada. *Bioconjugate Chem.* 1995;6(1):123–30.

[97] T. Iwasawa T, P. Wash, C. Gibson, Jr J. Rebek. *Tetrahedron* 2007;63(28):6506–11.

[98] K. Kishi and S. Ikeda, J. Phys. Chem., 1974, 78, 107–112.

[99] G. Kresse and D. Joubert, Phys. Rev. B 59, 1758 (1999).

[100] G. Kresse and J. Furthmuller, Comput. Mater. Sci 6, 15 (1996).

[101] J. Antony and S. Grimme. *Phys. Chem. Chem. Phys.*, 2006, 8, 5287–5293.

[102] M. Amft, S. Lebesgue, O. Eriksson, N. V. Skorodumova, J. Phys.: *Condens. Matter* 23 (2011) 395001.

[103] J. P. Perdew, K. Burke and M Ernzerhof 1996 *Phys. Rev. Lett*. 77 3865.

[104] H. J. Monkhorst and J. D. Pack 1976 *Phys. Rev. B* 13 5188.

[105] R. Haering, *Can. J. Phys*. 36 (1958) 352-362.

[106] P. L., Jr Walker, *Carbon*, 28(3-4):261-279 (1990).

[107] W. T. Pong and C. Durkan C *J. Phys. D* 38 R329 (2005).

[108] M. Kuwabara, D. R. Clarke and D. A. Smith *Appl. Phys. Lett*. 56 2396. (1990)

[109] J. Osing and I. V. Shvets *Surf. Sci*. 417 145 (1998).

[110] Z. Y. Rong and P. Kuiper. *Phys. Rev. B* 48 17427 (1993).

[111] E. Fermi, 'Possibility of a Chain Reaction, USAEC Report CP-383', University of Chicago, (1942).

[112]E. P. Wigner, USAEC Report CP-387, University of Chicago (1942).

[113] H.H.W. Losty,' Radiation Effects on Mechanical Properties', in: R.E. Nightingale (Ed.) Nuclear Graphite', Academic Press, New York and London, (1962).

[114] R. H. Telling and M. I. Heggie *Phil. Mag.* 87 4797–846. (2007).

[115] Kelly B T 2000 Fundamentals of Radiation Damage in Graphite Due to Energetic Neutrons (TECDOC) vol 1154 (Vienna: IAEA) chapter 1 pp 1–34.

[116] J. Rossato, R. J. Baierle, A. Fazzio and R. Mota, *Nano Lett*., 2004, 5, 197–200.

[117] I. Gerber, M. Oubenali, R. Bacsa, J. Durand, A. Gonçalves, M. F. R. Pereira, F. Jolibois, L. Perrin, R. Poteau and P. Serp, *Chem. Eur. J*., 2011, 17, 11467–11477.

[118] Coulson C A, Herraez M A, Leal M, Santos E and Senent S 1963 *Proc. R. Soc. Lond*. A 274 461–79.

[119] C. Van der Wall and J. Neugebuer, *J. Appl. Phys.* 95 3851 (2004).

[120] L. Li, S. Reich, J. Robertson Phys. Rev. B 72 184109 (2005)

[121] E. Kaxiras and K. C. Pandey, Phys. Rev. Lett. 61 2693 (1998).

[122] A. A. El-Barbary, R. H. Telling, C. P. Ewels, M. I. Heggies, P. R. Briddon, Phys. Rev. B. 68, 1441107 (2003).

[123] A. Krasheninnikov, P. Lehtinen, A. Foster, and R. Nieminen, *Chem. Phys. Lett*. 418, 132 (2006).

[124] G. Henkelman, H. Jonsson, J. Chem. Phys. 113 (2000) 9978.

[125] A.V. Krasheninnikov, P.O. Lehtinen, A.S. Foster, R.M. Nieminen, *Chem. Phys. Lett.* 418 (2006) 132.

[126] Latham C D, Heggie M I, Alatalo M, O¨ berg S and Briddon P R *2013 J. Phys.: Condens. Matter* 25 135403.

[127] G. Lee, C.Z. Wang, E. Yoon, N. Hwang, D. Kim, K.M. Ho*, Phys. Rev. Lett*. 95 (2005) 205501.

[128] S. Picozzi, S. Santucci, L. Lozzi, L. Valentini and B. Delley, *J. Chem. Phys*., 2004, 120, 7147–7152.

[129] S. H. Yang, W. H. Shin and J. K. Kang*, J. Chem. Phys.*, 2006, 125, 084705.

[130] K. S. Novoselov, A. K. Geim, S. V. Morozov, D. Jiang, Y. Zhang, S. V. Dubonos, I. V. Grigorieva and A. A. Firsov, *Science*, 2004, 306, 666–669.

[131] G. R. Jenness and K. D. Jordan, *J. Phys. Chem. C*, 2009, 113, 10242–10248.

[132] A. I. Frolov, K. Kirchner, T. Kirchner and M. V. Fedorov, *Faraday Discuss*., 2012, 154, 235–247.

[133] R. R. Q. Freitas, R. Rivelino, F. d. B. Mota and C. M. C. de Castilho, *J. Phys. Chem. A*, 2011, 115, 12348–12356.

[134]P. Cabrera-Sanfelix and G. R. Darling. *J. Phys. Chem. C,* Vol. 111, No. 49, 2007

[135] Xu, Z. et al. Sci. Rep. 4, 6450; DOI:10.1038/srep06450 (2014).

Chapter 4

Pristine graphite surfaces do not have a sufficient number of reactive sites. The only active sites are found at the unsaturated carbons which located at the edges or defects on the surface represent the only source of reactivity. These unsaturated carbon atoms may chemisorb oxygen or water from exposure to the atmosphere, originating surface group. These groups can act as active sites in various reactions, and their type and concentration can be further increased by oxidative treatments. In this chapter, the anchoring property of O-functionalised graphite surface will be investigated. The experimental results will be presented before to discuss the computational results which are aimed to support the experimental findings. The investigation on the interaction between gold nanoparticles and functionalised graphite was carried out using the dispersion corrections method of DFT-D2 which demonstrate to be an indispensable tool in capturing the long-range interactions.

4.1. Nitric acid treatment of graphite surface.

In the previous chapter, it was described the change in topography of HOPG surfaces when are treated with water and diluted HCl. The atomic force microscopy showed that, after acid treatment, some topological features were appeared on the graphitic surface. These were attributed to local area delamination and by DFT we were able to suggest that these features stem from defects and species intercalated between the layers. In addition, as largely described in the previous chapter, the presence of dangling bond at defect sites facilitates the functionalisation of the surfaces with oxygen-containing

groups. Computational simulations clearly show how the presence of foreign species on the surface may easily modify the interlayer bonding. These observations motivated further investigations aimed to identify the functional groups which were formed on the HOPG surface after acid treatment. Derivation method was used. By such a method, it was possible to observe that after acid treatment, hydroxyl groups were formed on the graphite surface and that subsequent heating was able to oxidize these group into carbonyl groups. These were finally identified as ketones. In that work, gold nanoparticles were also used but the collected data were limited to high gold coverage. In order to collect more information, the experiment was repeated and to verify if the chemical behaviour of the graphite surface was the same, a more powerful oxidant, the nitric acid, was used. In addition, to study the deposition of noble metal catalysts on graphitic surfaces, gold nanoparticles, from aqueous solutions, was deposited on the HOPG support.

In analogy with the results which were obtained using diluted HCl, the AFM imaging of HOPG surfaces which were treated with diluted HNO_3 showed the presence of spherical features (Fig.1).

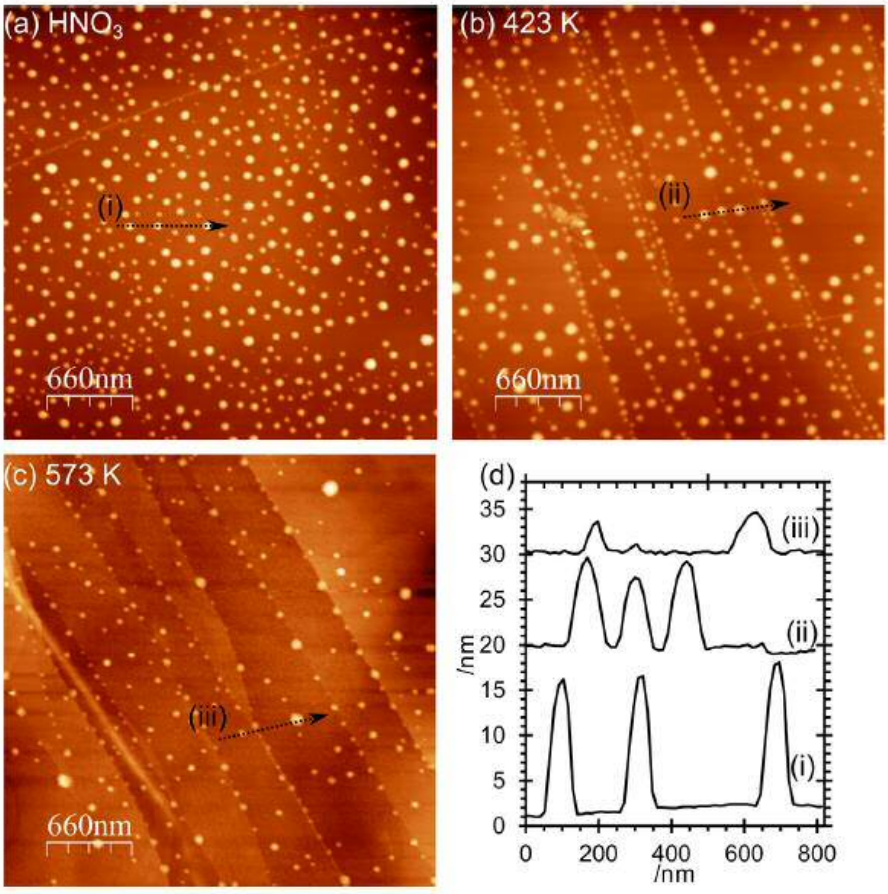

Fig. 1 AFM imaging shows the HOPG after treatment with 0.5 M of HNO_3 a) after treatment with acid for 30 minutes, b) after treatment heating to 423 K for 1h and c) after heating to 573 K for 1h d) line profile which is recorded from AFM images. These pictures were obtained by permission of the authors [1].

The corresponding XP spectra are shown in Fig. 2 and reveal a single peak in the O(1s) region at 532.8 eV with a calculated surface concentration of 6.3 10^{14} cm^{-2} corresponding to ~0.16 monolayers.

Changes in the C(1s) spectrum are too small to be detected against the background carbon signal but there is a small increase in the N(1s) region with the development of a peak with a surface concentration corresponding to ~1.4 1014 cm^{-2} at a binding energy of 400.2 eV indicative of an amine rather than a nitrate. In the previous experiment, it was seen that heating the sample in stages causes a decrease in the number of feature in the AFM images with an accompanying decline in the overall features. Unlikely HCl however, some features persisted after heating to 573 K.

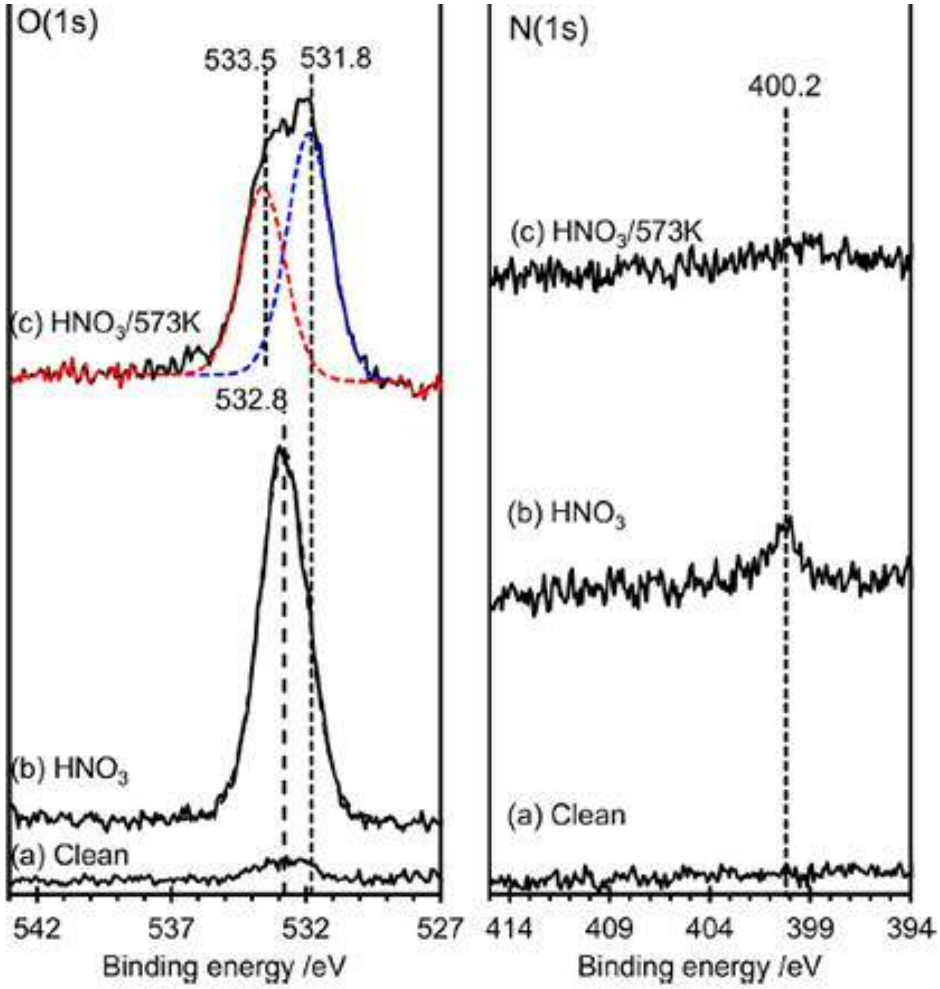

Fig. 2 XP spectra of HOPG after treatment with 0.5 M HNO3 and subsequent heating to 573 K. (a) Clean surface; (b) after treatment with 0.5 M HNO3 for 30 min; (c) after heating to 573 K for 1 h and cooling to ambient. These images were obtained by permission of the authors [1].

In Fig. 2, it is possible to see that in XP spectra that the peak in the N(1s) region disappears 573 K whereas the single peak in the oxygen region splits into two with binding energies of 531.8 and 533.5 eV. There is no significant change in the surface oxygen concentration on heating from 290 K to 573 K. Derivation methods which have been explained in Chap. 3 were used to identify the functional group at acid treated surfaces. Thus, in order to identify the hydroxyl groups the surface was treated with HNO_3 and then exposed to TFAA. The XP spectra is shown in Fig. 3 and suggests that the HNO_3 treatment of graphite surfaces generates a high concentration of hydroxyl

species, with a characteristic binding energy of ~532.7 eV. The fluoroacetate produced from the reaction of the TFAA with this hydroxyl will have two distinct oxygen species, a carbonyl can be assigned unambiguously to the O(1s) peak at 533.5 eV whilst the metoxy must contribute to the peak at 532 eV.

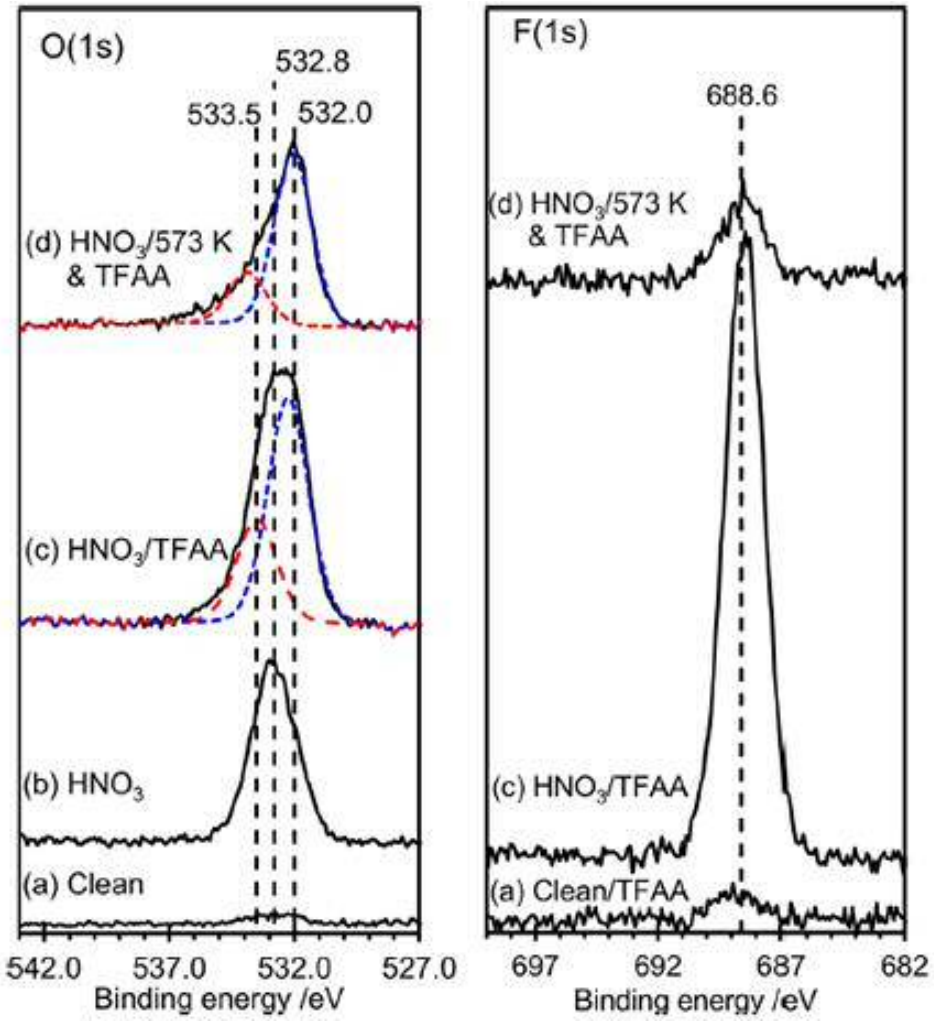

Fig. 3 XP spectra showing O(1s) and F(1s) regions of HOPG after treatment with HNO3 and TFAA. (a) Clean HOPG exposed to TFAA; (b) (in O(1s) spectra only for comparison), HOPG treated with 0.5 M HNO3 for 30 min; (c) surface in (b) after exposure to TFAA; (d) after heating (b) to 573 K for 1 h followed by exposure to TFAA. The images were adopted by the scientific report [1].

To identify the carboxylic groups on the surface, the derivatisation reactants TFE/CF_3CH_2OH/DTBC were used. After exposition of the surface to these reactants for 24 hours the XP spectra, which are shown in Fig. 4, revealed that carbonyl groups were not present on the clean HOPG surface whereas on the heated HNO3-treated surface to the TFE/DTBC mixture also results in only a minimal uptake in fluorine. Thus it was possible to conclude that mild HNO3 treatment of the HOPG surface does not lead to significant quantities of carboxylic functionality.

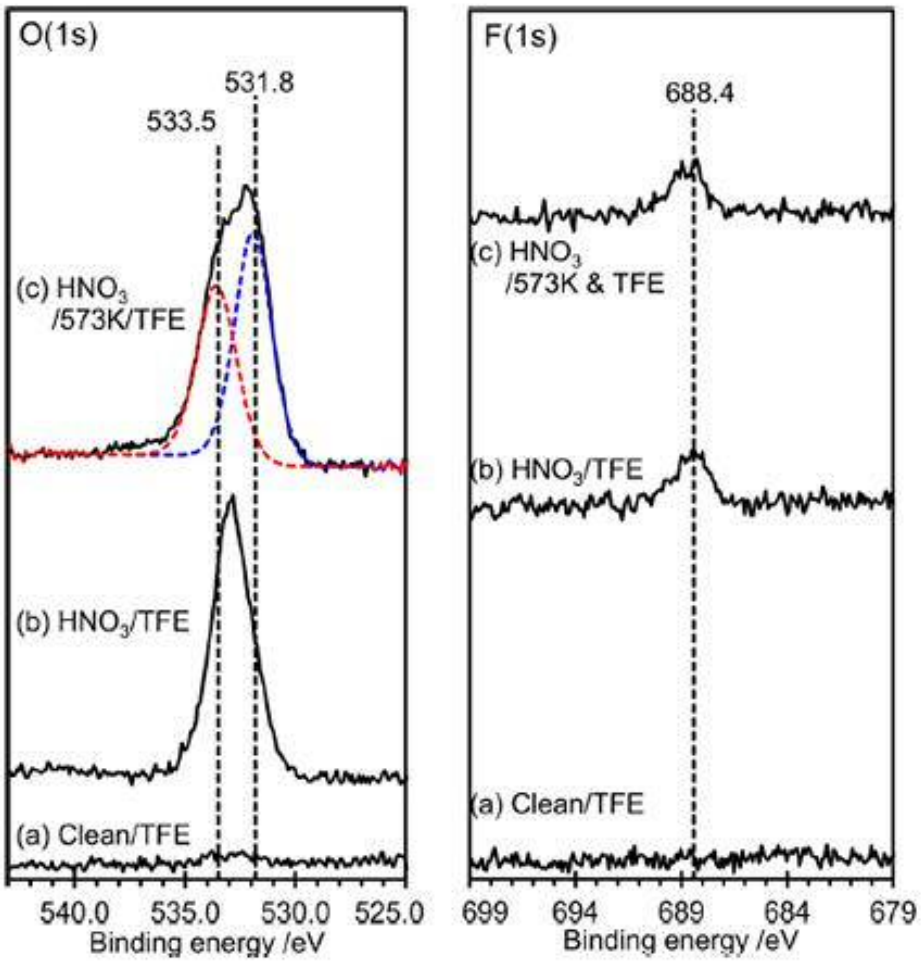

Fig. 4 The identification of carboxylic group by derivation reactant TFE/DTBC. XP spectra of HNO3-treated HOPG surface exposed to TFE vapour. (a) Clean HOPG surface exposed to TFE; (b) HOPG surface treated with 0.5 M HNO3 and subsequently exposed to TFE; (c) HOPG surface treated with 0.5 M HNO3 and heated for 1 h to 573 K before exposure to TFE. The images were adopted from the scientific report [1].

The identification of carbonyl group was conducted using trifluoroethyl hydrazine (TFH) which revealed that exposure of the HOPG surface to TFH after HNO_3 washing and subsequent heating to 573 K results in much more extensive reaction. A strong peak develops in the fluorine region at 688.4 eV accompanied by a strong peak at 400.5 eV in the N(1s) region. The presence of the peak at 531.9 eV could be assigned to the hydroxyl group which being in close proximity with hydrazine group could be the reason for the shifting of the OH binding energy significantly from that of the hydroxyl group observed after HCl treatment.

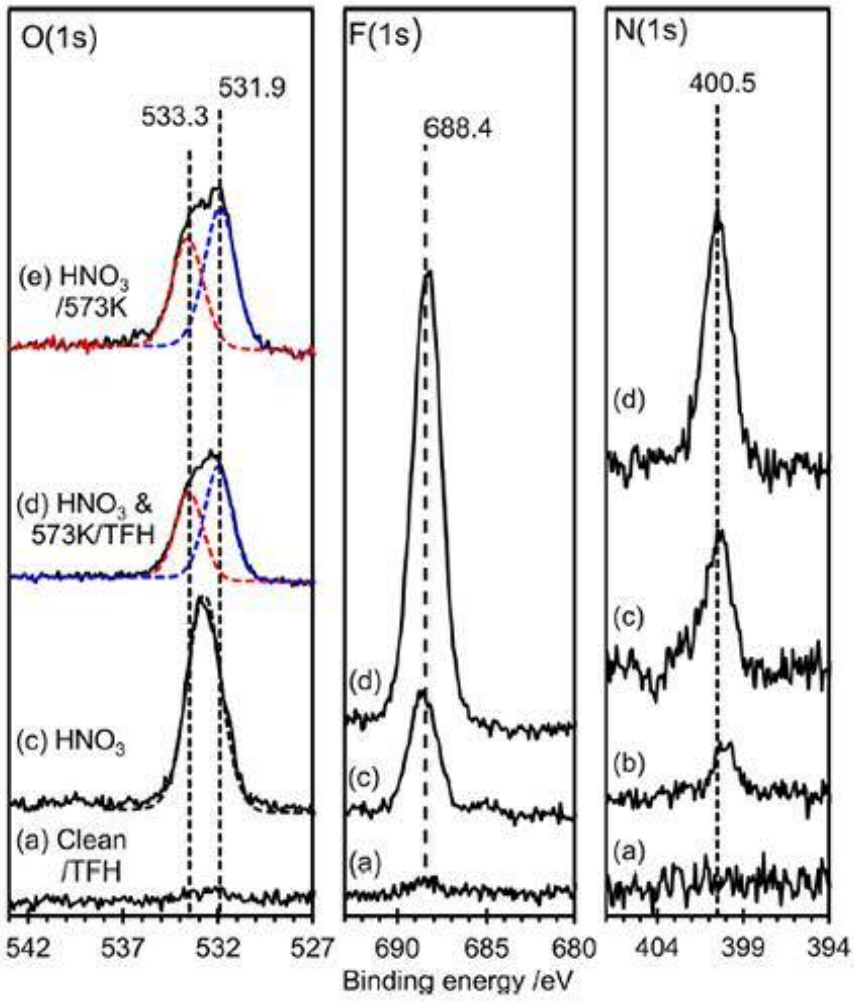

Fig. 5. XP spectra of HNO3-treated HOPG surface exposed to TFH vapour. (a) Clean HOPG surface exposed to TFH; (b) (N(1s) spectra only), HOPG surface treated with 0.5 M HNO3; (c) HOPG surface treated with 0.5 M HNO3 and subsequently exposed to TFH; (d) HOPG surface treated with 0.5 M HNO3 and heated for 1 h to 573 K before

exposure to TFH; (e) (O(1s) spectra only), HNO3-treated surface heated to 573 K surface without TFH exposure for comparison.

4.2 Gold deposition at acid treated HOPG surfaces.

The process of heating to high temperature the acid treated HOPG surfaces allows one to isolate specific functional groups which are formed on the surfaces and explore how these groups influence gold nucleation from solution to carbon. The XP spectra of deposited gold on surfaces containing mostly hydroxyl, carbonyl and ethers groups are reported in Fig. 6 are reported the AFM images of the HOPG surface after gold deposition from a solution of $HAuCl_4$.

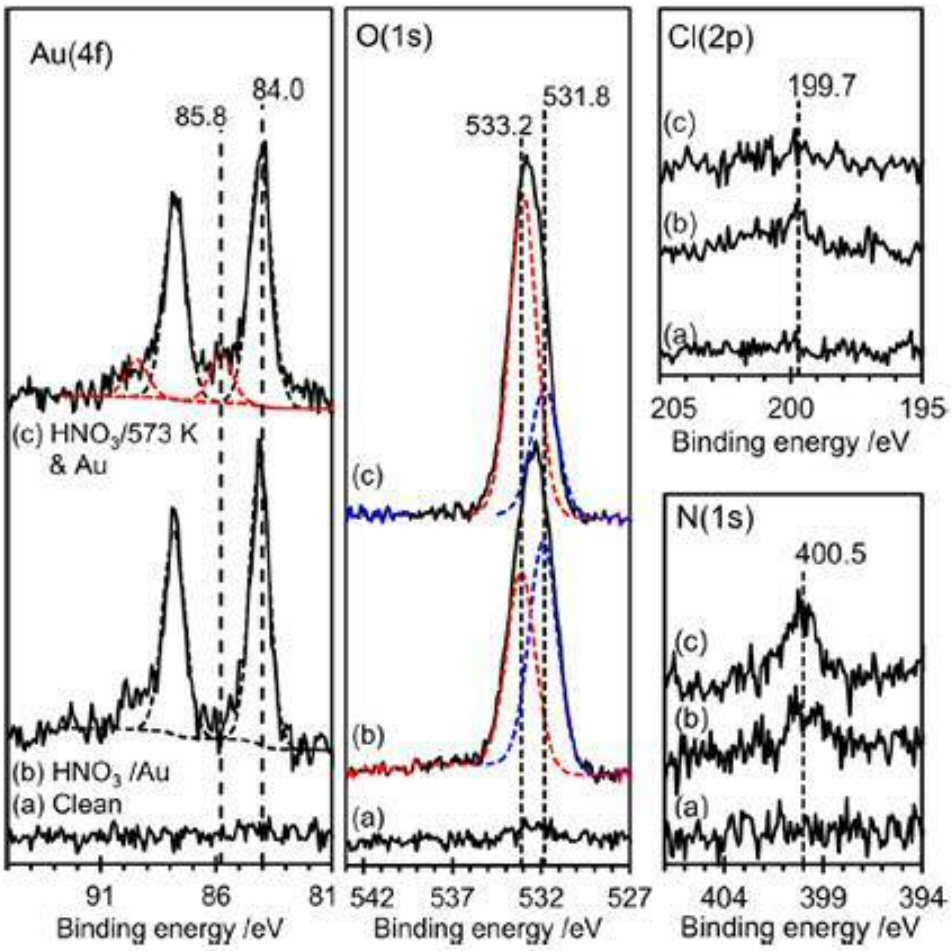

Fig. 6 XP spectra of the HOPG surface after gold deposition from a solution of chloroauric acid: in a) Clean HOPG surface, in b) HOPG surface treated with 0.5 M

HNO_3 which was dried and then exposed to the chloroauric acid c) HOPG surface treated with acid, dried and heated to 573 K. These images have been obtained from reference [1] by the permission of the authors.

The XP spectra reveals that gold is present in a single state, in fact the peak at 84.0 eV indicates Au^0. On the other hand the surface which is covered with ketones and ethers shows the presence of the second component, at 85.8 eV which can be identified as Au^{3+}.

AFM images reveal that the majority of gold nucleation takes places at the step edges when freshly cleaned HOPG is used whereas on HNO_3 treated surfaces, gold nanoparticles show a better dispersion. When gold were deposited on acid treated surfaces which were heated to oxidise the hydroxyl to ketones, it was observed a decrease of the number of particles accompanied with an increase of their sizes.

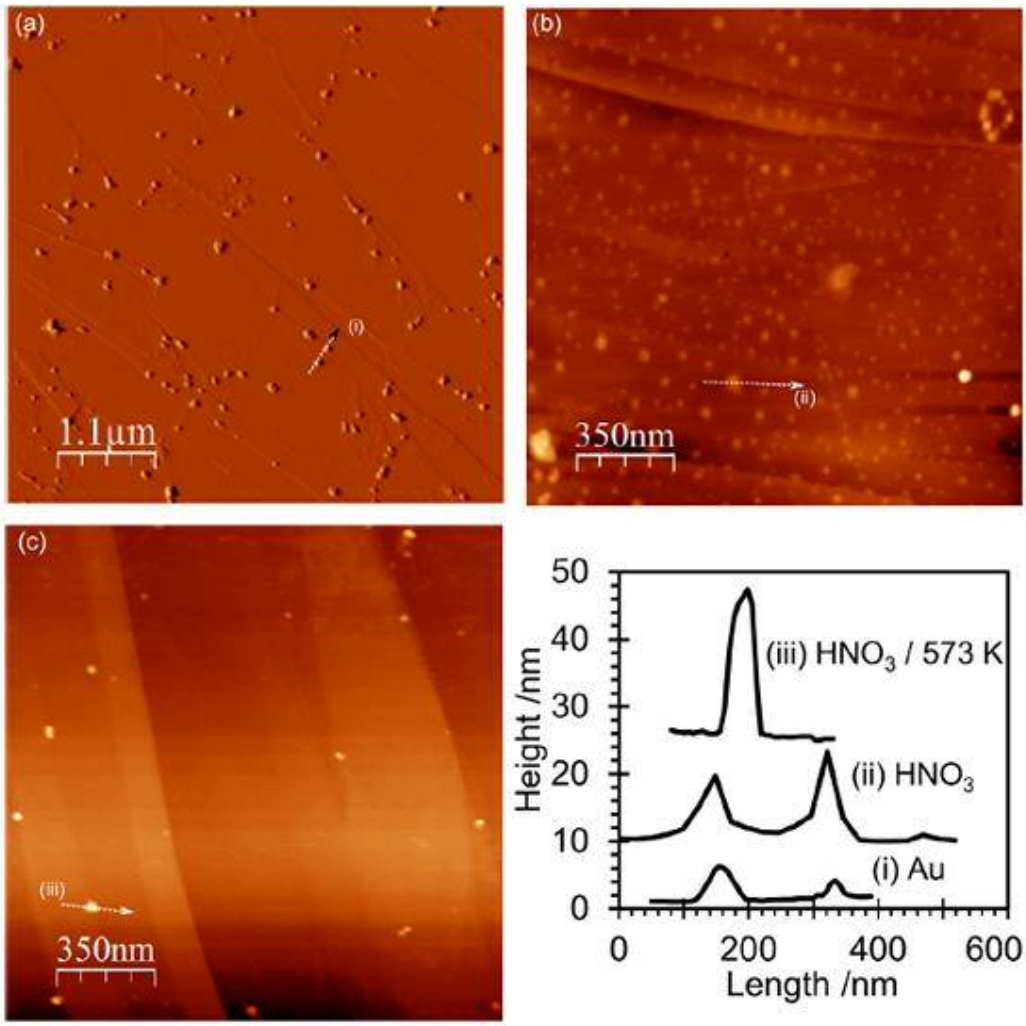

Fig. 7 AFM images of the HOPG surface after gold deposition from a solution of chloroauric acid: (a) Freshly cleaved HOPG surface exposed to a solution of HAuCl4; (b) HOPG treated with 0.5 M HNO3, dried and then exposed to a solution of HAuCl4; (c) HOPG treated with 0.5 M HNO3, dried and heated to 573 K (1 h) before cooling and exposure to a solution of HAuCl4; (d) line profiles from the AFM images. The use of these images have been obtained by the permission of the authors [1].

4.3 Computational methodology.

To support the experimental investigation, spin-polarised density functional theory (DFT) calculations were performed within the periodic plane-wave basis set code VASP 5.3 [2–5]. Projector augmented waves (PAW) potentials have been used to describe the ion cores leaving valence electronic configurations C(2s22p2), O(2s22p4), and Au(6s15d10) to be explicitly calculated whilst the ultrasoft pseudopotential has been employed for the H atoms. Exchange–correlation interaction was treated by generalised gradient approximation (GGA) in the parameterisation of Perdew, Burke, and Ernzerhof (PBE). The weak van der Waals interactions operating between the graphitic layers have been taken into account by the semi-empirical method of Grimme, DFT-D2 [6], as implemented in VASP. The dispersion coefficient, C_6, and van der Waals radius, R_0, for gold were taken to be 40.62 J nm6 mol^{-1} and 1.772 Å, respectively, as reported by Amft et al. [7]. For calculations on the bulk unit cell a *k*-point mesh of 5 5 3 was used which was reduced for the supercell calculations on surfaces to 3 3 1, in either case a Monkhorst–Pack grid was used for *k*-point sampling [8, 9]. The plane-wave basis set was defined by a 500 eV cutoff for all calculations. The width of the Gaussian smearing for the occupation of electronic levels was 0.01 eV and for surface calculations dipole corrections along the three directions of the unit cell vectors were included. All structures were optimised until a convergence of 10^{-5} eV was reached and the Hellman–Feynman forces on each relaxed ion were smaller than 10^{-4} eV $Å^{-1}$. In calculations on surfaces all atoms in the cell are optimised with the cell size and shape held fixed. The hexagonal unit cell of the most common Bernal structure for graphite [10–11] has experimental lattice constants of $a_0 = b_0 = 2.46$ Å and $c_0 = 6.78$ Å with c = 120 [12,13]. Following the above methodology these unit cell dimensions were optimised by a systematic scaling of the a_0 and b_0 lattice parameters, which define the intra-layer periodicity, followed by

scaling of the c_0 parameter, which gives the inter-layer repeat distance. The optimised cell parameters are $a_0 = b_0 = 2.465$ Å and $c_0 = 6.297$ Å. The in-plane CAC bond length of 1.420 Å is in good agreement the experimental value of 1.421 Å [13,14]. The inter-layer separation 3.149 Å is shorter than observed experimentally (3.354 Å) [14,15] by ~6% although it is in line with previous simulations using similar functionals [15,16]. Functionalisation of graphite is expected to take place preferentially at step edges where the more reactive edges of graphene sheets are available. Graphene simulation of the functionalization of sheet edges with oxygen-containing groups has been studied in detail by Mauri and co-workers [14,16–17]. We have chosen to work with stable termination at armchair edges which present isolated C-C bonds for addition of oxygen species. The unit cell was first redefined as a = a0, b = a0 + 2b0, c = c0, in this setting armchair step edges are created for Miller indices (10X) with X controlling the terrace length. All the simulations were performed using the (105) surface which gave sufficient separation between step edges for Au to be adsorbed at an effectively isolated step edge. The thickness of the simulation cell was set so that four aromatic rings separate oxygen functionalities on the same graphene sheet but opposite sides of the slab. We also employ a 2 2 surface supercell for all slab calculations so that periodic images of Au atoms are well separated in the direction parallel to the step edge and there are three empty steps in the simulations cell (Fig. 9). This gives a slab which contains 144 C, 16 O, and 32 H atoms. The adsorption energies of a gold atom at functionalised surfaces have been calculated by the expression:

were, is the total energy of the gold nanoparticle adsorbed on the surface, is the energy of the isolated surface and is the energy of the adsorbate in gas phase.

4.4 Hydroxyl and carbonyl group at step edges

Periodic DFT calculations using the PBE + D2 approach were used to give structures for an armchair edge containing hydroxyl and ketone functional groups. In each case, the additional valence of the edge carbon atoms is taken up with H atoms. In our previous work, we considered the energetics of producing the hydroxylated edge from reaction with water and determined the lowest energy arrangement of the functional groups along the step edge [18]. To accommodate adsorption of a gold atom, we have used a cell doubled in the step edge direction for this work. For the ketone functionalised edge, we have moved the hydroxyl H atom to the neighbouring edge carbon atom, so that the slab structures have the same stoichiometry. This gives simple models to compare the adhesion of gold to the two types of surface oxygen-containing groups on the graphite surface. The relaxed structures of the functionalised edges are shown in Fig. 8 and 9. In both cases, the oxygen groups move significantly out of the plane of the graphene

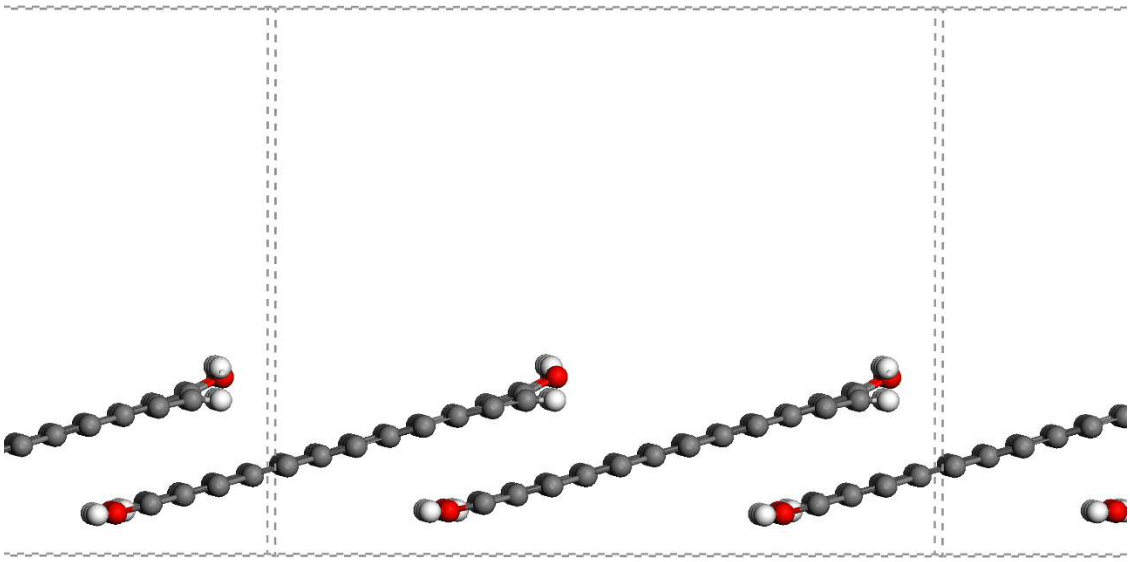

Fig. 8 Slab structure of hydroxylated graphite step edges. This images was adopted from the reference [1] and used under the permission of the authors.

In the free standing graphite which has been functionalised with hydroxyl groups, the interatomic distance between oxygen and hydrogen is 0.977 Å. The bond length between the carbon atom and oxygen is of 1.368 Å. The interatomic distance C-C is of 1.376 Å while the bond length between C-H is of 1.085 Å.

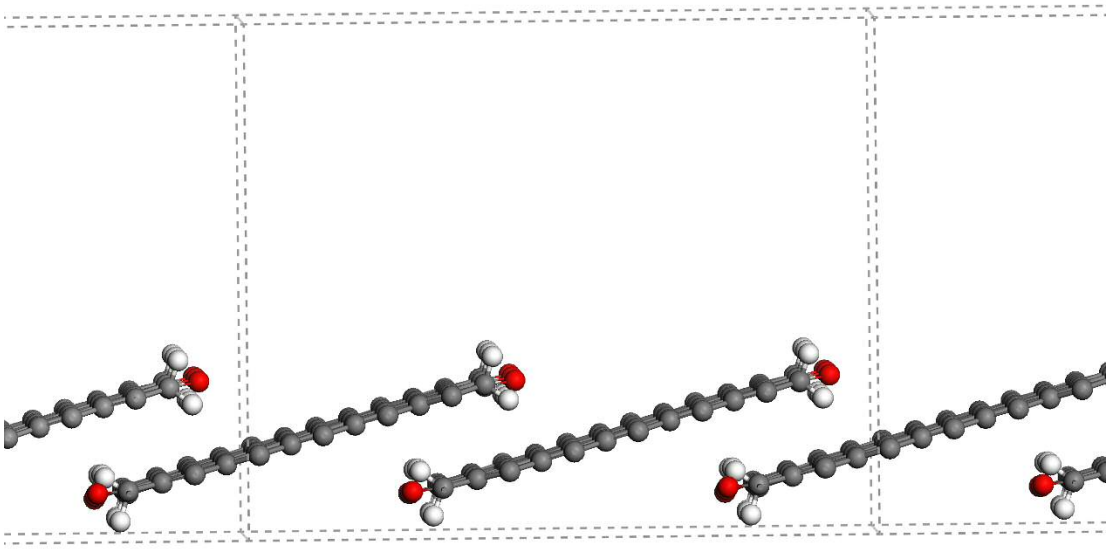

Fig. 9 Slab structure of carbonylated graphite step edges. This images was adopted from the reference [1] and used under the permission of the authors.

In the graphite surface that is functionalised with carbonyl groups, the C-O bond distance is of 1.241 Å and the interatomic distance between carbon and hydrogen is of 1.097 Å. Finally the C-C bond length is of 1.476 Å.

4.5 Gold clusters on hydroxylated surface

The structures and stabilisation of gold clusters Au_n (n=1…5) supported on hydroxylated surface have been investigate and the results of the geometry optimisation are here summarised. In correspondence of hydroxylated armchair step edges there are several adsorption sites. In this work, gold atoms were optimised in diverse locations relative to the step edges oxygen functionalization and to the carbon atoms of the terrace to find the preferential adsorption site which lead to the best stability. In other words, Gold clusters were positioned at atop, bridge and hollow sites on the terraces and in correspondence of oxygen or hydrogen atoms of the functional groups. In other words, all possible combinations were evaluated. Tab. 1 summarizes the relative stabilities of gold clusters on functionalised surfaces.

	O-H (Å)	C-O (Å)	Au-H (Å)	C-Au (Å)	Energy eV
Au	1.043	1.242	2.072	3.445	-1.791
Au_2	0.981	1.386	-	3.328	-2.668
Au_3	1.007	1.353	2.285	3.130	-3.114
Au_4	0.988	1.362	2.503	3.129	-2.804
Au_4 (Y)	0.983	1.363	2.797	3.119	-3.137
Au_5	1.013	1.369	2.189	3.529	-3.371

Tab 1. Relative energies and selected parameters resulting from the optimised structures.

Fig. 10 shows the optimised atomic arrangement of a gold atom at hydroxylated step edge graphite. The adsorption of gold is an exothermic process which involve 1.791 eV. The distances between gold and hydrogens are of 2.054 and 2.245 Å. The distance between the gold

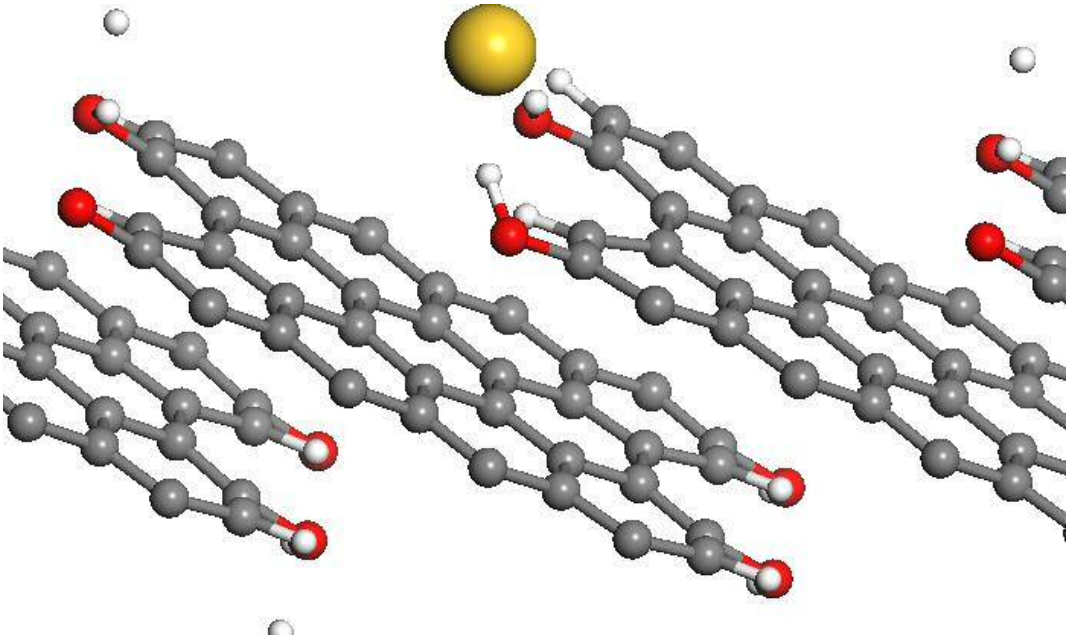

Fig. 10 Gold atom physisorbed at hydroxylated graphite step edges.

atom and the nearest carbon of the underlying layer is of 3.44 Å. The distance between hydrogen and oxygen is of 1.043 Å. Finally the distance between carbon and oxygen is of 1.242 Å. From Tab. 1, it is possible to see that with respect to the free standing reactants, the interaction between Au_5 and the hydroxyl group lead to the largest stabilisation.

Carbonyl	C-H (Å)	C-O (Å)	Au-O (Å)	C-Au (Å)	Energy eV
Au	1.098	1.260	2.367	3.260	-0.690
Au_2	1.094	1.238	2.131	3.281	-1.564
Au_3	1.099	1.286	2.123	3.174	-2.291
Au_4	1.097	1.233	2.231	3.251	-1.667
Au_4 (Y)	1.095	1.259	2.111	3.732	-2.511
Au_5	1.098	1.277	2.102	3.111	-2.752

Tab. 2 Relative energy of the optimised atomic arrangements of Au_n (n=1…5) clusters which are physisorbed on carbonyl groups at graphite step edges.

The Au_5 cluster adsorbed on carbonyl is another interesting structure because it is able to interact with two oxygen. The adsorption energy stabilises this structure at -3.942 eV. The C-H bond length is not affected by the adsorption of the cluster at functional group the C-O bond lengths of those oxygens which interact with gold are stretched of 0.036 and 0.041 Å. The shortest bond length between gold and oxygen is of 2.101 Å. Fig. 11 shows the Au_5 cluster physisorbed to the carbonylated surface. Figure 12 summarises the adhesion energies collected in the Tab 1 and 2. The trend suggests that hydroxyl groups better stabilise the small gold nanoparticles whereas the stabilisation decreases for large nanoparticles. On the other hand, the stabilisation resulting from the interaction between gold and carbonyl group is the same for both small and larger clusters.

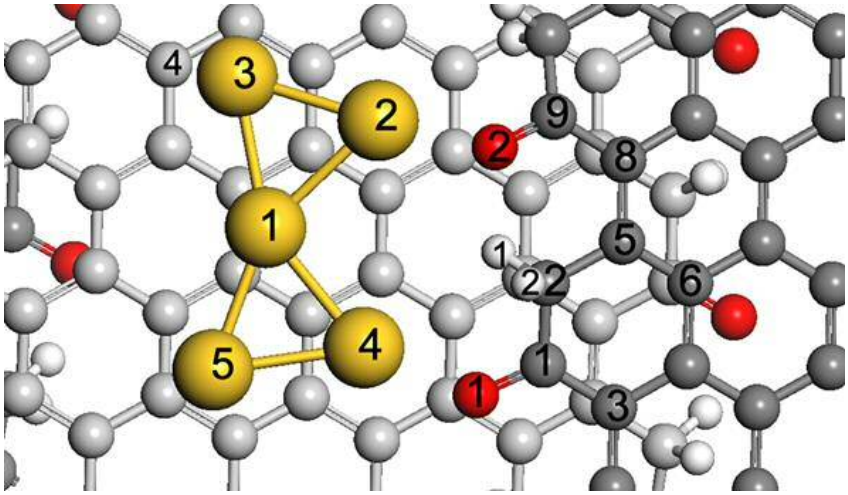

Fig. 11 Au_5 adsorbed at carbonylated graphite edges.

Comparing the energies collected in Tab. 1 and 2, it results that gold cluster are stabilised by carbonyl groups more than hydroxyl groups. This results is in good agreement with the experimental results which found that hydroxyl groups represent a better anchoring site for gold nanoparticles [1].

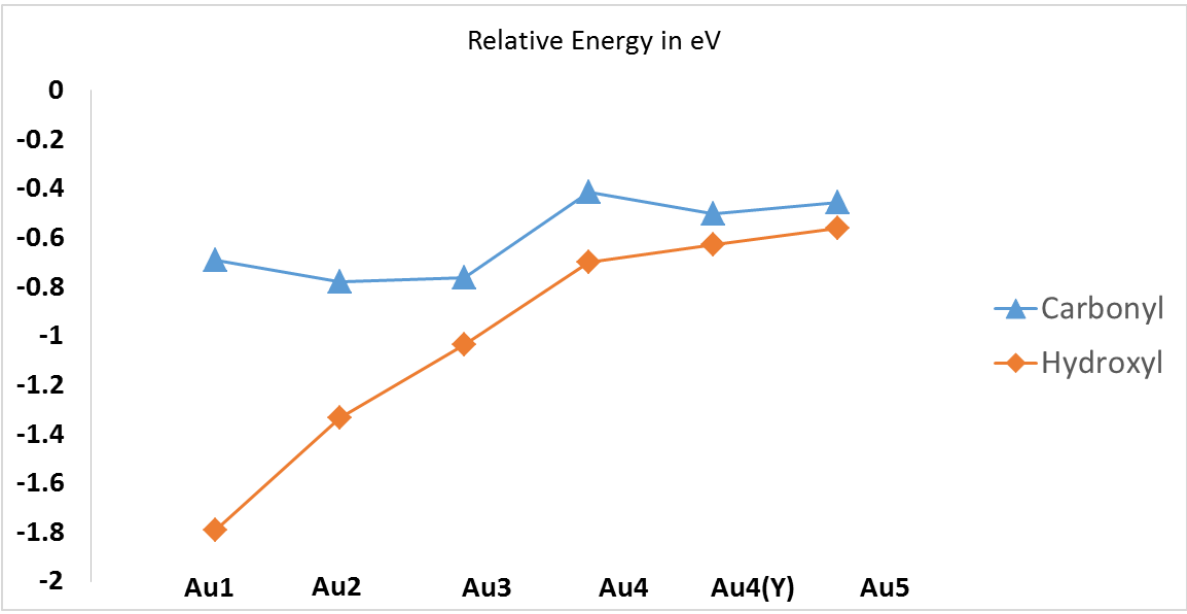

Fig. 12 Adhesion energy per Au atom/eV as function of the adsorbed clusters on carbonyl and hydroxyl functional groups.

References

[1] Rebecca Burgess, Carlo Buono, Philip R. Davies, Robert J. Davies, Thomas Legge, Amy Lai, Ryan Lewis, David J. Morgan, Neil Robinson , David J. Willock *Journal of Catalysis* 323 (2015) 10–18.

[2] G. Kresse, J. Hafner, Phys. Rev. B 47 (1993) 558–561.

[3] G. Kresse, J. Hafner, Phys. Rev. B 49 (1994) 14251–14269.

[4] G. Kresse, J. Furthmuller, Phys. Rev. B 54 (1996) 11169–11186.

[5] G. Kresse, J. Furthmuller, Comput. Mater. Sci. 6 (1996) 15–50.

[6] S. Grimme, J. Comput. Chem. 27 (2006) 1787–1799.

[7] M. Amft, S. Lebegue, O. Eriksson, N.V. Skorodumova, J. Phys.: Condens. Matter 23 (2011) 395001.

[8] H. Monkhorst, J. Pack, Phys. Rev. B 13 (1976) 5188–5192.

[9] R. Haering, Can. J. Phys. 36 (1958) 352–362.

[10] H. Lipson, A.R. Stokes, Proc. R. Soc. London, Ser. Math. Phys. Sci. 181 (1942) 101–105.

[11] D. McKie, C. McKie, Essentials of Crystallography, second ed., Blackwell Science Inc, 1986.

[12] D.R. Lide, CRC Handbook of Chemistry and Physics, 85th ed., CRC Press, 2004.

[13] A.P. Seitsonen, A.M. Saitta, T. Wassmann, M. Lazzeri, F. Mauri, Phys. Rev. B 82 (2010) 115425.

[14] G. Graziano, J. Klimes, F. Fernandez-Alonso, A. Michaelides, J. Phys.: Condens. Matter 24 (2012) 424216.

[15] T. Wassmann, A.P. Seitsonen, A.M. Saitta, M. Lazzeri, F. Mauri, J. Am. Chem. Soc. 132 (2010) 3440–3451.

[16] T. Wassmann, A.P. Seitsonen, A.M. Saitta, M. Lazzeri, F. Mauri, Phys. Status Solidi B: Basic Solid State Phys. 246 (2009) 2586–2591.

[17] T. Wassmann, A.P. Seitsonen, A.M. Saitta, M. Lazzeri, F. Mauri, Phys. Rev. Lett. 101 (2008) 096402.

Chapter 5

Hydrochlorination of acetylene is a process for the production of vinyl chloride monomer on industrial scale. The reaction may proceed by a mercury-free route via Au/C catalyst and, in this case, the experimental protocol for loading gold on graphitic materials suggests acid washing the support for removing impurities and creating hydrophilic functional groups on the carbonaceous surface [1]. Such a treatment has a direct effect on both the chemistry and the structure of the carbonaceous support. Diverse sources of carbon give rise to a various mixture of functional groups resulting in different properties. Considerable efforts have been made to understand the nature of such functional groups, the complex interactions that take place and their role in the nucleation of other functional materials at the surface. Since these finding are important in the context of understanding how carbon supports stabilise active components in heterogeneous catalysis, a systematic study combining both spectroscopic and computational methods was carried out. In this conclusive chapter, the obtained results are presented and discussed.

1. Conclusions and Outlook

In this research project, the density functional theory (DFT) formulation of quantum-mechanics has been used to obtain information, at molecular level, about processes occurring when functional groups are introduced on clean graphitic surface by diluted acid treatment. The computational study was aimed to support the results of experimental investigation on the identity of the functional groups formed by the acids,

on the effect of the heat treatment on functionalised surfaces and on the deposition of gold nanoparticles from aqueous solution [2, 3].

Since highly ordered pyrolytic graphite (HOPG) was used as model on which the fundamental properties of specific functional groups and their interactions with deposited nanoparticles can be characterised.

The first and most important step is that of finding a theoretical method capable to account for the dispersion interactions which play a fundamental role in layered materials. In chapter 2, the standard GGA xc functional in form of PBE [4] was used to study bulk properties. The comparison of computational results with experimental values showed that, although PBE gives a good description of the in-plane C-C bonds, it overestimated the interlayer binding. Thus, in order to improve upon the standard GGA xc functional, Grimme D2 dispersion corrections [5] have been incorporated into the PBE xc method and resulted that the performance of PBE-D2 (DFT-D2) was notably superior to that of PBE. Since DFT-D2 gives a more realistic description of graphite bulk properties, it has been used in all the following investigations.

Graphite has two types of surfaces, the basal planes ( ) and the prismatic planes which lead to the zig-zag ( ) and armchair (11 1) edges. A preliminary investigation on the reactivity of these surfaces was carried out considering the interactions with water molecules. Water can be placed onto the graphite surface in several orientations such as with one or both the hydrogens pointing toward the surface, in a horizontal position when the plane formed by the atoms is parallel to the plane of carbons of graphite layers and, finally, in the orientation where the oxygen atom is toward the carbon layer. It is well known that graphite repels water and the results of chapter 3 support the hydrophobic nature of graphite. In fact, water is only physisorbed on pristine graphite (000) surface and the most stable arrangement has been found when the distance between the hydrogen atom and the nearest neighbour carbon is of 2.450 Å.

When water is adsorbed in this position, the system releases 170 meV with respect to the free standing reactants. The insertion of a water molecule in the interlayer space was also investigated. Although all the possible space arrangements of the water molecules were considered, the unique arrangement resulting for the intercalated water is in the flat geometry, namely, the molecular plane of water is parallel to the graphite layers. The presence of intercalated water modifies dramatically the geometry of the

two nearest layers which are no more perfectly flat but present some curvatures in correspondence of the water molecule. The distance between the graphitic carbon planes is increased of 2.156 Å. The process of water intercalation is endothermic and calculated the calculated energy is of 1.377 eV. These finding have been used to support the experimental observations. The raised features are due to the presence of intercalated compounds which are also responsible for the delamination of graphite layers.

Since the pristine basal surface is inert to water, in order to find more reactive graphitic surfaces, point defects were introduced on the external graphite layer. The behaviour of a water molecule on a defected graphite surfaces was then investigated to understand which role is played by unsaturated carbon atoms. Water is chemisorbed on graphitic surfaces presenting point defects such as mono- and di- vacancies. In the first case, the chemisorption of a water molecule at the mono-vacancy defect leads to a carbonyl group. Four different arrangements of two hydrogen and one oxygen are possible. The most stable arrangement is obtained when the oxygen atom is on the top of the graphitic layer and the two hydrogens point in the two opposite directions of the graphene plane. With respect to the free standing reactants, the chemisorption of water is an exothermic process involving the release of 3.568 eV.

The reaction between the water molecule and a di-vacancy defect produces a pyran ring. The oxygen is coplanar to the five carbons while the hydrogens are placed on top and bottom of the graphitic plane. The formation of an aromatic ring is responsible of the large energy release which in this case is of -4.956 eV.

The Stone Wales defect was also considered, but no chemisorption was observed. The physisorbtion of water on a Stone Wales defect is more exothermic than on pristine graphite surface.

The introduction of functional groups results easier on defected surfaces but the formation of defects has a high cost in term of formation energy as it has been discussed in chapter 3. Since uncoordinated carbons are very reactive, it is expected that the functionalisation occurs preferentially on these sites. Thus, graphite prismatic surfaces were considered.

Graphite has two types of prismatic surfaces which are largely known with the names of armchair and zig-zag edges. Their characteristics have been discussed in chapter 4. The armchair edges are more stable than zig-zag edges and this can be also easily explained in terms of the number of resonance structures.

In chapter 4, the hydroxylated and carbonylated edges have been studied. About the hydroxylated edges, it is noteworthy mentioning that the more stable configuration is that where the hydrogens atoms of the hydroxyl groups point directly toward the nearest neighbour oxygen atoms.

The adsorption of gold adatoms and gold clusters consisting of up to five gold atoms was investigated. In good agreement with the experimental observations [2], stronger interactions between the metal and hydroxyl groups were found. This result suggests that the gold electronic cloud can be polarized leading to an induced dipole. Thus, it is possible to conclude that hydroxyl groups are better anchoring sites than carbonyl groups.

At this stage, it is also possible to suggest the next steps to follow in the understanding the role which functional groups have in gold catalysis.

Since the interaction of the gold catalyst with hydroxyl groups involves the polarisation of the metal electronic cloud, the effect of the partially removing electrons from gold catalyst could improve the ability of the metal in accepting electrons from coordinated acetylene molecules, in other words the hydroxyl groups improves the Lewis base character of the metal.

The effect of electron polarisation on the gold may be appreciated by the study of reaction pathways of acetylene hydrochlorination via gold catalyst which is supported by hydroxylated graphite and carbonylated graphite and then comparing the high of the energy barriers.

5.2 References

1. Conte M, Carley AF, Heirene C, Willock DJ, Johnston P, Herzing AA, et al. J. Catal. 2007 Sep; 250(2):231–9.
2. Burgess R., Buono C, Davies P R, Davies, R J., Legge, T, Lai A, Lewis, Ryan, et al. Journal of Catalysis 323, pp. 10-1.
3. Davies, Philip Rosser, Buono, Carlo, et al. Faraday Discussions 173 , pp. 257-272
4. J. P. Perdew, K. Burke and M. Ernzerhof, Phys. Rev. Lett., 1996, 77, 3865–3868.
5. S. Grimme, J. Comput. Chem., 2006, 27, 1787–1799.

ANNEX 1:
Specimen layout for Declaration/Statements page to be included in a thesis.

DECLARATION

This work has not been submitted in substance for any other degree or award at this or any other university or place of learning, nor is being submitted concurrently in candidature for any degree or other award.

Signed …… ……..…(candidate) Date…30/09/2016…..……

STATEMENT 1

This thesis is being submitted in partial fulfillment of the requirements for the degree of PhD (insert MCh, MD, MPhil, PhD etc, as appropriate)

Signed … ……..…… (candidate)
Date……..30/09/2016……

STATEMENT 2

This thesis is the result of my own independent work/investigation, except where otherwise stated, and the thesis has not been edited by a third party beyond what is permitted by Cardiff University's Policy on the Use of Third Party Editors by Research Degree Students. Other sources are acknowledged by explicit references. The views expressed are my own.

Signed …… ……..…… (candidate) Date……..30/09/2016……

STATEMENT 3

I hereby give consent for my thesis, if accepted, to be available online in the University's Open Access repository and for inter-library loan, and for the title and summary to be made available to outside organisations.

Signed …… ……..…..….. (candidate) Date 30/09/2016……

STATEMENT 4: PREVIOUSLY APPROVED BAR ON ACCESS

I hereby give consent for my thesis, if accepted, to be available online in the University's Open Access repository and for inter-library loans after expiry of a bar on access previously approved by the Academic Standards & Quality Committee.

Signed …… ……..…… (candidate) Date 30/09/2016……